
Statistical Physics of Active Particles

Ion Santra 

Supervisor: Sanjib Sabhapandit

Theoretical Physics Group,
Raman Research Institute, Bengaluru 560080, India.



A thesis submitted for the degree of *Doctor of Philosophy* to
Jawaharlal Nehru University, New Delhi

Declaration

I, *Ion Santra* (Enrolment No.: RRI/2018/020), declare that the work reported in this thesis titled '*Statistical physics of active particles*', is entirely original. This thesis has been composed independently by me at *Raman Research Institute (RRI)* under the supervision of *Prof. Sanjib Sabhapandit* and is the result of my own work unless otherwise stated. I further declare that the subject matter presented in this thesis has not previously formed the basis for the award of any degree, diploma, membership, associateship, fellowship or any other similar title of any university or institution. I also declare, this thesis has been checked using the software TURNITIN.

Sanjib Sabhapandit

Prof. Sanjib Sabhapandit

Supervisor

ion santra

Ion Santra

Candidate

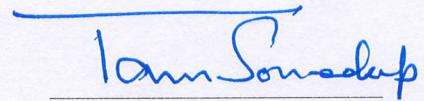
Certificate

This is to certify that the work contained in the thesis titled '*Statistical physics of active particles*', submitted by *Ion Santra* (Enrolment No.: RRI/2018/020) to the Jawaharlal Nehru University for the award of the degree of *Doctor of Philosophy (Ph.D.) in Physical Sciences*, is the bonafide record of original research work carried out by Ion Santra under my guidance and supervision at *Raman Research Institute (RRI)*, Bengaluru, India. The results embodied in the thesis have not been submitted to any other University or Institute for the award of any degree or diploma.



Prof. Sanjib Sabhapandit

Supervisor



Prof. Tarun Souradeep

Director

Synopsis

Brownian motion, which describes the typical movement of a colloidal particle in a fluid, is one of the most popular and well-understood stochastic processes. It has been successfully used to model diffusion in equilibrium media in different branches of natural science. However, many real-world systems are intrinsically out of equilibrium due to their ability to generate, absorb and dissipate energy, caused by some internal mechanical and dynamical processes. One popular class of such systems is ‘active matter,’ which refers to a collection of particles that have the ability to generate dissipative, persistent motion by extracting energy from their surroundings at an individual level[1, 2]. Numerous examples of such active systems can be found in nature, ranging from bacterial motion to cellular and tissue motility, granular matter, schools of fish, flocks of birds, etc. They exhibit many novel emergent collective behavior like motility-induced phase separation, clustering, and the absence of well-defined pressure [3, 4]. In recent years, high-accuracy single-particle tracking experiments have shown that, though the active particles move randomly, their motion is quite distinct from a typical Brownian motion [5]. For example, an *E. coli* bacterium runs in straight lines for some time, then turns abruptly to some other direction and runs in straight line along that direction, while an artificially created Janus particle moves along a fluctuating body axis with a constant velocity. These unusual, persistent dynamics lead to rich statistical properties even at the single-particle level [6, 7]. Thus the study of active particles, both as building blocks of active matter and as nonequilibrium stochastic processes, has attracted considerable interest in the statistical physics community, experimentalists, and theorists alike.

In this thesis, we investigate how the nonequilibrium nature of the active particle motion is manifested in their different physical observables. We start with minimal stochastic models that mimic the different active particle motions and study their statistical properties analytically. Due to their small size (typically a few micrometers), the effects of inertia on the movement of active particles are negligible and mathematically their motion is well-described by an overdamped Langevin equation $\dot{x}(t) = v(t) - \frac{\partial V(x)}{\partial x}$, which looks very similar to the description of overdamped Brownian motion $\dot{x}(t) = \eta(t) - \frac{\partial V(x)}{\partial x}$ [$V(x)$ is the external potential].

However, unlike delta-correlated Gaussian white noise $\eta(t)$ of the Brownian motion, the active velocity $v(t)$ has a stochastic dynamics of its own and is correlated in time. The correlation time serves as a measure of the activity. This stochastic dynamics of the velocity $v(t)$ leads to a violation of the fluctuation-dissipation theorem. Evidently, the single-particle equation of motion renders a picture out of equilibrium. One of the main objectives of this thesis is the analysis of simple dynamical models of active particles and infer possible differences with passive (Brownian) systems.

Since free Brownian motion [in the absence of any external potential $V(x)$] has no intrinsic time-scale, the description remains same at all times—the position distribution is Gaussian, and the fluctuations can be characterized by the second moment only, which follows a diffusive scaling. For active particles, the presence of the characteristic time-scale(s) leads to many different behaviors. In particular, at times shorter than the characteristic time-scale(s), the effect of activity is maximal—the position fluctuations are generically non-Gaussian (except special cases like active Ornstein-Uhlenbeck processes), and the corresponding distributions have non-trivial functional forms and shapes. At large times, much larger than the correlation time, the effects of the noise correlations almost die down, and discretizing the Langevin equation into uncorrelated intervals, one can heuristically show that the typical fluctuations are expected to be Gaussian with a diffusive scaling. The effect of activity, however, is not entirely lost, and its most prominent signatures are encoded in the large deviation function associated with the $x \sim O(t)$ fluctuations. Unfortunately, these correspond to the rare events that are hard to access experimentally, where one is often limited to the events of $x \sim O(\sqrt{t})$ fluctuations. So characterizing the higher-order non-Gaussian corrections at the scale $x \sim \sqrt{t}$ becomes very important.

Putting a Brownian particle in a confining (trapping) potential $V(x)$ introduces a characteristic time-scale in the system, which is related to the strength of the potential. If we wait till times larger than this characteristic time-scale, the particle equilibrates to the famous Boltzmann distribution $\propto \exp[-V(x)/(K_B T)]$. Though an active particle also reaches a stationary state in the long time limit, the distribution in general is non-Boltzmann. In fact, there is no general prescription to obtain the stationary distribution. It depends on the particular forms of the confining potential and stochastic dynamics of the active veloc-

ity. Moreover, even for specific forms of $V(x)$ and $v(t)$ dynamics, the stationary state is determined by a competition of the active and trapping time-scales. Naturally, exploring the stationary-state behavior of various active motions in confining potentials is of significant interest.

An essential observable for active particles is the time it takes to search for a particular target, such as a food source, a weak spot of the host, or toxins. From our everyday experience, a natural tendency to optimize the search time is to return to the starting point after a period of unsuccessful search and restart the search. This strategy is implemented in dynamical processes by ‘stochastic resetting,’ where a dynamic process is intermittently stopped and restarted from the initial starting position [8]. In addition to optimizing searching times, resetting leads to a host of interesting features like attaining a nonequilibrium stationary state at long times, dynamical transition in relaxation to the stationary states, unusual thermodynamic properties, universal extreme value statistics, etc. even for a standard Brownian particle. A natural question is how active particles react when they have additional resetting dynamics.

One of the primary objectives of nonequilibrium statistical physics is to understand energy transport in low dimensional systems connected to equilibrium/nonequilibrium reservoirs [9]. Though most works in this field have used equilibrium reservoirs, nonequilibrium reservoirs are being explored more recently due to their rich behavior. Collections of active particles, which have their own energy depot, serve as paradigmatic examples of nonequilibrium reservoirs. So an obvious question is what happens to the transport properties of an extended system when it is connected to two such ‘active reservoirs’.

This thesis attempts to address the issues discussed above to a reasonable extent. It is organized as follows. In chapter 1, we introduce active particle systems and discuss their importance both as building blocks of many naturally occurring complex systems and as a class of new and interesting stochastic processes. In this context, we also briefly review some results of ordinary Brownian motion, which will often be referred to in the remaining part of the thesis, for comparisons with similar counterparts of active systems.

In chapter 2, which consists of our work in [10], we study a set of run-and-tumble particle dynamics in two spatial dimensions. The particle “runs” in straight lines with a constant

speed along an internal spin/orientation direction, which also changes stochastically, resulting in the “tumbles”. The orientation vector in two-dimensions can be fully specified by an angle θ , which can take discrete or continuous values. We consider two different classes of RTPs where θ assumes (i) n discrete directions in space and (ii) continuous values in the range $[0, 2\pi]$. We compute the exact marginal position distributions for $n = 3, 4$ and the continuous case. We find that strong signatures of activity are seen in the short-time regime in the form of spatial anisotropy and/or ballistic nature of the motion. We also show that, in the long-time regime, while the typical fluctuations in position are characterized by Gaussian distributions for all the models, the atypical fluctuations still contain signatures of activity, which we characterize by explicitly calculating the large deviation functions.

Chapter 3 talks about the work in [11]. Here we study a minimal model, direction reversing active Brownian particle (DRABP), which mimics the motion of a class of bacteria like *Myxococcus xanthus* and *Pseudomonas putida*. The internal orientation vector has two independent stochastic dynamics here—it undergoes a rotational diffusion like an active Brownian particle (ABP) and intermittent reversal events, which changes the internal orientation angle by π . We show that, for such a motion in two dimensions, the presence of the two time scales set by the rotational diffusion constant D_R and the reversal rate γ gives rise to four distinct dynamical regimes: (I) $t \ll \min(\gamma^{-1}, D_R^{-1})$, (II) $\gamma^{-1} \ll t \ll D_R^{-1}$, (III) $D_R^{-1} \ll t \ll \gamma^{-1}$, and (IV) $t \gg \max(\gamma^{-1}, D_R^{-1})$, showing distinct behaviors. We characterize these behaviors by analytically computing the position distribution and persistence exponents. The position distribution shows a crossover from a strongly non-diffusive and anisotropic behavior at short-times to a diffusive isotropic behavior via an intermediate regime (II) or (III). In regime (II), we show that, the position distribution along the direction orthogonal to the initial orientation is a function of the scaled variable $z \propto x_{\perp}/t$ with a non-trivial scaling function, $f(z) = (2\pi^3)^{-1/2}\Gamma(1/4 + iz)\Gamma(1/4 - iz)$. Furthermore, by computing the exact first-passage time distribution, we show that a novel persistence exponent $\alpha = 1$ emerges due to the direction reversal in this regime.

In chapter 4, we discuss our work in [12], where we develop a general framework for studying the long-time behavior of a class of active particle dynamics and illustrate it using the most common and widely used models, namely, run-and-tumble particle, active Ornstein-

Uhlenbeck particle, active Brownian particle, and direction reversing active Brownian particle. Treating the ratio of the correlation-time of the active noise to the observation time as the small parameter, we show that the position distribution generically satisfies the diffusion equation at the leading order. We further show that the sub-leading contributions, at each order, satisfy an inhomogeneous diffusion equation, where the source term depends on the previous order solutions. We explicitly obtain a few sub-leading contributions to the Gaussian position distribution. As a part of our framework, we also prescribe a way to find the position moments recursively and compute the first few explicitly for each model.

Chapter 5 discusses our work in [13], where we study the direction reversing active Brownian particle in the presence of a harmonic trap of strength μ . The presence of the trap ensures that the position of the particle eventually reaches a steady-state where it is bounded within a circular region of radius $\propto \mu^{-1}$, centered at the minimum of the trap. Due to the interplay between the rotational diffusion constant D_R , reversal rate γ , and the trap strength μ , the steady-state distribution shows four different types of shapes, which we refer to as active-I & II, and passive-I & II phases. In the active-I phase, the weight of the distribution is concentrated along an annular region close to the circular boundary, whereas in active-II, an additional central diverging peak appears giving rise to a Mexican hat-like shape of the distribution. The passive-I is marked by a single Boltzmann-like centrally peaked distribution in the large D_R limit. On the other hand, while the passive-II phase also shows a single central peak, it is distinguished from passive-I by a non-Boltzmann like divergence near the origin. We characterize these phases by calculating the exact analytical forms of the distributions in various limiting cases. In particular, we show that for $D_R \ll \gamma$, the shape transition of the two-dimensional position distribution from active-II to passive-II occurs at $\mu = \gamma$. We compliment these analytical results with numerical simulations beyond the limiting cases and obtain a qualitative phase diagram in the (D_R, γ, μ^{-1}) space.

In chapter 6, which contains our work in [14], we study the effect of stochastic resetting on an active particle, namely, the continuous run and tumble particle in two spatial dimensions. We consider a resetting protocol which affects both the position and orientation of the RTP: with a constant rate the particle undergoes a positional resetting to a fixed point in space and orientation randomization. We compute the radial and x -marginal stationary

state distributions and show that while the former approaches a constant value as $r \rightarrow 0$, the latter diverges logarithmically as $x \rightarrow 0$. On the other hand, both the marginal distributions decay exponentially with the same exponent far away from the origin. We also study the temporal relaxation of the RTP and show that the position distribution undergoes a dynamical transition to a stationary state. We also study the first passage properties of the RTP in the presence of the resetting and show that the optimization of the resetting rate can minimize the mean first passage time. We also give a brief discussion on the stationary states for resetting to the initial position with fixed orientation.

As discussed before, how the transport properties of an extended system is affected by coupling to active reservoirs is a significant, yet virtually unexplored question. In chapter 7, which is also the work in [15] and [16], we address this issue in the context of energy transport between two active reservoirs connected by a chain of harmonic oscillators. The couplings to the reservoirs, which exert correlated stochastic forces on the boundary oscillators, lead to fascinating behavior of the energy current and kinetic temperature profile, which we compute exactly in the thermodynamic limit. We show that the stationary active current (i) changes non-monotonically as the activity of the reservoirs are changed, leading to a negative differential conductivity (NDC), and (ii) exhibits an unexpected direction reversal at some finite value of the activity drive. For the example of a dichotomous active force, we find the physical origin of the NDC using nonequilibrium response formalism. It turns out that the kinetic temperature profile remains uniform at the bulk, and can be expressed in a form similar to the thermally driven case. We show that despite this apparent similarity, no effective thermal picture can be consistently built in general. However, such a picture emerges in the small activity limit, where many of the well-known results are recovered.

Finally, we conclude in chapter 8 with a discussion on the significance of the results obtained in the thesis and possible open questions that it leads to.

List of publications¹

- *1 *Run-and-tumble particles in two dimensions: Marginal position distributions*, Phys. Rev. E **101** (6), 062120 (2020), I. Santra, U. Basu, S.Sabhapandit.
- *2 *Active Brownian Motion with Directional Reversals*
Phys. Rev. E **104**, L012601 (2021), I. Santra, U. Basu, S.Sabhapandit.
- *3 *Universal framework for the long-time position distribution of free active particles*, J. Phys. A: Math. Theor. **2022** 55 385002 (2022), I. Santra, U. Basu, S.Sabhapandit.
- *4 *Direction reversing active Brownian particle in a harmonic potential*, Soft Matter **17** (44), 10108 (2022), I. Santra, U. Basu, S.Sabhapandit.
- *5 *Run-and-tumble particles in two dimensions under stochastic resetting conditions*, J. Stat. Mech.: Theor. **2020** Exp. 11, 113206 (2020), I. Santra, U. Basu, S.Sabhapandit.
- *6 *Dynamical fluctuations of a tracer coupled to active and passive particles*, J. Phys. Complex. **2023** 4 015013 (2023), I. Santra.
- *7 *Activity driven Transport in harmonic chains*, SciPost Phys. **13**, 041 (2022), I. Santra, U. Basu.
- 8 *Quantum Brownian motion: Drude and Ohmic baths as continuum limits of the Rubin model*, Phys. Rev. E **102** (6), 062130 (2020), A. Das, A. Dhar, I. Santra, U. Satpathi, S.Sinha.
- 9 *Brownian motion under intermittent harmonic potentials*, J. Phys. A: Math. Theor. **2021** 54 334001 (2021), I. Santra, S. Das, S. K. Nath.
- 10 *Effect of tax dynamics on linearly growing processes under stochastic resetting: a possible economic model*, Europhysics Letters, **137** (5), 52001 (2022), I. Santra.
- 11 *Effect of stochastic resetting on Brownian motion with stochastic diffusion coefficient*, J. Phys. A: Math. Theor. **2022** 55 414002 (2022), I. Santra, U. Basu, S.Sabhapandit.

¹ * denotes the publications included in this thesis

- 12 *Long time behavior of run-and-tumble particles in two dimensions*, J. Stat. Mech: Theor. and Expt. **2023** (3), 033203 (2023), I. Santra, U. Basu, S.Sabhapandit.
- 13 *Stationary states of activity driven harmonic chains*, Physical Review E 107 (1), 014123 (2023), R Sarkar, I Santra, U Basu.

Prof. Sanjib Sabhapandit
Supervisor

Ion Santra
Candidate

Ob-La-Di, Ob-La-Da
Life goes on...

To love, life, dreams, and growing up

Acknowledgements

Unlike active particles, which can self-propel without the need for any external drivings, this thesis was greatly fueled by many external drivings. If you are reading this thesis and appreciating (or not) its contents, you must know a little about these external drives.

First on the list comes my supervisor—Sanjib has been very nice to me in all aspects I can think of, and I have learnt a lot from him over these past four years. Board discussion sessions with him are always a treat, which I will definitely miss when I leave RRI. His patience, whether it was dealing with ugly integrals or my careless typos in a manuscript, is unparalleled. I am very grateful that not only did he let me explore my own thoughts and questions, but he was also there to listen to them when I needed. The next person I want to thank is Urna (or UrnaDi, as I usually call her), who also happens to be a member of my thesis committee. She was very friendly and approachable from day one, which was helpful as the theory department had no senior stat. phys. students during my early days. While in the early days, I mostly went to her with doubts and questions about the problem at hand, diverse discussions began post the first Covid lockdown. We would discuss new papers on arxiv, possible new problems (many of them still in our bucket list) everyday over lunch. I benefited a lot from them. We even had lots of discussions outside of academics, on politics, movies and people, which were really enjoyable. Working together with Sanjib and Urna was an amazing experience and I do wish that we can keep working together, despite our other commitments.

My family, parents and elder brother, have been the backbone of my strength throughout my life. My father, a retired chemistry professor, with whom I have never agreed on any of my life decisions, be it choosing physics (instead of chemistry, of course) or the places I joined since high school. In fact, joining RRI was very much against his wish, but he was one of the happiest persons when he found me enjoying it here. Being diagnosed with tongue cancer, he had a major operation and received radiotherapy in 2007; but showing an amazing fighting spirit, he recovered and rejoined his teaching duties in less than a year. My mother, on the other hand, has mostly been supportive of my decisions and also provided the strength to

go ahead and actually execute them. Undoubtedly, she has the maximum contributions to whatever I have achieved in life till now. My brother has been my first friend and continues to be so. He is also now the sponsor for the things I can't afford with my fellowship and my part-time fashion advisor. A major chunk of my PhD tenure was spent working from home due to the pandemic; being together with them in such troubled times really helped me continue my research smoothly.

I was also grateful to have Aritri alongside me throughout this journey, who had been another pillar of my strength over the past few years—from listening to my long rants about everyday miseries to backing me up on every occasion. I also want to thank her for helping me get different perspectives on life and thus improving me as a person (at least to some extent).

Coming to RRI for my PhD, was the first time that I was staying away from home in my life, and naturally, I was very sad and homesick. Ranita, Saikat, Anirban and Sandeep let that feeling slip away very quickly. I have really missed our Sunday lunch and dinner outings, post the pandemic. Hopefully, we can do them again someday, somewhere. I am incredibly grateful to them, specially Ranita and Saikat, who very much served as my local guardians in the initial few months.

I would like to extend my thanks to Anupam and Abhishek for agreeing to be part of my thesis committee and thesis external member, respectively. Many interesting questions always came up in meetings with them, be it during my annual assessment or in the tea queue at some conference. I want to thank Sayantan (Majumdar) and Pramod for giving me the experimental perspectives on many soft matter systems. Of course, Sayantan da was another of the approachable faculties in RRI, with whom I had innumerable discussions outside of academia too. I am also thankful to Dibyendu for the post-dinner discussions on my coursework and Jadavpur University. I have also had many insightful discussions with Sam and Supurna pre-pandemic, which I really enjoyed. Going back, Dhruba da, my teacher at Jadavpur University, who actually gave me my first research problem, was an inspiration and one of the reasons I took up statistical physics. Chitrak, with whom I wrote my first preprint, has always been a great friend and guide both in the world of physics and life. Though we had minimal overlap in terms of time at RRI, Sujit, Santanu and Deepak, have

been very nice to me whenever I needed their help. I hope we can work together more often in the future. I was also lucky to have Urbashi and Avijit as my collaborators, sessions with them were always enjoyable. I must thank Urbashi di and Suman da for inviting me to the wholesome ‘paatla machher jhol-bhat’ dinner at their place so many times. Chats with Aritra, Bhadra, Jyotirmoy, Rohan, Anupam, and Soumen were refreshing and always cherishable. Despite the pandemic, I always have had good discussions with Prashant, Jitendra, Saikat, Apurba, Ritwik, Tanmoy, Anjaneya, and other statistical physicists of my age. I hope we can continue this association in the years to come.

It was very nice to have Abhishek (Mathur) as an office mate in my early days at RRI. Escaping coursework assignments and discussing mathematics puzzles with him and Sujit was fun. Post-pandemic, I also enjoyed physics and football discussions with Vishnu. I was also very lucky to have very nice juniors in Rupak and Shashank. I thank Swarnadeep, my roommate in the first year at RRI, who was very understanding and helpful. I will never forget the late-night chats in Avik’s room with Swarnadeep and Shovan. I would miss the deep philosophical discussions with Sachi (which never ended in agreement) and high-intensity discussions with Sukhjoan. I made good friends with some amazing people like Sayan, Sebanti, Bapan, Maheswar, Bidyut, Gokul, Numan, Saichand, Tanuman, Agnibha, Sanchari, Arun, Kinjal, Soumen, Ingita, Moitri, Siman, Shivam, Aniruddh, Manish, Dipak. I am very thankful to the entire football and table-tennis contingent, the crews of the plays that I wrote during my time here.

I want to thank the office members of RRI. Starting with our administrative officer, Naresh, who in spite of his busy schedule was always reachable by a text/call. Mahadevji has always been there when I needed him. I express my sincere thanks to him. I also thank our group secretaries Manju, Gayathri, Chaitanya, and Harshitha. I thank my friend Manju (KP), Nagaraj and other library staff for maintaining a great library, which is really one of a kind. Though I had a huge beef with the canteen staff and the food at RRI during my early days, I gradually discovered that most of them were very nice and we really go along very well now. I want to thank them, as well as the security staff at RRI.

I also want to thank ICTS for the numerous scientific programs they sponsor, where I learnt a lot; S. N. B. Centre for Basic Sciences, Kolkata, for giving me the student associate

position at their institute. I am thankful to MPI pks for sponsoring my seven week visit there. It was wonderful to meet Asmi, Akhil, Arghya, Krishanu, Suchismita, and Abhik da during this visit. They were super helpful and kept me sane amidst a four day delay in my return (back to India) due to flight cancellations. I also want to thank SERB for giving me the International travel support during August-September 2022.

Of course, there are little regrets and grievances everywhere. But the fun and happiness in work and play here outgrew it by some orders of magnitude. All in all, it was five (almost now) beautiful years spent at RRI, which I can happily fall back to from time to time.

Contents

1	Introduction	19
1.1	History, motivation, and scope	19
1.2	Brownian motion	22
1.2.1	Stochastic modeling: Langevin equation	22
1.2.2	Fokker-Planck equations	24
1.2.3	Path integral formalism	25
1.3	Modeling active motion	27
1.3.1	Run-and-tumble particles in one dimension	30
1.4	Outline of the thesis	33
2	Run-and-tumble particles in two dimensions	37
2.1	Models	37
2.2	Three-state ($n = 3$) dynamics	41
2.2.1	Marginal distribution along x -axis	42
2.2.2	Marginal distribution along y -axis	47
2.3	Four state ($n = 4$) dynamics	52
2.3.1	Marginal distribution along x -axis	53
2.4	Continuous θ	57
2.4.1	Moments and Cumulants	57
2.4.2	Position Distribution	58
2.4.3	Marginal Distribution	61
2.5	Summary	62
3	Active Brownian motion with directional reversal	64
3.1	Model	65
3.1.1	Effective noise correlations	66
3.1.2	Position Moments	67
3.2	Position Distribution	70

3.2.1	Short time regime (I)	70
3.2.2	Intermediate time regime (II)	72
3.2.3	Long-time regime (IV)	75
3.2.4	Intermediate-time regime (III)	76
3.3	Survival probability	77
3.4	Summary	80
4	Universal framework for the long-time position distribution of active particles	81
4.1	Perturbative framework and main results	82
4.2	Application to obtain long-time distribution of DRABP	85
4.2.1	Moments	86
4.2.2	Position distribution	89
4.3	Summary	97
5	Stationary states of direction reversing active Brownian particles in a harmonic trap	99
5.1	Stationary Phases	100
5.2	Position distributions	103
5.2.1	Passive-I phase: $D_R \gg \mu$	104
5.2.2	Active-I phase: $\gamma \ll D_R \ll \mu$	106
5.2.3	The novel active and passive phases: $D_R \ll (\mu, \gamma)$	108
5.2.4	Crossover from active-I to active-II	113
5.3	Summary	114
6	Effect of stochastic resetting on run-and-tumble particles	116
6.1	Stationary State distribution	117
6.2	Relaxation to stationary state and position distributions	122
6.3	First Passage Properties	124
6.4	Summary	129

7	Active reservoirs: microscopic model and energy transport	130
7.1	Active reservoir model	130
7.2	Model for studying active transport	135
7.3	Stationary energy current	137
7.4	Kinetic temperature	141
7.5	Summary	143
8	Conclusion	145
9	Appendix	149
9.1	Calculation of the Propagator for the θ Processes and 2-point σ Correlations	149
9.2	Details of the 3-state X Marginal Distribution	151
9.3	Computation of the Inverse Fourier Transform for 4-state Marginal Distribution	155
9.4	Laplace Fourier Inversion of $\mathcal{G}(k, s)$ of the Continuous Process in the main chapter	158
9.5	Exact first-passage time of a DRABP in the intermediate regime (II)	159
9.6	Intermediate steps in the computation of $A_0^4(y, t)$ and $A_0^6(y, t)$ for DRABP	165
9.7	Variance and kurtosis of the position distribution	168
9.8	Saddle Point Integral	171
9.9	Stationary state Current	173
9.10	Kinetic temperature profile	179
9.10.1	\hat{T}_l near left boundary	180
9.10.2	\hat{T}_l near right boundary	183

Chapter 1

Introduction

“How can the events in space and time which take place within the spatial boundary of a living organism be accounted for by physics and chemistry?” Since this comment made by Erwin Schrödinger in his famous book ‘What is life?’ [17], a huge number of physicists, chemists, mathematicians and even computer scientists have devoted their careers in trying to develop the physics behind biological systems. He further wrote *“The obvious inability of present-day physics and chemistry to account for such events is no reason at all for doubting that they can be accounted for by those sciences”*, as he believed that the statistical nature of the interactions between the atoms and molecules, the fundamental constituents of all living systems, must be responsible for the different observed phenomena. ‘Active matter’ is a recent, emerging field in the domain of nonequilibrium statistical physics, which takes the same philosophical approach to understand the emergent physical observables of living systems. In this thesis, we attempt to try to understand the physics of ‘active particles’—the constituent elements of active matter, by studying simplistic physical models.

1.1 History, motivation, and scope

In 1827, the eminent botanist Robert Brown observed that pollen grains of size of the order of microns (μm), suspended in water, undergo a continuous random jittery motion [18]. Initially, he suspected that this strange motion was because the pollen grains were alive. But to his surprise, when he repeated the same experiment with life-less inorganic matter, the observations were no different. This forced him to rule out the hypothesis that this unusual movement had anything related to life. The physical explanation of this strange motion, termed as Brownian motion, came much later from Albert Einstein, who showed that the random motion of the micron-sized object was due to bombardment of the huge number of water molecules of the medium in which it was suspended [19, 20] and thus,

anything that impacted the movement of the water molecules, would impact the movement of the pollen grains—higher temperature, smaller particle size, higher number of particles, low viscosity of the medium increased the rate of the Brownian motion. Interestingly, since its discovery and subsequent explanation in the early 1900s, Brownian motion has emerged as one of the simplest stochastic models and found its applications in different branches of physics, mathematics, chemistry, biology, economics, computer science, and a host of other disciplines [21, 22, 23, 24, 25].

The motion of similar-sized living objects, which was also one of the initial hypotheses to explain Brownian motion, is also random, albeit quite different fundamentally[26]. Unlike the ‘passive’ Brownian particles, they can generate and dissipate energy by extracting resources from the environment and use this energy to propel themselves along preferred directions, mostly their body axis (also commonly called internal orientation vector). These random, yet persistent motion are called ‘active’ motion, and the entities executing such motion are called ‘active particles’ [2, 1, 3, 4, 27]. This ‘activity’ is a fundamental property of living organisms and is observed and investigated in a huge number of living objects: microorganisms like bacteria [28, 28], protozoa [29], self-organizing bio-polymers like microtubules and actin [30, 31], sperm cells [31], algae [31], fish schools [32, 33], bird flocks [34, 35] include some popular examples. Similar motion is also observed in many non-living systems: artificially synthesized Janus particles [36, 37], micro and nano-bots used for targeted drug delivery [38], vibrated granular medium [39], active water droplets [38], semiflexible rods in rotating magnetic fields [40, 41], etc. Due to the ability to generate and dissipate energy on their own, these entities undergoing active motion are inherently nonequilibrium. This leads to a lot of non-trivial behaviors with or without interaction, which are never seen in passive systems. Collections of active particles, popularly called active matter, exhibit numerous interesting collective phenomena like pattern formation [42], motility-induced phase separation [43], clustering [44], absence of equation of state for mechanical pressure [45], etc. These interesting emergent phenomena, occurring solely due to the nonequilibrium nature of the individual constituents, have motivated statistical physicists to take up the challenge of studying the physics of active matter. Notably, while huge progress has been made over the last two decades on the experimental front, the physics remains incompletely understood

for most active systems as the underlying processes are nonequilibrium in nature and unlike equilibrium systems, there is no general framework to describe and understand the systems out of equilibrium.

The collective phenomena witnessed in active matter are often studied using phenomenological hydrodynamic equations for different fields like (density, momentum, energy, etc.) developed on the basis of symmetries, conservation laws, and nature of interactions followed by such systems [3, 46, 47, 4, 48, 49]. Though such phenomenological models have been greatly successful in understanding the emergent collective phenomena like pattern formation, motility induced phase separation, etc., they do not take into account the dynamical behavior of individual active particles. In fact, single particle tracking experiments have established that single active particles can extract and dissipate energy from their environment, and as a result, even in the absence of interactions among each other, they exhibit a lot of interesting non-trivial properties. This has led to another popular technique of studying active matter, namely, developing minimal stochastic models that mimic the dynamics of the different real world active systems and trying to understand their statistical properties. These models take into account a minimal number of degrees of freedom that are required to capture the essential features of the real systems and help in understanding the building blocks of active matter better [50, 51, 6, 52, 53, 54, 55, 56, 57, 58, 59, 60, 10, 61, 62, 14, 63, 11, 64, 65, 13, 66, 12, 67]. Moreover, these dynamical models have often been coarse-grained to reproduce or improve the phenomenological hydrodynamic models [51, 68, 69]. The microscopic modeling of active dynamics has also been found useful in other branches of physics like astrophysics and quantum mechanics—for example, explaining the suprathermal tails occurring in the velocity distribution of astrophysical plasmas [70] and diffraction of Dirac electrons [71].

Though all active particles show persistent motion, the exact dynamics vary widely in different classes of active systems seen in real world. The goal of this thesis is to understand how these different dynamics lead to different observable properties by studying minimal stochastic models which mimic the dynamics of the different classes of active particles found in nature. We study the statistical properties of these simple models analytically and try to infer possible differences of the active systems from the passive (Brownian) systems, which are used to model equilibrium dynamics. Understanding these differences not only helps us

characterize the signatures of different nonequilibrium dynamics better but also allows us to study other interesting questions, like nonequilibrium energy transport, in the context of active systems.

Before going on to the active motion, we first briefly review the passive Brownian motion and its statistical properties.

1.2 Brownian motion

1.2.1 Stochastic modeling: Langevin equation

How does one mathematically model the random jittery motion of pollen grains in water observed by Robert Brown? Imagine a particle (Brownian particle) of mass m immersed in a fluid in thermal equilibrium, at temperature T in one dimension (generalization to higher dimensions is trivial). The Newton's equation of motion for the particle is,

$$m\dot{v}(t) = F_{\text{int}}(t) + f_{\text{ext}}(x, t), \quad (1.1)$$

where $v(t)$ is the instantaneous velocity of the Brownian particle, $f_{\text{ext}}(x, t)$ denotes the external force on the system, and $F_{\text{int}}(t)$ denotes the forces due to the interaction with the fluid molecules. For starters, let us consider that no external force is acting on the Brownian particle, $f_{\text{ext}}(x, t) = 0$. Now, if we know the position and velocities of the fluid molecules are known in time, then $F_{\text{int}}(t)$ should, in principle, be completely deterministic. However, it is quite impractical to look for an exact form of $F_{\text{int}}(t)$ as it involves a large number $O(10^{23})$ of molecules. Instead, $F_{\text{int}}(t)$ is modelled as a force which has two parts: (i) A dissipative component proportional to the instantaneous velocity of the particle, which arises due to the movement of the particle relative to the fluid molecules, and (ii) A fluctuating component, uncorrelated in time, which arises due to the collision with the fluid molecules. The uncorrelated nature of the fluctuating force is due to the fact that there is a separation of time-scales between the molecules of the fluid and the Brownian particle— the fluid molecules are much faster than the Brownian particle. As a result, the Brownian particle undergoes a large number of collisions in a short time interval, causing any memory between the forces at different times to be lost.

The effective equation of motion of the Brownian particle can thus be written as,

$$m\dot{v}(t) = \Gamma\eta(t) - \nu v(t), \quad (1.2)$$

where the first and second terms on the right-hand side (rhs) denote the fluctuating and dissipative terms, respectively. Here, $\Gamma > 0$ denotes the strength of the fluctuating force and $\nu > 0$ denotes the damping coefficient; $\eta(t)$ denotes a delta-correlated Gaussian white noise, defined by,

$$\langle \eta(t) \rangle = 0 \quad \text{and} \quad \langle \eta(t)\eta(t') \rangle = \delta(t - t'). \quad (1.3)$$

Equation (1.2) is the famous Langevin equation [72]. Note that ignoring any of the two terms on the rhs would lead to unphysical consequences (the velocity decays to zero/ keeps increasing with time). Since the fluid medium is in thermal equilibrium, the particle should also relax to the same thermal equilibrium. In other words, the average kinetic energy of the Brownian particle should be proportional to T , following the equipartition theorem,

$$\frac{1}{2}m\langle v^2(t) \rangle = \frac{1}{2}k_{\text{B}}T \quad \text{as } t \rightarrow \infty. \quad (1.4)$$

On the other hand, from the Langevin equation (1.2), the instantaneous velocity can be written as,

$$v(t) = v(0)e^{-\nu t/m} + \frac{\Gamma}{m}e^{-\nu t/m} \int_0^t ds e^{\nu s/m} \eta(s), \quad (1.5)$$

which leads to,

$$\langle v^2(t) \rangle = v(0)^2 e^{-2\nu t/m} + \frac{\Gamma^2}{2m\nu} \left(1 - e^{-2\nu t/m}\right). \quad (1.6)$$

Taking the $t \rightarrow \infty$ limit of the above equation and comparing with Eq. (1.4), we get the famous Einstein-Sutherland relation [73, 74, 19, 20],

$$\Gamma = \sqrt{2\nu k_{\text{B}}T}. \quad (1.7)$$

Thus, the strength of the fluctuating force is determined by the temperature of the fluid and the friction coefficient. This relation connecting the fluctuating part to the dissipation is also called the Fluctuation Dissipation theorem (FDT) and is a signature of the underlying equilibrium dynamics [75, 76].

Mean-squared displacement can also be calculated using Eq. (1.5) and the noise correlations Eq. (1.3). Assuming the particle starts at the origin,

$$\langle x^2(t) \rangle = \begin{cases} \frac{k_B T}{m} t^2 & t \ll m/\nu \\ 2D_T t & t \gg m/\nu, \end{cases} \quad (1.8)$$

with the diffusion coefficient $D_T = \frac{k_B T}{\nu}$. Clearly, from Eq. (1.6), $\tau_v = m/\nu$ corresponds to the time-scale for velocity relaxation. For a colloidal particle [of size $O(10^{-6}m)$] in water at room temperature, τ_v is $O(10^{-9}s)$. Thus, for most of the practical purposes, in the limit of $\tau_v \ll 1$, the inertial term can be neglected to get the overdamped Langevin equation for the Brownian particle,

$$\dot{x} = -\frac{1}{\nu} V'(x) + \sqrt{2D_T} \eta(t), \quad (1.9)$$

which describes the net observable motion very well. In the absence of any external potential $V(x) = 0$, the mean squared displacement for this overdamped motion can be easily calculated from the above equation, using the autocorrelations of $\eta(t)$ and one can immediately see the diffusive growth $\langle x^2(t) \rangle = 2D_T t$. Note that, though Eq. (1.2) is a one-dimensional stochastic differential equation, the generalization to higher dimensions is straightforward, as the motion along different directions is independent.

1.2.2 Fokker-Planck equations

Equation (1.9) is a stochastic differential equation, where different realizations of $\{\eta(t)\}$ lead to different final values of the position $x(t)$. Another equivalent description of Brownian motion is the Fokker-Planck equation, which is a deterministic partial differential equation governing the time evolution of the probability density $P(x, t)$ [77, 78]. The Fokker-Planck

equation corresponding to the process in Eq. (1.9) is given by,

$$\frac{\partial P(x, t)}{\partial t} = -\frac{\partial}{\partial x} \left[-\frac{1}{\nu} V'(x) P(x, t) - D_T \frac{\partial P(x, t)}{\partial x} \right]. \quad (1.10)$$

The above equation can also be viewed as a continuity equation, with the quantity in the square brackets acting like a current $J(x, t)$ —the first term is the drift current due to the external potential, while the second term denotes the diffusive current. When there is no external potential, i.e., $V(x) = 0$, this reduces to the famous diffusion equation,

$$\frac{\partial P(x, t)}{\partial t} = D_T \frac{\partial^2 P(x, t)}{\partial x^2}. \quad (1.11)$$

This can be easily solved by taking a Fourier transform with respect to space and the propagator $\mathcal{G}(x, t|x_0, 0)$, i.e., the probability that a Brownian particle starting from x_0 at $t = 0$ reaches x at time t , is given by,

$$\mathcal{G}(x, t|x_0, 0) = \frac{1}{\sqrt{4\pi D_T t}} \exp \left[-\frac{(x - x_0)^2}{4D_T t} \right]. \quad (1.12)$$

This implies that the position distribution of a passive Brownian motion is always a Gaussian and is fully specified by its mean x_0 and variance $2D_T t$.

In the presence of an external confining potential $V(x)$, the particle reaches a stationary state, where the position distribution does not change in time, i.e., the lhs of Eq. (1.10) is zero. Moreover, since in such a case, there should not be any net current in the system, i.e., $J(x) = 0$, the stationary distribution reduces to the equilibrium Boltzmann distribution,

$$P(x, t \rightarrow \infty) = P_{\text{eq}}(x) = \mathcal{Z}_0^{-1} \exp \left[-\frac{V(x)}{k_B T} \right], \quad (1.13)$$

where $\mathcal{Z}_0 = \int_{-\infty}^{\infty} dx \exp \left[-\frac{V(x)}{k_B T} \right]$ is the normalization constant.

1.2.3 Path integral formalism

A third way of analytical treatment of Brownian motion is the path integral formalism [79, 80, 81]. Since the function $\eta(t)$ in Eq. (1.9) is a Gaussian white noise, the joint probability

distribution of a particular realization $\left[\{\eta(s)\}, \text{ for } s \in [0, t]\right]$ can be written as,

$$Prob[\{\eta(t)\}] \propto \exp\left[-\frac{1}{2} \int_0^t ds \eta^2(s)\right], \quad (1.14)$$

where $Prob[\cdot]$ denotes the path weight of a particular trajectory. Using the Langevin equation (1.9), we have,

$$Prob[\{\eta(t)\}] \propto \exp\left[-\frac{1}{4D_T} \int_0^t ds \left(\frac{dx}{ds}\right)^2\right], \quad (1.15)$$

The propagator for the process is the contribution from all such possible trajectories, which is given by the Feynman path integral,

$$\mathcal{G}(x, t|x_0, 0) = \int_{x(0)=0}^{x(t)=x} \mathcal{D}x \exp\left[-\frac{1}{4D_T} \int_0^t ds \left(\frac{dx}{ds}\right)^2\right]. \quad (1.16)$$

Identifying D_T as $\hbar^2/(2m)$, the path integral in the above equation can be mapped to the propagator of a quantum free particle in imaginary time ($t \rightarrow it/\hbar$),

$$\mathcal{G}(x, t|x_0, 0) = \langle x|e^{-Ht}|x_0\rangle, \quad (1.17)$$

with the Hamiltonian $H = -\frac{\hbar^2}{2m} \frac{\partial^2}{\partial x^2}$. Remembering the eigenfunctions $\psi_k(x) = \langle k|x\rangle = \frac{1}{\sqrt{2\pi}} e^{ikx}$ and eigenvalues $E_k = \hbar^2 k^2/(2m) = D_T k^2$ of this Hamiltonian [82], the propagator can be written as,

$$\mathcal{G}(x, t|x_0, 0) = \frac{1}{2\pi} \int_{-\infty}^{\infty} dk e^{-ikx} e^{-D_T k^2 t} e^{ikx_0}. \quad (1.18)$$

Upon doing the k -integral we get the propagator Eq. (1.12).

This formalism, popularly called Feynman-Kac formalism, is of great use in understanding the statistical properties of Brownian functionals defined as, $B = \int_0^t ds u[x(s)]$, and will be used quite often in this thesis. Here $x(s)$ is a Brownian motion, and $u(x)$ is an arbitrary specified function. Each realization of a Brownian trajectory leads to a different value of B , and thus the probability distribution of B is an obvious quantity of interest. Beyond the scope of this thesis, Brownian functionals emerge in a wide variety of problems from

various fields, including first-passage properties of Brownian motion, fluctuating interfaces, stock-market, weather analysis, economic models, etc [81, 83, 84, 85, 86].

1.3 Modeling active motion

Active motion, though random like passive Brownian motion, exhibits directed self-propulsion along their body axis. The dynamics of this self-propulsion also vary largely in different classes of active particles— a wild type *E. coli* moves more or less in a straight line along its body axis, interrupted by intermittent ‘tumbles’ changing the direction of the motion randomly; a non-mutant variety of *E. coli* or a Janus colloid moves by slow, continuous, albeit random changes in orientation of the body axis; the motion of microorganisms like *Myxococcus xanthus* and *P. citronelis* in addition to the slow continuous change, exhibits complete intermittent directional reversals. A few experimentally observed trajectories of different active particles are shown in fig. 1.1. Minimalistic models of active particles, designed to mimic these dynamics, consider them to be overdamped¹, point particles having an internal orientation vector $\hat{\mathbf{n}}$, representing the body axis. The directed motion is modeled by adding a stochastic propulsion velocity $\mathbf{u}(t)$, always pointing in the direction of $\hat{\mathbf{n}}$, to the Langevin equation (1.9) of a passive Brownian particle,

$$\dot{\mathbf{x}} = \sqrt{2D_T}\boldsymbol{\eta}(t) + \mathbf{u}(t). \quad (1.19)$$

Different stochastic models of $\mathbf{u}(t)$ are used to mimic the various dynamics of active particle dynamics seen in the real world. These different dynamical models, however, share one common property— the are temporally correlated, $\langle u_i(t)u_j(t') \rangle = \mathcal{F}_{ij}(|t - t'|)$. Usually, the autocorrelation function are found to be exponentially decaying $\mathcal{F}_{ij}(t) \propto \exp[-t/\tau_a]$, which implies that active particles typically remember their orientation for a finite time τ_a , during which the particle moves along the chosen preferred orientation. The correlation time τ_a is a direct measure of the activity of the system—larger τ_a implies larger activity.

¹Active particles like bacteria are of the same size as the colloidal particles and in usual fluid media, the velocity relaxation time $\tau_v = m/\nu$ is very small. Thus, the overdamped description works very well. However, for large-sized active particles [like mini-robots, macroscopic swimmers like beetles flying at water interfaces] or those suspended in very dilute media [like gas instead of fluid] inertial effects do become important and one has to consider underdamped equations similar to Eq. (1.2) [87].

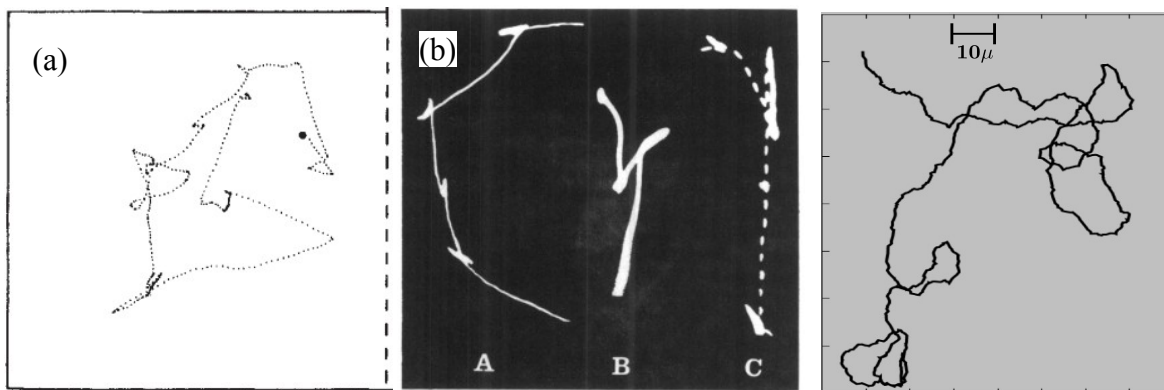


Figure 1.1: Trajectories of active particles obtained from single particle tracking experiments. (a) Planar projection of three-dimensional plots of an *E. coli* bacteria [28]. (b) Tracks of *P. citronellolis* observed in a dark field with a stroboscopic lamp operating at different [A, B, and C] frequencies [88]. (c) The trajectory of a Platinum coated polystyrene Janus particle [89].

It is important to understand the relative contribution of the two terms on the rhs of Eq. (1.19) to the motion of the particle. Experimental observations suggest that the thermal fluctuations are negligible compared to the active fluctuations. For example, a micron-sized *E. coli* bacteria typically travels $\sim 30-40 \mu m$ when alive, which reduces to $\sim 0.3-1 \mu m$ when it is dead (driven by only thermal fluctuations of the fluid medium at room temperature). Thus, we ignore the effects of the former in this thesis and consider overdamped Langevin equations of the form,

$$\dot{\mathbf{x}} = \mathbf{u}(t), \quad (1.20)$$

to describe the motion of active particles. The simplicity of these models lies in the fact that the complex activity is modeled only by the stochastic propulsion velocity $\mathbf{u}(t)$, and by modeling the dynamics of $\mathbf{u}(t)$ one can replicate the various different swimming patterns observed in different real world bacteria and synthetic microswimmers. For example, the run-and-tumble dynamics model the motion of a typical wild type *E. coli* that moves in almost straight lines, interrupted by intermittent tumblings; an active Brownian motion is used to describe the dynamics of artificially synthesized Janus particles; a direction reversing active Brownian particle mimics the motion of *M. xanthus*, *P. citronelis* etc., which follow an active Brownian-like motion interrupted by intermittent tumbling events [see Fig. 1.2 for

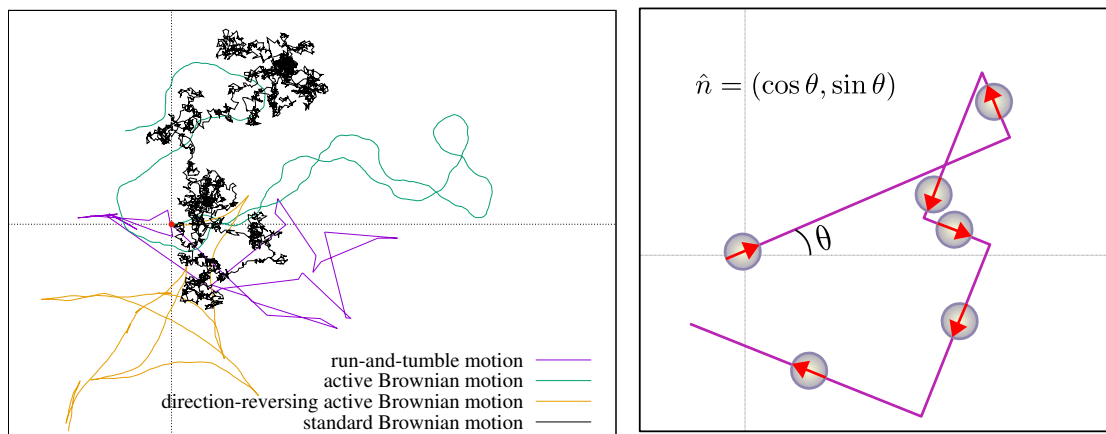


Figure 1.2: (a) Comparison of simulated trajectories of active particles (colored lines) and standard Brownian motion (black line) in two dimensions for the same duration, starting from the origin. (b) A zoomed trajectory of a two-dimensional run and tumble particle: the shaded circle denotes the active particle, with the red arrow pointing towards the internal orientation vector \hat{n} .

some typical trajectories of active particles corresponding to different $\mathbf{u}(t)$ dynamics]. Clearly, the addition of the fluctuating propulsion velocity in Eq. (1.19) leads to a violation of the fluctuation-dissipation theorem. This highlights the nonequilibrium nature of these models.

It is important to note that for Brownian motion of dimensions higher than one, the dynamics in all the other directions evolve independently, making the generalization to higher dimensions trivial. This, however, is not true for active particles as they move persistently along a preferred direction, making the different components correlated. In this thesis, we will mainly consider two-dimensional active particles, where the internal orientation is specified by the angle θ , which the body axis makes with the positive x -axis. In single particle tracking experiments, one usually looks at the projected motion of active particles in two-dimensions [28]. Thus, studying two-dimensional motions are also relevant from the experimental point of view.

Let us briefly discuss one of the simplest models of active particles to get a flavor of the differences with the passive Brownian motion.

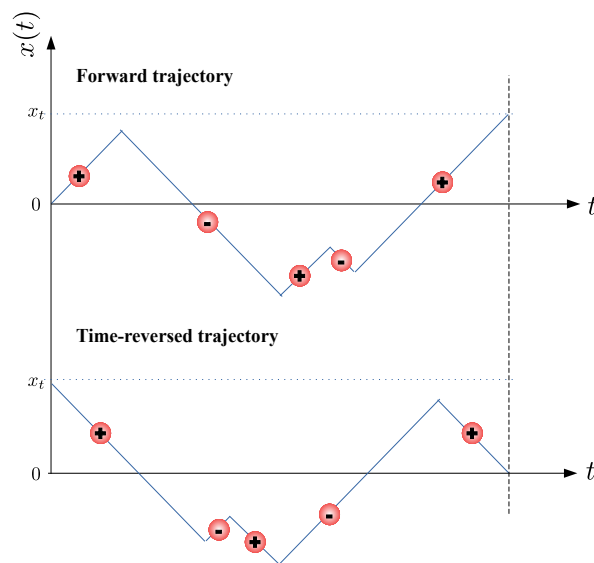


Figure 1.3: Trajectory of an RTP in one-dimension at $T = 0$: the marked circles on each run phase denotes the instantaneous orientation of the RTP—the ‘+’ and ‘-’ signs imply $v(t) = \pm v_0$, respectively. The upper plot shows the forward trajectory, while the bottom one shows the corresponding time-reversed trajectory.

1.3.1 Run-and-tumble particles in one dimension

The run-and-tumble particle (RTP) in one dimension is perhaps the simplest active particle model, described by the Langevin equation,

$$\dot{x} = u(t). \quad (1.21)$$

Here $u(t) = v_0\sigma(t)$ is the stochastic propulsion velocity with $\sigma(t)$ being a dichotomous random variable that switches stochastically between $+1$ and -1 at a rate γ via intermittent tumbling events [51, 55, 90, 59]. A typical trajectory of a one-dimensional RTP with four tumbling events, starting from $x = 0$ at $t = 0$ to $x = x_t$ at time t is shown in fig. 1.3 (upper panel). Let us first discuss very briefly about the time-reversibility of the process before proceeding further. A stochastic process is called time-reversible if the weight of the forward trajectory is the same as the weight of the time-reversed trajectory. The lower panel of fig. 1.3 shows the time reversed trajectory, corresponding to the upper panel, which starts from $x = x_t$ at $t = 0$ and ends at $x = 0$ at time t . The path weight of the forward trajectory is finite and can be calculated. However, the time-reversed trajectory has zero path weight, since the RTP in

a state $u(t) = v_0$ (or $u(t) = -v_0$) cannot move toward the negative (or positive) x axis. Note that, if $T \neq 0$, then the path weight of the time-reversed trajectory is not zero, as the RTP can still take the reversed path if the thermal fluctuations are strong enough. However, the path weights of the forward and backward trajectories are still different. This inequivalence is a typical trait of nonequilibrium systems. It is worth mentioning that, for a one-dimensional RTP, however, one can look at the full trajectory $(\{x(s)\}, \{u(s)\}; 0 < s < t)$. In this case, assuming that the propulsion velocity for the time-reversed trajectory $u_{\text{reversed}}(t-s) = -u(s)$, leads to a generalized reversibility [91]. This generalized reversibility is very specific to the one-dimensional RTP with two orientation states and does not hold in general for other models, even one-dimensional RTPs with higher orientational states[91, 10].

The mean and autocorrelation of the propulsion velocity for this process is given by,

$$\langle v(t) \rangle = u(0) e^{-t/\tau_a} \quad \text{and} \quad \langle v(t)v(t') \rangle = v_0^2 e^{-|t-t'|/\tau_a}, \quad (1.22)$$

where the characteristic active time-scale $\tau_a = (2\gamma^{-1})$. The mean displacement of such a particle, starting with velocity v_0 , is given by,

$$\langle \Delta x(t) \rangle = v_0 \tau_a \left(1 - e^{-t/\tau_a} \right). \quad (1.23)$$

Thus, it implies that, on an average, the RTP moves along its initial orientation, unlike Brownian motion, where the average displacement is always zero. The characteristic time-scale τ_a separates the observable time range into (i) a short-time regime ($t \ll \tau_a$), and (ii) a long-time regime ($t \gg \tau_a$), which show very different behaviors. The mean squared displacement, for example, shows a crossover from ballistic behavior at early times to a diffusive behavior at very late times,

$$\langle (\Delta x)^2 \rangle \approx \begin{cases} v_0^2 t^2 & t \ll \tau_a \\ 2D_{\text{RT}} t & t \gg \tau_a \end{cases} \quad \text{with} \quad D_{\text{RT}} = \frac{v_0^2}{2\gamma}. \quad (1.24)$$

The short-time ballistic behavior is a common trait of the active nature of the dynamics and can be understood very easily—at times much less than τ_a , there are very few tumbling events as a result of which, the particle shows a ballistic growth with a speed v_0 along its

initial orientation.

These different behaviors are also seen if one looks at the time evolution of the position distribution of the particle. The Fokker-Planck equations for the joint distribution $P_\sigma(x, t)$, which denotes the probability that the particle is at position x , with $\sigma(t) = \sigma$ at time t , is given by,

$$\frac{\partial P_\sigma(x, t)}{\partial t} = -v_0\sigma \frac{\partial P_\sigma(x, t)}{\partial x} - \alpha P_\sigma(x, t) + \alpha P_{-\sigma}(x, t), \quad (1.25)$$

where σ can take values ± 1 . Interestingly, this had been known since the late 1800s as the Telegraphers equation, used to describe the voltage and current on an electrical transmission line with distance and time and the exact result for the initial conditions $P_\sigma(x, 0) = \delta(x)/2$, is given by [55],

$$P(x, t) = \frac{e^{-\gamma t}}{2} [\delta(x - v_0 t) + \delta(x + v_0 t)] + \frac{e^{-\gamma t}}{2} \left[I_0(\gamma t \sqrt{1 - (x/v_0 t)^2}) + \frac{I_1(\gamma t \sqrt{1 - (x/v_0 t)^2})}{\sqrt{1 - (x/v_0 t)^2}} \right] \Theta(v_0 t - |x|), \quad (1.26)$$

which is quite complex and physically rich compared to the simple Gaussian distribution of Brownian motion. The δ -functions correspond to the trajectories where there has been no tumbling events up to time t , while the remainder comes from the trajectories with at least one flipping. Figure 1.4(a) shows how the position distribution evolves: at short-times there are very few tumbles, and the particle propels itself ballistically, leading to the boundary peaks; as time increases, the number of tumbles also increases and the central region starts populating more and more, leading to a change in shape from a bimodal to a unimodal distribution about the initial orientation [see 1.4(a)]; at very large times, the distribution coincides with a Gaussian distribution with variance $2D_{\text{RT}} t$. [LDF]

Unlike Brownian particles, the stationary distribution of an active particle in the presence of confining potentials does not relax to the traditional Boltzmann form Eq. (1.13). In fact, for the one-dimensional RTP, in the presence of potentials of the form $V(x) = h|x|^p$ (with $p > 0$), the stationary position distribution $P_{ss}(x)$ has a rich behavior in the (p, h) plane [90, 59]. For $p > 1$, $P_{ss}(x)$ always has finite supports on the one dimensional line, and there exists a critical line that separates a passive-like phase ($P_{ss}(x) \rightarrow 0$ at the boundaries) from an

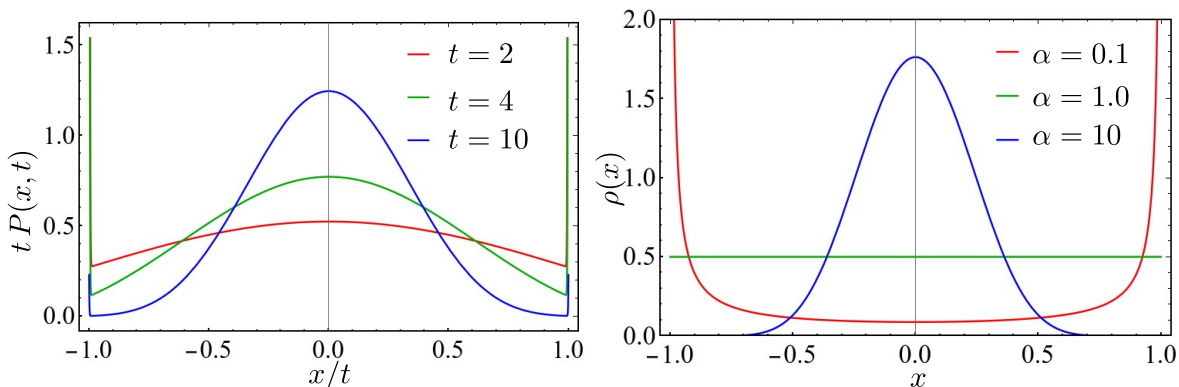


Figure 1.4: Position distribution of an RTP at $T = 0$: (a) without any confining potential Eq. (1.26) at different times with $\alpha = 1$, (b) in presence of a harmonic trap $V(x) = x^2/2$ [59].

active-like phase ($P_{ss}(x)$ diverges at the boundaries). A plot of the stationary distributions of a one-dimensional RTP in a harmonic confinement (i.e., $p = 2$) is shown in fig. 1.4(b).

The emergence of such interesting physical properties in one of the simplest active processes, where the propulsion velocity is a two-state Markov jump process with equal transition rates, naturally leads to the question: what happens if the $\mathbf{u}(t)$ dynamics is more complicated so as to mimic the actual physical scenarios? This is the central issue we try to address in this thesis.

1.4 Outline of the thesis

In this thesis, we investigate how the nonequilibrium dynamics of individual active particles are manifested in the different physical quantities, like the position fluctuations, first-passage properties, and try to understand the observable differences with passive particles. The contents of this thesis can be broadly divided into three categories as described below.

I. Behavior of free active particles: This category, which includes the contents of the Chapters 2, 3 and 4, deal with active particle dynamics with no external potential. We already saw for a simple model of a one-dimensional run and tumble particle that the position fluctuations have significant differences from passive Brownian particles.

A natural question is, what the effects of the different microscopic dynamics are on the position fluctuations of the different active particles? In this context, we study a set of run-

and-tumble dynamics in two dimensions in Chapter 2 (based on [10]). We find that there are qualitative features, like maximal probability of obtaining the active particles away from the origin at early-times, typical diffusive Gaussian behavior in the long-time regime, which hold true for any microscopic dynamics. However, the specific forms of these behaviors, for example, the shape of the boundary of the probability distributions at short-times, effective diffusion constant or large-deviation functions at long times, depend explicitly on the microscopic dynamics. In Chapter 3, based on [11], we study an active particle model called the ‘direction reversing active Brownian motion’, which models the dynamics of a wide range of microorganisms like *Myxococcus xanthus*, *Pseudomonas putida*, which are seen in nature. It is one of the first active particle models, studied analytically, that had two active time-scales— one set by the active Brownian-like motion and the other by the rate of direction reversal. The behavior of the active particles is governed by a competition between the two time-scales and gives rise to some interesting new features in the position fluctuations and the first-passage properties.

For all these models, we find that at large times, irrespective of the nature of the active particle dynamics at the microscopic level, the typical position fluctuations at long times are always Gaussian with diffusive scaling. The effect of activity, however, is not entirely lost, and its most prominent signatures are encoded in the $x \sim O(t)$ fluctuations, which are characterized by the large deviation functions [56, 10]. Though in some models like the run-and-tumble particles the exact forms of the large deviation functions can be extracted, it is very difficult to get the same for more complicated models like a direction reversing active Brownian particle. Moreover, these $x \sim O(t)$ fluctuations correspond to the rare events that are hard to access experimentally, where one is often limited to the events of $x \sim O(\sqrt{t})$ fluctuations. So characterizing the higher-order non-Gaussian corrections at the scale $x \sim \sqrt{t}$ becomes very important. We investigate this issue in Chapter 4 (based on [12]) and find that active particles show a universal behavior even beyond the leading order Gaussian distribution—the subleading corrections to the long-time Gaussian distribution always follow an inhomogeneous diffusion equation, where the source term depends on the previous order corrections, irrespective of the different microscopic dynamics like RTP, AOUP, ABP, DRABP, etc.

II. *Stationary states of active particles due to external forcing:* In Chapters 5 and 6, we discuss two ways in which the position fluctuations of an active particle can reach a stationary state. As we saw for a passive Brownian particle, one of the easiest and most common ways is by trapping the particle in a confining potential $V(x)$. An active particle, subjected to such confining potentials, also relax to a stationary state at long times, but unlike a passive Brownian particle, the stationary state distribution is, in general, non-Boltzmann. Moreover, there is no general prescription to obtain the stationary states. We study the stationary state of a DRABP trapped in a harmonic potential and show that the stationary state position distribution is determined by a competition between the trapping time-scale and the two active time scales. In particular, we find new stationary phases which are qualitatively different than the usual ones seen in active particle systems [13].

Another way in which a stochastic process reaches a stationary state is if the process is stopped and restarted intermittently. This is popularly called stochastic resetting and has gained immense popularity in recent years in the context of search processes. For a standard Brownian particle, stochastic resetting leads to a host of interesting features like attaining a nonequilibrium stationary state at long times, non-trivial relaxation dynamics, optimizing search times, unusual thermodynamic properties, universal extreme value statistics, etc. In Chapter 6, we discuss the effects of stochastic resetting on a two-dimensional RTP. This is based on the work in [14], which was one of the earliest ones to investigate the effect of resetting on active particles.

III. *Transport properties of active reservoirs:* Energy transport in low dimensional systems connected to thermal reservoirs [92, 93] has been a topic of paramount interest. Collections of active particles, which have their own energy depot, serve as paradigmatic examples of nonequilibrium reservoirs. So an obvious question is what happens to the transport properties of an extended system when it is connected to two such ‘active reservoirs’. We try to address this question in the final part of the thesis. In the first part of Chapter 7 (based on Ref. [15]), we first propose a simple model for active reservoirs and study the dynamical fluctuations of a Hamiltonian probe immersed in it. Having a description of an active reservoir, we proceed to investigate the obvious question— what happens to the transport properties of an extended system when it is connected to two such ‘active reservoirs’. This part of the chapter is based

on Ref. [16] which was the first work to address the question of activity driven transport in extended systems. Finally, we conclude the thesis with some general remarks and future directions in Chapter 8.

Chapter 2

Run-and-tumble particles in two dimensions

An archetype of bacterial motion is exhibited by the well-studied model organisms *Escherichia coli* and *Salmonella typhi*. They have flagella on the surface of their body, which rotate alternating in a anti-clockwise and clockwise manner. When rotating in the anticlockwise manner, the flagella all work together to form a bundle and propel the bacterium along their body axis, causing 'runs' in almost straight lines. During clockwise rotation the bundle breaks up, causing the bacteria to 'tumble' which causes it to rotate randomly. A sequence of these two patterns are termed as 'run-and-tumble' motion. The 'run' durations are usually much larger than the 'tumble' durations, eg., in *E. coli* a typical run phase is ~ 1 s, while tumbles typically happen at the order of ~ 0.1 s

To understand the above dynamics in two dimensions, we model the bacteria by a point particle with an internal orientation vector, representing the body axis, denoted by $\hat{\mathbf{n}} = (\cos \theta, \sin \theta)$. The dynamics is modeled by Eq. (1.20) with the stochastic propulsion velocity $\mathbf{u}(t) = v_0 \hat{\mathbf{n}}(t)$, where $\theta(t)$ evolves stochastically— $\theta(t)$ remains unchanged during the run phase and then changes to a new value during a tumble phase. In this chapter, we consider two scenarios— (I) *n-state model*: $\theta(t)$ changes by fixed amount during tumbles (II) *continuous model*: $\theta(t)$ changes to any value $\in [0, 2\pi]$. Since the typical tumble durations are much smaller than the run durations, we model the tumblings as instantaneous events.

We introduce the models in the Sec. 2.1. We then study the models in Secs. 2.2, 2.3, and 2.4; we finally summarize the results in Sec. 2.4.

2.1 Models

Let us begin by introducing the different tumble dynamics, i.e., how the orientation changes due to a tumbling event.

I. *n-state model*: In this case, θ can have n possible discrete values $\theta = 0, 2\pi/n, 4\pi/n, \dots (n-$

$1)2\pi/n$ and evolves following a jump process – the orientation of the particle changes by an amount $\pm 2\pi/n$ (*i.e.*, the spin rotates either clockwise or anti-clockwise) with rate $\gamma/2$. The θ -dynamics is independent of the position degree of freedom, and is nothing but a symmetric continuous time random walk on a one dimensional ring with n sites with jump rate $\gamma/2$. It is straightforward to calculate (see Appendix 9.1 for the details) the corresponding propagator $P(\theta, t|\theta_0, 0)$, *i.e.*, the probability that the orientation is θ at time t , starting from θ_0 at time $t = 0$, and it is given by,

$$P(\theta, t|\theta_0, 0) = \frac{1}{n} \sum_{k=0}^{n-1} e^{ik(\theta-\theta_0)} e^{-\gamma t \left(1 - \cos \frac{2\pi k}{n}\right)}. \quad (2.1)$$

Note that the $n \rightarrow \infty$ limit, with a rescaling $\gamma \propto n^2$, yields the active Brownian motion. On the other hand, for any finite n , at large-times $t \rightarrow \infty$ each of the θ -values become equally likely. Here, we study the specific cases: the 3 state model (where θ can take value 0, $2\pi/3$ and $4\pi/3$) and 4 state model (where θ can take value 0, $\pi/2$, π and $3\pi/2$).

II. Continuous model: In this case, θ can take any real value in the range $[0, 2\pi]$. At any time t , with rate γ , $\theta \rightarrow \theta'$, where θ' is chosen uniformly from $[0, 2\pi]$. In this case also, we can immediately write down the propagator,

$$P(\theta, t|\theta_0, 0) = e^{-\gamma t} \delta(\theta - \theta_0) + (1 - e^{-\gamma t}) \frac{1}{2\pi}. \quad (2.2)$$

Here the first term corresponds to the scenario where θ has not flipped up to time t and the second term corresponds to at least one flip. Note that, this continuous model is not the $n \rightarrow \infty$ limit of the discrete model introduced before.

Figure 2.1 (upper panel) shows schematic representations of all the three dynamics. A set of corresponding typical trajectories are shown in Fig. 2.1 (lower panel).

In all the cases described above, components of the stochastic propulsion velocity $\mathbf{u}(t) = \{u_x(t), u_y(t)\} = v_0\{\sigma_x(t), \sigma_y(t)\}$ [$\sigma_x(t)$ and $\sigma_y(t)$ are the effective noise along the x and y direction of the RTP] have an exponentially decaying autocorrelation,

$$\langle \sigma_i(s) \sigma_i(s') \rangle \sim e^{-a_0 \gamma |s-s'|}, \quad (2.3)$$

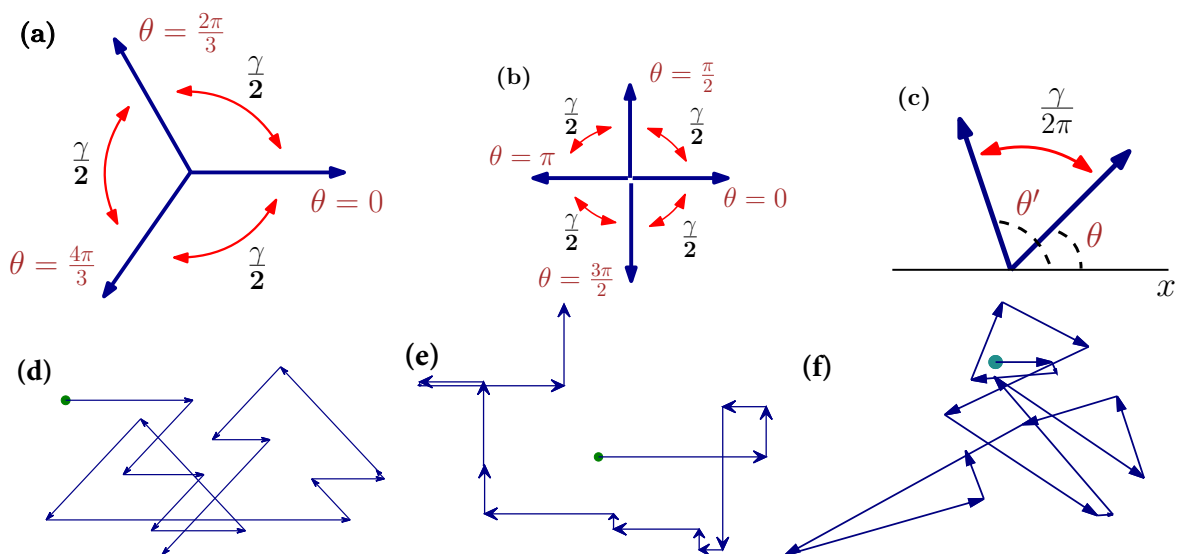


Figure 2.1: Schematic representation of the three different RTP dynamics considered (Upper Panel) and the corresponding trajectories (Lower Panel). (a) and (d) correspond to the 3-state model while (b) and (e) correspond to the 4-state model and (c) and (f) correspond to the continuous model.

where a_0 is some numerical constant depending on the specific dynamics of the model. For any finite γ , the correlation decays exponentially which means that the noise is strongly correlated at short times ($|s - s'| \ll \gamma^{-1}$). This gives rise to strong memory effects in the short-time regime $t \ll \gamma^{-1}$ and the signatures of activity are very much apparent. On the other hand, at long-times, the memory effects vanish and a typical Gaussian behaviour is expected. The change in nature of the motion of these two-dimensional run-and-tumble particles is illustrated in Fig. 2.2 where we show the time evolution of the position probability distribution in the $x - y$ plane, obtained from numerical simulations. The left most panel corresponds to a time $t \ll \gamma^{-1}$. Clearly, in this regime the shape of the probability distribution is very different in all the three models. However, there is one common feature, namely, the distribution attains its maximum value along some curve which is away from the origin implying the particle is likely to be away from the origin. This feature is similar to what has been observed in other active particle models, like active Brownian Particles etc [55, 56]. As time increases, the distribution changes its shape, the peak shifts towards the origin, and at long times $t \gg \gamma^{-1}$ a single-peaked Gaussian-like distribution is observed.

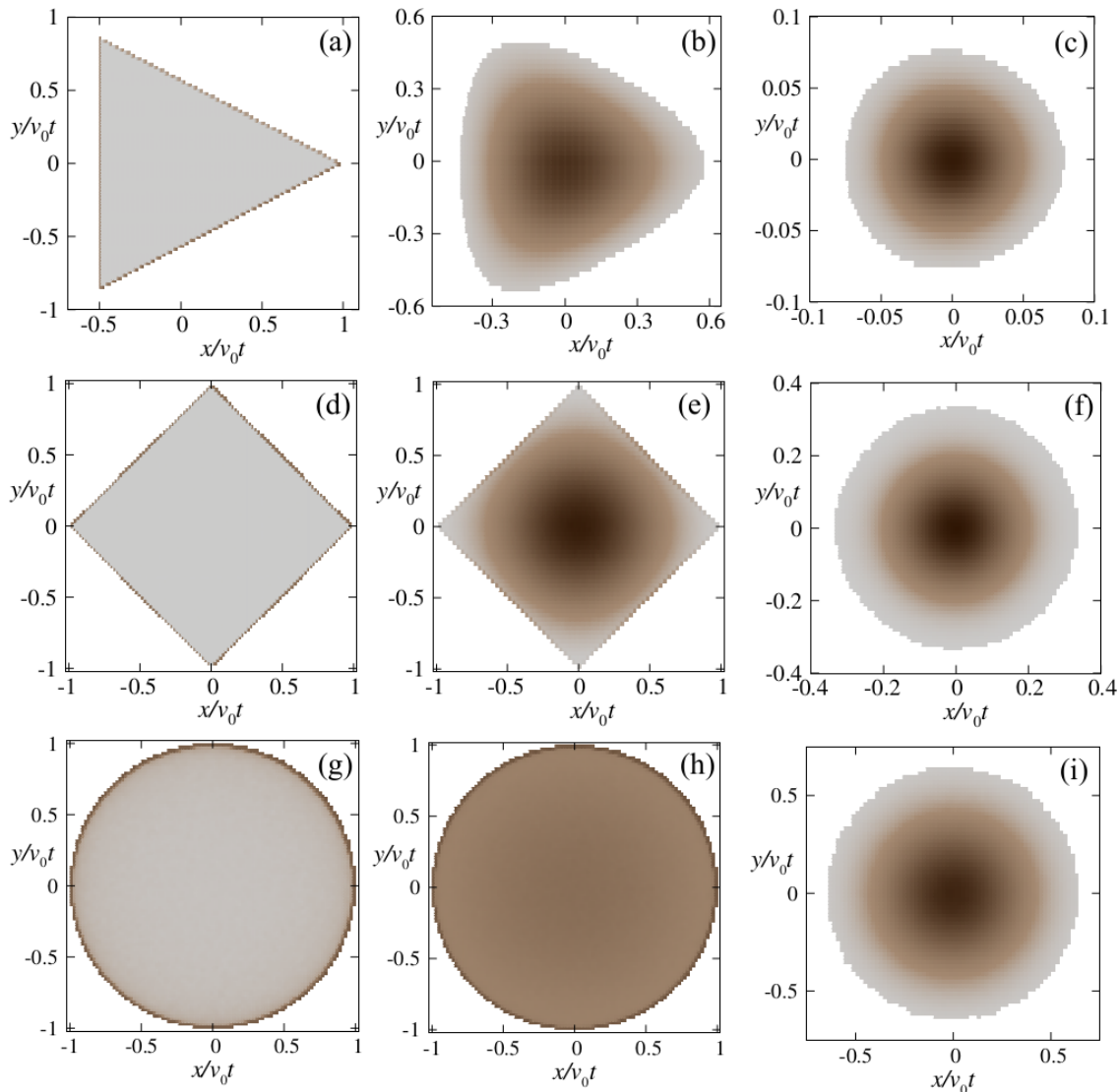


Figure 2.2: Plot of the two-dimensional position distribution $P(x, y; t)$, obtained from numerical simulations, of $n = 3$ ((a) , (b) , (c)) ; $n = 4$ ((d) , (e) , (f)) ; and continuous ((g) , (h) , (i)) models for $\gamma = 0.1$. The left, middle and right panels correspond to $t \ll \gamma^{-1}$ ((a) , (d) , (g)) ; $t \sim \gamma^{-1}$ ((b) , (e) , (h)) ; and $t \gg \gamma^{-1}$ ((c) , (f) , (i)) respectively. The lighter grey shade indicates lower values of $P(x, y; t)$ while darker shades indicate progressively higher values. Here we have used $v_0 = 1$.

2.2 Three-state ($n = 3$) dynamics

In this Section we consider the case where the internal orientational degree of freedom θ can take three discrete values $\theta = 0, 2\pi/3, 4\pi/3$. The orientation changes by a rotation of $\pm 2\pi/3$ (clockwise or anti-clockwise) with rate $\gamma/2$ (see Fig. 2.1 (a) for a schematic representation). A typical trajectory of the particle, starting from the origin and oriented along $\theta = 0$ is shown in Fig. 2.1(d).

At short-times $t \ll \gamma^{-1}$ we see a crowding away from the centre, along the boundary of a triangular region (see Fig. 2.2(a)). To understand this behaviour, let us first note that, starting from the origin, the particle can cover a maximum distance of $v_0 t$ along its initial orientation, if there are no flips during this interval $[0, t]$. For the three different values of the initial θ_0 these corresponds to the points $(v_0 t, 0)$, $(-\frac{v_0 t}{2}, \frac{\sqrt{3}v_0 t}{2})$ and $(-\frac{v_0 t}{2}, -\frac{\sqrt{3}v_0 t}{2})$ in the $x-y$ plane. For one or more flips, even though the total length traversed by the particle remains $v_0 t$, the net distance covered is smaller. Thus, the position of the particle, at any time t , is always bounded by the triangle formed by the above three points. It should be noted that this boundary can be reached by directed paths only, *i.e.* say the side of the triangle between $(v_0 t, 0)$ and $(-\frac{v_0 t}{2}, \frac{\sqrt{3}v_0 t}{2})$ is formed by particles which start with $\theta = 0$ or $\frac{2\pi}{3}$ and till time t , flip in between these two states only, while flip to any other state, *i.e.* $\theta = \frac{4\pi}{3}$ here, would result in some point inside of the said boundary. Similarly the other two sides of the triangle can be explained. As time increases the probability of such directed paths decrease and the centre starts populating. As is evident from Fig. 2.2(b) and (c), the population at the centre increases and we get a centrally peaked distribution at times larger than γ^{-1} .

We are interested in the position probability distribution $P(x, y, t) = \sum_{\theta} \mathcal{P}_{\theta}(x, y, t)$ where $\mathcal{P}_{\theta}(x, y, t)$ denotes the probability that at time t the RTP has a position (x, y) and orientation θ . It is straightforward to write the corresponding Fokker-Planck (FP) equations,

$$\begin{aligned}
 \frac{\partial}{\partial t} \mathcal{P}_0 &= -v_0 \frac{\partial \mathcal{P}_0}{\partial x} + \frac{\gamma}{2} (\mathcal{P}_{\frac{2\pi}{3}} + \mathcal{P}_{\frac{4\pi}{3}}) - \gamma \mathcal{P}_0 \\
 \frac{\partial}{\partial t} \mathcal{P}_{\frac{2\pi}{3}} &= \frac{v_0}{2} \frac{\partial \mathcal{P}_{\frac{2\pi}{3}}}{\partial x} - \frac{v_0 \sqrt{3}}{2} \frac{\partial \mathcal{P}_{\frac{2\pi}{3}}}{\partial y} + \frac{\gamma}{2} (\mathcal{P}_0 + \mathcal{P}_{\frac{4\pi}{3}}) - \gamma \mathcal{P}_{\frac{2\pi}{3}} \\
 \frac{\partial}{\partial t} \mathcal{P}_{\frac{4\pi}{3}} &= \frac{v_0}{2} \frac{\partial \mathcal{P}_{\frac{4\pi}{3}}}{\partial x} + \frac{v_0 \sqrt{3}}{2} \frac{\partial \mathcal{P}_{\frac{4\pi}{3}}}{\partial y} + \frac{\gamma}{2} (\mathcal{P}_0 + \mathcal{P}_{\frac{2\pi}{3}}) - \gamma \mathcal{P}_{\frac{4\pi}{3}}.
 \end{aligned} \tag{2.4}$$

Here we have suppressed the argument of \mathcal{P}_θ for brevity. It is possible to formally solve these coupled first order differential equations using Fourier transformation. However, it is hard to invert the Fourier transformation to extract information about the spatial position distribution. Instead, in the following, we look at the evolution of the x and y -components separately and calculate the marginal distributions which, with a slight abuse of notation we denote as $P(x, t)$ and $P(y, t)$ for simplicity.

2.2.1 Marginal distribution along x -axis

The x -component of the position of the 3-state RTP evolves by the Langevin equation $\dot{x}(t) = v_0 \sigma_x(t)$. Hence, starting from the origin $x = 0$ at time $t = 0$, the position at time t is given by,

$$x(t) = v_0 \int_0^t ds \sigma_x(s). \quad (2.5)$$

Here $\sigma_x = \cos \theta$ takes two distinct values $1, -\frac{1}{2}$, so, at any time t , $x(t)$ is bounded in the region $-v_0 t/2 \leq x(t) \leq v_0 t$.

To understand the nature of the marginal position distribution $P(x, t)$ let us first look at the dynamical behaviour of the effective noise σ_x : σ_x can jump from 1 to $-\frac{1}{2}$ through two channels, namely, $(\theta = 0) \rightarrow (\theta = 2\pi/3)$ and $(\theta = 0) \rightarrow (\theta = 4\pi/3)$ and hence the jump rate for $\sigma_x = 1 \rightarrow -\frac{1}{2}$ is given by γ . On the other hand the jump, $\sigma_x = -\frac{1}{2} \rightarrow 1$ corresponds to either $(\theta = 2\pi/3) \rightarrow (\theta = 0)$ or $(\theta = 4\pi/3) \rightarrow (\theta = 0)$ and the corresponding jump rate is just $\gamma/2$. This effective dynamics is shown schematically in Fig. 2.3. Note that we consider a uniform initial condition for θ and hence the σ_x process is stationary at all times t with $\langle \sigma_x(t) \rangle = 0$. It is instructive to calculate the auto-correlation of σ_x (see Appendix 9.1),

$$\langle \sigma_x(s) \sigma_x(s') \rangle = \frac{1}{2} \exp \left[-\frac{3}{2} \gamma |s - s'| \right]. \quad (2.6)$$

As already mentioned in the previous section, the exponential form of the auto-correlator indicates that the noise is highly correlated at the short-time regime and consequently one can expect strong signatures of activity in this regime.

The simplest way to see these signatures is to look at the behaviour of the moments.

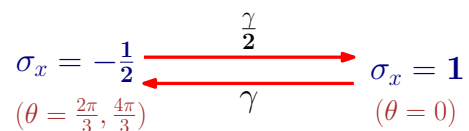


Figure 2.3: The effective 2-state jump process characterizing the time-evolution of σ_x for the 3-state model.

As a direct consequence of the fact that $\langle \sigma_x(t) \rangle = 0$, the mean position $\langle x(t) \rangle$ vanishes at all times. The first non-trivial moment is then the variance $\langle x^2(t) \rangle$ which can be calculated exactly using Eq. (2.6) and is given by,

$$\langle x^2(t) \rangle = \frac{2v_0^2}{3\gamma} \left[t - \frac{2}{3\gamma} \left(1 - e^{-\frac{3\gamma t}{2}} \right) \right]. \quad (2.7)$$

At short-times $t \ll \gamma^{-1}$ the variance grows quadratically,

$$\langle x^2(t) \rangle = v_0^2 t^2 + O(t^3) \quad (2.8)$$

indicating a ballistic behaviour. Note that, the speed of the particle in this ballistic regime is simply v_0 , it does not depend on γ . On the other hand, in the long-time regime a diffusive behaviour is recovered

$$\langle x^2(t) \rangle \simeq 2D_{\text{eff}} t \quad (2.9)$$

where the effective diffusion constant $D_{\text{eff}} = v_0^2/3\gamma$.

To understand the change in behaviour in more details we investigate the position probability $P(x, t) = P_+(x, t) + P_-(x, t)$ where $P_+(x, t)$ (respectively $P_-(x, t)$) denotes the probability that position is x and $\sigma_x = 1$ (respectively $\sigma_x = -\frac{1}{2}$) at time t . The corresponding Fokker-Planck equations are given by

$$\begin{aligned} \frac{\partial P_+}{\partial t} &= -v_0 \frac{\partial P_+}{\partial x} - \gamma P_+ + \frac{\gamma}{2} P_- \\ \frac{\partial P_-}{\partial t} &= \frac{v_0}{2} \frac{\partial P_-}{\partial x} - \frac{\gamma}{2} P_- + \gamma P_+. \end{aligned} \quad (2.10)$$

Note that this set of FP equations can also be obtained directly from Eq. (2.4) by integrating both sides over y and then identifying $P_+(x, t) = \int dy \mathcal{P}_0(x, y, t)$ and $P_-(x, t) =$

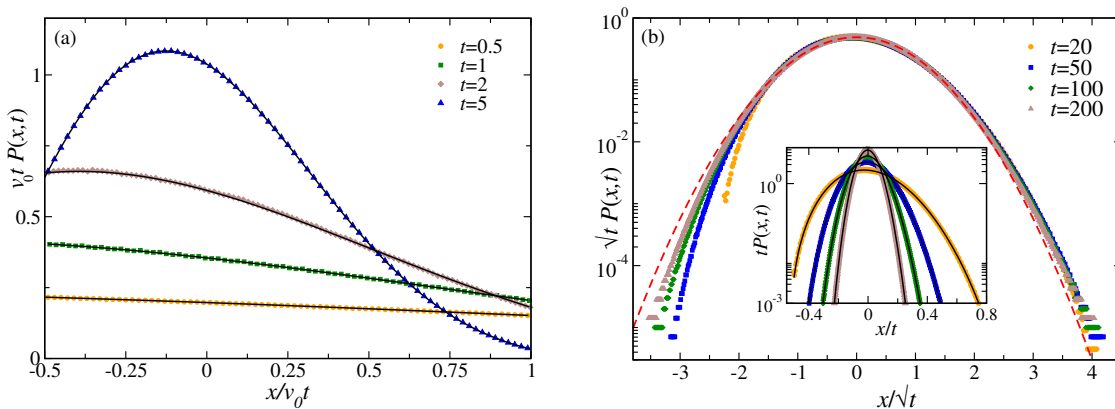


Figure 2.4: 3-state model: (a) Plot of $P(x, t)$ for $\gamma = 1$ and for different values of t . The solid black lines correspond to the analytical prediction Eq. (2.14) and the symbols correspond to the data obtained from the numerical simulations. For better visibility we have excluded the delta functions at the two boundaries. (b) Plot of $P(x, t)$ obtained from numerical simulations, as a function of the scaled variable $w = x/\sqrt{t}$ for different (large) values of t and $\gamma = 1$. The red dashed line shows the Gaussian distribution (see Eq. (2.20)). The inset shows the same data as a function of x/t . The solid black lines there correspond to the analytical prediction Eq. (2.14). Here we have used $v_0 = 1$.

$$\int dy [\mathcal{P}_{2\pi/3}(x, y, t) + \mathcal{P}_{4\pi/3}(x, y, t)].$$

We choose the initial conditions to be such that at $t = 0$ the RTP can be in any of the σ -states with equal probability, *i.e.*,

$$P_+(x, 0) = \frac{1}{3}\delta(x) \text{ and } P_-(x, 0) = \frac{2}{3}\delta(x). \quad (2.11)$$

Taking a Laplace transform, $\hat{P}_\pm(x, s) = \int_0^\infty dt e^{-st} P_\pm(x, t)$, of Eq. (2.10), we get,

$$\begin{aligned} v_0 \hat{P}'_+ &= -(s + \gamma) \hat{P}_+ + \frac{\gamma}{2} \hat{P}_- + \frac{1}{3} \delta(x) \\ v_0 \hat{P}'_- &= (2s + \gamma) \hat{P}_- - 2\gamma \hat{P}_+ - \frac{4}{3} \delta(x), \end{aligned} \quad (2.12)$$

where $'$ denotes the derivative with respect to x . Note that the boundary condition for these equations are simply $\lim_{x \rightarrow \pm\infty} \hat{P}(x, s) = 0$. The solution of this set of coupled differential

equation is obtained for $x \neq 0$ as (see Appendix 9.2 for details),

$$\hat{P}(x, s) = \begin{cases} \frac{6\gamma + 5s - \lambda}{2v_0\lambda} \exp\left[-\frac{x}{2v_0}(\lambda - s)\right] & \text{for } x > 0 \\ \frac{6\gamma + 5s + \lambda}{2v_0\lambda} \exp\left[\frac{x}{2v_0}(\lambda + s)\right] & \text{for } x < 0, \end{cases} \quad (2.13)$$

where where $\lambda = \sqrt{3s(3s + 4\gamma)}$.

The inverse Laplace transform can be performed exactly [see Appendix 9.2 for details] and we get the marginal distribution $P(x, t)$ as,

$$P(x, t) = \Theta(v_0t - x)\Theta\left(x + \frac{v_0t}{2}\right) G_x(x, t) + \frac{1}{3}e^{-\gamma t}\delta(x - v_0t) + \frac{2}{3}e^{-\frac{\gamma t}{2}}\delta\left(x + \frac{v_0t}{2}\right) \quad (2.14)$$

Here $G_x(x, t)$ is the bulk distribution, obtained from the branch-cut integral, whose explicit form is given below in Eq. (2.15). The Dirac-delta functions at $x = v_0t$ and $x = -v_0t/2$ correspond to the cases where initially $\sigma_x = 1$ (respectively $-\frac{1}{2}$) and σ_x does not change its value up to time t . Presence of such delta-functions are typical to RTP-like dynamics in free space, and has been observed also for one-dimensional RTP [55]. The presence of the Θ -functions multiplying $G_x(x, t)$ alludes to the fact that, at any time t , the particle is always bounded between $x = v_0t$ and $x = -v_0t/2$.

The bulk distribution $G_x(x, t)$, obtained from the branch cut integral is given by,

$$G_x(x, t) = \frac{1}{6\pi v_0} \int_0^a du e^{-u(t + \frac{x}{2v_0})} \left[-3 \sin \frac{3x}{2v_0} \sqrt{u(a-u)} + \frac{(6\gamma - 5u)}{\sqrt{u(a-u)}} \cos \frac{3x}{2v_0} \sqrt{u(a-u)} \right], \quad (2.15)$$

where $a = 4\gamma/3$. Upon doing this integral (See Appendix 9.2 for details), we get,

$$G_x(x = zv_0t, t) = \frac{\gamma e^{-\frac{\gamma t}{3}(z+2)}}{9v_0} \left[4I_0\left(\frac{2\gamma t}{3}w(z)\right) + \frac{5-2z}{\sqrt{(2z+1)(1-z)}} I_1\left(\frac{2\gamma t}{3}w(z)\right) \right], \quad (2.16)$$

where $w(z) = \sqrt{(2z+1)(1-z)}$ and $I_\nu(z)$ is the modified Bessel function of the first kind [94]. Figure 2.4 compares the exact analytical $P(x, t)$ for different values of t with the same obtained from numerical simulations.

As mentioned already, we are particularly interested in the behaviour of $P(x, t)$ in the short-time ($t \ll \gamma^{-1}$) and long-time ($t \gg \gamma^{-1}$) regimes. At short times, Taylor expanding the right hand side of Eq. (2.16) around $t = 0$, we get,

$$G_x(x = zv_0t, t) = \frac{2\gamma}{9v_0} \left[2 - \left(z + \frac{1}{2} \right) \gamma t + O(t^2) \right]. \quad (2.17)$$

Clearly, the distribution is linear in the bulk while the δ -function dominates at the boundaries. This linear nature of $P(x, t)$ at short times is clearly visible from the $t = 0.5$ curve in Fig. 2.4 a.

At long times ($t \gg \gamma^{-1}$), using the asymptotic behavior of Bessel functions, we have the large deviation form

$$P(x = zv_0t, t) \sim e^{-t\phi(z)}, \quad (2.18)$$

where the large deviation function is given by

$$\phi(z) = \frac{\gamma}{3} \left[z + 2 - 2\sqrt{(2z+1)(1-z)} \right]. \quad (2.19)$$

Around $z = 0$, the large deviation function is quadratic, $\phi(z) = \frac{3}{4}\gamma z^2 + O(z^3)$. Consequently, the typical fluctuations of x around the origin are of the order \sqrt{t} and are Gaussian in nature, *i.e.*, the distribution of the scaled variable $w = x/\sqrt{t}$ is given by

$$P(w, t) \simeq \sqrt{\frac{3\gamma}{4\pi v_0^2}} \exp\left(-\frac{3\gamma w^2}{4v_0^2}\right). \quad (2.20)$$

Figure 2.4(b) shows a plot of $P(w, t)$ as a function of the scaled variable $w = x/\sqrt{t}$ which leads to a scaling collapse following Eq. (2.20) near the peak at $w = 0$. However, the signature of the active nature of the system is clearly visible at the tails where the distribution remains non-Gaussian.

Another interesting feature of $P(x, t)$ is that it is asymmetric about the origin. To quantify the asymmetry we calculate the skewness which is defined in terms of second and third cumulants. In this case the first moment $\langle x \rangle = 0$, and hence, the skewness is given by, $\kappa_3 = \frac{\langle x^3 \rangle}{\langle x^2 \rangle^{3/2}}$. To calculate the third moment, we need the three point σ - correlation, which

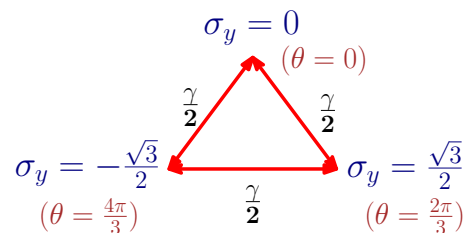


Figure 2.5: 3-state model: Schematic representation of the jump-process governing the time evolution of σ_y .

can be calculated using Eq. (2.1) and turns out to be (see Appendix 9.1)

$$\langle \sigma_x(s_1)\sigma_x(s_2)\sigma_x(s_3) \rangle = \frac{1}{4}e^{-\frac{3}{2}\gamma|s_3-s_1|} \quad (2.21)$$

Thus, the third moment is given by,

$$\langle x^3(t) \rangle = \frac{2v_0^3}{9\gamma^3} \left((4 + 3\gamma t)e^{-\frac{3\gamma t}{2}} + 3\gamma t - 4 \right). \quad (2.22)$$

Using the above expression and Eq. (2.7), κ_3 can be easily calculated. It turns out that $\kappa_3(t) > 0$ for all finite t , indicating a positively skewed distribution. This, however, goes to zero $\kappa_3(t) \sim t^{-1/2}$ as $t \rightarrow \infty$, indicating a slow approach towards a symmetric distribution at long times.

2.2.2 Marginal distribution along y -axis

A direct consequence of the inherent anisotropy of the 3-state model is that the time evolution of the y -component of position is very different from its x counterpart. In this section we focus on the marginal distribution $P(y, t)$ of the 3-state model. In this case, the effective equation of motion along y is given by $\dot{y} = v_0\sigma_y(t)$. Consequently, starting from the origin $y = 0$ at time $t = 0$, we have,

$$y(t) = v_0 \int_0^t ds \sigma_y(s) \quad (2.23)$$

where $\sigma_y = \sin\theta$ takes 3 distinct values $0, \pm\sqrt{3}/2$. Thus, σ_y evolves according to a 3-state jump process, with the jump rates being $\frac{\gamma}{2}$ for all the transitions (see Fig. 2.5 for

a schematic representation of the σ_y process). Note that, at any time t , $y(t)$ is bounded between $[-\frac{\sqrt{3}}{2}v_0t, \frac{\sqrt{3}}{2}v_0t]$.

As before, we first look at the moments to get an idea about the behaviour of this effective 1-d process. Similar to the x -component, the first moment $\langle y(t) \rangle$ vanishes at all times. The second moment can be calculated in a straight-forward manner using the auto-correlation of $\sigma_y(t)$, which is same as that of $\sigma_x(t)$

$$\langle \sigma_y(s)\sigma_y(s') \rangle = \frac{1}{2} \exp \left[-\frac{3}{2}\gamma|s - s'| \right] \quad (2.24)$$

Consequently, the variance,

$$\langle y^2(t) \rangle = \frac{2v_0^2}{3\gamma} \left[t - \frac{2}{3\gamma} \left(1 - e^{-3\gamma t/2} \right) \right] \quad (2.25)$$

is identical with $\langle x^2(t) \rangle$. Hence, once again we see a ballistic behaviour at short times ($t \ll \gamma^{-1}$), $\langle y^2 \rangle \sim v_0^2 t^2$, which goes over to a long-time diffusive behaviour ($t \gg \gamma^{-1}$) with $\langle y^2 \rangle \sim \frac{2v_0^2}{3\gamma} t$. So the effective diffusion constant $D_{\text{eff}} = \frac{v_0^2}{3\gamma}$, same as for the x component. Though the qualitative short and long time behaviours are similar, the x and y motions are very different which is evident from the Fig. 2.2 (a), (b), and will become more clear from the full distribution $P(y, t)$ which we study below.

To calculate the time-dependent distribution $P(y, t)$ of the y -component, we proceed in the same way as before and write the FP equations for $P_\alpha(y, t)$, which denotes probability of finding the particle at position y at time t with $\sigma_y = \alpha$. Note that for notational simplicity we denote the marginal probability distribution of the y -component also with the letter P . The corresponding Fokker-Planck equations are,

$$\begin{aligned} \frac{\partial P_0}{\partial t} &= -\gamma P_0 + \frac{\gamma}{2}(P_+ + P_-) \\ \frac{\partial P_+}{\partial t} &= -v \frac{\partial P_+}{\partial y} - \gamma P_+ + \frac{\gamma}{2}(P_0 + P_-) \\ \frac{\partial P_-}{\partial t} &= v \frac{\partial P_-}{\partial y} - \gamma P_- + \frac{\gamma}{2}(P_0 + P_+) \end{aligned} \quad (2.26)$$

where we have denoted $v = \frac{\sqrt{3}}{2}v_0$; we have suppressed the argument of the P_α in the above equation for brevity. The initial conditions are chosen in such a way that all the three values

of σ_y are equally likely at time $t = 0$ and since we consider that the particle starts from the origin, we must have

$$P_\alpha(y, 0) = \frac{1}{3}\delta(y) \quad \forall \alpha. \quad (2.27)$$

Taking a Laplace transform of Eqs. (2.26) w.r.t., time, we get,

$$\begin{aligned} \hat{P}_0 &= \frac{\gamma}{2(s+\gamma)}(\hat{P}_+ + \hat{P}_-) + \frac{\delta(y)}{3(s+\gamma)}, \\ v\hat{P}'_+ &= -(s+\gamma)\hat{P}_+ + \frac{\gamma}{2}(\hat{P}_0 + \hat{P}_-) + \frac{\delta(y)}{3}, \\ v\hat{P}'_- &= (s+\gamma)\hat{P}_- + \frac{\gamma}{2}(\hat{P}_0 + \hat{P}_+) - \frac{\delta(y)}{3}. \end{aligned} \quad (2.28)$$

where $'$ denotes the derivative with respect to y . We want the full distribution, *i.e.*, $\hat{P} = \hat{P}_0 + \hat{P}_- + \hat{P}_+$. Solving Eqs. (2.28) we get,

$$\hat{P}(y, s) = \frac{(2s+3\gamma)^2}{12v\sqrt{s}(s+\gamma)^{\frac{3}{2}}} \exp\left[-\frac{(2s+3\gamma)}{2v}\sqrt{\frac{s}{s+\gamma}}|y|\right] + \frac{\delta(y)}{3(s+\gamma)}. \quad (2.29)$$

To find the position distribution as a function of the time t we need to compute the inverse Laplace transformation of $\hat{P}(y, s)$. Let us first note that, the last term in Eq. (2.29), when inverted, results in $\frac{1}{3}e^{-\gamma t}\delta(y)$, which denotes the probability that the particle started with $\sigma_y = 0$ and σ_y did not flip up to time t . To invert the first, more complicated term (in Eq. (2.29)), one needs to compute a Bromwich Integral in the complex s -plane. It is easy to see that this integral involves a Branch-cut along the negative s -axis which can be converted to a real line integral following the same procedure as in Sec. 2.2.1 (see Appendix 9.2). Finally, we have,

$$P(y, t) = G_y(y, t)\Theta(vt - |y|) + \frac{e^{-\gamma t}}{3}\left[\delta(y) + \delta(y - vt) + \delta(y + vt)\right] \quad (2.30)$$

where,

$$G_y(y, t) = \int_0^{\gamma-\epsilon} \frac{du e^{-ut}}{12\pi v} \frac{(3\gamma - 2u)^2}{\sqrt{u}(\gamma - u)^{\frac{3}{2}}} \cos\left[\frac{(3\gamma - 2u)y}{2v}\sqrt{\frac{u}{\gamma - u}}\right] - \frac{e^{-\gamma t}}{3\pi y} \sin\left(\frac{\gamma^{3/2}y}{2v\sqrt{\epsilon}}\right) + O(\sqrt{\epsilon}). \quad (2.31)$$

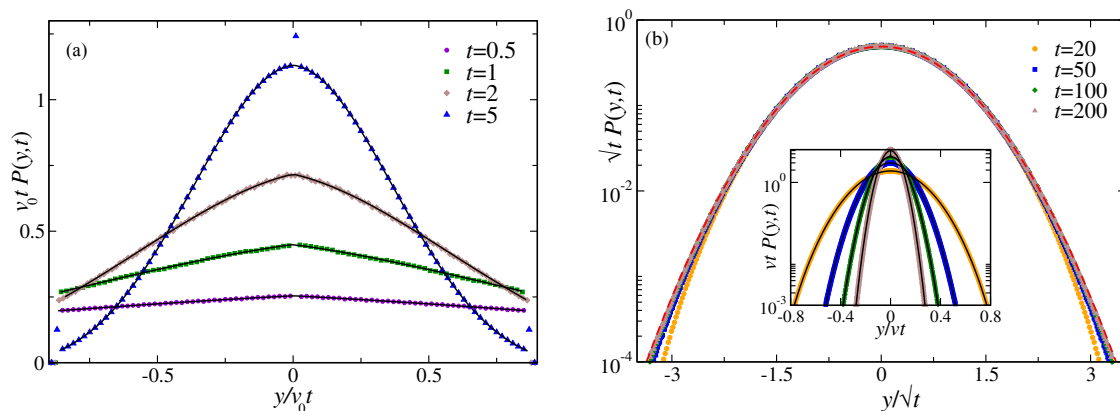


Figure 2.6: 3-state model: (a) Plot of $P(y, t)$ for $\gamma = 1$ and for different values of t . The solid black lines correspond to the analytical predictions Eq. (2.34) for $t = 0.5, 1$; Eq. (2.31) for the other cases and the symbols correspond to the data obtained from the numerical simulations. For better visibility we have excluded the delta functions at the origin and the boundaries. (b) Plot of $P(y, t)$ obtained from numerical simulations, as a function of the scaled variable $w = x/\sqrt{t}$ for different (large) values of t and $\gamma = 1$. The red dashed line shows the Gaussian distribution (see Eq. (2.37)). The inset shows the same data as a function of x/t . The solid black lines there correspond to the analytical prediction Eq. (2.31). Here we have used $v_0 = 1$.

where ϵ is a very small number. Eq. (2.31) can be evaluated numerically for small ϵ . It turns out that this agrees well with numerical simulations for times greater than γ^{-1} . For $t \lesssim \gamma^{-1}$ numerical evaluation of Eq. (2.31) becomes difficult. In this regime we adopt a different approach and write $\hat{P}(y, s)$ in Eq. (2.29) as a series in s for $y \neq 0$,

$$\hat{P}(y \neq 0, s) = \frac{1}{12v} \sum_{n=0}^{\infty} \frac{(-y/v)^n}{2^n n!} (3\gamma)^{n+2} \sum_{m=0}^{n+2} \binom{n+2}{m} \left(\frac{2}{3\gamma}\right)^m \frac{s^{m+(n-1/2)}}{(s+\gamma)^{n+3/2}}. \quad (2.32)$$

Then, taking the inverse Laplace transformation of the above equation with respect to s gives

$$G(y = zvt, t) = \frac{9\gamma^2 t}{12v} \sum_{n=0}^{\infty} \frac{(-|z|)^n}{2^n n!} (3\gamma t)^n \sum_{m=0}^{n+2} \binom{n+2}{m} \left(\frac{2}{3\gamma t}\right)^m {}_1\bar{F}_1\left(\frac{n+3}{2}, 2-m, -\gamma t\right), \quad (2.33)$$

where ${}_p\bar{F}_q(a, b, z)$ is the regularized Hypergeometric function [94].

Using this result, we can get closed form expressions for the probability distribution function at short and long times. At short times, the distribution is dominated by the three δ -functions, to get the bulk distribution it is sufficient to calculate the first few terms of the

series to get the leading order behaviour. The short-time distribution thus comes out to be

$$G(y, t) = \frac{\gamma}{\sqrt{3}v_0} - \frac{\gamma^2 t}{4\sqrt{3}v_0} + \frac{\gamma^2 y}{18v_0^2}(5\gamma t - 6) + O(t^2). \quad (2.34)$$

At large times, the regularized Hypergeometric function in Eq. (2.33) can be approximated to the highest order in t , as

$${}_1\bar{F}_1\left(\frac{n+3}{2}, 2-m, -\gamma t\right) \approx \frac{(\gamma t)^{(n+3)/2}}{\Gamma((1-n)/2-m)}.$$

The summation over m can then be performed to give

$$G(y = zvt, t) \approx \frac{9\gamma}{12v} \sum_{n=0,2,\dots}^{\infty} \left(-\frac{3}{2}\right)^{\frac{3n+1}{2}} \frac{(\gamma|z|)^n U\left(\frac{1+n}{2}, \frac{7+3n}{2}, -\frac{3\gamma t}{2}\right)}{n! \Gamma\left(\frac{1-n}{2}\right)} \quad (2.35)$$

where $U(a, b, z)$ is the Hypergeometric- U function. The presence of $\Gamma((1-n)/2)$ restricts the sum to only over even n . Expanding the HypergeometricU function to the leading order in t and using the properties of the Γ -function, we get a Gaussian in this large time regime,

$$G(y, t) \approx \sqrt{\frac{3\gamma}{4\pi t v_0^2}} \exp\left(-\frac{3\gamma y^2}{4v_0^2 t}\right). \quad (2.36)$$

As before, it is useful to introduce the scaled variable $w = y/\sqrt{t}$, which has the distribution,

$$P(w, t) \approx \sqrt{\frac{3\gamma}{4\pi v_0^2}} \exp\left(-\frac{3\gamma w^2}{4v_0^2}\right). \quad (2.37)$$

Fig. 2.6 compares the analytical expression for the probability distribution function with numerical simulations. For times $t \lesssim \gamma^{-1}$, we use Eq. (2.34) while Eq. (2.31) is used for the other cases.

Let us briefly summarize the results of the 3-state model. We have calculated the exact time dependent marginal distributions, short time distributions for both x and y are dominated by δ -functions, however in the bulk the leading order contribution to x distribution is quadratic, while for y , it is linear. The y distribution is symmetric at all times, unlike the x distribution which is highly asymmetric at short times which decreases with time.

2.3 Four state ($n = 4$) dynamics

In this section we consider the case $n = 4$, *i.e.*, where the internal spin can take 4 values, $\theta = 0, \frac{\pi}{2}, \pi, \frac{3\pi}{2}$. The orientation thus changes by $\pm\frac{\pi}{2}$ (*i.e.*, clockwise or anti-clockwise) with a rate $\frac{\gamma}{2}$ (see Fig. 2.1 (b)). A typical trajectory of the particle starting from the origin can be seen in Fig. 2.1(e).

The time evolution of the full 2d distribution obtained from numerical simulations is shown in Fig. 2.2((d), (e), (f)). At time scales less than γ^{-1} , there is a crowding away from the origin. This can be explained in the same way as the $n = 3$ case, if the particle starts from the origin with $\theta = 0, \frac{\pi}{2}, \pi$ and $\frac{3\pi}{2}$ with equal probability at $t = 0$, then at time t , it can go to $(v_0t, 0)$, $(0, v_0t)$, $(-v_0t, 0)$ and $(0, -v_0t)$ in the $x - y$ plane which form a diamond Fig. 2.2(f), the sides of the diamond are formed by directed paths. This marks the boundary of the distribution in the $x - y$ plane. As time increases the crowding at the boundary decreases and the centre starts populating as is evident from Fig. 2.2(e). Finally we get a centrally peaked distribution at times larger than γ^{-1} Fig. 2.2(f).

This model has been introduced recently in [95] where the stationary distribution in the presence of external potential has been studied. Here we calculate the position distribution in the free space. The position probability distribution $\mathcal{P}(\xi, \dagger, \sqcup) = \sum_{\theta} \mathcal{P}_{\theta}(\xi, \dagger, \sqcup)$ where $\mathcal{P}_{\theta}(\xi, \dagger, \sqcup)$ denotes the probability that the particle is at position (x, y) with orientation θ at time t . These probabilities evolve according to the Fokker-Planck (FP) equations,

$$\begin{aligned}
 \frac{\partial}{\partial t} \mathcal{P}_0(x, y, t) &= -v_0 \frac{\partial \mathcal{P}_0}{\partial x} + \frac{\gamma}{2} (\mathcal{P}_{\frac{\pi}{\epsilon}} + \mathcal{P}_{\frac{3\pi}{\epsilon}}) - \gamma \mathcal{P}_0, \\
 \frac{\partial}{\partial t} \mathcal{P}_{\frac{\pi}{2}}(x, y, t) &= -v_0 \frac{\partial \mathcal{P}_{\frac{\pi}{2}}}{\partial y} + \frac{\gamma}{2} (\mathcal{P}_0 + \mathcal{P}_{\pi}) - \gamma \mathcal{P}_{\frac{\pi}{2}}, \\
 \frac{\partial}{\partial t} \mathcal{P}_{\pi}(x, y, t) &= v_0 \frac{\partial \mathcal{P}_{\pi}}{\partial x} + \frac{\gamma}{2} (\mathcal{P}_{\frac{\pi}{\epsilon}} + \mathcal{P}_{\frac{3\pi}{\epsilon}}) - \gamma \mathcal{P}_{\pi}, \\
 \frac{\partial}{\partial t} \mathcal{P}_{\frac{3\pi}{2}}(x, y, t) &= v_0 \frac{\partial \mathcal{P}_{\frac{3\pi}{2}}}{\partial y} + \frac{\gamma}{2} (\mathcal{P}_0 + \mathcal{P}_{\pi}) - \gamma \mathcal{P}_{\frac{3\pi}{2}}.
 \end{aligned} \tag{2.38}$$

where the arguments of the \mathcal{P}_{θ} s have been suppressed on the r.h.s. for brevity. These coupled differential equations again can be formally solved by writing a 4×4 matrix in Fourier space, but the eigenvalues and eigenvectors are complicated and it is very hard to get the inverse transform. So as in the previous case we concentrate on the marginal distributions only.

2.3.1 Marginal distribution along x -axis

In this model, σ_x and σ_y have the same dynamics, so the process is symmetric in x and y at all times, unlike the $n = 3$ case. Thus, it is sufficient to calculate the distribution along any one direction (say x). The position $x(t)$ evolves according to the equation $\dot{x} = v_0\sigma_x(t)$, where $\sigma_x = \cos\theta$ is the effective 3-state internal spin degree of freedom which can take 3 values, $0, \pm 1$ corresponding to $\theta = 0, \frac{\pi}{2}, \pi$ respectively. Here, at anytime t , the motion is bounded in the region $|x| < v_0t$.

The effective noise σ_x can jump to 0 from $\sigma_x = \pm 1$ which corresponds to the flip in θ from $0 \rightarrow \frac{\pi}{2}$ and $\pi \rightarrow \frac{\pi}{2}$. Hence the rate for these jump processes are γ each. σ_x can also jump from $0 \rightarrow \pm 1$, corresponding to the flips $\theta = \frac{\pi}{2} \rightarrow 0$ and $\theta = \frac{\pi}{2} \rightarrow \pi$. So the jump rates for these two processes are $\frac{\gamma}{2}$ each. This dynamics is illustrated in Fig. 2.7.

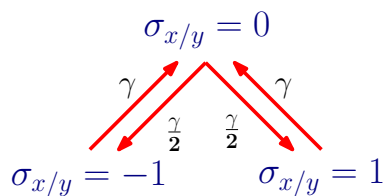


Figure 2.7: The effective 3-state jump process for the 4-state model

The σ_x process is stationary at all times with $\langle \sigma_x(t) \rangle = 0$ and the autocorrelation function (see Appendix 9.1),

$$\langle \sigma_x(s)\sigma_x(s') \rangle = \frac{1}{2}e^{-\gamma|s'-s|}. \quad (2.39)$$

Though the qualitative behaviour of the σ -correlations are very similar to the $n = 3$ case, the decay constant is different. Using Eq. (2.39) we can readily calculate the first two moments of $x(t)$. The mean, $\langle x(t) \rangle$, is zero at all times as $\langle \sigma_x(t) \rangle = 0$, while using Eq. (2.39) the variance comes out to be

$$\langle x(t)^2 \rangle = \frac{v_0^2}{\gamma^2} [\gamma t - (1 - e^{-\gamma t})]. \quad (2.40)$$

So, at short times ($t \ll \gamma^{-1}$),

$$\langle x^2(t) \rangle = \frac{v_0^2 t^2}{2} + O(t^3). \quad (2.41)$$

Thus indicating ballistic behaviour with an effective speed $v_{\text{eff}} = v_0/\sqrt{2}$. However, at long times ($t \gg \gamma^{-1}$),

$$\langle x^2(t) \rangle \approx \frac{v_0^2 t}{\gamma}.$$

i.e., the motion is diffusive with $D_{\text{eff}} = \frac{v_0^2}{2\gamma}$, different from the $n = 3$ case.

With this information at hand, we look at the full time-dependent position distribution $P(x, t)$ in terms of $P_\alpha(x, t)$, the probability that the particle is at position x at time t and $\sigma_x = \alpha$. The corresponding Fokker-Planck equations are,

$$\begin{aligned} \frac{\partial P_+}{\partial t} &= -v_0 \frac{\partial P_+}{\partial x} - \gamma P_+ + \frac{\gamma}{2} P_0, \\ \frac{\partial P_-}{\partial t} &= v_0 \frac{\partial P_-}{\partial x} - \gamma P_- + \frac{\gamma}{2} P_0, \\ \frac{\partial P_0}{\partial t} &= -\gamma P_0 + \gamma(P_+ + P_-). \end{aligned} \quad (2.42)$$

We write $P_{\pm 1}$ as P_\pm and drop the arguments of P_α s for brevity.

We choose the initial conditions such that all σ values are equally likely, *i.e.*,

$$P_0(x, 0) = \frac{1}{2} \delta(x), \quad \text{and} \quad P_\pm(x, 0) = \frac{1}{4} \delta(x). \quad (2.43)$$

To solve Eqs. (2.42), it is convenient to introduce the Fourier transform of $P_\alpha(x)$ with respect to x , *i.e.*, $\tilde{P}_\alpha(k) = \int_{-\infty}^{\infty} e^{ikx} P_\alpha(x) dx$. Upon doing the Fourier transform, Eqs. (2.42) reduce to a set of coupled ordinary differential equations,

$$\frac{\partial}{\partial t} \bar{P} = \Omega \bar{P} \quad \text{with} \quad \bar{P} = \begin{bmatrix} \tilde{P}_+ \\ \tilde{P}_- \\ \tilde{P}_0 \end{bmatrix}; \quad \Omega = \begin{bmatrix} -\gamma + ikv_0 & 0 & \gamma/2 \\ 0 & -\gamma - ikv_0 & \gamma/2 \\ \gamma & \gamma & -\gamma \end{bmatrix} \quad (2.44)$$

The solution of the above set of equations can be written in terms of the eigenvalues and

eigenvectors of the matrix Ω ,

$$\tilde{P}(k, t) = e^{-\gamma t} \left(a_0 \bar{A}_0 + a_+ e^{\lambda t} \bar{A}_+ + a_- e^{-\lambda t} \bar{A}_- \right) \quad (2.45)$$

where we have used the fact that the eigenvalues of Ω are $-\gamma, -\gamma \pm \lambda$, with $\lambda = \sqrt{\gamma^2 - k^2 v_0^2}$. $\bar{A}_{0,\pm}$ are the corresponding eigenvectors,

$$\bar{A}_0 = \begin{bmatrix} \frac{i\gamma}{2kv_0} \\ -\frac{i\gamma}{2kv_0} \\ 1 \end{bmatrix}; \quad \bar{A}_{\pm} = \begin{bmatrix} \frac{ikv_0 \pm \sqrt{\gamma^2 - k^2 v_0^2}}{2\gamma} \\ \frac{ikv_0 \mp \sqrt{\gamma^2 - k^2 v_0^2}}{2\gamma} \\ 1 \end{bmatrix}. \quad (2.46)$$

The coefficients $a_{\alpha s}$ can be determined using the initial conditions Eq. (2.43),

$$a_0 = \frac{-q^2}{2(1-q^2)}; \quad a_{\pm} = \frac{1 \pm \sqrt{1-q^2}}{4(1-q^2)}, \quad (2.47)$$

with $q = \frac{kv_0}{\gamma}$. Substituting these coefficients in Eq. (2.45), we get,

$$\tilde{P}(k = \frac{\gamma q}{v_0}, t) = \frac{e^{-\gamma t}}{2(q^2 - 1)} \left(-q^2 + (2 - q^2) \cosh(\gamma t \sqrt{1 - q^2}) + 2\sqrt{1 - q^2} \sinh(\gamma t \sqrt{1 - q^2}) \right). \quad (2.48)$$

Eq. (2.48) can be inverted exactly using Bessel Function identities [The Fourier inversion is carried out in detail in Appendix 9.3.

$$P(z = \frac{x}{v_0 t}, t) = \gamma t \frac{e^{-\gamma t}}{2} \left[\frac{1}{\sqrt{1-z^2}} I_1(\gamma t \sqrt{1-z^2}) + I_0(\gamma t \sqrt{1-z^2}) - \frac{\gamma t |z|}{4} \right. \\ \left. - \frac{1}{2\gamma t} \int_{|z|}^1 d\omega \left(\frac{\partial^2}{\partial z^2} \right) I_0(\gamma t \sqrt{\omega^2 - z^2}) \right] + \frac{e^{-\gamma t}}{4v_0 t} \left(2\delta(z) + \delta(z-1) + \delta(z+1) \right). \quad (2.49)$$

Note that this solution is valid for $|z| < 1$, $P(z, t)$ is zero otherwise. The integral in the above equation can be evaluated numerically to arbitrary accuracy for any x . $P(x, t)$ obtained from Eq. (2.49) is compared with numerical simulations in Fig. 2.8 (a) for $\gamma = 1$ and different values of t which show an excellent match.

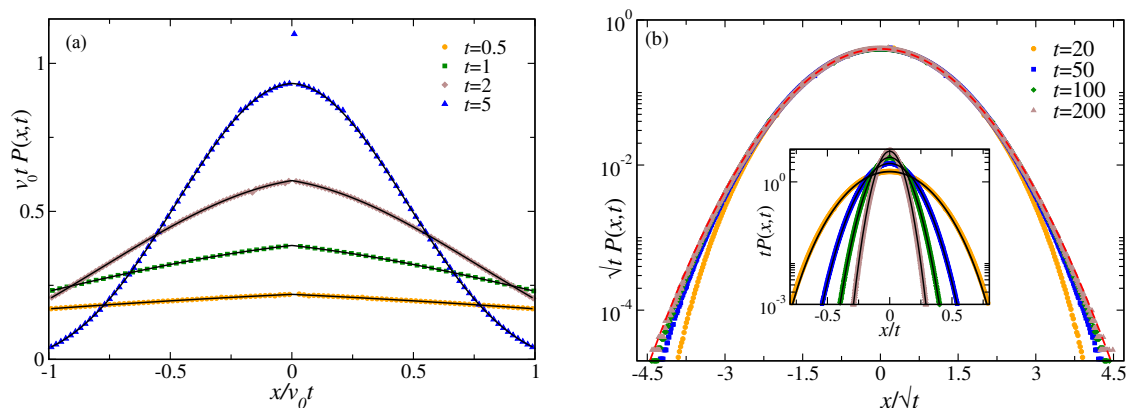


Figure 2.8: 4-state model: (a) Plot of x -marginal for different values of t and $\gamma = 1.0$. The solid black lines correspond to the analytical prediction Eq. (2.49) and the symbols correspond to the data from numerical simulations. For better visibility we have excluded the delta functions at the origin and the boundaries. (b) Plot of $P(x,t)$ obtained from numerical simulations, as a function of the scaled variable $w = x/\sqrt{t}$ for different (large) values of t and $\gamma = 1$. The red dashed lines show the corresponding Gaussian distribution. The inset shows the same data as a function of x/t . The solid black lines there correspond to the analytical prediction Eq. (2.51). Here we have used $v_0 = 1$.

The asymptotic forms of the distribution are easy to calculate from Eq. (2.49). At short times ($t \ll \gamma^{-1}$), the distribution is dominated by the three δ -functions at $0, \pm v_0 t$ while in the bulk it is linear,

$$P(z,t) \approx \frac{\gamma t}{2} \left(1 - \frac{\gamma t |z|}{2} - \frac{\gamma t}{4} \right). \quad (2.50)$$

At long times ($t \gg \gamma^{-1}$), using the asymptotic expressions for the modified Bessel functions I_0 and I_1 , we get a large deviation form,

$$P(z,t) = \frac{v_0 e^{-\gamma t(1-\sqrt{1-z^2})}}{\sqrt{4\pi D_{\text{eff}}/t}} \quad (2.51)$$

with the large deviation function $\phi(z) = \gamma(1 - \sqrt{1-z^2})$. The typical fluctuations in x are $\sim \sqrt{t}$ and Gaussian in nature. Thus the distribution near the origin can be written in terms of the scaled variable $w = x/\sqrt{t}$ as

$$P(w,t) \simeq \frac{1}{\sqrt{4\pi D_{\text{eff}}}} \exp\left(-\frac{\gamma w^2}{2v_0^2}\right). \quad (2.52)$$

A comparison of the obtained large deviation form, Eq. (2.51) (solid lines) and numerical simulation is shown in Fig. 2.8 (b) inset for $t = 100$ and three values of γ . Figure. 2.8 (b) shows a plot of $P(w, t)$ as a function of the scaled variable w , a collapse is seen near the peak at $w = 0$. However the tails are non Gaussian and do not collapse.

Thus in this model, we see again the short time distribution dominated by three δ -functions and linear in the bulk. This 3-peaked structure evolves in time to a single Gaussian like peak at the centre.

2.4 Continuous θ

In this section we consider the case where the orientation of the RTP is a continuous variable and can take any real values in the range $[0, 2\pi]$, *i.e.*, the particle travels at a constant speed v_0 , along the direction $\hat{n} = (\cos \theta, \sin \theta)$ until it flips and changes its orientation to a new θ' , it then moves with the same constant speed v_0 along the new orientation θ' . The rate of this flipping is γ , while the new orientation is chosen from a uniform distribution $\in [0, 2\pi]$. Thus the effective rate of flipping from $\theta \rightarrow \theta'$ is given by $\frac{\gamma}{2\pi}$, see Fig. 2.1 (c). A typical trajectory following such dynamics is illustrated in Fig. 2.1 (f).

The time evolution of the 2d distribution obtained from numerical simulations is shown in Figs. 2.2(g), (h) and (i). The distribution is isotropic at all times, however at times $t \ll \gamma^{-1}$, the particles crowd away from the origin taking the form of a circle of radius $v_0 t$. This marks the boundary of the distribution in the $x - y$ plane. As time increases the crowding at the boundary decreases and the origin starts populating as is evident from Fig. 2.2(h). Finally we get a centrally peaked distribution at times larger than γ^{-1} (Fig. 2.2(i)).

This model has been studied previously [96, 97], where exact expressions for the radial distribution is obtained. We present a simpler derivation leading to the same results and then go on to discuss the exact and large deviation form of the marginal distribution which shows some intriguing behaviour.

2.4.1 Moments and Cumulants

Let us first look at the moments to see the short and long time behaviour of the particle. We assume that the initially the particle is oriented along a random direction $\theta_0 \in [0, 2\pi]$ with

probability $\frac{1}{2\pi}$. The new orientation at each tumble event is also chosen from a uniform distribution in $[0, 2\pi]$; because of this rotational symmetry the x and y directions are equivalent and the odd moments are zero at all times. The first non-zero moment, the variance can be calculated using the 2-point σ correlations (See Appendix 9.1).

$$\langle x^2(t) \rangle = \frac{v_0^2}{\gamma} \left(t - \frac{1 - e^{-\gamma t}}{\gamma} \right) \quad (2.53)$$

Thus, at short times ($t \ll \gamma^{-1}$) $\langle x^2(t) \rangle = v_0^2 t^2 + O(t^3)$, indicating a short-time ballistic regime. This goes over to being diffusive at large times ($t \gg \gamma^{-1}$), $\langle x^2(t) \rangle \simeq 2D_{\text{eff}}t$ with an effective diffusion constant $D_{\text{eff}} = \frac{v_0^2}{2\gamma}$. Thus we see that the behaviour of this model is qualitatively same as the two discrete models considered in the previous sections.

2.4.2 Position Distribution

Let us consider that the particle begins from origin at $t = 0$, pointing along $\hat{n}_0 = (\cos \theta_0, \sin \theta_0)$, where θ_0 can be any angle between $[0, 2\pi]$, then $\mathcal{P}(\vec{\nabla}, \theta, \square | \theta_0)$ denotes the probability for the particle to be at (\vec{r}, θ) at time t , given θ_0 . It evolves according to the Fokker-Planck equation,

$$\frac{\partial}{\partial t} \mathcal{P}(\vec{r}, \theta, t | \theta_0) = -v_0 \hat{n} \cdot \vec{\nabla} \mathcal{P}(\vec{r}, \theta, t | \theta_0) - \gamma \mathcal{P}(\vec{r}, \theta, t | \theta_0) + \gamma \int \frac{d\theta'}{2\pi} \mathcal{P}(\vec{r}, \theta', t | \theta_0), \quad (2.54)$$

where the first term on the right is the drift term, the second term is the probability that the RTP can flip to some other orientation at rate γ , while the third term takes into account that the RTP can flip to θ from any other θ' in $[0, 2\pi]$. Let us define the Fourier-Laplace transform of $\mathcal{P}(\vec{r}, \theta, t | \theta_0)$,

$$\hat{\mathcal{P}}(\vec{k}, \theta, s | \theta_0) = \int_0^\infty dt e^{-st} \int d\vec{r} e^{i\vec{k} \cdot \vec{r}} \mathcal{P}(\vec{r}, \theta, s | \theta_0) \quad (2.55)$$

where $\vec{k} = (k_1, k_2)$. We need to solve Eq. (2.54) with the initial condition,

$$\mathcal{P}(\vec{r}, \theta, 0 | \theta_0) = \delta^2(\vec{r}) \delta(\theta - \theta_0) \quad (2.56)$$

where θ_0 is some arbitrary angle in $[0, 2\pi]$. Using Eq. (2.56) and Eq. (2.55), Eq. (2.54) becomes,

$$s\hat{\mathcal{P}}(\vec{k}, \theta, s | \theta_0) = \delta(\theta - \theta_0) + iv_0\vec{k}\cdot\hat{n}\hat{\mathcal{P}}(\vec{k}, \theta, s | \theta_0) - \gamma\hat{\mathcal{P}}(\vec{k}, \theta, s | \theta_0) + \gamma \int \frac{d\theta'}{2\pi} \hat{\mathcal{P}}(\vec{k}, \theta', s | \theta_0). \quad (2.57)$$

Solving for $\hat{\mathcal{P}}(\vec{k}, \theta, s | \theta_0)$, we have,

$$\hat{\mathcal{P}}(\vec{k}, \theta, s | \theta_0) = \frac{\left(\delta(\theta - \theta_0) + \gamma \int_0^{2\pi} \frac{d\theta'}{2\pi} \hat{\mathcal{P}}(\vec{k}, \theta', s | \theta_0) \right)}{s + \gamma - iv_0\vec{k}\cdot\hat{n}}.$$

Integrating over the final and initial orientations θ and θ_0 , Eq. (2.58) reduces to an algebraic equation,

$$G(\vec{k}, s) = \int_0^{2\pi} d\theta \int_0^{2\pi} \frac{d\theta_0}{2\pi} \hat{\mathcal{P}}(\vec{k}, \theta, s | \theta_0) = \frac{f(\vec{k}, s)}{1 - \gamma f(\vec{k}, s)} \quad (2.58)$$

where

$$f(\vec{k}, s) = \int_0^{2\pi} \frac{d\theta}{2\pi} \frac{1}{s + \gamma - iv_0\vec{k}\cdot\hat{n}} = \left((\gamma + s)^2 + v_0^2 k^2 \right)^{-1/2}. \quad (2.59)$$

Note that, $k^2 = |\vec{k}|^2 = k_1^2 + k_2^2$. Finally we get the characteristic function $G(\vec{k}, s)$ in the Laplace space as,

$$G(\vec{k}, s) = \frac{1}{\sqrt{(\gamma + s)^2 + v_0^2 k^2} - \gamma}. \quad (2.60)$$

Now, to obtain the position distribution, we need to find the Laplace-Fourier inverse of $G(\vec{k}, s)$. For simplicity, we drop the vector notation of k in G and f henceforth, as both depend only on k^2 . $G(k, s)$ has contributions from all the events where the particle does not flip or flips multiple times till time t . It turns out that to invert Eq. (2.60) it is convenient if we subtract the contribution of the no flip event, from $G(k, s)$. The contribution of the no-flip event to the probability distribution can be easily written as, $e^{-\gamma t} \delta(x - v_0 \cos \theta_0 t) \delta(y - v_0 \sin \theta_0 t)$, which

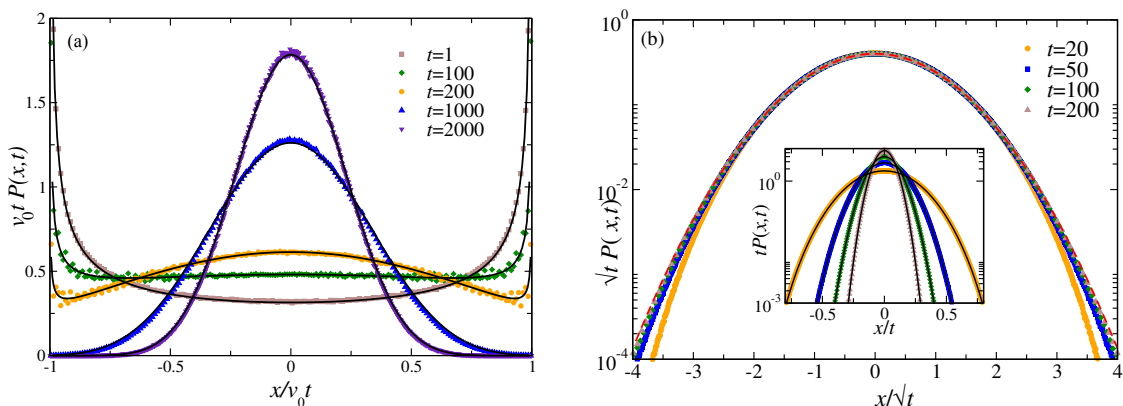


Figure 2.9: Continuous θ model: (a) Plot of x -marginal for different values of t and $\gamma = 1.0$. The solid black lines correspond to the analytical prediction Eq. (2.64) and the symbols correspond to the data from numerical simulations. For better visibility we have excluded the delta functions at the origin and the boundaries. (b) Plot of $P(x,t)$ obtained from numerical simulations, as a function of the scaled variable $w = x/\sqrt{t}$ for different (large) values of t and $\gamma = 1$. The red dashed line shows the corresponding Gaussian distribution. The inset shows the same data as a function of x/t . The solid black lines there correspond to the analytical prediction Eq. (2.66). Here we have used $v_0 = 1$.

upon taking a Fourier-Laplace transform and averaging over all θ_0 gives $f(\tilde{k}, s)$. We define,

$$\mathcal{G}(k, s) = G(k, s) - f(k, s). \quad (2.61)$$

The inversion of $\mathcal{G}(k, s)$ is non-trivial and has been carried out in details in Appendix 9.4.

The resulting contribution to the probability distribution is

$$P(r, t) = \frac{\gamma e^{-\gamma t} \exp\left[\frac{\gamma}{v_0} \sqrt{v_0^2 t^2 - r^2}\right]}{2\pi v_0 \sqrt{v_0^2 t^2 - r^2}}. \quad (2.62)$$

To get the full distribution we have to add the contribution of the no-flip event to the above equation, which is given by $e^{-\gamma t} \delta(r - v_0 t)/(2\pi r)$. Thus, we have the exact position distribution at any time t ,

$$\mathcal{P}(r, t) = e^{-\gamma t} \left[\frac{\delta(r - v_0 t)}{2\pi r} + \frac{\gamma}{2\pi v_0} \frac{\exp\left[\frac{\gamma}{v_0} \sqrt{v_0^2 t^2 - r^2}\right]}{\sqrt{v_0^2 t^2 - r^2}} \Theta(v_0 t - r) \right]. \quad (2.63)$$

The Θ function implies that the distribution is always bounded. This expression is identical to the ones obtained in [96, 97].

2.4.3 Marginal Distribution

We now look at the marginal distribution along either x or y . For this purpose, we rewrite Eq. (2.63) in terms of the Cartesian coordinates, by substituting $r = \sqrt{x^2 + y^2}$ in Eq. (2.63), and thereafter integrate over y , to obtain,

$$P(x, t) = \frac{\gamma e^{-\gamma t}}{2v_0} \left(L_0 \left[\frac{\gamma}{v_0} W(x) \right] + I_0 \left[\frac{\gamma}{v_0} W \right] \right) + \frac{e^{-\gamma t}}{\pi W(x)} \quad (2.64)$$

where $W(x) = \sqrt{v_0^2 t^2 - x^2}$; $I_0(z)$ is the the modified Bessel function of the first kind and $L_0(z)$ is the modified Struve function [94].

The interesting difference between the marginal distribution of this model and the two previously discussed discrete models is that the divergence at the boundaries is not a δ -function divergence but an algebraic divergence. The analytic expression of the distribution function found in Eq. (2.64) is compared with numerical simulation for $\gamma = 0.01$ for different values of t in Fig. 2.9(a). We can immediately look at the asymptotic limits of the distribution, using the asymptotic forms of the modified Bessel and modified Struve functions [94], where the active and passive characteristics are more prominent. At very short times ($t \ll \gamma^{-1}$), the distribution is dominated by the no flip process, given by

$$P(z = \frac{x}{v_0 t}, t) \approx \frac{e^{-\gamma t}}{\pi \sqrt{1 - z^2}}, \quad (2.65)$$

while at large times ($t \gg \gamma^{-1}$) we get a large deviation form from the asymptotic expansions of I_0 and L_0 . Thus,

$$P(z, t) \approx \frac{v_0 t e^{-\gamma t(1 - \sqrt{1 - z^2})}}{\sqrt{4\pi D_{\text{eff}} t}}. \quad (2.66)$$

with the large deviation function $\phi(z) = \gamma(1 - \sqrt{1 - z^2})$.

The large deviation form of the distribution obtained in Eq. (2.66) is compared with the results of numerical simulation at $t = 2000$ for four different values of γ in the inset of

Fig. 2.9 (b) The typical fluctuations in x are Gaussian and scale as \sqrt{t} . Thus the distribution near the origin in terms of the scaled variable $w = x/\sqrt{t}$ becomes

$$P(w, t) \simeq \frac{1}{\sqrt{4\pi D_{\text{eff}}}} \exp\left[-\frac{\gamma w^2}{2v_0^2}\right]. \quad (2.67)$$

Figure 2.9 (b) shows a plot of $P(w, t)$ with the scaled variable w . We see a scaling collapse near the peak while near the boundaries there is no collapse indicating non-Gaussian tails.

Summarizing, we see at short times, this model is dominated by the divergence at the boundaries, like the discrete models described in the previous two sections. However here, the nature of divergence is algebraic unlike the δ -functions of the previous two models. This short time 2-peaked distribution goes over to a single Gaussian like peak at large times.

2.5 Summary

We studied a set of RTP models in two spatial dimensions, where the orientation θ of the particle can take either discrete or continuous values. We show that, for all the models, at short-time regime, the RTP shows a ballistic behaviour, *i.e.*, in this regime, the mean-squared displacement $\propto v_{\text{eff}}^2 t^2$ where the effective velocity depends on the specific model. On the other hand, in the long-time regime, the RTP shows a diffusive behaviour, *i.e.*, the mean-squared displacement grows linearly with time $\sim 2D_{\text{eff}}t$, where, the effective diffusion constant D_{eff} is also model specific. The symmetry of the orientation dynamics manifests in the short-time behaviour of the probability distribution (see Fig. 2.2). The particles cluster away from the origin along some boundary whose shape depends crucially on the microscopic dynamics. These features disappear at long times, where the crowding is near the origin. We calculate the time-dependent marginal position distributions, and also the full two-dimensional distribution for the continuous case and show that the ballistic to diffusive crossover is associated to qualitatively different behaviours of the marginal position distributions at the short-time and long-time regimes. We characterize these by obtaining closed form expressions for the distributions at the two regimes. We find that, independent of the model, the typical position fluctuations are Gaussian at long-times. However, the atypical fluctuations are different for the different models and are characterized by large deviation function which we calculate

explicitly.

Though run-and-tumble motion has been widely studied both theoretically and experimentally, they model a specific kind of dynamics with only a single active time-scale. In many organisms, the activity manifests itself as two distinct kinds of motion, leading to two different activity time-scales. In the next chapter, we will discuss one such dynamics.

Chapter 3

Active Brownian motion with directional reversal

Like RTP another popular and well-known active particle model is the so called active Brownian particle (ABP)—where the particle shows a persistent motion along the body axis, the orientation of which evolves by a Brownian motion. In two dimensions the position distribution evolves by the Langevin equation,

$$\dot{\mathbf{r}} = v_0 \hat{\mathbf{n}} \quad \text{where} \quad \dot{\theta}(t) = \sqrt{2D_R} \eta(t). \quad (3.1)$$

Here η is a δ -correlated Gaussian white noise, while the rotational diffusion coefficient D_R sets the activity time-scale. They show qualitatively similar behavior as run-and-tumble particles—a short-time active regime, characterized by a non-diffusive variance and a non-Gaussian distribution, while at late times the typical distribution becomes a Gaussian with a diffusive scaling. Though both RTP and ABP have been extremely successful as microscopic models to study the different collective phenomena like motility induced phase separation, they are limited as they mimic the motion of only a certain class of bacteria like *E. coli* and different catalytic swimmers (respectively).

Many microorganisms such as *Myxococcus xanthus* [98, 99, 100, 101], *Pseudomonas putida* [102, 103], *Pseudoalteromonas haloplanktis* and *Shewanella putrefaciens* [104, 105], and *Pseudomonas citronellolis* [106] shows a distinctly different dynamics—they perform an ABP-like motion, while completely reversing their direction intermittently. The origin of such reversals is different in different organisms, eg., internal protein oscillations reverse the cell polarity which causes the directional reversal in *Myxococcus xanthus* [98, 100] while a reversal of swimming direction occurs due to the reversal in the rotation direction of polar flagella in *Pseudomonas putida* [102, 103]. The addition of the drastic reversal dynamics to the rotational diffusion gives rise to a host of emergent collective phenomena including fruiting body formation [99], generation of rippling patterns [107] and accordion waves [108]. Despite

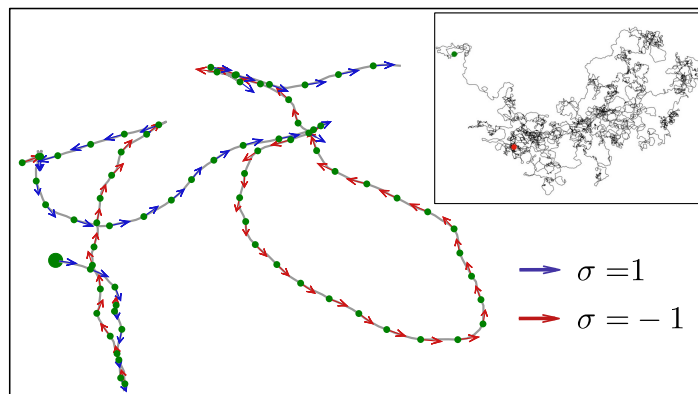


Figure 3.1: A typical trajectory of a DRABP generated by discretizing (3.1), where in a small interval Δt , the particle reverses the direction with probability $\gamma\Delta t$ and with probability $1-\gamma\Delta t$ performs an ABP: $\{\Delta x(t), \Delta y(t)\} = v_0\sigma(t)\Delta t\{\cos\theta(t), \sin\theta(t)\}$; $\Delta\theta(t) = \sqrt{2D_R\Delta t}\chi$, where χ is drawn from a standard normal distribution. The arrows indicate the instantaneous velocity vectors. The inset shows a long-time trajectory [which resembles a Brownian trajectory] with the two end-points marked.

the widespread appearance of this direction reversing active Brownian particles (DRABP), a theoretical understanding of it was still lacking—even at the level of single particle position distribution. In this chapter, we try to bridge that gap. In Sec. 3.1 we introduce the model of DRABP and discuss some basic features of the DRABP dynamics, like effective noise autocorrelation and position moments. In Sec. 3.2, we study the position distribution of the DRABP in these dynamical regimes. We discuss the first-passage properties of the DRABP in Sec. 3.3 and summarize in Sec. 3.4.

3.1 Model

In two dimensions, the position $\mathbf{r} = (x, y)$ and orientation θ of a DRABP evolve according to the Langevin equations,

$$\dot{x}(t) = v_0 \sigma(t) \cos\theta(t) \equiv \zeta_x(t), \quad (3.2a)$$

$$\dot{y}(t) = v_0 \sigma(t) \sin\theta(t) \equiv \zeta_y(t), \quad (3.2b)$$

$$\dot{\theta}(t) = \sqrt{2D_R} \eta(t), \quad (3.2c)$$

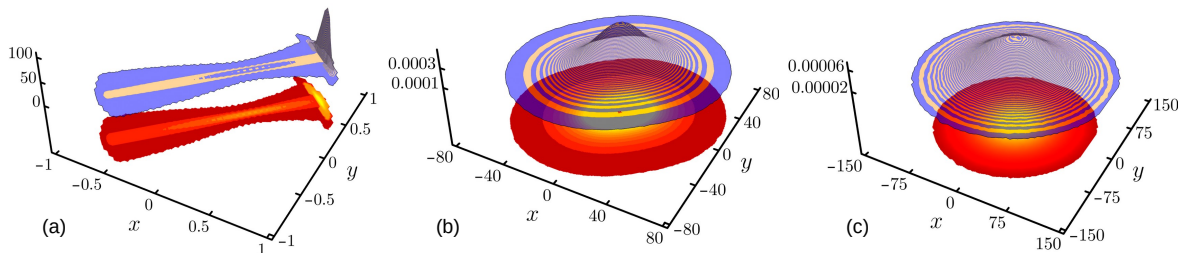


Figure 3.2: Dynamical evolution of the position distribution $P(x, y, t)$ for the case $\gamma > D_R$ obtained from numerical simulations. Here we have taken $\gamma = 0.1$, $D_R = 0.01$ and initial orientation $\theta_0 = \pi/4$. The panels (a), (b) and (c) correspond to $t = 1$ [regime (I)], $t = 50$ [regime (II)] and $t = 200$ [regime (IV)], respectively. The strong anisotropy in regime (I) persists in the intermediate regime (II) eventually disappearing at large times (IV). For $\gamma < D_R$ the intermediate regime (b) is replaced by regime (III) which looks similar to (c).

where D_R is the rotational diffusion coefficient, $\eta(t)$ is a Gaussian white noise with $\langle \eta(t) \rangle = 0$ and $\langle \eta(t)\eta(t') \rangle = \delta(t - t')$. The dichotomous noise $\sigma(t)$ alternates between ± 1 at a constant rate γ , triggering the direction reversal (similar to the propulsion velocity of a one-dimensional run-and-tumble particle). We introduce $\zeta_x(t)$ and $\zeta_y(t)$ for notational convenience, they denote the effective noise (propulsion velocity) along x and y directions. Figure 3.1 shows a typical trajectory following the above dynamics. The presence of orientational diffusion along with the directional reversals leads to the emergence of two time-scales in the system given by D_R^{-1} and γ^{-1} , respectively. Experimental evidences indicate that these two time scales are very well-separated, for example, for *Myxococcus xanthus* $\gamma^{-1} \sim 10^2 s$, while $D_R^{-1} \sim 10^6 s$ [109]. These well separated time-scales gives rise to four distinct dynamical regimes: (I) $t \ll \min(\gamma^{-1}, D_R^{-1})$, (II) $\gamma^{-1} \ll t \ll D_R^{-1}$, (III) $D_R^{-1} \ll t \ll \gamma^{-1}$, and (IV) $t \gg \max(\gamma^{-1}, D_R^{-1})$.

3.1.1 Effective noise correlations

Let us first look at the correlations of the effective noises $\zeta_x(t)$ and $\zeta_y(t)$. To this end, we first note that, since the σ and θ processes are independent, it suffices to compute the correlations of σ and $\cos \theta$, $\sin \theta$ separately. Using the propagators of the σ -process,

$$\Psi(\sigma, t | \sigma_0, 0) = \frac{1}{2} \left(1 + \sigma \sigma_0 e^{-2\gamma t} \right), \quad (3.3)$$

and that for the θ -process (note that, though θ is bound $\in [0, 2\pi]$, as we are interested in the correlations of $\cos \theta$, $\sin \theta$, we can consider $\theta \in (-\infty, \infty)$),

$$\Phi(\theta, t | \theta_0, 0) = \frac{1}{\sqrt{4\pi D_R t}} \exp \left[-\frac{(\theta - \theta_0)^2}{4D_R t} \right], \quad (3.4)$$

we can easily compute the mean autocorrelations of the effective noises. For a DRABP startiis known to beng with $\theta(t) = \theta_0$ and $\sigma(0) = 1$, they turn out to be,

$$\langle \zeta_x(s) \rangle = v_0 \langle \sigma(s) \rangle \langle \cos \theta(s) \rangle = v_0 \sigma_0 \cos \theta_0 e^{-(D_R + 2\gamma)s}, \quad (3.5a)$$

$$\langle \zeta_y(s) \rangle = v_0 \langle \sigma(s) \rangle \langle \sin \theta(s) \rangle = v_0 \sigma_0 \sin \theta_0 e^{-(D_R + 2\gamma)s}, \quad (3.5b)$$

and

$$\begin{aligned} \langle \zeta_x(s) \zeta_x(s') \rangle &= v_0^2 \langle \sigma(s) \sigma(s') \rangle \langle \cos \theta(s) \cos \theta(s') \rangle \\ &= \frac{v_0^2}{2} \left[e^{-(D_R + 2\gamma)|s-s'|} + e^{-2\gamma|s-s'| - D_R(s+s'+2\min[s,s'])} \cos 2\theta_0 \right], \\ \langle \zeta_y(s) \zeta_y(s') \rangle &= v_0^2 \langle \sigma(s) \sigma(s') \rangle \langle \sin \theta(s) \sin \theta(s') \rangle \\ &= \frac{v_0^2}{2} \left[e^{-(D_R + 2\gamma)|s-s'|} - e^{-2\gamma|s-s'| - D_R(s+s'+2\min[s,s'])} \cos 2\theta_0 \right] \\ \langle \zeta_x(s) \zeta_y(s') \rangle &= v_0^2 \langle \sigma(s) \sigma(s') \rangle \langle \cos \theta(s) \sin \theta(s') \rangle \\ &= \frac{v_0^2 \sin 2\theta_0}{2} e^{-2\gamma|s-s'| - D_R(s+s'+2\min[s,s'])}. \end{aligned} \quad (3.6a)$$

3.1.2 Position Moments

From Eq. (3.2a) and (3.2b), we can easily write the first two moments of DRABP as,

$$\langle x(t) \rangle = \int_0^t ds \langle \zeta_x(s) \rangle, \quad \langle x^2(t) \rangle = \int_0^t \int_0^t ds ds' \langle \zeta_x(s) \zeta_x(s') \rangle \quad (3.7)$$

$$\langle y(t) \rangle = \int_0^t ds \langle \zeta_y(s) \rangle, \quad \langle y^2(t) \rangle = \int_0^t \int_0^t ds ds' \langle \zeta_y(s) \zeta_y(s') \rangle. \quad (3.8)$$

Further, using the explicit forms of the mean and autocorrelations of the effective noises

in Eqs. (3.5b)-(3.6), we obtain the mean,

$$\langle x(t) \rangle = \frac{v_0 \cos \theta_0}{2\gamma + D_R} \left(1 - e^{-t(2\gamma + D_R)}\right); \quad \langle y(t) \rangle = \frac{v_0 \sin \theta_0}{2\gamma + D_R} \left(1 - e^{-t(2\gamma + D_R)}\right), \quad (3.9)$$

and the second moments,

$$\begin{aligned} \langle x^2(t) \rangle &= \frac{v_0^2 t}{(2\gamma + D_R)} + \frac{v_0^2 (e^{-(2\gamma + D_R)t} - 1)}{(2\gamma + D_R)^2} \\ &+ \frac{v_0^2 \cos 2\theta_0}{(3D_R - 2\gamma)} \left[\frac{e^{-4D_R t} - 1}{4D_R} + \frac{1 - e^{-(D_R + 2\gamma)t}}{(D_R + 2\gamma)} \right], \end{aligned} \quad (3.10a)$$

$$\begin{aligned} \langle y^2(t) \rangle &= \frac{v_0^2 t}{(2\gamma + D_R)} + \frac{v_0^2 (e^{-(2\gamma + D_R)t} - 1)}{(2\gamma + D_R)^2} \\ &- \frac{v_0^2 \cos 2\theta_0}{(3D_R - 2\gamma)} \left[\frac{e^{-4D_R t} - 1}{4D_R} + \frac{1 - e^{-(D_R + 2\gamma)t}}{(D_R + 2\gamma)} \right]. \end{aligned} \quad (3.10b)$$

Before proceeding further, it is interesting to look at how the variances $\langle x^2(t) \rangle_c = \langle x^2(t) \rangle - \langle x(t) \rangle^2$ and $\langle y^2(t) \rangle_c = \langle y^2(t) \rangle - \langle y(t) \rangle^2$ behave in the different dynamical regimes.

Short-time regime (I): $t \ll \min(\gamma^{-1}, D_R^{-1})$,

The leading order behavior in this regime can be obtained by simply expanding the variance Eqs. (3.10) in a Taylor series in t , about $t = 0$,

$$\langle x^2(t) \rangle_c = \frac{v_0^2 t^3}{3} (D_R + 2\gamma - (D_R - 2\gamma) \cos 2\theta_0) + O(t^4), \quad (3.11a)$$

$$\langle y^2(t) \rangle_c = \frac{v_0^2 t^3}{3} (D_R + 2\gamma + (D_R - 2\gamma) \cos 2\theta_0) + O(t^4). \quad (3.11b)$$

Clearly, there is an anisotropy in the system if we begin from arbitrary θ_0 (except when $\cos 2\theta_0 = 0$).

Intermediate regime (II): $\gamma^{-1} \ll t \ll D_R^{-1}$

In this regime, the behavior of the variance is obtained by neglecting terms $\sim e^{-2\gamma t}$ and then expanding the resulting expression in a series in t ,

$$\langle x^2(t) \rangle_c \approx \frac{v_0^2 t}{2\gamma} (1 + \cos 2\theta_0) - \frac{v_0^2 t^2 D_R}{\gamma} \cos 2\theta_0 + O(t^3), \quad (3.12a)$$

$$\langle y^2(t) \rangle_c \approx \frac{v_0^2 t}{2\gamma} (1 - \cos 2\theta_0) + \frac{v_0^2 t^2 D_R}{\gamma} \cos 2\theta_0 + O(t^3). \quad (3.12b)$$

Thus in this regime, the anisotropy persists. In fact, by setting $\theta_0 = 0$ in Eq. (3.12) yields, $\langle x^2(t) \rangle_c \equiv \langle x_{\parallel}^2(t) \rangle_c \propto t$ and $\langle y^2(t) \rangle_c \equiv \langle x_{\perp}^2(t) \rangle_c \propto t^2$. The notations $x_{\parallel}(t)$ and $x_{\perp}(t)$ correspond to the displacement in the directions along and orthogonal to which the DRABP starts its motion.

Intermediate regime (III): $D_R^{-1} \ll t \ll \gamma^{-1}$

In this regime $D_R t \gg 1$ while $\gamma t \ll 1$ and one can neglect terms $\sim e^{-D_R t}$. Expanding the resulting expression in a series of t we get the variance behavior,

$$\langle x^2(t) \rangle_c = \langle y^2(t) \rangle_c \approx \frac{v_0^2 t}{D_R} \quad (3.13)$$

which indicates that if $D_R > \gamma$, the anisotropy vanishes already in the intermediate regime and the motion becomes diffusive with an effective diffusion coefficient $v_0^2/(2D_R)$.

Long-time regime (IV)

Finally, for $t \gg \max(\gamma^{-1}, D_R^{-1})$, we have,

$$\langle x^2(t) \rangle_c = \langle y^2(t) \rangle_c \approx 2D_{\text{eff}} t. \quad (3.14)$$

The dynamics is isotropic and diffusive with an effective diffusion constant $D_{\text{eff}} = \frac{v_0^2}{2(D_R + 2\gamma)}$.

3.2 Position Distribution

In this section, we will discuss the position distribution of the DRABP in the different dynamical regimes.

3.2.1 Short time regime (I)

In this regime the time is much smaller than both the characteristic time scales of the system *i.e.*, $t \ll \min(\gamma^{-1}, D_R^{-1})$. Let us suppose that the particle starts from an initial orientation θ_0 , then the Langevin equations can be written as,

$$\dot{x}(t) = v_0 \sigma(t) \cos[\theta_0 + \phi(t)] \quad \text{and} \quad \dot{y}(t) = v_0 \sigma(t) \sin[\theta_0 + \phi(t)] \quad (3.15)$$

where $\phi(t) = \sqrt{2D_R} \int_0^t ds \eta(s)$ is a standard Brownian motion. At times $t \ll D_R^{-1}$, $\phi(t) \sim \sqrt{D_R t} \ll 1$, so we can use the approximation $\cos \phi \simeq 1$ and $\sin \phi \simeq \phi$ to the leading order in ϕ . Equations (3.15) then reduce to,

$$\dot{x}(t) \approx \sigma(t)(A - B\phi(t)) \quad (3.16a)$$

$$\dot{y}(t) \approx \sigma(t)(B + A\phi(t)). \quad (3.16b)$$

where we have used,

$$A = v_0 \cos \theta_0 \quad \text{and} \quad B = v_0 \sin \theta_0, \quad (3.17)$$

for notational simplicity. Now, let us assume that during time t there are n orientational reversals. We can thus divide the duration $[0, t]$ into $n + 1$ intervals, such that σ changes sign at the beginning of each interval and remains constant throughout the interval. Let s_i be the duration of the i -th interval as shown in Fig. 3.3 and $\sigma_i = (-1)^{i-1}$ denotes the value of σ in this interval. For the sake of convenience we also define $t_i = \sum_{j=1}^i s_j$ which is the total time elapsed before the start of the $(i + 1)$ -th interval. Obviously, $t_0 = 0$ and $t_{n+1} = t$.

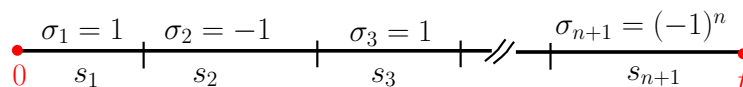


Figure 3.3: Schematic representation of the reversal process: s_i denotes the interval between i^{th} and $(i + 1)^{\text{th}}$ reversal events during which $\sigma_i = (-1)^{i-1}$ remains constant.

For a given trajectory $\{\sigma_i, s_i\}$, the final position of the particle can then be expressed as,

$$x(t) = A \sum_{i=1}^{n+1} \sigma_i s_i - B \sum_{i=1}^{n+1} \sigma_i z_i, \quad \text{and} \quad y(t) = B \sum_{i=1}^{n+1} \sigma_i s_i + A \sum_{i=1}^{n+1} \sigma_i z_i \quad (3.18a)$$

where we have denoted $z_i = \int_{t_{i-1}}^{t_i} ds \phi(s)$. Since $\phi(s)$ is an ordinary Brownian motion, its integral should follow a Gaussian distribution—in fact, $\{z_i; i = 1, 2, \dots, n + 1\}$ form a set of $(n + 1)$ correlated Gaussian variables with the correlation matrix $C_{ij} = \langle z_i z_j \rangle$. The linear combination $\sum_{i=1}^{n+1} \sigma_i z_i$ then also follows a Gaussian distribution with the variance

$$b_n = \sum_{i,j=1}^{n+1} \sigma_i \sigma_j C_{ij} = 2D_R \sum_{i=1}^{n+1} \left[\sum_{j=1}^{i-1} (-1)^{i+j} s_i s_j (t_j + t_{j-1}) + \frac{s_i^2}{3} (t_i + 2t_{i-1}) \right], \quad (3.19)$$

where to derive the final equality, we have used $\langle \phi(s) \phi(s') \rangle = 2D_R \min(s, s')$. From Eq. (3.18), we can then write the marginal position distributions for a given trajectory $\{\sigma_i, \tau_i\}$,

$$\mathcal{P}(x, \{\sigma_i, s_i\}) = \frac{1}{B\sqrt{2\pi b_n}} \exp \left[-\frac{(x - A \sum_{i=1}^{n+1} \sigma_i s_i)^2}{2b_n B^2} \right], \quad (3.20a)$$

$$\mathcal{P}(y, \{\sigma_i, s_i\}) = \frac{1}{A\sqrt{2\pi b_n}} \exp \left[-\frac{(y - B \sum_{i=1}^{n+1} \sigma_i s_i)^2}{2b_n A^2} \right]. \quad (3.20b)$$

Note that, for notational simplicity we have used the same letter \mathcal{P} to denote both x and y distributions.

To obtain the actual position distribution $P(x, t)$ in this regime, we need to take into account the contributions from all possible trajectories $\{\sigma_i, s_i; i = 1, 2, \dots, n + 1\}$ with all

possible values of n ,

$$P(x_i, t) = \sum_{n=0}^{\infty} \gamma^n e^{-\gamma t} P_n(x_i, t)$$

$$\text{where } P_n(x, t) = \int_0^t \prod_{i=1}^{n+1} ds_i \delta(t - \sum_i s_i) \mathcal{P}(x_i, \{\sigma_i, s_i\}) \quad (3.21)$$

denotes the contribution from the trajectories with n number of reversals and x_i can be either x or y .

Equation (3.21) provides the exact time-dependent marginal distribution in this regime. Even though the infinite series cannot be summed explicitly to obtain a closed-form expression, it can be systematically evaluated numerically to obtain $P(x, t)$ for arbitrary γ and t . In fact, for $t \lesssim \gamma^{-1}$, it suffices to consider the first few terms to get a reasonably good estimate of the marginal distributions. Figure 3.4(a) compares this estimate, evaluated up to $n = 2$ terms, with $P(x, t)$ obtained from numerical simulations. Clearly, this perturbative approach is extremely successful in accurately predicting the characteristic shape of the distribution, with a wide plateau near the origin and a peak near $x = v_0 t$, in this short-time regime (I).

Physically, the peak in the distribution is a manifestation of the ABP nature of the motion—the $n = 0$ term, corresponding to the no reversal case, correctly predicts the peak. The emergence of the plateau, however, is a direct consequence of the reversal events—for $t \ll D_R^{-1}$, the orientation θ evolves slowly, and the dynamics can be thought of as a one-dimensional RTP with an effective velocity $v_0 \cos \theta_0$. Now, for small values of γ , the trajectories with a single flip contribute a constant value (the plateau) $\gamma e^{-\gamma t} / (2v_0 \cos \theta_0)$. This agrees well with the exact result [Eq. (3.21)] to leading order in γ .

3.2.2 Intermediate time regime (II)

The correlated noise leads to an intriguing behavior in this regime $\gamma^{-1} \ll t \ll D_R^{-1}$. Since $t \ll D_R^{-1}$ is still true, the small $\phi(t)$ approximation in Eq. (3.16) is still valid. Moreover, for $t \gg \gamma^{-1}$, the frequent reversals lead to a Gaussian white noise $\xi(t)$ with zero-mean and the correlator $\langle \xi(t)\xi(t') \rangle = \gamma^{-1} \delta(t - t')$. Thus, the effective equations in this regime become,

$$\dot{x}(t) \approx v_0 \xi(t)(A - B\phi(t)) \quad \text{and} \quad \dot{y}(t) \approx v_0 \xi(t)(B + A\phi(t)), \quad (3.22)$$

where the constants A and B are given by Eq. (3.17). The above equations describe a Brownian motion with stochastically evolving diffusion coefficients. Some specific versions of such models have been studied recently [110] in a different context.

The characteristic function for the joint distribution can be written as,

$$\langle \exp(i\mathbf{k} \cdot \mathbf{x}) \rangle = \left\langle \exp \left(i \int_0^t ds \xi(s) [k_x (A - B\phi(s)) + k_y (B + A\phi(s))] \right) \right\rangle_{(\xi, \phi)}, \quad (3.23)$$

where the averaging is over both $\{\xi(t)\}$ and $\{\phi(t)\}$ trajectories. The Gaussian nature of $\xi(t)$, for a fixed $\{\phi(s)\}$ trajectory, allows us to evaluate the characteristic function,

$$\langle e^{i\mathbf{k} \cdot \mathbf{x}} \rangle = \left\langle \exp \left[-\frac{1}{2} \mathbf{k}^T \boldsymbol{\Sigma}(t) \mathbf{k} \right] \right\rangle_{\phi}, \quad \text{where } \mathbf{k} = (k_x, k_y)^T. \quad (3.24)$$

The correlation matrix is given by,

$$\begin{aligned} \boldsymbol{\Sigma}(t) &= \begin{bmatrix} \langle x^2(t) \rangle_{\xi} & \langle x(t)y(t) \rangle_{\xi} \\ \langle x(t)y(t) \rangle_{\xi} & \langle y^2(t) \rangle_{\xi} \end{bmatrix} \\ &= \frac{1}{\gamma} \begin{bmatrix} \int_0^t ds (A - B\phi(s))^2 & \int_0^t ds (A - B\phi(s))(B + A\phi(s)) \\ \int_0^t ds (A - B\phi(s))(B + A\phi(s)) & \int_0^t ds (B + A\phi(s))^2 \end{bmatrix} \end{aligned} \quad (3.25)$$

Remembering that $\phi(s)$ is a standard Brownian motion, the rhs of Eq. (3.24) can be evaluated using path integral [24],

$$\langle \exp(i\mathbf{k} \cdot \mathbf{x}) \rangle = \int_{-\infty}^{\infty} dX \int_0^X \mathcal{D}\phi \exp \left[-\int_0^t ds \left(\frac{Z_1^2}{2\gamma} (\phi + Z_2/Z_1)^2 + \frac{\dot{\phi}^2}{4D_R} \right) \right], \quad (3.26)$$

where $Z_1 = (k_y A - k_x B)$ and $Z_2 = (k_x A + k_y B)$. Using the variable shift $\phi \rightarrow \phi + \frac{Z_2}{Z_1}$ and $X \rightarrow X + \frac{Z_2}{Z_1}$, Eq. (3.26) reduces to,

$$\langle \exp(i\mathbf{k} \cdot \mathbf{x}) \rangle = \int_{-\infty}^{\infty} dX \int_{Z_2/Z_1}^X \mathcal{D}\phi \exp \left[-\int_0^t ds \left(\frac{\dot{\phi}^2}{4D_R} + \frac{Z_1^2}{2\gamma} \phi^2 \right) \right]. \quad (3.27)$$

The form of the path integral in the above equation corresponds to the imaginary time propagator of a quantum harmonic oscillator with Hamiltonian $H = -\frac{\hbar^2}{2m} \frac{d^2}{dx^2} + \frac{1}{2} m \omega^2 x^2$,

upon setting $\hbar = 1$, $m = \frac{1}{2D_R}$ and $\omega^2 = \frac{2Z_1^2 D_R}{\gamma}$. It propagates from initial position $\frac{Z_2}{Z_1}$ to the final position X in time t . Thus, we have,

$$\langle \exp(i\mathbf{k} \cdot \mathbf{x}) \rangle = \int_{-\infty}^{\infty} dX U(X, Z_2/Z_1, t), \quad (3.28)$$

where, $U(X_f, X_i, t)$ is the propagator of a quantum harmonic oscillator with initial and final points X_i and X_f respectively in imaginary time t . This is well known in literature [111] and with the mappings mentioned earlier we have,

$$U(X_f, X_i, t) = \sqrt{\frac{\omega}{4\pi D_R \sinh(\omega t)}} \exp \left[-\frac{\omega}{4D_R \sinh(\omega t)} \left((X_f^2 + X_i^2) \cosh(\omega t) - 2X_f X_i \right) \right] \quad (3.29)$$

Using the above expression in Eq. (3.28) and performing the integral over X , we obtain,

$$\langle e^{i\mathbf{k} \cdot \mathbf{x}} \rangle = \frac{1}{\sqrt{\cosh \omega t}} \exp \left[-\frac{\omega \tanh \omega t}{4D_R} \left(\frac{k_x + k_y \tan \theta_0}{k_y - k_x \tan \theta_0} \right)^2 \right], \quad (3.30)$$

Of particular interest are the distributions along and orthogonal to the initial orientation, denoted by x_{\parallel} and x_{\perp} respectively. Setting $\theta_0 = 0$ gives $x_{\perp} \equiv y$ and $x_{\parallel} \equiv x$. From Eq. (3.30), we get

$$\langle e^{ikx_{\perp}} \rangle = \left[\cosh \left(v_0 k t \sqrt{\frac{2D_R}{\gamma}} \right) \right]^{-1/2} \quad \text{and} \quad \langle e^{ikx_{\parallel}} \rangle = \exp \left(-\frac{k^2 v_0^2 t}{2\gamma} \right). \quad (3.31)$$

This can be inverted exactly to yield,

$$P(x_{\perp}, t) = \frac{1}{v_0 t} \sqrt{\frac{\gamma}{8D_R}} f \left(\frac{x_{\perp}}{v_0 t} \sqrt{\frac{\gamma}{8D_R}} \right), \quad \text{with} \quad f(z) = \frac{1}{\sqrt{2\pi^3}} \Gamma \left(\frac{1}{4} + iz \right) \Gamma \left(\frac{1}{4} - iz \right) \quad (3.32)$$

and

$$P(x_{\parallel}, t) = \frac{\sqrt{\gamma}}{v_0 \sqrt{t}} h \left(\frac{x_{\parallel} \sqrt{\gamma}}{v_0 \sqrt{t}} \right), \quad \text{with} \quad h(z) = \frac{1}{\sqrt{2\pi}} \exp(-z^2/2). \quad (3.33)$$

Thus, we see that in this intermediate time regime (II) the direction parallel to the initial orientation is already a Gaussian with a diffusive scaling. The perpendicular direction, on

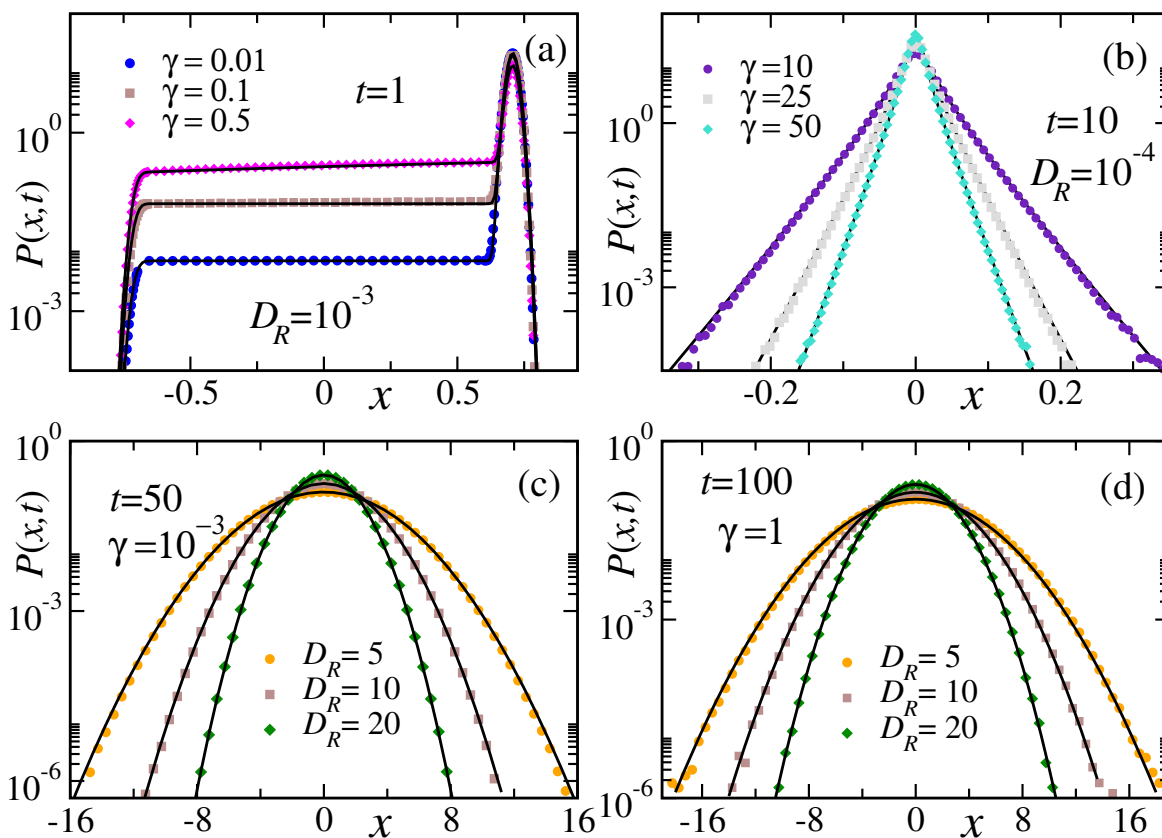


Figure 3.4: Marginal position distribution $P(x, t)$ in the different dynamical regimes: (a) $t \ll \min(D_R^{-1}, \gamma^{-1})$, (b) $\gamma^{-1} \ll t \ll D_R^{-1}$, (c) $D_R^{-1} \ll t \ll \gamma^{-1}$, (d) $t \gg \max(D_R^{-1}, \gamma^{-1})$. The symbols are from numerical simulations while solid black lines correspond to the analytical predictions given by Eqs. (3.21) [up to $n = 2$], (3.32), (3.37) and (3.35) for (a)-(d) respectively. Here $v_0 = 1$ and we have used initial orientation $\theta_0 = \pi/4$ for (a), (c) and (d) and $\theta_0 = \pi/2$ for (b).

the other hand, has a non-trivial scaling distribution. The tails of this distribution decay exponentially, $\exp[-\pi|z|]$ (with $z = x_{\perp}\sqrt{\gamma}/(2v_0t\sqrt{2D_R})$). This drastically different nature of the fluctuations for x_{\parallel} and x_{\perp} lead to the anisotropic distribution seen in Fig. 3.2 (b).

3.2.3 Long-time regime (IV)

This regime corresponds to the time where the observation time is much larger than both the time-scales of the system, i.e., D_R^{-1} and γ^{-1} . Mathematically, for a given time t , this regime can be accessed by taking both D_R and γ large ($\gg t^{-1}$). In this limit, the effective-noise

autocorrelations Eqs. (3.6) become

$$\langle \zeta_a(t) \zeta_b(t') \rangle \approx \frac{v_0^2}{(D_R + 2\gamma)} \delta_{a,b} \delta(t - t') = 2D_{\text{eff}} \delta_{a,b} \delta(t - t') \quad \text{where } a, b \equiv x, y. \quad (3.34)$$

This results in the isotropic Gaussian distribution,

$$P(x, y, t) \approx \frac{1}{2D_{\text{eff}}t} G\left(\frac{x}{\sqrt{2D_{\text{eff}}t}}, \frac{y}{\sqrt{2D_{\text{eff}}t}}\right), \quad (3.35)$$

with $G(\tilde{x}, \tilde{y}) = e^{-(\tilde{x}^2 + \tilde{y}^2)/2}/(2\pi)$. The corresponding x -marginal distribution (which, obviously, is also a Gaussian) is plotted in Fig. 3.4(d) along with the data from numerical simulations; an excellent agreement validates our prediction.

3.2.4 Intermediate-time regime (III)

This regime occurs in place of the intermediate time regime (II) when $D_R > \gamma$ and corresponds to $D_R \gg t^{-1} \gg \gamma$. In this regime the autocorrelations of the effective noise in Eqs. (3.6) become,

$$\langle \zeta_a(t) \zeta_b(t') \rangle \rightarrow (v_0^2/D_R) \delta_{a,b} \delta(t - t') \quad \text{where } a, b \equiv x, y \quad (3.36)$$

Therefore, the typical position distribution is a Gaussian of the width $v_0\sqrt{t/D_R}$,

$$P(x, y, t) \approx \frac{D_R}{v_0^2 t} G\left(\frac{x}{v_0\sqrt{t/D_R}}, \frac{y}{v_0\sqrt{t/D_R}}\right), \quad (3.37)$$

with $G(\tilde{x}, \tilde{y}) = e^{-(\tilde{x}^2 + \tilde{y}^2)/2}/(2\pi)$. Note that this result is same as in the case of ABP for $t \gg D_R^{-1}$ [56] —adding directional reversal does not change the physical scenario in this regime. We validate this prediction with numerical simulations in Fig. 3.4(c).

The distributions in the long-time regime (IV) and the intermediate (III), though heuristic, give a good quantitative prediction around the typical region. We however will provide a better derivation of the diffusive behavior in the next chapter.

Persistence Exponent	I	II	III	IV
α_{\perp}	1/4	1	1/2	1/2
α_{\parallel}	0	1/2	1/2	1/2

Table 3.1: Persistence exponents for the x_{\perp} and x_{\parallel} components of the DRABP as defined by decay of the survival probability $S(t) \sim t^{-\alpha}$ in the different dynamical regimes: (I) $t \ll \min(D_R^{-1}, \gamma^{-1})$, (II) $\gamma^{-1} \ll t \ll D_R^{-1}$, (III) $D_R^{-1} \ll t \ll \gamma^{-1}$, and (IV) $t \gg \max(\gamma^{-1}, D_R^{-1})$.

3.3 Survival probability

The first-passage probability is defined as the probability that a particle, starting from undergoing a stochastic dynamics, reaches a given location at a specified time t for the first time. Alternatively, one can also look at the survival probability, which denotes the probability that the particle has not reached the given location till time t . In the absence of confining potentials or any other constraints like stochastic resetting, the survival probability decreases as $t^{-\alpha}$, where α is called the persistence exponent.

For active particles like bacteria, the first-passage time [112, 113] to reach a particular target such as food source, weak spot of the host or toxins is a very significant observable. For example, certain starvation induced complex processes have been seen in *Myxococcus xanthus* [99] and *Pseudomonas putida* [114], which in turn would depend on the first-passage properties. In this section we will discuss a few first-passage properties of the DRABP.

For this section we consider a DRABP, starting with $\theta(0) = 0$ and $\sigma(0) = 1$, so that $x_{\parallel} = x$ and $x_{\perp} = y$. We are interested in the first-passage events (i) in the direction orthogonal to the initial orientation: the y -component of the position of a DRABP, starting from some arbitrary position $y(0) = y_0$, has not crossed the $y = 0$ line up to time t , and (ii) in the direction parallel to the initial orientation: the x -component of the position of a DRABP, starting from some arbitrary position $x(0) = x_0$, has not crossed the $x = 0$ line up to time t . The survival probabilities corresponding to the two events are denoted by $S_{\perp}(t; y_0)$ and $S_{\parallel}(t; x_0)$. A summary of the persistence exponents in the different dynamical regimes are summarized in Table 3.1.

The most interesting scenario appears for $\gamma > D_R$ where $S_{\perp}(t)$ shows three distinct persistence behaviors in the three different dynamical regimes. For $\theta_0 = 0$, the Langevin

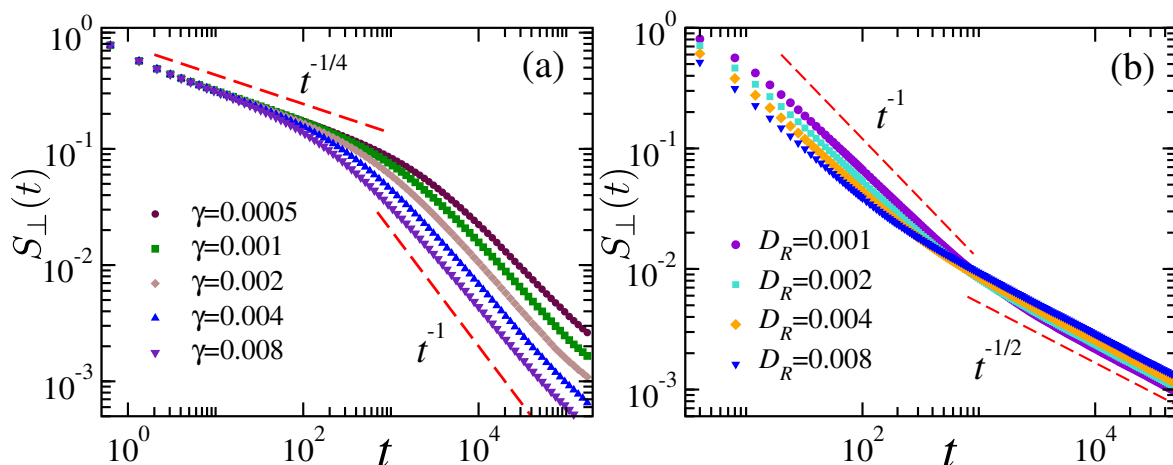


Figure 3.5: $S_y(t)$ vs t for $\gamma > D_R$: (a) shows the crossover from $\alpha_y = 1/4$ (I) to $\alpha_y = 1$ (II) for a fixed $D_R = 10^{-5}$ and $y_0 = 0.001$. (b) shows the crossover from $\alpha_y = 1$ (II) to $\alpha_\perp = 1/2$ (IV) for $\gamma = 1$ and $y_0 = 0.1$.

equation Eq. (3.22) at very short times $t \ll D_R^{-1}$, can be written as,

$$\dot{y} = v_0 \sigma(t) \phi(t), \quad \text{where } \dot{\phi}(t) = \sqrt{2D_R} \eta(t). \quad (3.38)$$

Now since $t \ll \gamma^{-1}$, the above equation can be further approximated as,

$$\dot{y} \simeq v_0 \sigma(0) \phi(t) = v_0 \phi(t), \quad (3.39)$$

where $\sigma(0) = 1$ is the initial condition. This is nothing but a random acceleration process for which the persistence exponent is known to be $1/4$ [115, 116]. Therefore, in the short-time regime (I), we expect $\alpha_y = 1/4$, which is verified in Fig. 3.5(a) using numerical simulations.

In the intermediate time regime (II), the effective y -dynamics can be approximated by [putting $\theta_0 = 0$ in Eq. (3.22)],

$$\dot{y} = v_0 \xi(t) \phi(t), \quad (3.40)$$

where $\xi(t)$ emulates a delta-correlated white noise. This is a diffusing diffusivity process, where the diffusion coefficient itself undergoes a diffusion process. We compute the survival probability by solving the corresponding Fokker Planck equation with an absorbing boundary

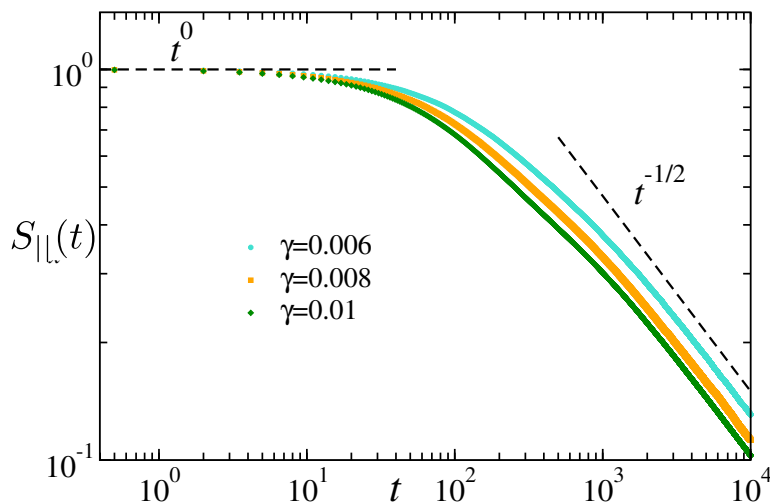


Figure 3.6: Survival probability $S_{\parallel}(t; x_0)$ for three values of γ , $D_R = 10^{-3}$ and $x_0 = 0.01$. The symbols denote the data obtained from numerical simulation. The black dashed lines indicate the analytical predictions.

condition at $y = 0$. This leads to a new persistence exponent $\alpha_{\perp} = 1$ in the context of active particles. In fact, in the limit $\gamma \rightarrow \infty$ and $D_R \rightarrow 0$, we find the exact first-passage time distribution [see Appendix 9.5]. This result is consistent with the recently obtained first-passage behavior for the diffusing diffusivity model [117]. We show the crossover from $\alpha_y = 1/4$ to $\alpha_y = 1$ near $t \sim \gamma^{-1}$ using numerical simulations in Fig. 3.5(a).

In the large time regime (IV), the particle behaves like an ordinary diffusion process with an effective diffusion constant. Consequently, the survival probability decays with the Brownian exponent $\alpha_{\perp} = 1/2$ as seen from the numerical simulations in Fig. 3.5(b). The crossover from $\alpha_{\perp} = 1$ to $\alpha_{\perp} = 1/2$ occurs around $t \sim D_R^{-1}$.

If $D_R > \gamma$, we effectively see two distinct exponents $\alpha_{\perp} = 1/4$ in the short-time regime (I), which crosses over to $\alpha_{\perp} = 1/2$ in regime (III) and remains the same for large times (IV).

On the other hand, the survival probability in the parallel direction is not very exciting. As we saw from the position distributions that fluctuations along the direction parallel to the initial orientation is diffusive Gaussian in both the intermediate time regimes (II) and (III), and the long-time regime (IV), the survival probability $S_{\parallel}(t)$ also shows a Brownian behavior at all times except in regime (I). In the short-time regime (I) as the particle starts at some x_0 pointing away from the target, it always survives for $t \ll \gamma^{-1}, D_R^{-1}$.

3.4 Summary

We studied a stochastic active particle model that mimics a wide range of bacterial motion. One of the important features of this model is the presence of two active time-scales governed by the rotational diffusion coefficient and the reversal rate. The competition among the two active time-scales give rise to many novel features —emergence of four distinct dynamical regimes each of which has a different position distribution and persistence exponent. In particular, we find that, the position distribution in the short-time and intermediate-time regimes have certain unique features, very different from ordinary ABP and RTP. The short-time regime is characterized by the emergence of a plateau. The intermediate regime (II) $\gamma^{-1} \ll t \ll D_R^{-1}$ shows a unique scaling behavior—ballistic and diffusive along the directions orthogonal and parallel to the initial orientations. We also find a novel persistence exponent $\alpha = 1$, which have not been seen in active motions so far, in the same regime.

Chapter 4

Universal framework for the long-time position distribution of active particles

In all the models of active particles considered in Chapters 2 and 3, we saw that, inspite of the very different microscopic stochastic dynamics, the long-time position distribution is always a Gaussian with a diffusive scaling. For the simpler models of RTP, considered in Chapter 2, we could explicitly show this Gaussian distribution by solving the Fokker-Planck equation explicitly. However, in many complicated models, like the DRABP, an exact solution of the Fokker-Planck equation is very difficult. One can still provide the following heuristic argument and explain the Gaussian nature. The total displacement $x(t)$ during a time interval $[0, t]$ can be expressed as $x(t) = \sum_{i=1}^N \Delta x_i$, with Δx_i being the increment over the time interval $[(i-1)\Delta t, i\Delta t]$, where $\Delta t = t/N$ is chosen to be much longer than the active time-scales. Thus, one can ignore the correlations among $\{\Delta x_i\}$ and treat them as independent random variables. Consequently, a diffusive Gaussian distribution for x , which is a sum of N independent random variables, is anticipated in the large N limit, by appealing to the central limit theorem. An exact systematic derivation of the diffusion equation corresponding to the Gaussian distribution, which is expected to be more involved, is still lacking. In this chapter, we develop a general perturbative formalism, treating the ratio of the active time-scale and observation time as a small parameter, to systematically derive the diffusion equation at the leading order. This formalism allows us to explicitly calculate the sub-leading corrections to the Gaussian, which cannot be obtained from the heuristic argument above. In the following, we first outline our framework in Sec. 4.1 and then illustrate its application by solving it explicitly for DRABP in Sec. 4.2. We summarize the results of this chapter in Sec. 4.3.

4.1 Perturbative framework and main results

In this section, we briefly outline the main steps of the general perturbative framework for a one-dimensional active motion. The details, of course, depend on the specific model under consideration. The full picture will become clear in the subsequent sections where we explicitly carry out this perturbative procedure for the different models.

The active particle models under consideration are generically described by the overdamped Langevin equation,

$$\dot{x}(t) = u(t), \quad (4.1)$$

where the propulsion velocity $u(t)$ independently evolves by a stochastic dynamics with a characteristic time τ_a . In all the popular models of active particles, the propulsion velocity u eventually reaches a stationary state with an exponentially decaying autocorrelation function $\langle u(t)u(t') \rangle \propto \exp(-|t - t'|/\tau_a)$.

The joint distribution $P(x, u, t)$ satisfies a Fokker-Planck or a master equation,

$$\frac{\partial P}{\partial t} = -u \frac{\partial P}{\partial x} + \mathcal{L}_u P, \quad (4.2)$$

where the specific form of the operator \mathcal{L}_u corresponding to the stochastic dynamics of u depends on the specific model. We expand the joint distribution $P(x, u, t)$ as,

$$P(x, u, t) = \sum_{n=0}^{\infty} \psi_n(u) F_n(x, t), \quad (4.3)$$

where $\psi_n(u)$ are the eigenfunctions of \mathcal{L}_u with $\psi_0(u)$ denoting the stationary state of u satisfying $\mathcal{L}_u \psi_0(u) = 0$. Evidently, the position distribution is given by,

$$\rho(x, t) = \int du P(x, u, t) = F_0(x, t), \quad (4.4)$$

as $\int du \psi_n(u) = \delta_{n,0}$. Note that, $\int du$ can also indicate a sum over possible discrete states as in RTP. For the sake of simplicity, we choose our initial conditions such that the position distribution is even, i.e., $\rho(x, t) = \rho(-x, t)$, at all times.

We show that when the initial propulsion velocity $u(0)$ is chosen from the stationary state $\psi_0(u)$, the marginal position distribution admits the series expansion in the dimensionless small perturbation parameter τ_a/t ,

$$\rho(x, t) \equiv F_0(x, t) = \sum_{k=0}^{\infty} \tau_a^k A_0^{2k}(x, t), \quad (4.5)$$

where t^{-k} is absorbed in the series coefficient $A_0^{2k}(x, t)$ for computational convenience [see (4.9) below]. The choice of the superscript $2k$ in the notation is essentially related to the fact that $A_0^{2k}(x, t)$ is an even function of x . It will become clear when we show the explicit calculation in later sections. We find that the leading term $A_0^0(x, t)$ always satisfies the diffusion equation,

$$\frac{\partial A_0^0}{\partial t} = D_{\text{eff}} \frac{\partial^2 A_0^0}{\partial x^2}, \quad (4.6)$$

resulting in the familiar long-time Gaussian distribution,

$$A_0^0(x, t) = \frac{1}{\sqrt{4\pi D_{\text{eff}} t}} \exp\left(-\frac{x^2}{4D_{\text{eff}} t}\right). \quad (4.7)$$

The explicit form of the effective diffusion coefficient D_{eff} depends on the specific model.

We also find that the subleading contributions $A_0^{2k}(x, t)$ with $k > 0$, to the large-time leading Gaussian behavior $A_0^0(x, t)$, generically satisfy an inhomogeneous diffusion equation of the form,

$$\left[\frac{\partial}{\partial t} - D_{\text{eff}} \frac{\partial^2}{\partial x^2} \right] A_0^{2k}(x, t) = S_{2k}(x, t), \quad (4.8)$$

where the source term $S_{2k}(x, t)$ is determined by the lower order solutions $\{A_0^{2n}(x, t); n < k\}$. Therefore, starting from the Gaussian solution $A_0^0(x, t)$, the higher order contributions $A_0^{2k}(x, t)$ can be solved recursively for arbitrary k . Incidentally, Eq. (4.6) and Eq. (4.7) suggest a diffusive scaling ansatz,

$$A_0^{2k}(x, t) = \frac{1}{t^k} q_{2k}\left(\frac{x}{\sqrt{4D_{\text{eff}} t}}\right) \frac{1}{\sqrt{4\pi D_{\text{eff}} t}} \exp\left(-\frac{x^2}{4D_{\text{eff}} t}\right). \quad (4.9)$$

Substituting the above ansatz in Eq. (4.7), along with the scaling form

$$S_{2k}(x, t) = \frac{1}{t^{k+1}} s_{2k}\left(\frac{x}{\sqrt{4D_{\text{eff}}t}}\right) \frac{1}{\sqrt{4\pi D_{\text{eff}}t}} \exp\left(-\frac{x^2}{4D_{\text{eff}}t}\right), \quad (4.10)$$

yields an inhomogeneous Hermite differential equation for $q_{2k}(z)$ as,

$$q_{2k}''(z) - 2z q_{2k}'(z) + 4k q_{2k}(z) = s_{2k}(z). \quad (4.11)$$

The two solutions of the corresponding homogeneous Hermite differential equation Eq. (4.11) are

$$U_{2k}(z) = H_{2k}(z) \quad \text{and} \quad V_{2k}(z) = z {}_1F_1\left(\frac{1}{2} - k, \frac{3}{2}, z^2\right). \quad (4.12)$$

where $H_{2k}(z)$ is the Hermite polynomial of order $2k$ and ${}_1F_1(a, b, z)$ is the confluent hypergeometric function. Note that, $U_{2k}(z)$ and $V_{2k}(z)$ are respectively even and odd functions of z . Therefore, remembering that $q_{2k}(z)$ must be an even function of z , the complete solution can be written as,

$$q_{2k}(z) = C_{2k} U_{2k}(z) + \int_0^z dy \left[V_{2k}(z) U_{2k}(y) - U_{2k}(z) V_{2k}(y) \right] \frac{s_{2k}(y)}{W_{2k}(y)}, \quad (4.13)$$

where the Wronskian is given by,

$$W_{2k}(y) = \begin{vmatrix} U_{2k}(y) & V_{2k}(y) \\ U_{2k}'(y) & V_{2k}'(y) \end{vmatrix} = (-1)^k \frac{(2k)!}{k!} e^{y^2}. \quad (4.14)$$

The arbitrary constant C_{2k} in Eq. (4.13) is determined by neither the normalization of $\rho(x, t)$ nor any symmetries of A_0^{2k} . We take recourse to the moments of the distribution to determine C_{2k} . To this end, starting from the Fokker-Planck or master equation, we derive the moments $\langle x^{2k} \rangle / (4D_{\text{RT}}t)^k$ and expand in powers of τ_a/t for $t \gg \tau_a$. On the other hand, the same can be also obtained from the distribution Eq. (4.5) and Eq. (4.9). In particular, the coefficient of $(\tau_a/t)^k$ is given by $\int_{-\infty}^{\infty} dz e^{-z^2} z^{2k} q_{2k}(z) / \sqrt{\pi}$ which involves C_{2k} . This can now be determined by comparing the coefficients of $(\tau_a/t)^k$ obtained by the two methods. Note that, given the initial and boundary conditions, one, in principle, has all the information

to find the complete solution of the Fokker-Planck equation. Therefore, at a first glance, it might seem surprising that the moments are needed to determine the coefficients C_{2k} . However, only the boundary conditions are used to go from Eq. (4.8) to Eq. (4.13), and it is the moments, through which the initial condition is used, albeit in an unconventional way.

In the following sections, we illustrate this framework with DRABP and calculate a few subleading contributions to the Gaussian distribution explicitly.

4.2 Application to obtain long-time distribution of DRABP

Direction reversing active Brownian particles (DRABP), as introduced in the previous chapter, follows the Langevin equations (3.2)

In this chapter, to study the long-time position distribution, we consider the initial condition where the particle starts at the origin with a random orientation $\theta(0)$ chosen uniformly from $[-\pi, \pi]$ and $\sigma(0) = \pm 1$ with equal probability $1/2$. Clearly, due to these set of initial conditions, the position distribution is isotropic at all times, and it is enough to look at the x -position only. So for simplicity, we consider only the (x, σ, θ) process, which is also a Markov process. The corresponding Fokker-Planck equation for $P_\sigma(x, \theta, t)$ is given by,

$$\frac{\partial P_\sigma}{\partial t} = -v_0 \sigma \cos \theta \frac{\partial P_\sigma}{\partial x} + D_R \frac{\partial^2 P_\sigma}{\partial \theta^2} - \gamma P_\sigma + \gamma P_{-\sigma}, \quad \text{where } \sigma = \pm 1 \quad (4.15)$$

with the initial condition,

$$P_\sigma(x, \theta, 0) = \frac{1}{2\pi} \delta(x) \left[\frac{\delta_{\sigma,1} + \delta_{\sigma,-1}}{2} \right]. \quad (4.16)$$

It is convenient to write Eq. (4.15) in terms of $P = P_+ + P_-$ and $Q = P_+ - P_-$ as,

$$\frac{\partial P}{\partial t} = -v_0 \cos \theta \frac{\partial Q}{\partial x} + D_R \frac{\partial^2 P}{\partial \theta^2}, \quad (4.17)$$

$$\frac{\partial Q}{\partial t} = -v_0 \cos \theta \frac{\partial P}{\partial x} + D_R \frac{\partial^2 Q}{\partial \theta^2} - 2\gamma Q. \quad (4.18)$$

Using the effective noise correlation in the long-time regime, we argued in the previous chapter that, the process $x(t)$, at times much longer than the correlation-time, becomes diffusive with the effective diffusion coefficient $D_{DR} = v_0^2/[2(D_R+2\gamma)]$. Therefore, anticipating

the diffusive scaling at long times, we rewrite the above equations in terms of the scaled variable $y = x/\sqrt{D_{DR}}$, as,

$$\varepsilon^2 \frac{\partial P}{\partial t} = -\varepsilon \sqrt{2(\lambda + 1)} \cos \theta \frac{\partial Q}{\partial y} + \mathcal{L}_\theta P, \quad (4.19a)$$

$$\varepsilon^2 \frac{\partial Q}{\partial t} = -\varepsilon \sqrt{2(\lambda + 1)} \cos \theta \frac{\partial P}{\partial y} + \mathcal{L}_\theta Q - \lambda Q, \quad (4.19b)$$

where the operator $\mathcal{L}_\theta = \partial^2/\partial\theta^2$, $\varepsilon^2 = 1/D_R$ is the persistence-time of the θ dynamics, and the dimensionless parameter $\lambda = 2\gamma/D_R$ denotes the ratio of the rotational diffusion and directional reversal time-scales.

The isotropic initial condition Eq. (4.16) leads to a symmetric marginal distribution $\rho(y, t) \equiv \int_{-\pi}^{\pi} d\theta P(y, \theta, t) = \rho(-y, t)$. As a result all the odd moments of position vanish. Moreover, it follows from Eq. (4.19) that $P(y, \theta, t)$ and $Q(y, \theta, t)$ remain invariant under the transformation $(y, \varepsilon) \rightarrow (-y, -\varepsilon)$. Consequently, $\rho(y, t)$ must contain only even powers ε .

As we have mentioned earlier, the $2n$ -th moment $\langle y^{2n}(t) \rangle$ is needed to completely determine the distribution at order $(\varepsilon^2/t)^n$; we first determine the moments recursively in the next section.

4.2.1 Moments

To determine the position moments $\langle y^{2n}(t) \rangle$, it is convenient to define the following *correlation functions*,

$$M(k, n, t) = \int_{-\infty}^{\infty} dy \int_{-\pi}^{\pi} d\theta y^k \cos(n\theta) P(y, \theta, t), \quad (4.20a)$$

$$L(k, n, t) = \int_{-\infty}^{\infty} dy \int_{-\pi}^{\pi} d\theta y^k \cos(n\theta) Q(y, \theta, t), \quad (4.20b)$$

such that $M(k, 0, t) = \langle y^k(t) \rangle$. Here, both n and k are non-negative integers.

Multiplying both sides of Eqs. (4.19) by $y^k \cos(n\theta)$ and then integrating over y and θ , we

get, for $n, k \geq 1$

$$\left[\varepsilon^2 \frac{d}{dt} + n^2 \right] M(k, n, t) = k\varepsilon \sqrt{\frac{\lambda+1}{2}} \left[L(k-1, n-1, t) + L(k-1, n+1, t) \right], \quad (4.21a)$$

$$\left[\varepsilon^2 \frac{d}{dt} + n^2 + \lambda \right] L(k, n, t) = k\varepsilon \sqrt{\frac{\lambda+1}{2}} \left[M(k-1, n-1, t) + M(k-1, n+1, t) \right]. \quad (4.21b)$$

For $n = 0$ and $k \geq 1$, we have,

$$\varepsilon^2 \frac{d}{dt} M(k, 0, t) = k\varepsilon \sqrt{2(\lambda+1)} L(k-1, 1, t), \quad (4.22a)$$

$$\left[\varepsilon^2 \frac{d}{dt} + \lambda \right] L(k, 0, t) = k\varepsilon \sqrt{2(\lambda+1)} M(k-1, 1, t). \quad (4.22b)$$

The initial conditions for Eqs. (4.21)-(4.22) are $M(k, n, 0) = L(k, n, 0) = 0$. Moreover, from the normalization and $\langle \cos(n\theta) \rangle = 0$, it respectively follows that,

$$M(0, 0, t) = 1 \quad \text{and} \quad M(0, n, t) = L(0, n, t) = 0 \quad \text{for } n > 0, \quad (4.23)$$

for all t . Using the initial conditions, the solutions for $n \geq 1$ and $k \geq 1$ are,

$$M(k, n, t) = \frac{k}{\varepsilon} \sqrt{\frac{\lambda+1}{2}} \int_0^t dt' e^{-\frac{(t-t')n^2}{\varepsilon^2}} \left[L(k-1, n-1, t') + L(k-1, n+1, t') \right] \quad (4.24a)$$

$$L(k, n, t) = \frac{k}{\varepsilon} \sqrt{\frac{\lambda+1}{2}} \int_0^t dt' e^{-\frac{(t-t')(n^2+\lambda)}{\varepsilon^2}} \left[M(k-1, n-1, t') + M(k-1, n+1, t') \right]. \quad (4.24b)$$

From Eq. (4.22a), the solution for the position moments $M(k, 0, t)$ can be written as,

$$M(k, 0, t) = \frac{k}{\varepsilon} \sqrt{2(\lambda+1)} \int_0^t dt' L(k-1, 1, t'). \quad (4.25)$$

The integral equations Eq. (4.24) can be used recursively to obtain the position moments $M(k, 0, t)$ from Eq. (4.25). It is evident from the structure of these equations, that recursive connections between the correlation functions $\{M(k, n, t), L(k, n, t)\}$, for different values of (k, n) , form two independent networks, sitting on even and odd $k+n$ sub-lattices. Since, on the $k=0$ boundary, the only non-zero term is $M(0, 0, t) = 1$, it follows that $M(k, n, t) = L(k, n, t) = 0$ when $k+n$ is odd. Therefore, to determine the non-zero position moments

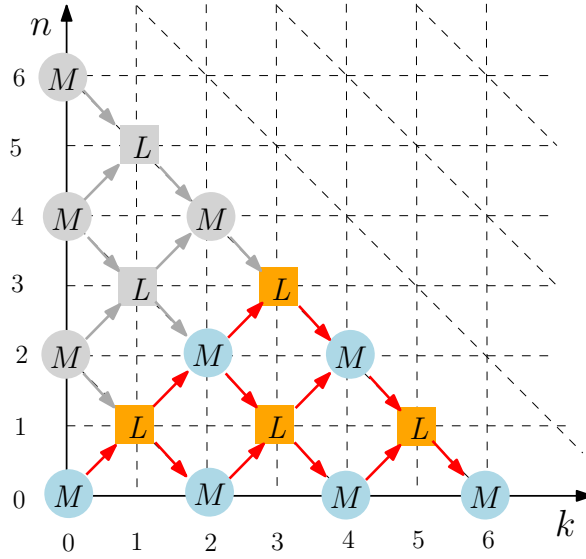


Figure 4.1: The illustration of recursive connections between the correlation functions $\{M(k, n, t), L(k, n, t)\}$, for different values of (k, n) with even $k + n$; see Eq. (4.24). In the $n > k$ sector, shown in grey, $M(k, n, t) = L(k, n, t) = 0$.

$M(k, 0, t)$ for even k , we need to stay on the even $k + n$ network. This network, with the relevant recursive connections is illustrated in Fig. 4.1. From this figure, it is further clear that $M(k, n, t)$ and $L(k, n, t)$ also vanish for $n > k$. On the $n = k$ boundary, Eq. (4.24) simplifies to,

$$M(k, k, t) = \frac{k}{\varepsilon} \sqrt{\frac{\lambda + 1}{2}} \int_0^t dt' e^{-\frac{(t-t')k^2}{\varepsilon^2}} L(k-1, k-1, t') \quad (4.26a)$$

$$L(k, k, t) = \frac{k}{\varepsilon} \sqrt{\frac{\lambda + 1}{2}} \int_0^t dt' e^{-\frac{(t-t')(k^2+\lambda)}{\varepsilon^2}} M(k-1, k-1, t'). \quad (4.26b)$$

We illustrate the recursive procedure by computing the position variance $M(2, 0, t)$ explicitly. To this end, we first need $L(1, 1, t)$ (see Fig. 4.1), which is straightforwardly obtained from Eq. (4.26) as,

$$L(1, 1, t) = \frac{\varepsilon}{\sqrt{2(\lambda + 1)}} \left(1 - e^{-\frac{(\lambda+1)t}{\varepsilon^2}} \right). \quad (4.27)$$

Using this, from Eq. (4.25), we get,

$$M(2, 0, t) = 2t - \frac{2\varepsilon^2}{\lambda + 1} \left(1 - e^{-\frac{(\lambda+1)t}{\varepsilon^2}} \right). \quad (4.28)$$

For $M(4, 0, t)$, we now need to compute two additional correlation functions $M(2, 2, t)$ and $L(3, 1, t)$, as the remaining required correlation functions have already been computed during the previous evaluation of $M(2, 0, t)$. In general, computation of the moment $M(2j - 2, 0, t)$, requires all the correlation functions in the triangular region $k \geq n$, $k + n \leq 2j - 2$ and $n \geq 0$, on the even $k + n$ sub-lattice. Therefore, subsequent computation of $M(2j, 0, t)$ requires the computation of only j additional correlation functions along the $k + n = 2j$ line, starting with $k = n = j$. Following this procedure, we also evaluate the fourth moment as,

$$\begin{aligned}
 M(4, 0, t) = & 12t^2 - \frac{3\varepsilon^2 t}{4(\lambda + 1)} \left[4(\lambda - 15) + e^{-\frac{(\lambda+1)t}{\varepsilon^2}} \frac{16(3\lambda - 5)}{(3 - \lambda)} \right] \\
 & + \frac{3\varepsilon^4}{4(\lambda + 1)^2} \left[87 - 10\lambda - \lambda^2 - 16e^{-\frac{(\lambda+1)t}{\varepsilon^2}} \frac{(49 - 38\lambda + 9\lambda^2)}{(\lambda - 3)^2} + e^{-\frac{4t}{\varepsilon^2}} (\lambda + 1)^4 \right],
 \end{aligned} \tag{4.29}$$

and the sixth moment $M(6, 0, t)$ as,

$$\begin{aligned}
 M(6, 0, t) = & 120t^3 + \frac{90\varepsilon^2 t^2}{\lambda + 1} \left[\lambda - 11 + e^{-\frac{(\lambda+1)t}{\varepsilon^2}} \frac{(3\lambda - 5)^2}{(\lambda - 3)^2} \right] + \frac{45\varepsilon^4 t}{(\lambda + 1)^2} \\
 & \times \left[\frac{67455 - 3375\lambda - 1755\lambda^2 - 45\lambda^3}{2(\lambda + 9)} + e^{-\frac{4t}{\varepsilon^2}} \frac{(\lambda + 1)^6}{2(\lambda - 3)^3(\lambda + 5)} \right. \\
 & \left. + \frac{e^{-\frac{(\lambda+1)t}{\varepsilon^2}}}{2(\lambda - 3)^3} (-2723 + 3544\lambda - 1638\lambda^2 + 288\lambda^3 + \lambda^4) \right] \\
 & + \frac{45\varepsilon^6}{16(\lambda + 1)^3} \left[\frac{-21659 - 172\lambda + 1150\lambda^2 + 148\lambda^3 + 5\lambda^4}{(\lambda + 9)^2} \right. \\
 & - 8e^{-\frac{4t}{\varepsilon^2}} \frac{(\lambda + 1)^6(\lambda(5\lambda + 18) - 3)}{(\lambda - 3)^4(\lambda + 5)^2} + \frac{e^{-\frac{(\lambda+1)t}{\varepsilon^2}}}{(\lambda - 3)^4} (173271 - 268158\lambda + 161953\lambda^2 \\
 & \left. - 46276\lambda^3 + 5737\lambda^4 + 34\lambda^5 - \lambda^6) + e^{-\frac{(\lambda+9)t}{\varepsilon^2}} \frac{(\lambda + 1)^6}{(\lambda + 5)^2(\lambda + 9)^2} \right].
 \end{aligned} \tag{4.30}$$

We will use the positions moments $M(2k, 0, t)$ with $k = 1, 2, \dots$ obtained here to determine the position distribution $\rho(y, t)$ perturbatively in ε .

4.2.2 Position distribution

Now, we look to obtain the position distribution perturbatively. For this purpose, it is important to first note that, the distribution of θ , evolving by the Fokker-Planck operator

\mathcal{L}_θ , reaches a steady state. Thus, we can always express the solution of Eq. (4.19) in the eigenbasis of \mathcal{L}_θ as,

$$P(y, \theta, t) = \sum_{n=0}^{\infty} p_n(\theta) F_n(y, t), \quad (4.31a)$$

$$Q(y, \theta, t) = \sum_{n=0}^{\infty} p_n(\theta) G_n(y, t), \quad (4.31b)$$

where,

$$p_0(\theta) = \frac{1}{2\pi} \quad \text{and} \quad p_n(\theta) = \frac{1}{\pi} \cos(n\theta) \quad \text{for } n \geq 1 \quad (4.32)$$

are the eigenvalues of \mathcal{L}_θ with eigenvalue $-n^2$,

$$\mathcal{L}_\theta p_n(\theta) = -n^2 p_n(\theta). \quad (4.33)$$

They obey the following orthonormality relations.

$$\int_{-\pi}^{\pi} d\theta \cos(m\theta) p_n(\theta) = \delta_{m,n}, \quad \text{and} \quad \int_{-\pi}^{\pi} d\theta \cos \theta \cos(m\theta) p_n(\theta) = \frac{1}{2}(\delta_{n-1,m} + \delta_{n+1,m}). \quad (4.34)$$

Note that, integrating Eq. (4.31) with respect to y , yields,

$$\int_{-\infty}^{\infty} P(y, \theta, t) dy = p_0(\theta), \quad \text{and} \quad \int_{-\infty}^{\infty} Q(y, \theta, t) dy = 0, \quad (4.35a)$$

due to the initial condition on θ , which is chosen from the stationary distribution $p_0(\theta)$. Our aim is to obtain the marginal position distribution,

$$\rho(y, t) \equiv \int_{-\pi}^{\pi} d\theta P(y, \theta, t) = F_0(y, t). \quad (4.36)$$

In general,

$$F_n(y, t) = \int_{-\pi}^{\pi} d\theta P(y, \theta, t) \cos(n\theta), \quad (4.37a)$$

$$G_n(y, t) = \int_{-\pi}^{\pi} d\theta Q(y, \theta, t) \cos(n\theta). \quad (4.37b)$$

However, the above relations are not much of a use as the functions $P(y, \theta, t)$ and $Q(y, \theta, t)$ are unknown. Now, since Eq. (4.19) is invariant under the transformation $(y, \varepsilon) \rightarrow (-y, -\varepsilon)$, the functions $F_n(y, t)$ and $G_n(y, t)$ also follow the same symmetry. For our initial conditions, the marginal position distribution is always symmetric about $y = 0$, i.e., $F_0(y, t) = F_0(-y, t)$. Therefore $F_0(y, t)$ is an even function of ε .

Putting Eqs. (4.31) in Eq. (4.19) and thereafter using the orthonormality relations for $p_n(\theta)$, we obtain PDEs for F_m and G_m . For $m = 0$,

$$\varepsilon^2 \frac{\partial F_0}{\partial t} = -\varepsilon \sqrt{2(\lambda + 1)} \frac{\partial G_1}{\partial y}, \quad (4.38a)$$

$$\left[\varepsilon^2 \frac{\partial}{\partial t} + \lambda \right] G_0 = -\varepsilon \sqrt{2(\lambda + 1)} \frac{\partial F_1}{\partial y}, \quad (4.38b)$$

and for all other $m > 0$,

$$\left[\varepsilon^2 \frac{\partial}{\partial t} + m^2 \right] F_m = -\varepsilon \sqrt{\frac{\lambda + 1}{2}} \left(\frac{\partial G_{m+1}}{\partial y} + \frac{\partial G_{m-1}}{\partial y} \right), \quad (4.39a)$$

$$\left[\varepsilon^2 \frac{\partial}{\partial t} + m^2 + \lambda \right] G_m = -\varepsilon \sqrt{\frac{\lambda + 1}{2}} \left(\frac{\partial F_{m+1}}{\partial y} + \frac{\partial F_{m-1}}{\partial y} \right). \quad (4.39b)$$

From Eq. (4.35), it is clear that we do not have a series in ν , so we straightaway look for series solution of F_m and G_m in the form,

$$F_m(y, t) = \sum_{k=0}^{\infty} \varepsilon^k A_m^k(y, t), \quad (4.40a)$$

$$G_m(y, t) = \sum_{k=0}^{\infty} \varepsilon^k B_m^k(y, t). \quad (4.40b)$$

By definition, $A_m^k = B_m^k = 0$ for $k < 0$. Moreover, since $A_0(y, t)$ is an even function of ε , we

must have $A_0^k = 0$ for odd integers k , i.e., $A_0^1 = A_0^3 = \dots = 0$. Therefore,

$$A_0(y, t) = \sum_{k=0}^{\infty} \varepsilon^{2k} A_0^{2k}(y, t). \quad (4.41)$$

The symmetry, $\int_{-\pi}^{\pi} d\theta P_{\sigma}(y, \theta, t) = \int_{-\pi}^{\pi} d\theta P_{-\sigma}(-y, \theta, t)$, implies that $\int_{-\pi}^{\pi} d\theta Q(y, \theta, t) = -\int_{-\pi}^{\pi} Q(-y, \theta, t)$. Therefore $B_0(y, t)$ should also be an odd function of ε ,

$$B_0(y, t) = \sum_{k=0}^{\infty} \varepsilon^{2k+1} B_0^{2k+1}(y, t). \quad (4.42)$$

Now, putting Eqs. (4.40a) and (4.40b) in Eq. (4.38) and comparing powers of ε ,

$$\frac{\partial A_0^{k-2}}{\partial t} = -\sqrt{2(\lambda+1)} \frac{\partial B_1^{k-1}}{\partial y}, \quad (4.43a)$$

$$\frac{\partial B_0^{k-2}}{\partial t} + \lambda B_0^k = -\sqrt{2(\lambda+1)} \frac{\partial A_1^{k-1}}{\partial y}. \quad (4.43b)$$

On the other hand, for $m \geq 1$, we get from Eq. (4.39),

$$m^2 A_m^k + \frac{\partial A_m^{k-2}}{\partial t} = -\sqrt{\frac{\lambda+1}{2}} \frac{\partial}{\partial y} [B_{m-1}^{k-1} + B_{m+1}^{k-1}], \quad (4.44a)$$

$$(m^2 + \lambda) B_m^k + \frac{\partial B_m^{k-2}}{\partial t} = -\sqrt{\frac{\lambda+1}{2}} \frac{\partial}{\partial y} [A_{m-1}^{k-1} + A_{m+1}^{k-1}]. \quad (4.44b)$$

Before finding solutions for A_m^k and B_m^k , let us first simplify the series in Eqs. (4.40a) and (4.40b). Putting $k = 0$ in Eq. (4.44a), we have $m^2 A_m^0 = 0$. Thus,

$$A_m^0 = \delta_{m,0} A_0^0, \quad (4.45)$$

i.e., $k = 0$ term in the series Eq. (4.40a) exists for $m = 0$ only.

Putting $k = 0$ in Eq. (4.43b) and (4.44b), we have $B_m^0 = 0$ for all $m \geq 0$. Using this fact and putting $k = 1$ in Eq. (4.44a), we have, $A_m^1 = 0$ for all $m \geq 1$. Note that, we already have

$A_0^1 = 0$. Again, putting $k = 1$ in Eq. (4.44b), we get

$$(m^2 + \lambda)B_m^1 = -\sqrt{\frac{\lambda + 1}{2}} \left(\frac{\partial A_{m-1}^0}{\partial y} + \frac{\partial A_{m+1}^0}{\partial y} \right). \quad (4.46)$$

Further, using Eq. (4.45), and combining with the earlier result for $m = 0$, we get,

$$B_m^1 = -\delta_{m,1} \frac{1}{\sqrt{2(\lambda + 1)}} \frac{\partial A_0^0}{\partial y} + \delta_{m,0} B_0^1. \quad (4.47)$$

One can systematically proceed by putting $k = 2, 3, 4, \dots$ and obtain non-vanishing coefficients A_m^k and B_m^k . This process is best illustrated graphically on the m - k plane (see Fig. 4.2). Since, A_m^k only depends on A_m^{k-2} and $B_{m\pm 1}^{k-1}$ and B_m^k also follow a similar pattern, it is clear that A_m^k are non-zero on even k lines while B_m^k are non-zero on odd k lines only. Moreover, both A_m^k and B_m^k vanish on the lower triangle $m > k$. Therefore, Eqs. (4.40a)-(4.40b) can be refined to,

$$A_m = \sum_{k=m}^{\infty} \varepsilon^{2k} A_m^{2k}, \quad (4.48a)$$

$$B_m = \sum_{k=m}^{\infty} \varepsilon^{2k+1} B_m^{2k+1}. \quad (4.48b)$$

Using the above series expansion, we now proceed to compute the marginal distribution $A_0(y, t)$ perturbatively. The leading order term A_0^0 satisfies

$$\frac{\partial A_0^0}{\partial t} = -\sqrt{2(\lambda + 1)} \frac{\partial B_1^1}{\partial y}. \quad (4.49)$$

which is obtained by putting $k = 2$ in Eq. (4.43a). Now, B_1^1 can be obtained by putting $k = 1, m = 1$ in Eq. (4.44b),

$$B_1^1 = -\frac{1}{\sqrt{2(\lambda + 1)}} \frac{\partial A_0^0}{\partial y}. \quad (4.50)$$

Inserting this back in Eq. (4.49) we get the diffusion equation,

$$\frac{\partial A_0^0}{\partial t} = \frac{\partial^2 A_0^0}{\partial y^2}. \quad (4.51)$$

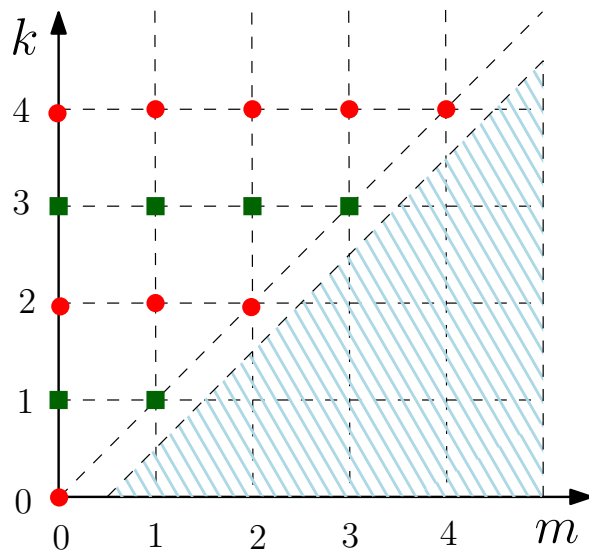


Figure 4.2: Graphical representation of recursive determination of non-vanishing A_m^k (red dots) and B_m^k (blue crosses) following the Eqs. (4.43a)-(4.44b).

Let us remark that, $A_0^0(y, t)$ should have the same properties as a normalized probability density function since $[A_0(y, t)/A_0^0(y, t)] \rightarrow 1$ as $t \rightarrow \infty$. This also demands that, $\int dy A_0^k(y, t) = 0$ for $k > 0$. Hence, the above equation can immediately be solved to obtain a Gaussian distribution,

$$A_0^0(y, t) = \frac{e^{-y^2/(4t)}}{\sqrt{4\pi t}}. \quad (4.52)$$

The subsequent coefficients $A_0^k(y, t)$ provide systematic correction to this Gaussian form. Noting that ε^2 has the dimension of time t , we expect the following diffusive scaling form,

$$A_0^{2k}(y, t) = \frac{e^{-\frac{y^2}{4t}}}{\sqrt{4\pi t}} \frac{1}{t^k} q_{2k}\left(\frac{y}{\sqrt{4t}}\right). \quad (4.53)$$

For the next order correction, putting $k = 4$ in Eq. (4.43a), we get,

$$\frac{\partial A_0^2}{\partial t} = -\sqrt{2(\lambda + 1)} \frac{\partial B_1^3}{\partial y}. \quad (4.54)$$

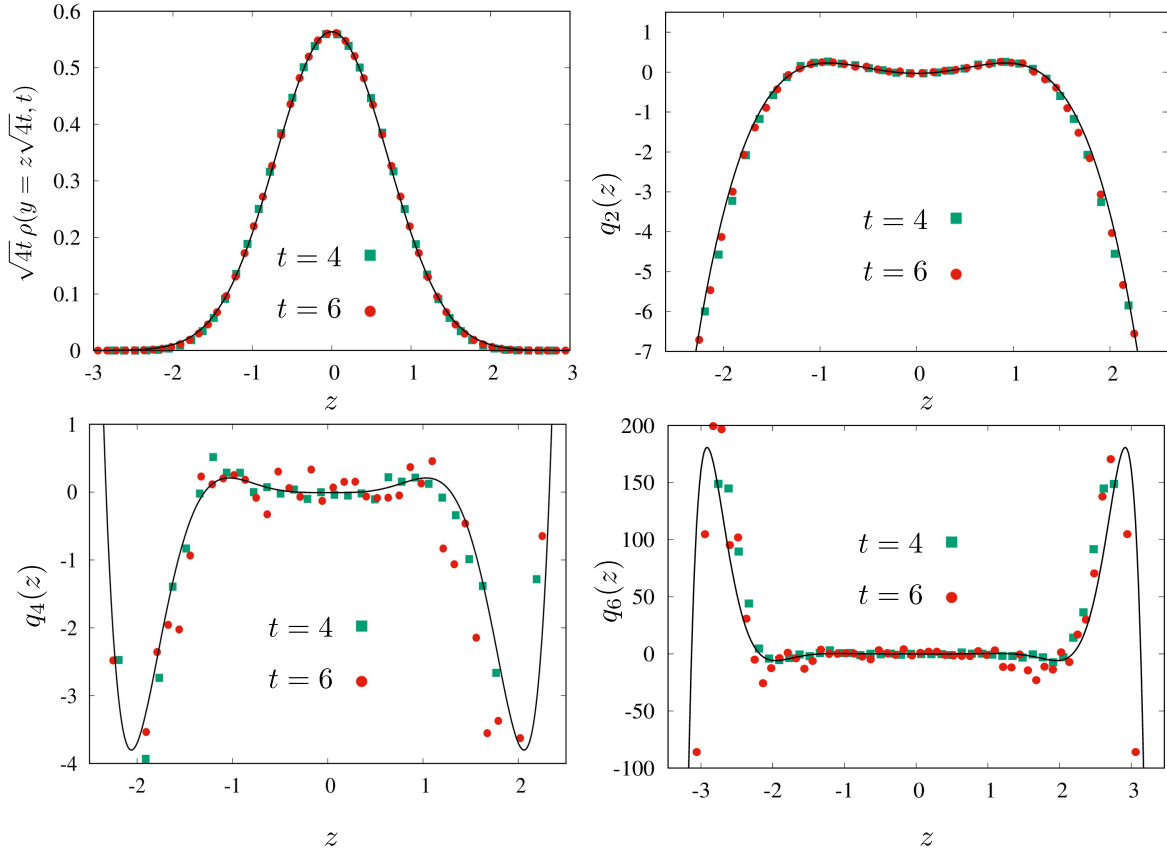


Figure 4.3: Plots for the long-time distribution of a DRABP with $D_R = 2.0$, $\gamma = 1$, at two different times—(a) compares the leading order contribution of the scaled Gaussian distribution Eq. (4.52) with that obtained from numerical simulation; (b), (c) and (d) compare $q_2(z)$, $q_4(z)$ and $q_6(z)$ obtained in Eq. (4.63), Eq. (9.69) and Eq. (9.75) with the same obtained from numerical simulations. In all the plots the black solid lines denote the theoretical predictions, while the numerical simulations are indicated by colored symbols.

Putting $k = 3$, $m = 1$ in Eq. (4.44b) to get B_1^3 ,

$$(\lambda + 1)B_1^3 = -\frac{\partial B_1^1}{\partial t} - \sqrt{\frac{\lambda + 1}{2}} \left(\frac{\partial A_0^2}{\partial y} + \frac{\partial A_2^2}{\partial y} \right). \quad (4.55)$$

Thereafter, using $k = 2$, $m = 2$ in Eq. (4.44a), to obtain A_2^2 , we get an inhomogeneous diffusion equation for A_0^2 ,

$$\left[\frac{\partial}{\partial t} - \frac{\partial^2}{\partial y^2} \right] A_0^2 = -\frac{\partial^2}{\partial y^2} \left(\frac{1}{\lambda + 1} \frac{\partial}{\partial t} - \frac{1}{8} \frac{\partial^2}{\partial y^2} \right) A_0^0, \quad (4.56)$$

as mentioned in Eq. (4.8). To solve the above equation, we anticipate the following scaling form for $A_0^2(y, t)$,

$$A_0^2(y, t) = \frac{e^{-y^2/(4t)}}{\sqrt{4\pi t}} \frac{1}{t} q_2 \left(\frac{y}{\sqrt{4t}} \right). \quad (4.57)$$

In fact, in general, for higher orders,

$$A_0^{2k}(y, t) = \frac{e^{-y^2/(4t)}}{\sqrt{4\pi t}} \frac{1}{t^k} q_{2k} \left(\frac{y}{\sqrt{4t}} \right). \quad (4.58)$$

Using the above mentioned scaling form and the expression for $A_0^0(y, t)$, we get for $q_2(z)$,

$$q_2''(z) - 2zq_2'(z) + 4q_2(z) = -\frac{(\lambda - 7)}{8(\lambda + 1)}(3 - 12z^2 + 4z^4). \quad (4.59)$$

This leads to the general solution for $q_2(z)$ using Eq. (4.13),

$$q_2(z) = c_2 H_2(z) + \frac{(\lambda - 7)}{16(\lambda + 1)} (-3z^2 + 2z^4). \quad (4.60)$$

The normalization condition $\int_{-\infty}^{\infty} dy A_0(y, t)$ is satisfied trivially for arbitrary values of C_2 and thus as mentioned before we take recourse to the moments to evaluate C_2 . In fact, at each order the constant C_{2k} is determined by comparing the coefficient of $(\tau/t)^k$ of $M(2k, 0, t)/(4t)^k$ obtained from the two methods: the exact computation in Sec. 4.2.1 and using the series Eq. (4.41); where the latter is simply given by,

$$\int_{-\infty}^{\infty} dz z^{2k} q_{2k}(z) e^{-z^2} / \sqrt{\pi}. \quad (4.61)$$

Following this procedure for $k = 1$, we get $C_2 = \frac{5-3\lambda}{64(\lambda+1)}$, which leads to,

$$q_2(z) = \frac{3\lambda - 5}{32(\lambda + 1)} + \frac{(13 - 3\lambda)}{8(\lambda + 1)} z^2 + \frac{(\lambda - 7)}{8(\lambda + 1)} z^4. \quad (4.62)$$

Similarly we can find the subleading contributions $A_0^4(y, t)$ and $A_0^6(y, t)$ (see 9.6). They

satisfy the inhomogeneous differential equation,

$$\left[\frac{\partial}{\partial t} - \frac{\partial^2}{\partial y^2} \right] A_0^{2k}(y, t) = S_{2k}(y, t), \quad (4.63)$$

as announced in (4.8). The explicit forms of S_4 and S_6 are given in the appendix. Substituting the ansatz,

$$A_0^{2k}(y, t) = \frac{e^{-y^2/(4t)}}{\sqrt{4\pi t}} \frac{1}{t^k} q_{2k} \left(\frac{y}{\sqrt{4t}} \right), \quad (4.64)$$

leads to inhomogeneous Hermite equation Eq. (4.11) for $q_4(z)$ and $q_6(z)$, whose general solution is given by (4.13). We find the explicit solutions (see Appendix) as,

$$q_{2k}(z) = \sum_{n=0}^{2k} \alpha_{2k,n}(\lambda) z^{2n}, \quad (4.65)$$

where $\alpha_{2k,n}(\lambda)$ is a polynomial in λ . The expressions of $\{\alpha_{4,n}; 0 \leq n \leq 4\}$ and $\{\alpha_{6,n}; 0 \leq n \leq 6\}$ are rather long and are given in 9.6. Figure 4.3 compares the leading order Gaussian along with the subleading corrections $q_2(z)$, $q_4(z)$ and $q_6(z)$ with the same extracted from the numerical simulations of DRABP and shows reasonably good agreement.

4.3 Summary

In summary, we develop a unifying framework to systematically study the position distribution $\rho(x, t)$ of active particles at late times t much larger than the activity time τ_a . In this regime, the position distribution admits a perturbative series in powers of τ_0/t . Using the model of DRABP, we show that the leading term generically satisfies the diffusion equation with an effective diffusion coefficient D_{eff} . We further find that the higher-order subleading corrections, again, generically satisfy an inhomogeneous diffusion equation, where the source term involves the previous order solutions. Consequently, the higher-order corrections also admit diffusive scaling. The distribution of the scaled position $z = x/\sqrt{4D_{\text{eff}}t}$ can be

generically written as

$$q(z, t) = (e^{-z^2}/\sqrt{\pi}) \sum_{k=0}^{\infty} (\tau_0/t)^k q_{2k}(z), \quad (4.66)$$

where $q_{2k}(z)$ is a $4k$ -th order polynomial in z that satisfies an inhomogeneous Hermite differential equation. This formalism has been shown to work for other popular models of active particles like RTP, AOUP, and ABP. In fact, it is supposed to work for all other active particle models which have a finite active time-scale.

Chapter 5

Stationary states of direction reversing active Brownian particles in a harmonic trap

Till this point, we have considered free active particle models, i.e., where there is no external potential on the active particles. Under confining potentials, it is expected that the active particle relaxes to a stationary state. As discussed in the introduction, unlike passive Brownian particles, the active particles do not always relax to the equilibrium Boltzmann distribution. In fact, it is a competition between the active time-scale τ_a and the characteristic time-scale of the confining potential that determines the exact nature of the stationary state. There have been a handful of theoretical studies that find exact results for the stationary state in such scenarios [68, 57, 61, 59, 95].

Of particular interest is the shape-transition of the position distribution from an *active phase*, characterized by an accumulation of probability density near the boundary of the confining region, to a Boltzmann-like *passive phase* [68, 57, 59, 95]. Importantly, most of these previous works consider active particles with a single active time-scale. In this chapter, we discuss the stationary properties of an active particle with two characteristic time-scales, namely, a DRABP, trapped in a harmonic potential $V(x, y) = \frac{\mu}{2}(x^2 + y^2)$. In such a scenario, the Langevin equations (3.1) become,

$$\dot{x} = -\mu x + v_0 \sigma(t) \cos \theta(t), \quad \text{an} \quad \dot{y} = -\mu y + v_0 \sigma(t) \sin \theta(t), \quad (5.1)$$

where the orientation still undergoes a standard Brownian motion with diffusion coefficient D_R . Note that, for $\gamma = 0$, this model reduces to the ABP in a harmonic potential, for which the stationary state has been studied in [57, 61]. On the other hand, for $D_R = 0$, since θ does not evolve, the model corresponds to a one-dimensional RTP along the initial orientation in a harmonic potential [59]. In the absence of any potential, for both $\gamma = 0$ (ABP) and $D_R = 0$ (RTP), the long-time dynamics becomes diffusive with effective diffusion

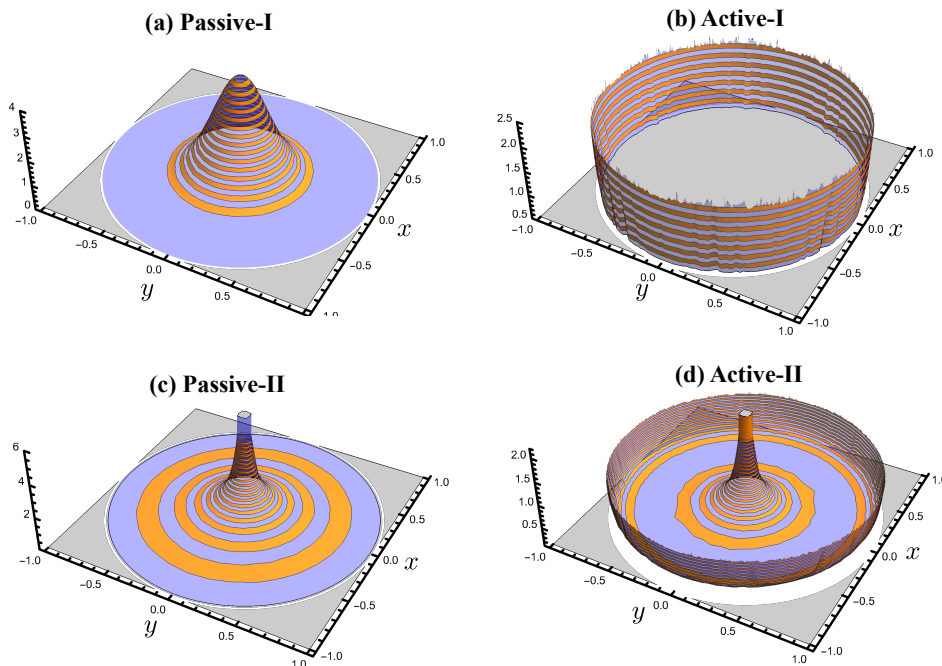


Figure 5.1: Typical shape of the stationary position distribution $P(x, y)$ for $r_0 = 1$ in the four phases—(a) Passive-I [(5.7)], (b) Active-I [(5.12)], (c) Passive-II [(5.20) for $\nu > 1$], (d) Active-II [(5.20) for $\nu < 1$].

coefficient $D_{AB} = v_0^2/(2D_R)$ and $D_{RT} = v_0^2/(2\gamma)$, respectively. For DRABP, i.e., both non-zero γ and D_R , the corresponding effective diffusion coefficient is $D_{DR} = v_0^2/[2(D_R + 2\gamma)]$. In this chapter, we discuss that, in the presence of a harmonic potential, the interplay of γ , D_R and μ leads to a host of interesting behaviors in the stationary state.

We first give a qualitative description of the different phases in terms of long-time trajectories in Sec. 5.1 and then provide detailed analytical derivations of the position distributions in the different phases in Sec. 5.2. We summarize the results of this chapter in Sec. 5.3.

5.1 Stationary Phases

In this section, we introduce the different phases and provide an intuitive picture based on the long-time trajectories, before going to the detailed analysis. For $\gamma \ll \mu$ or $D_R \ll \mu$, the system is in an *active phase*, where the probability density accumulates near the circular boundary of radius r_0 . On the other hand, for $\gamma \gg \mu$ or $D_R \gg \mu$ the system is in a

passive phase where the distribution has a single central peak. A unique feature of this DRABP in harmonic potential is that for $D_R \ll \gamma$, the distribution at the center always diverges (algebraically for the two-dimensional position distribution and logarithmically for the marginal) irrespective of whether the system is in the active or the passive phase. To take this into account, we further subdivide the each of two phases into two sub-phases based on our analytical results in the limiting cases.

Passive-I ($D_R \gg \mu$, for arbitrary γ): In this case, the stationary distribution is Boltzmann-like which has a Gaussian form for the harmonic potential considered here [see Fig. 5.1(a)]. This is similar to the typical passive phase seen for ABP ($\gamma = 0$) in an external potential.

Active-I ($\gamma \ll D_R \ll \mu$): Here the stationary distribution is concentrated at the circular boundary $|\mathbf{r}| = r_0$ [see Fig. 5.1(b)]. This is also the active phase for ABP, where $\gamma = 0$.

Passive-II ($\gamma > \mu \gg D_R$): In this passive phase also, the position distribution has a single central peak. However, the distribution diverges at the center which distinguishes it from the passive-I phase [see Fig. 5.1(c)].

Active-II ($\mu > \gamma \gg D_R$): This phase is characterized by a Mexican hat-like shape [see Fig. 5.1(d)] of the distribution that is concentrated both at the center and at the circular boundary $|\mathbf{r}| = r_0$.

While we have characterized the above phases analytically only in the limiting cases, the general qualitative features hold even beyond these limits, which we verify using numerical simulations for some other parameters (see Fig. 5.9). The phases are best represented in the γ , D_R and μ^{-1} space and a qualitative phase diagram is provided in Fig. 5.2. In order to develop a physical understanding of the emergence of the different shapes, we look at the typical trajectories in the different phases in the following section.

To understand the stationary behavior of DRABP, it is useful to characterize the long-time trajectories in the different phases.

Passive-I: A typical trajectory of DRABP in this phase, shown in Fig. 5.3(a), resembles that of an ordinary Brownian particle in a harmonic trap. This is because the randomization time-scale D_R^{-1} of the orientation is much smaller than the relaxation time-scale μ^{-1} of the trap. Increasing γ decreases the randomization time-scale to $(D_R + 2\gamma)^{-1}$. Consequently, the description of DRABP at a time-scale larger than this randomization time-scale is given by

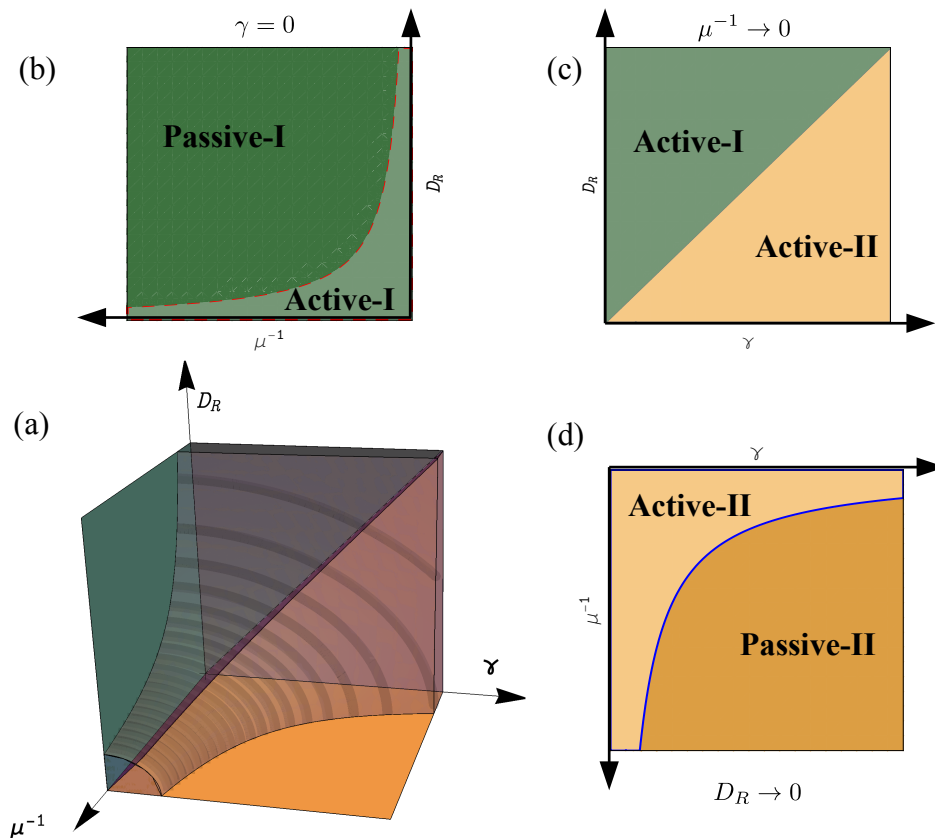


Figure 5.2: A simplistic schematic phase diagram for the steady state of DRABP in a harmonic trap. (a) The phase diagram in the (γ, D_R, μ^{-1}) space. For $\gamma = 0$, the phase diagram of DRABP becomes that of an ABP in a harmonic trap [shown separately in (b)], where we see the active-I phase for $D_R \ll \mu$ (light green shaded region), which crosses over to the passive-I phase for $D_R \gg \mu$ (dark green shaded region). Although we do not know the crossover/transition curve analytically, for simplicity, it is shown by the schematic dotted red line. The $D_R \rightarrow 0$ plane [shown separately in (d)] shows a transition from the active-II to passive-II phase, where the transition line, marked by a solid blue line, is known exactly (see Sec. 5.2.3). Numerical evidence suggests (see Sec. 5.2.4) that the behaviors shown in (b) and (c) extend for $\gamma > 0$ and $D_R > 0$ respectively, implying some kind of transition/crossover between active-I and active-II as well as passive-I and passive-II phases. The active (I & II) region shrinks as μ^{-1} increases, indicating the funnel-like shape of the surface separating the active (I & II) and the passive (I & II) phases shown in (a). However, the actual shape of this surface may have more complex structure [see Fig. 5.9(b)] than the simple schematic surface shown here. For $\mu^{-1} \rightarrow 0$ [shown separately in (c)], the passive region disappears (i.e., pushed to infinity) leaving only the active phases.

an Ornstein-Uhlenbeck process with an effective diffusion constant D_{DR} .

Active-I: Figure 5.3(b) shows a typical trajectory in this phase. Except a very few detours to the interior region, the particle mostly stays near the boundary, where the net force on the particle is zero when its orientation vector \hat{n} is along \mathbf{r} . This is due to the fact that in this regime θ changes slowly as well as reversal events are very rare.

Passive-II: Figure 5.3(c) shows a typical trajectory in this regime. Unlike active-I, the large number of directional reversals makes the persistence length $\sim v_0/\gamma$ smaller than the diameter of the confining region $\sim v_0/\mu$. As a result, the particle is confined near the origin. However, unlike passive-I, since D_R is small here, trajectory-segments between consecutive reversals are almost straight and pass through the central region, leading to a qualitatively different distribution.

Active-II: As seen from Figure 5.3(d), since D_R is small, in this regime also the particle passes through the central region almost in a straight line. However, unlike the passive-II, since the persistence length $\sim v_0/\gamma$ is larger than the diameter of the confining region $\sim v_0/\mu$, it goes all the way to the boundary and spends a considerable time there leading to a concentration of probabilities at the boundary as well as the center.

These four classes of different trajectories lead to four qualitatively different shapes of the stationary distribution, which we analyze in the following section.

5.2 Position distributions

The Fokker-Planck equation for the probability density function $P_\sigma(x, y, \theta, t)$ corresponding to the Langevin equations (5.1) is given by,

$$\frac{\partial P_\sigma}{\partial t} = - \left[\frac{\partial}{\partial x} (-\mu x + v_0 \sigma \cos \theta) + \frac{\partial}{\partial y} (-\mu y + v_0 \sigma \sin \theta) \right] P_\sigma - \gamma P_\sigma + \gamma P_{-\sigma} + D_R \frac{\partial^2 P_\sigma}{\partial \theta^2}. \quad (5.2)$$

We are interested in the steady state position distribution

$$P(x, y) \equiv \int_0^{2\pi} d\theta \sum_{\sigma=\pm 1} P_\sigma(x, y, \theta), \quad (5.3)$$

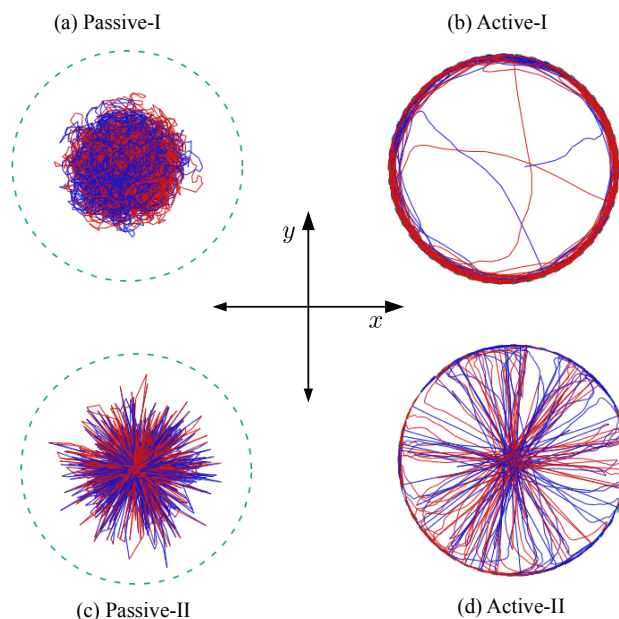


Figure 5.3: Long-time trajectories of a DRABP in a harmonic trap with $\mu = 1$ in the different phases. The finite support of the position distribution, a circle of radius $r_0 = 1$, is marked by dashed green lines. (a) passive-I phase: $\gamma = 0.1$ $D_R = 10$; (b) active-I phase: $\gamma = 0.001$ $D_R = 0.05$ (c) passive-I phase: $\gamma = 5$ $D_R = 0.01$ (d) active-II phase: $\gamma = 0.1$ $D_R = 0.01$. The blue and red colors indicate the instantaneous state $\sigma = +1$ and -1 respectively.

where the stationary distribution $P_\sigma(x, y, \theta) \equiv P_\sigma(x, y, \theta, t \rightarrow \infty)$ is the solution of Eq. (5.2) with $\partial P_\sigma / \partial t = 0$ [note that, for notational simplicity, we are using the same letter P to denote all the probability distributions] The exact solution of Eq. (5.2) is hard to obtain in practice, for arbitrary values of μ , γ and D_R , even for the steady state. Hence we analyze the distribution $P(x, y)$ in the limiting cases where one of the parameters is much smaller than the others, giving rise to distinct phases characterized by the shape of the position distribution. Let us start with the most familiar passive phase (passive-I) where the stationary state is Boltzmann-like.

5.2.1 Passive-I phase: $D_R \gg \mu$

In this case it is useful to rewrite Eq. (5.1) as,

$$\dot{x} = -\mu x + \zeta_x(t), \quad \text{and} \quad \dot{y} = -\mu y + \zeta_y(t), \quad (5.4)$$

where the auto-correlation of the effective noises $\zeta_x(t) = v_0\sigma(t) \cos \theta(t)$ and $\zeta_y(t) = v_0\sigma(t) \sin \theta(t)$ become [see Eq. (3.6)]

$$\langle \zeta_x(t)\zeta_x(t') \rangle = \langle \zeta_y(t)\zeta_y(t') \rangle \rightarrow \frac{v_0^2}{2} e^{-(D_R+2\gamma)|t-t'|}, \quad (5.5)$$

for $t, t' \gg D_R^{-1}$ and arbitrary γ , while the cross-correlation $\langle \zeta_x(t)\zeta_y(t') \rangle \rightarrow 0$. Now, for large D_R , we can evolve Eq. (5.4) at a time step $D_R^{-1} \ll dt \ll \mu^{-1}$, where the effective noises emulate two independent white noises with auto-correlations

$$\langle \zeta_a(t)\zeta_b(t') \rangle \rightarrow 2D_{\text{DR}} \delta_{a,b} \delta(t-t'), \quad \text{with } \{a, b\} \in \{x, y\} \quad (5.6)$$

and $D_{\text{DR}} = v_0^2/[2(D_R + 2\gamma)]$. Thus, the Langevin equations (5.4) reduce to an Ornstein-Uhlenbeck process, where the stationary state is given by the Boltzmann distribution,

$$P(x, y) = \frac{\mu}{2\pi D_{\text{DR}}} \exp \left[-\frac{\mu(x^2 + y^2)}{2D_{\text{DR}}} \right]. \quad (5.7)$$

This is the passive-I phase [see Fig. 5.1(a)] as announced in Sec. 5.1. The corresponding marginal distribution is evidently also a Gaussian,

$$P(x) = \sqrt{\frac{\mu}{2\pi D_{\text{DR}}}} \exp \left(-\frac{\mu x^2}{2D_{\text{DR}}} \right). \quad (5.8)$$

which is compared with the numerical simulations in Figure 5.4(a).

Note that, the variance of the above distribution agrees with the expression obtained from the exact Eq. (9.80) by taking the limit $v_0 \rightarrow \infty$, $D_R \rightarrow \infty$ keeping v_0^2/D_R constant for arbitrary γ . Moreover, the exact kurtosis given by Eq. (9.85) tends to zero in this limit, consistent with the Gaussian form of the above distribution [see Eq. (9.86)].

In the limit $\gamma \rightarrow 0$, the above distribution reduces to that of an ABP in a harmonic potential in the passive phase [56],

$$P(x, y) = \frac{\mu}{2\pi D_{\text{AB}}} \exp \left[-\frac{\mu(x^2 + y^2)}{2D_{\text{AB}}} \right], \quad (5.9)$$

where $D_{\text{AB}} = v_0^2/(2D_R)$. The corresponding marginal distribution is also obviously a Gaus-

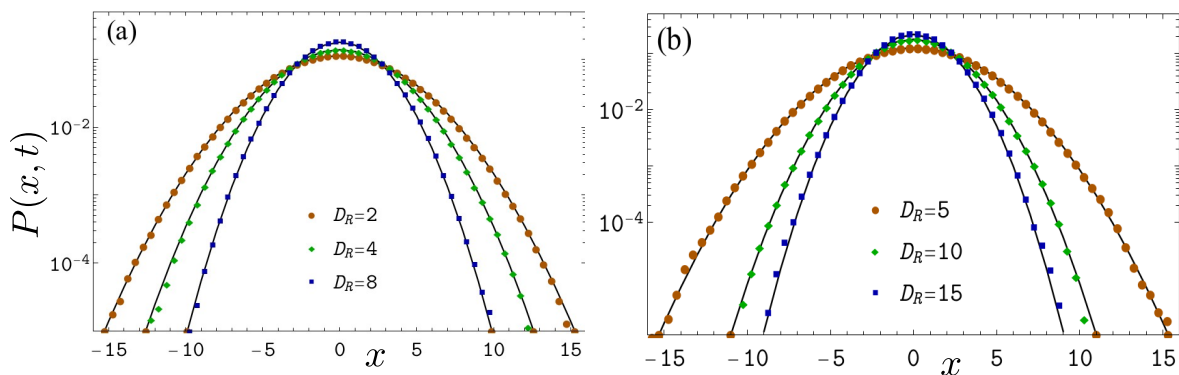


Figure 5.4: The stationary marginal distribution $P(x)$ in the passive-I phase for $\mu = 0.01$ and $v_0 = 1$. The analytical predictions for $P(x)$ given by Eq. (5.8) and (5.10) (solid black lines) are compared with numerical simulations (solid symbols) for $\gamma = 1$ (a) and $\gamma = 10^{-4}$ (b) respectively.

sian,

$$P(x) = \sqrt{\frac{\mu}{2\pi D_{AB}}} \exp\left(-\frac{\mu x^2}{2D_{AB}}\right), \quad (5.10)$$

which we compare with numerical simulations in Fig. 5.4(b).

Next we discuss the most commonly seen active phase where the stationary probability density is concentrated near the boundary.

5.2.2 Active-I phase: $\gamma \ll D_R \ll \mu$

In the limit $\gamma/D_R \rightarrow 0$, the Fokker-Planck equation (5.2) becomes,

$$\frac{\partial P_\sigma}{\partial t} = - \left[\frac{\partial}{\partial x}(-\mu x + v_0 \sigma \cos \theta) + \frac{\partial}{\partial y}(-\mu y + v_0 \sigma \sin \theta) \right] P_\sigma + D_R \frac{\partial^2 P_\sigma}{\partial \theta^2}, \quad (5.11)$$

where P_\pm represents two non-interacting ABPs with constant velocities v_0 and $-v_0$ respectively. Since the stationary state of an ABP does not depend on the sign of the velocities (alternatively, the initial orientation), in this limit we get the same stationary distributions as that of an ABP in a harmonic potential [56, 61].

Therefore, for $\gamma \ll D_R \ll \mu$, the probability density is concentrated along a ring $x^2 + y^2 = r_0^2$ thereby indicating that the particle is in an active phase. In other words, the position

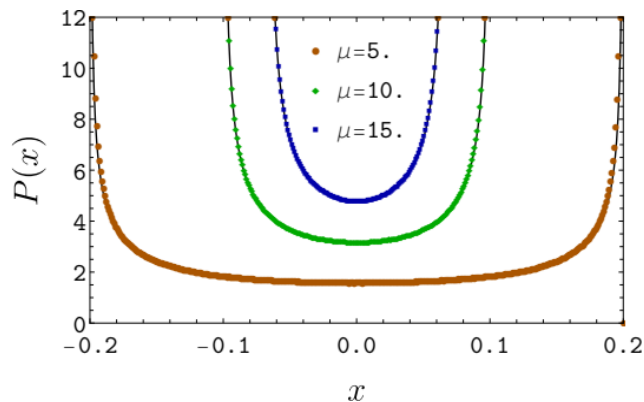


Figure 5.5: The stationary marginal distribution $P(x)$ in the active-I phase. The symbols are obtained from numerical simulations for $D_R = 0.05$ and $\gamma = 10^{-4}$ and solid black lines are from the analytical prediction Eq. (5.12).

distribution takes the limiting form

$$P(x, y) = \frac{1}{2\pi r_0} \delta\left(\sqrt{x^2 + y^2} - r_0\right). \quad (5.12)$$

We refer to this ABP-like active phase of DRABP as active-I to distinguish it from a novel active phase obtained in Sec. 5.2.3, emerging from the direction reversal. The marginal distribution is obtained by integrating Eq. (5.12) over y as,

$$P(x) = \frac{1}{\pi\sqrt{r_0^2 - x^2}} \Theta(r_0 - |x|), \quad (5.13)$$

where the $\Theta(z)$ is the Heaviside-theta function. We compare this theoretical prediction with numerical simulations in Fig. 5.5 and find an excellent agreement. Interestingly, this active-I phase even extends to $\gamma/D_R = O(1)$, where the shape of the distribution remains qualitatively same (weighted near the boundary), as discussed later in Sec. 5.2.4. The variance and the kurtosis corresponding to Eq. (5.13) are $r_0^2/2$ and $-3/2$ respectively, which are consistent with the direct calculation of the same; see Eq. (9.87). Note that, the Fokker-Planck equation (5.11) still holds for $\gamma \ll \mu \ll D_R$. The corresponding passive phase (passive-I) is characterized by a Boltzmann distribution as given in Eq. (5.9).

Finally, we discuss two novel phases, where the directional reversal leads to a diverging central peak along with the active and passive like features.

5.2.3 The novel active and passive phases: $D_R \ll (\mu, \gamma)$

The directional reversal leads to two new phases which are best seen in the $D_R/\mu \rightarrow 0$ limit. It is useful to divide both sides of Eq. (5.2) by μ , which gives,

$$\frac{\partial P_\sigma}{\partial(\mu t)} = - \left[\frac{\partial}{\partial x} (-x + r_0 \sigma \cos \theta) + \frac{\partial}{\partial y} (-y + r_0 \sigma \sin \theta) \right] P_\sigma - \nu [P_\sigma - P_{-\sigma}] + \frac{D_R}{\mu} \frac{\partial^2 P_\sigma}{\partial \theta^2}, \quad (5.14)$$

where $\nu = \gamma/\mu$. In the limit $D_R/\mu \rightarrow 0$ while keeping r_0 and ν finite, θ evolves very slowly. As a first approximation, θ can be kept fixed. This is equivalent to neglecting the second order derivative with respect to θ in Eq. (5.14), resulting in the Fokker-Planck equation for the conditional distribution $P_\sigma(x, y, t|\theta)$ for a given θ .

Now, for a fixed θ , it is convenient to make a rotation of the coordinate system

$$\begin{bmatrix} x_{\parallel} \\ x_{\perp} \end{bmatrix} = \begin{bmatrix} \cos \theta & \sin \theta \\ -\sin \theta & \cos \theta \end{bmatrix} \begin{bmatrix} x \\ y \end{bmatrix}, \quad (5.15)$$

where x_{\parallel} and x_{\perp} are respectively the axes parallel and perpendicular to the θ -direction. In the $(x_{\parallel}, x_{\perp})$ coordinates, the Fokker-Planck equation for $P_\sigma(x_{\parallel}, x_{\perp}, t|\theta)$ becomes,

$$\frac{\partial P_\sigma}{\partial(\mu t)} = - \frac{\partial}{\partial x_{\parallel}} [(-x_{\parallel} + r_0 \sigma) P_\sigma] - \nu [P_\sigma - P_{-\sigma}] - \frac{\partial}{\partial x_{\perp}} [-x_{\perp} P_\sigma]. \quad (5.16)$$

It is evident from the above equation that the dynamics of x_{\parallel} is nothing but that of a one-dimensional RTP along θ in a harmonic potential. On the other hand, x_{\perp} independently undergoes a deterministic overdamped motion in a harmonic potential, resulting in $x_{\perp} \rightarrow 0$ as $t \rightarrow \infty$. Therefore, the steady state position distribution $P(x_{\parallel}, x_{\perp}|\theta) = \sum_{\sigma=\pm 1} P_\sigma(x_{\parallel}, x_{\perp}, t \rightarrow \infty|\theta)$ can be obtained using the steady state result of 1D RTP in a harmonic trap [59],

$$P(x_{\parallel}, x_{\perp}|\theta) = \frac{\delta(x_{\perp}) 2^{1-2\nu}}{r_0 B(\nu, \nu)} \left[1 - \left(\frac{x_{\parallel}}{r_0} \right)^2 \right]^{\nu-1} \Theta(r_0 - |x_{\parallel}|), \quad (5.17)$$

where $B(\nu, \nu)$ is the beta function.

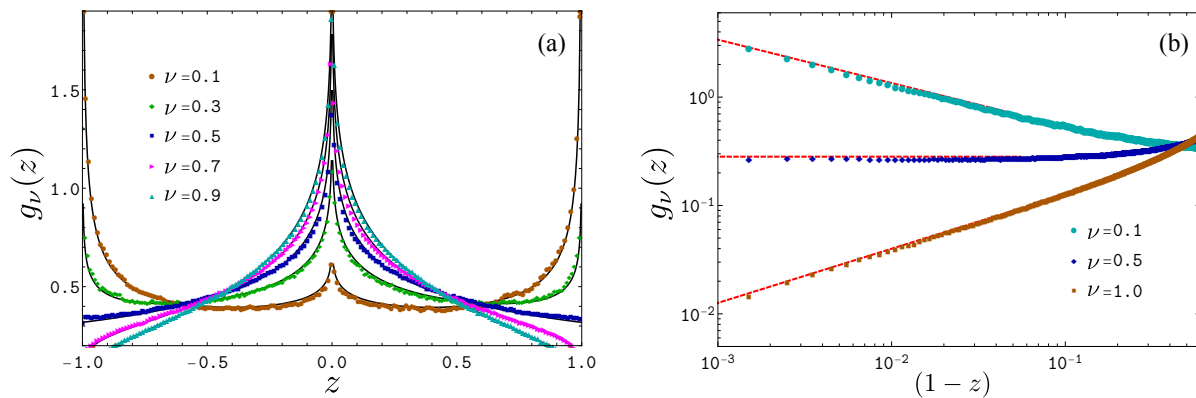


Figure 5.6: (a) Comparison of theoretical stationary state marginal distribution $g_\nu(z)$ given by (5.22) as a function of the scaled variable $z = \mu x/v_0$ in the $D_R \rightarrow 0$ limit (solid black lines) with numerical simulations (symbols) for $D_R = 10^{-4}$, and $\mu = v_0 = 1$, for different values of $\nu = \gamma/\mu$. This plot shows the transition from the Active-II to Passive-II at $\gamma = \mu/2$ as predicted by Eq. (5.23). (b) Comparison of Eq. (5.23) (red dashed lines) with the simulations (symbols) for the same set of remaining parameters as in (a), which highlights the different tail behavior in the two phases.

Subsequently, in terms of the original coordinates (x, y) , the position distribution becomes,

$$P(x, y|\theta) = \frac{2^{1-2\nu}}{r_0 B(\nu, \nu)} \left[1 - \frac{x^2 + y^2}{r_0^2} \right]^{\nu-1} \delta(-x \sin \theta + y \cos \theta) \Theta \left(r_0 - \sqrt{x^2 + y^2} \right). \quad (5.18)$$

The dynamics of θ is independent of that of (x, y) , whose distribution evolves by the diffusion equation, leading to the uniform steady state for $\theta \in [0, 2\pi]$ for $t \gg D_R^{-1}$. Averaging Eq. (5.18) with respect to the steady state distribution θ , we get the scaling form for the distribution,

$$P(x, y) = \int_0^{2\pi} \frac{d\theta}{2\pi} P(x, y|\theta) = \frac{1}{r_0^2} f_\nu \left(\frac{x}{r_0}, \frac{y}{r_0} \right), \quad (5.19)$$

with the scaling function,

$$f_\nu(z_1, z_2) = \frac{2^{1-2\nu}}{\pi B(\nu, \nu)} \frac{(1 - z_1^2 - z_2^2)^{\nu-1}}{\sqrt{z_1^2 + z_2^2}} \Theta(1 - z_1^2 - z_2^2). \quad (5.20)$$

Plots of the scaling distribution $f_\nu(z_1, z_2)$ are shown in Fig. 5.1(c) and (d) for $\nu > 1$ and $\nu < 1$ respectively. For $\nu < 1$, the distribution looks like a Mexican hat with algebraic divergences both at the origin and at the boundary $z_1^2 + z_2^2 = 1$. On the other hand for $\nu > 1$, the

distribution goes to zero at the boundaries, while it still retains the algebraic divergence at the origin.

The marginal distribution can be obtained by integrating Eq. (5.19) over one of the coordinates. Integrating over y yields the scaling form,

$$P(x) = \frac{1}{r_0} g_\nu \left(\frac{x}{r_0} \right). \quad (5.21)$$

The corresponding scaling function is given by,

$$g_\nu(z) = \frac{1}{\pi} (1 - z^2)^{\nu - \frac{1}{2}} {}_2F_1 \left(\frac{1}{2}, \nu, \nu + \frac{1}{2}, 1 - z^2 \right) \Theta(1 - z^2), \quad (5.22)$$

where ${}_2F_1(a, b, c, y)$ denote the Hypergeometric function.

The moments of the above distribution can be computed by using the series representation of the hypergeometric function. The variance $\langle x^2 \rangle = r_0^2/[2(2\nu + 1)]$ and the kurtosis $\kappa = 3(2\nu - 3)/[2(2\nu + 3)]$ obtained from Eq. (5.22) agree with the direct calculations of the same (see Eq. (9.88)).

Figure 5.6(a) shows a very good agreement between Eq. (5.22) and numerical simulations for small values of D_R . As seen in Fig. 5.6(a), the shape of the distribution near the boundaries shows three qualitatively different behaviors. Indeed, it follows from Eq. (5.22) that the behavior of the tails near $z = \pm 1$ undergoes a transition as a function of ν ,

$$g_\nu(z) \simeq \frac{1}{\pi} \times \begin{cases} [2(1 - |z|)]^{-(1/2-\nu)} & 0 < \nu < 1/2, \\ 1 & \nu = 1/2, \\ [2(1 - |z|)]^{\nu-1/2} & \nu > 1/2. \end{cases} \quad (5.23)$$

It is evident from the above equation that at the boundaries $z = \pm 1$, the marginal distribution diverges for $\nu < 1/2$, while it vanishes for $\nu > 1/2$. We compare this theoretical prediction with numerical simulations in Fig. 5.6(b) and find excellent agreement.

One distinctive feature of the scaling function in Eq. (5.22) is that, for all values ν , it has

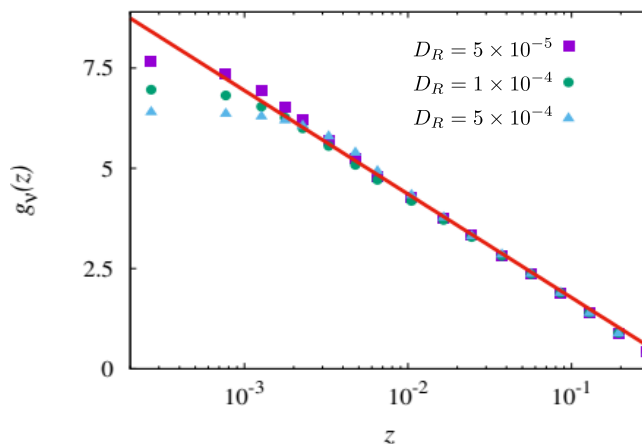


Figure 5.7: The central logarithmic divergence for the marginal stationary state distribution in the passive-II phase. The symbols denote the scaled distribution obtained using numerical simulations for $\gamma = 10$, $\mu = \nu_0 = 1$, while the solid red line indicates the analytical prediction in Eq. (5.24). We see progressively better agreement for smaller values of D_R .

a logarithmic divergence at the center,

$$g_\nu(z) = -\frac{\Gamma(\nu + \frac{1}{2})}{\pi^{3/2}\Gamma(\nu)} \left[\log\left(\frac{z^2}{4}\right) + E + \psi(\nu) \right] + O(z^2), \quad (5.24)$$

where $\Gamma(\nu)$ is the gamma function, $E = 0.5772\dots$ is the Euler-Mascheroni constant, and $\psi(\nu) = \Gamma'(\nu)/\Gamma(\nu)$ is the digamma function. We illustrate the above small z behavior of $g_\nu(z)$ and compare it with numerical simulation in Fig. 5.7. As expected, we find progressively better agreement for smaller values of D_R/μ for a fixed value of ν .

The divergence of $f_\nu(z_1, z_2)$ in Eq. (5.20) at the boundary $z_1^2 + z_2^2 = 1$ for $\nu < 1$ is a signature of activity, implying the accumulation of particles near the boundary. However, this phase [see Fig. 5.1 (d)] is different from the active-I phase discussed earlier [see Fig. 5.1 (b)] marked by the presence of an additional central diverging peak. We refer to this phase as active-II. On the other hand, the distribution has only a central peak for $\nu > 1$, which is characteristic of the passive phase. However, the diverging nature of the central peak distinguishes this phase [see Fig. 5.1 (c)] from the usual passive-I phase [see Fig. 5.1 (a)] discussed earlier. We refer to this phase as passive-II. Note that, the transition from active-II to passive-II occurs at $\nu = 1/2$ for the marginal distribution [see Eq. (5.23)], in contrast to $\nu = 1$ for the two-dimensional joint distribution.

To further highlight the novel features of the passive-II phase in $d = 2$, we analyze the position distribution (5.20) in the typical diffusive scaling limit of RTP, $\gamma \rightarrow \infty$ and $v_0 \rightarrow \infty$ while keeping $v_0^2/\gamma = 2D_{\text{RT}}$ fixed. This is equivalent to taking the limit $\nu \rightarrow \infty$ and $z_1, z_2 \rightarrow 0$, keeping $z_1\sqrt{\nu}$ and $z_2\sqrt{\nu}$ finite. This leads to the scaling form,

$$f_\nu(z_1, z_2) = \nu h(z_1\sqrt{\nu}, z_2\sqrt{\nu}), \quad (5.25)$$

and consequently, $P(x, y)$ has the scaling form,

$$P(x, y) = \frac{\mu}{2D_{\text{RT}}} h\left(x\sqrt{\frac{\mu}{2D_{\text{RT}}}}, y\sqrt{\frac{\mu}{2D_{\text{RT}}}}\right). \quad (5.26)$$

The corresponding scaling function is given by, $h(w_1, w_2) = e^{-(w_1^2+w_2^2)}/\sqrt{\pi^3(w_1^2+w_2^2)}$ with $\{w_1, w_2\} \in (-\infty, \infty)$.

While $P(x, y)$ has the Boltzmann tail $\propto \exp[-V(x, y)/D_{\text{RT}}]$ with the potential $V(x, y) = \mu(x^2 + y^2)/2$, it has a novel algebraic divergence at the origin, unlike the passive-I case. By integrating (5.26) over y , we get the marginal distribution $P(x) = \sqrt{\frac{\mu}{2D_{\text{RT}}}} q\left(x\sqrt{\frac{\mu}{2D_{\text{RT}}}}\right)$, where the scaling function $q(w) = \int_{-\infty}^{\infty} h(w, w') dw'$ is given by,

$$q(w) = \frac{1}{\pi^{3/2}} K_0\left(\frac{w^2}{2}\right) \exp\left(-\frac{w^2}{2}\right). \quad (5.27)$$

Here $K_0(z)$ is the zeroth order modified Bessel function of second kind and the normalization $\int_{-\infty}^{\infty} q(w) dw = 1$ is easily checked.

The asymptotic behavior $K_0(w^2/2) \sim \exp(-w^2/2)$ as $w \rightarrow \infty$, leads to the Boltzmann distribution at the tails as expected. However, the small- w behavior $K_0(w^2/2) = -[\log(w^2/4) + E] + O(w^4)$, leads to a logarithmic divergence,

$$q(w) = -[\log(w^2/4) + E] + O(w^2), \quad (5.28)$$

near the origin. This is in agreement with Eq. (5.24) for large ν and taking $w = z\sqrt{\nu}$ as the scaling variable.

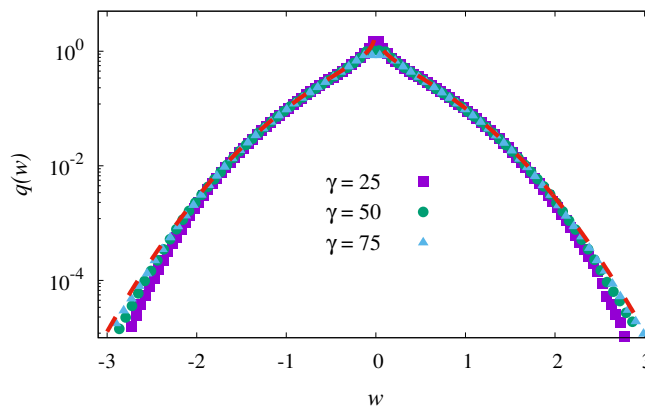


Figure 5.8: The stationary marginal distribution in the passive-II phase in the scaling limit $\gamma \rightarrow \infty$, $v_0 \rightarrow \infty$ keeping $D_{\text{RT}} = v_0^2/(2\gamma)$ finite, as a function of the scaled variable $w = x\sqrt{\mu}/\sqrt{2D_{\text{RT}}}$. The symbols denote the data obtained from numerical simulations, while the dashed red line corresponds to the scaling function given by Eq. (5.28). As expected, departure from the predicted scaling behavior occurs for larger values of w and increases with lower values of γ . We have used $\mu = 1$, $v_0 = 10$ and $D_R = 10^{-4}$.

5.2.4 Crossover from active-I to active-II

As discussed in Sec. 5.2.1, the scenario where μ^{-1} is the largest among the three time-scales yields the passive-I phase. On the other hand, the complementary scenario where μ^{-1} is the smallest time-scale, can lead to both active-I and active-II phases, as discussed earlier in Secs. 5.2.2 and 5.2.3 respectively. It arises from the two limits of the Fokker-Planck equation (5.14) in the rescaled time (μt): it leads to the active-I phase for $\gamma/D_R \rightarrow 0$, while for $D_R/\gamma \rightarrow 0$, it gives the active-II phase. To understand the crossover from the active-I to the active-II, as γ/D_R is varied, we take recourse to numerical simulations and study the phase diagram on the (γ, D_R) planes for fixed values of μ .

We scan the (γ, D_R) plane for a range of values of γ and D_R at an interval of $\Delta\gamma = \Delta D_R = 0.05$, and obtain the marginal stationary state distribution from simulation at these points. To distinguish between the different phases, we numerically detect the existence of the peaks near the origin and the boundaries. To detect if there is a peak away from the origin, we check, whether, for some $\epsilon \ll r_0$, the first order finite difference $\rho(x_0) - \rho(x_0 - \epsilon)$ is positive for some $x_0 \in (0, r_0)$ — suggesting $\rho(x)$ increases with x , and thus, there is an accumulation away from the origin. This is the signature of active phase. Now, to differentiate between active-I and active-II, we further check the existence of an additional peak at the origin.

This central peak is detected by monitoring the sign of the second order finite difference $\rho(-\epsilon) + \rho(\epsilon) - 2\rho(0)$, where the negative sign corresponds to a maximum at the origin.

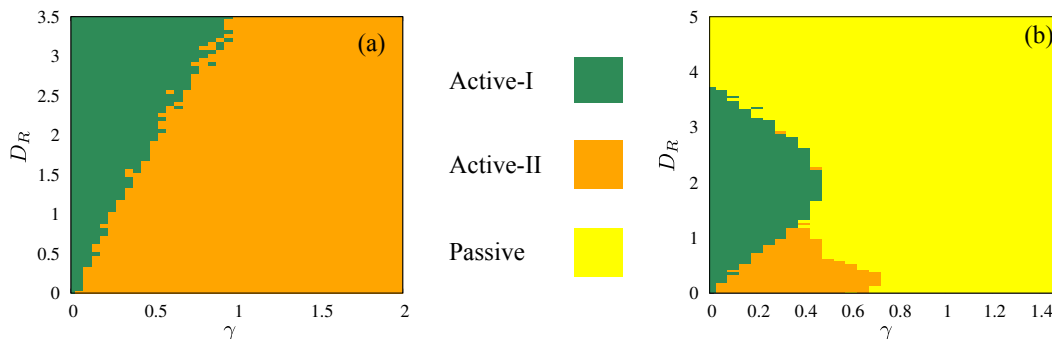


Figure 5.9: The different phases in the (γ, D_R) plane for $\mu = 10$ (a) and $\mu = 2$ (b). (a) shows the phases active-I (green region) and active-II (orange region) detected numerically using the procedure described in Sec. 5.2.4. This phase plane is schematically represented in Fig. 5.2 (c). The passive phases appear for larger values of γ/μ and D_R/μ , which is visible (yellow region) in (b) for $\mu = 2$.

We use this method with $\epsilon = 0.02$ to obtain the phase diagram shown in Fig. 5.9, which illustrates the transition (a) from active-I to active-II for $\mu = 10$ and (b) between active and passive phases for $\mu = 2$. We make two observations from our numerically obtained phase diagram. First, the boundary between the active-I and active-II phases is almost linear and passes through the origin. Secondly, the cross-sectional area corresponding to the combined active regions shrinks with increasing μ^{-1} , thus implying a funnel-like surface. However, the shape of the boundary between the active and passive phases suggest that the surface of the funnel may have more complex structure than the simple schematic representation shown in Fig. 5.2(a).

5.3 Summary

We studied the stationary state position distribution of a DRABP under a harmonic confinement. We find that the presence of two active time-scales leads to a richer stationary state behavior compared to the previously known active particle models, like RTP and ABP (both of which have a single active time-scale). We find that for $D_R \gg \mu$, the system always relaxes to a Boltzmann-like distribution, for any γ , which we refer to as the passive-I phase. On the other hand, for $D_R \ll \mu$, depending on the strength of γ relative to the two other

parameters, we get three different phases: For $\gamma \ll D_R$, an ABP-like active phase emerges where the particle is most likely to be found near the circular boundary of radius v_0/μ . This is referred to as the active-I phase. For $D_R \ll \gamma < \mu$, a new active phase (active-II) emerges which crosses over to a new passive phase (passive-II) for $\gamma > \mu$. Both these new phases are characterized by the presence of a non-Gaussian, diverging central peak of the position distribution. However, the active-II is distinguished from the passive-II phase by the presence of the typical accumulation of probability density near the circular boundary. The exact position distribution obtained analytically in the $D_R \rightarrow 0$ limit yields the exact transition line in the (γ, μ^{-1}) plane.

Chapter 6

Effect of stochastic resetting on run-and-tumble particles

An essential observable for active particles is the time it takes to search for a particular target, such as a food source, a weak spot of the host, or toxins. From our everyday experience, a natural tendency to optimize the search time is to return to the starting point after a period of unsuccessful search and restart the search. This strategy is implemented in dynamical processes by ‘stochastic resetting,’ where a dynamic process is intermittently stopped and restarted from the initial starting position [8]. This has found applications in the biology, economics and even social scienc [118, 119, 120]. Over the past decade, the effect of resetting has been studied in many stochastic systems, the paradigmatic example being a Brownian diffusive particle [121]. This simple process leads to a set of interesting behaviors including a non-equilibrium stationary state, dynamical transition in the relaxation [122] to it as well as a non-monotonic behaviour of mean first passage time [8, 123, 124, 125, 126]. Over the years the effect of stochastic resetting on diffusion-like systems, like underdamped diffusions, Lévy processes, random acceleration and diffusing diffusivity processes [127, 128, 129, 130, 131], have gained great interest.

A very natural question is, what is the effect of resetting when the underlying dynamics is active, instead of ordinary diffusion. In this chapter, we seek answers to this question by studying introducing a stochastic resetting the the continuous two-dimensional RTP model, introduced in Chapter 2. We consider an RTP in two dimensions starting from the origin, with an orientation angle θ distributed uniformly $\in [0, 2\pi]$. At randomly chosen times t_i the RTP is reset back to the origin with the orientation also being reset to a random angle in $\in [0, 2\pi]$ with unifrom probability. We choose the reset times t_i from an exponential

distribution,

$$p(s) = \alpha \exp[-\alpha s], \quad (6.1)$$

i.e., the RTP is reset at a constant rate α . Note that, the tumble dynamics of the RTP, which also happens at a constant rate γ is independent of the resetting dynamics. Since the particle is reset to the origin at a constant rate, it is expected that the particle would eventually reach a stationary state. We study the stationary state position distribution of the RTP in Sec. 6.1, and the approach to the stationary state in Sec. 6.2. In Sec. 6.3, we discuss the first-passage properties of the RTP in presence of stochastic resetting. We summarize the results of this chapter in Sec. 6.4.

6.1 Stationary State distribution

In this section, we will compute the long-time stationary position distribution of the RTP. To this end it is important to note that the time evolution of the RTP under stochastic resetting can be viewed as a renewal process, where the resetting events renew the process at a rate α and between two successive renewal events, the particle undergoes free run-and-tumble motion. So to investigate the position distribution of the RTP with resetting, we will use a renewal equation technique instead of the usual Fokker-Planck approach used in the remainder of the thesis. It turns out, that since we know the exact distribution of the RTP in the absence of resetting, the renewal equation technique is much simpler.

For this resetting mechanism that we consider, it is straightforward to write a last renewal equation for the position probability distribution,

$$\begin{aligned} P_\alpha(\vec{r}, t) &= e^{-\alpha t} P(\vec{r}, t) + \alpha \int_0^t ds e^{-\alpha s} \int_{-\infty}^{\infty} d\vec{r}' P_\alpha(\vec{r}', t-s) P(\vec{r}, s) \\ &= e^{-\alpha t} P(\vec{r}, t) + \alpha \int_0^t ds e^{-\alpha s} P(\vec{r}, s) \end{aligned} \quad (6.2)$$

where $P_\alpha(\vec{r}, t)$ denotes the probability distribution of the RTP in the presence of resetting, while $P_0(\vec{r}, t)$ denote the same in the absence of resetting. The first term on the rhs of the above equation corresponds to the situation where there are no resetting events during $[0, t]$.

The second term contains the contribution from all the trajectories where the last resetting occurred at a time $t - s$. We have used the normalization condition of $P_\alpha(\vec{r}, t)$ in going from the first line to the second line. In this chapter, we are particularly interested in the marginal radial distributions $\mathcal{P}_\alpha(r, t) = \int_0^{2\pi} d\phi r P_\alpha(\vec{r}, t)$ [where ϕ denotes the polar angle] in the presence of the resetting. It is easy to see that the marginal radial distribution $\mathcal{P}_\alpha(r, t)$ also follow renewal equations of the same structure,

$$\mathcal{P}_\alpha(r, t) = e^{-\alpha t} \mathcal{P}(r, t) + \alpha \int_0^t ds e^{-\alpha s} \mathcal{P}(r, s), \quad (6.3)$$

where the distribution in the absence of resetting $\mathcal{P}(r, s)$ was already obtained in Chapter 2 [see Eq. (2.63)]. The stationary distribution is obtained by taking the $t \rightarrow \infty$ limit in the above equation, where the first term on the rhs goes to zero and we have,

$$\mathcal{P}_\alpha^s(r) = \int_0^\infty ds e^{-\alpha s} \mathcal{P}(r, s) = \frac{\alpha}{v_0} e^{-(\alpha+\gamma)\frac{r}{v_0}} + H(r) \quad (6.4)$$

$$\text{where } H(r) = \frac{\alpha\gamma r}{v_0} \int_{r/v_0}^\infty ds e^{-(\alpha+\gamma)s} \frac{\exp\left(\frac{\gamma}{v_0} \sqrt{v_0^2 s^2 - r^2}\right)}{\sqrt{v_0^2 s^2 - r^2}} \quad (6.5)$$

where we have used the exact expression of $\mathcal{P}(r, s)$ from Chapter 2. Using two successive variable transforms, $y = v_0 s / r$ and $\omega = y - 1$, it reduces to,

$$H(r) = \frac{1}{v_0} e^{-(\alpha+\gamma)\frac{r}{v_0}} \int_0^\infty d\omega e^{-(\alpha+\gamma)\frac{r\omega}{v_0}} \frac{\exp\left(-\frac{r\gamma}{v_0} \sqrt{\omega(\omega+2)}\right)}{\sqrt{\omega(\omega+2)}}. \quad (6.6)$$

This integral can be computed exactly by using the series expansion of the second exponential in the integrand, and integrating each term separately thereafter. This exercise leads to an exact expression for $H(r)$ as a sum of an infinite series,

$$H(r) = \frac{\sqrt{\pi}}{v_0} \sum_{n=0}^\infty \frac{B_n}{n!} \left(\gamma \sqrt{\frac{2r}{(\alpha+\gamma)v_0}} \right)^n K_{\frac{n}{2}} \left(\frac{(\alpha+\gamma)r}{v_0} \right). \quad (6.7)$$

where, $K_\nu(z)$ is the modified Bessel function of the second kind [94] and,

$$B_n = \frac{\sec \frac{n\pi}{2}}{\Gamma(\frac{1-n}{2})} = \begin{cases} \frac{1}{\pi} (\frac{n-1}{2})! & \text{for odd } n \\ \frac{1}{\sqrt{\pi}} \frac{n!}{2^n (n/2)!} & \text{for even } n. \end{cases} \quad (6.8)$$

Finally, we have the stationary radial distribution,

$$\mathcal{P}_\alpha^s(r) = \frac{\alpha}{v_0} e^{-(\alpha+\gamma)\frac{r}{v_0}} + \frac{\alpha\gamma\sqrt{\pi}r}{v_0^2} \sum_{n=0}^{\infty} \frac{B_n}{n!} \left(\frac{2\gamma^2 r}{(\alpha+\gamma)v_0} \right)^{\frac{n}{2}} K_{\frac{n}{2}} \left(\frac{(\alpha+\gamma)r}{v_0} \right), \quad (6.9)$$

where B_n is given by Eq. (6.8). Figure 6.1 (a) compares this prediction with the data obtained from numerical simulations for $\mathcal{P}_\alpha^s(r)$ for different values of α for a fixed γ ; the solid lines correspond to the analytical prediction Eq. (6.9), with the sum truncated after a few terms, and the symbols correspond to the numerical simulation results. This Figure illustrates that the series converges pretty fast, and can be used to compute stationary distribution at any r to arbitrary accuracy.

It is interesting to look at the asymptotic behavior of $\mathcal{P}_\alpha^s(r)$. Using the series expansion of $K_{\frac{n}{2}}(z)$ near $z = 0$, we get, for small r ,

$$\mathcal{P}_\alpha^s(r) = \frac{\alpha}{v_0} - \frac{\alpha\gamma}{v_0^2} r \ln r + \frac{\alpha\gamma r}{v_0^2} \left(\gamma \ln \frac{\alpha}{2v_0} + \gamma(\Gamma_E + 1) + \alpha \right) + O(r^2 \ln r), \quad (6.10)$$

where Γ_E is the Euler-Mascheroni constant. This is compared with the numerical simulations in Figure 6.1(b).

Next we look at the large r behavior of the stationary state distribution. It is difficult to extract the large r behavior directly from Eq. (6.9); instead we recast Eq. (6.6) in a different form,

$$H(r) = \frac{1}{v_0} e^{-(\alpha+\gamma)r} \int_0^\infty d\omega \frac{e^{-\frac{r}{v_0}\Lambda(\omega)}}{\sqrt{\omega(\omega+2)}},$$

where $\Lambda(\omega) = (\alpha+\gamma)\omega - \gamma\sqrt{\omega(\omega+2)}$. It is straightforward to check that $\Lambda(\omega)$ is a non-monotonic function of ω with a minimum at $\omega_0 = \frac{\alpha+\gamma}{\sqrt{\alpha^2+2\alpha\gamma}} - 1$. Thus, for large r , the above

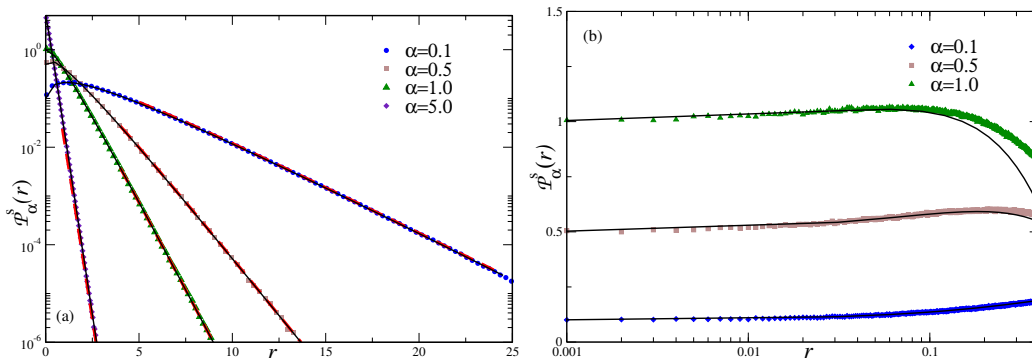


Figure 6.1: Plot of stationary state radial distribution $P_\alpha^s(r)$ as a function of r , different values of α and a fixed $\gamma = 1$. The symbols in both panels correspond to the data obtained from numerical simulations. In (a), the solid black lines are from the numerical evaluation of the series sum Eq. (6.9) keeping upto $n = 60$ terms while the red dashed lines represent the large deviation function as given by Eq. (6.12). (b) shows the same distribution zoomed in near $r = 0$ along with the theoretical prediction in Eq. (6.10) (solid black lines).

integral can be evaluated using saddle point method (See 9.8), which yields

$$H(r) \approx \left(\frac{2\pi}{v_0 r \sqrt{\alpha^2 + 2\alpha\gamma}} \right)^{1/2} \exp \left[-\frac{r}{v_0} \sqrt{\alpha^2 + 2\alpha\gamma} \right]. \quad (6.11)$$

Since this exponential decays much slower than the first term in Eq. (6.5), the large r behavior of the radial distribution is dominated by this term, and we have,

$$\mathcal{P}_\alpha^s(r) \approx \frac{\alpha\gamma}{v_0^{3/2}} \left(\frac{2\pi r}{\sqrt{\alpha^2 + 2\alpha\gamma}} \right)^{1/2} \exp \left[-\frac{r}{v_0} \sqrt{\alpha^2 + 2\alpha\gamma} \right]. \quad (6.12)$$

This exponential decay for large r is compared with the results from numerical simulations in Figure 6.1(a) which shows an excellent agreement.

It is interesting to compare the stationary state distribution obtained here with those studied previously in the context of diffusion [124]. For a passive diffusive particle in $d = 2$, it has been shown that the presence of stochastic resetting results into a radial distribution which vanishes at the origin $\sim r \ln r$, while showing an exponential decay for large r . In contrast, here we see that, the introduction of stochastic resetting to an underlying 2d RTP dynamics leads to a finite value of the radial probability density at $r = 0$ [see Eq. (6.10)]. Physically, this difference can be understood from the following argument. The leading

contribution to the radial position distribution near the origin comes from the trajectories which undergo none or very few tumblings between two consecutive resetting events. For example, the non-zero contribution at the origin comes from the first term of Eq. (2.63) which is actually the position distribution of the free RTP in the short time active regime. Such trajectories, with small number of tumblings carry the signature of the active nature of the underlying system, which in turn shows up in the stationary state distribution in the presence of resetting. On the other hand, the distribution decays exponentially, similar to a Brownian particle, with a characteristic decay length $\sqrt{\alpha^2 + 2\alpha\gamma}$. This exponent is identical to the one obtained in Ref. [132] in the context of resetting of 1d RTP, and thus appears to be robust in any dimensions.

It is useful to consider some special limiting scenarios.

- *Diffusive limit:* In the absence of resetting, the RTP dynamics reduces to ordinary diffusion in the limit $\gamma \rightarrow \infty$, $v_0 \rightarrow \infty$ but with a finite ratio $\frac{v_0^2}{2\gamma} = D_{\text{eff}}$ which plays the role of an effective diffusion constant. It is easy to see that, in this limit, both the radial and x -marginal distributions for the RTP reduce to the corresponding known results for diffusive particles. For example, using the limit $\gamma \rightarrow \infty$, $v_0 \rightarrow \infty$, and finite D_{eff} in Eq. (6.5) we have,

$$\mathcal{P}_\alpha^s(r) = \frac{\alpha r}{2D_{\text{eff}}} \int_0^\infty \frac{ds}{s} e^{-\alpha s} \exp\left(-\frac{r^2}{4D_{\text{eff}} s}\right) = \frac{\alpha r}{D_{\text{eff}}} K_0\left(\sqrt{\frac{\alpha}{D_{\text{eff}}}} r\right), \quad (6.13)$$

which is identical to the result obtained in Ref. [124].

- *Small flip rate $\gamma \rightarrow 0$:* In this limit the second term in the expression for the radial distribution Eq. (6.5) goes to zero. Thus we find that the stationary state distributions decay exponentially with a decay constant $\frac{v_0}{\alpha}$ which is the mean distance traveled by the particle between two consecutive resetting events when there are no flips.

It is also interesting to look how the system relaxes to the stationary state discussed above.

6.2 Relaxation to stationary state and position distributions

It is interesting to look at how the non-equilibrium stationary state as described in the previous section is attained. In this section we look at how the radial and marginal position distributions relax to the respective stationary state distributions.

We start from the renewal equation Eq. (6.3), using Eq. (2.63), we have the full time-dependent radial distribution,

$$\mathcal{P}_\alpha(r, t) = e^{-(\alpha+\gamma)t} \delta(r - v_0 t) + \frac{\gamma r e^{-t(\alpha+\gamma-\gamma\sqrt{1-(r/v_0 t)^2}}}{v_0^2 t \sqrt{1-(r/v_0 t)^2}} + \frac{\alpha}{v_0} e^{-(\alpha+\gamma)r/v_0} + H(r, t) \quad (6.14)$$

where,

$$H(r, t) = \frac{\alpha\gamma r}{v_0^2} \int_{\frac{r}{v_0}}^t ds \frac{e^{-s(\alpha+\gamma-\gamma\sqrt{1-(r/v_0 s)^2}}}{s\sqrt{1-(r/v_0 s)^2}}. \quad (6.15)$$

To evaluate the integral in $H(r, t)$, we make a change of variable $s = t\tau$ and obtain,

$$\begin{aligned} H(r = zv_0 t, t) &= \frac{\alpha\gamma z v_0 t}{v_0^2} \int_z^1 d\tau e^{-(\alpha+\gamma)t\tau} \frac{\exp\left[\gamma t \sqrt{\tau^2 - z^2}\right]}{\sqrt{\tau^2 - z^2}} \\ &= \frac{\alpha\gamma z v_0 t}{v_0^2} \int_z^1 d\tau e^{-t\phi(z, \tau)} \frac{1}{\sqrt{\tau^2 - z^2}} \end{aligned} \quad (6.16)$$

where $z = r/v_0 t$, ($z \in [0, 1]$) and $\phi(z, \tau) = (\alpha + \gamma)\tau - \gamma\sqrt{\tau^2 - z^2}$. Now at very large t and fixed z we can estimate $H(r, t)$ by saddle point method (worked out in details in 9.8). The dominant contribution to the integral comes from the minimum of $\phi(z, \tau)$ at $\tau_0 = \frac{z(\alpha+\gamma)}{\sqrt{\alpha^2+2\alpha\gamma}}$.

Now there can be two possibilities:

(I) $\tau_0 < 1$: In this case the minimum of $\phi(z, \tau)$ lies within the limits of integration ($z, 1$) (note that τ_0 is always greater than z). Thus for $\tau_0 < 1$,

$$H(r = zv_0 t, t) \approx \frac{\alpha\gamma\sqrt{zv_0 t}\sqrt{\pi/2}}{v_0^2(\alpha^2 + 2\alpha\gamma)^{1/4}} e^{-zt\sqrt{\alpha^2+2\alpha\gamma}} \quad (6.17)$$

We drop the prefactors going forward as we are only interested in the behavior at the tails.

Thus from Eq. (6.3) and Eq. (6.14), we have for the region $\tau_0 < 1$, *i.e.*, for $z < \frac{\sqrt{\alpha^2 + 2\alpha\gamma}}{\alpha + \gamma}$,

$$\mathcal{P}_\alpha(z, t) \sim \exp \left[-z t \sqrt{\alpha^2 + 2\alpha\gamma} \right] \quad (6.18)$$

Note that the third term on the rhs of Eq. (6.14) has been dropped as the corresponding length scale $\frac{v_0}{\alpha + \gamma}$ is much smaller than that in $H(r, t)$ which is $v_0 \sqrt{\alpha^2 + 2\alpha\gamma} / (\alpha + \gamma)$.

(II) $\tau_0 > 1$: The minimum of $\phi(z, \tau)$ lies outside the limits of integration, the minimum value of $\phi(z, \tau)$ within the integration limits is at the boundary $\tau = 1$. Thus the dominant contribution to the integral comes from near $\tau = 1$,

$$H(r = z v_0 t, t) \sim e^{-(\alpha + \gamma)t + \gamma t \sqrt{1 - z^2}}. \quad (6.19)$$

This is of the same order as the second term on the rhs of Eq. (6.14), which indicate to the fact that this contribution physically correspond to the trajectories that have undergone none or very few resets until time t . So for the region $\tau_0 > 1$, *i.e.*, $z > \frac{\sqrt{\alpha^2 + 2\alpha\gamma}}{\alpha + \gamma}$

$$\mathcal{P}_\alpha(z, t) \sim \exp \left[-(\alpha + \gamma)t + \gamma t \sqrt{1 - z^2} \right] \quad (6.20)$$

Combining the above equations, we have, $\mathcal{P}_\alpha(z, t) \sim \exp[-t\psi(z)]$, with

$$\psi(z) = \begin{cases} z \sqrt{\alpha^2 + 2\alpha\gamma} & \text{for } z < \frac{\sqrt{\alpha^2 + 2\alpha\gamma}}{\alpha + \gamma} \\ (\alpha + \gamma) - \gamma \sqrt{1 - z^2} & \text{for } z > \frac{\sqrt{\alpha^2 + 2\alpha\gamma}}{\alpha + \gamma}. \end{cases} \quad (6.21)$$

Writing in terms of the original variable $r = z v_0 t$, this translates to,

$$\mathcal{P}_\alpha(r, t) \sim \begin{cases} e^{-\frac{r}{v_0} \sqrt{\alpha^2 + 2\alpha\gamma}} & \text{for } r < r_0(t) \\ e^{-(\alpha + \gamma)t + \gamma \sqrt{t^2 - (r/v_0)^2}} & \text{for } r > r_0(t). \end{cases} \quad (6.22)$$

where $r_0(t) = \frac{\sqrt{\alpha^2 + 2\alpha\gamma}}{\alpha + \gamma} t$. Thus we see that at a large time t , the position distribution for the region $r < r_0(t)$ is time independent and has the exact same form as the stationary state large deviation function in Eq. (6.12), while for the region $r > r_0(t)$ the distribution is time dependent. Since $r_0(t)$ is linear in t , the region which has reached stationary state grows at a constant speed as shown in Figure 6.2(a). The relaxation of the position distribution

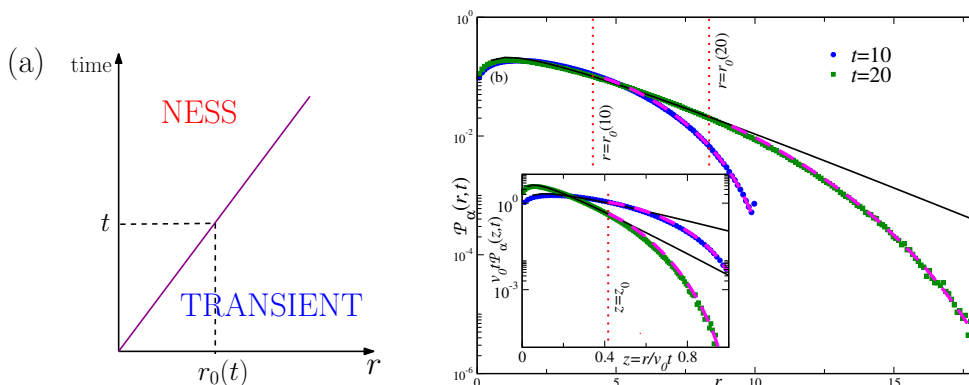


Figure 6.2: Approach to the non-equilibrium stationary state: (a) Diagrammatic representation of how the relaxation occurs in the r -space; (b) Comparison of the numerical simulation results with our analytical predictions for $\gamma = 1$ and $\alpha = 0.1$. The symbols represent the data obtained from numerical simulation and the solid black lines indicate the large deviation form Eq. (6.12). The dashed magenta lines represent the transient part of the distribution as given in Eq. (6.21) and Eq. (6.22) with proper prefactors (see 9.89). The main plot shows the radial distribution; the dashed red vertical lines indicate $r = r_0(t)$ for two values of $t = 10, 20$. The plot in the inset shows the distribution in terms of the scaled variable z , the dashed red vertical line denotes $z = \frac{\sqrt{\alpha^2 + 2\alpha\gamma}}{\alpha + \gamma}$.

calculated from the numerical simulation is compared with our results Eq. (6.22) in Figure 6.2(b).

6.3 First Passage Properties

In this section we discuss the probability of survival of an RTP $S_\alpha(x_0, t)$, starting from a position $(x_0, 0)$ at $t = 0$ and undergoing stochastic resetting (by the same protocol, as considered in the previous section), in the presence of an absorbing boundary at $x = x_{\text{abs}}$. In the context of a search process $x = x_{\text{abs}}$ is the target; and an event in which the RTP reaches the line $x = x_{\text{abs}}$ corresponds to the searcher successfully locating the target.

Even in the absence of resetting, the exact calculation of the survival probability of an RTP is difficult in dimensions greater than one because the orientation is a continuous variable. However, for the special case $x_0 = x_{\text{abs}} = 0$ the survival probability $S(0, t)$ of a d -dimensional RTP was calculated in [62],

$$S(0, t) = \frac{e^{-\gamma t/2}}{2} \left[I_0 \left(\frac{\gamma t}{2} \right) + I_1 \left(\frac{\gamma t}{2} \right) \right]. \quad (6.23)$$

In the following, we use the above result to investigate the survival probability for a two-dimensional RTP under resetting. We begin by writing down a renewal equation for the survival probability $S_\alpha(x_0, t)$ for the protocol of resetting the position of the particle to the some point (x_r, y_r) and randomizing the orientation (velocity) at each reset event.

$$S_\alpha(x_0, t) = e^{-\alpha t} S(x_0, t) + \alpha \int_0^t ds e^{-\alpha s} S(x_r, s) S_\alpha(x_0, t - s). \quad (6.24)$$

where S denotes the survival probability without resetting. The first term on the RHS is due to the trajectories which have not undergone resetting. The second term, on the other hand, integrates over all those survived trajectories where the last resetting occurred at a time $t - s$, which accounts for the factor $\alpha e^{-\alpha s}$. We consider $x_{\text{abs}} = x_r = 0$. Taking a Laplace transform, $\tilde{S}_\alpha(x, s) = \int_0^\infty dt e^{-st} S_\alpha(x, t)$, on both sides of Eq. (6.24) and setting the initial position $x_0 = 0$, we get,

$$\tilde{S}_\alpha(0, s) = \frac{\tilde{S}_0(0, \alpha + s)}{1 - \alpha \tilde{S}_0(0, \alpha + s)}. \quad (6.25)$$

We are now in a position to use Eq. (6.23). Taking a Laplace transform $t \rightarrow s$, we have

$$\tilde{S}_0(0, s) = \frac{1}{\sqrt{s(\gamma + s)}}. \quad (6.26)$$

Putting this is in Eq. (6.25), we get the survival probability in s -space as

$$\tilde{S}_\alpha(0, s) = \frac{1}{s + \sqrt{(s + \alpha)(s + \alpha + \gamma)}}. \quad (6.27)$$

To invert the Laplace transform we need to write the corresponding Bromwich integral,

$$S_\alpha(0, t) = \frac{1}{2\pi i} \int_{c-i\infty}^{c+i\infty} ds \frac{e^{st}}{s + \sqrt{(s + \alpha)(s + \alpha + \gamma)}} \quad (6.28)$$

where c is chosen such that all the singularities of the integrand lie to the left of the line $\text{Re}[s] = c$. Clearly, the above integral involves a branch-cut along the real s -axis in addition

to a simple pole at $s = -\frac{\alpha(\gamma+\alpha)}{2\alpha+\gamma}$. Taking into account all the contributions, we finally have,

$$S_\alpha(0, t) = \frac{2\alpha(\gamma + \alpha)}{(\gamma + 2\alpha)^2} e^{-\frac{\alpha(\gamma+\alpha)}{2\alpha+\gamma}t} + \frac{e^{-\alpha t}}{\pi} \int_0^\gamma du \frac{e^{-ut} \sqrt{u(\gamma-u)}}{\alpha^2 + (2\alpha + \gamma)u} \quad (6.29)$$

The second term involves a convergent integral, which unfortunately does not yield any closed form solution. If we write the numerator of the second term as an infinite series and do the u -integral we have the full survival probability as,

$$S_\alpha(0, t) = \frac{2\alpha(\gamma + \alpha)}{(\gamma + 2\alpha)^2} e^{-\frac{\alpha(\gamma+\alpha)}{2\alpha+\gamma}t} + \frac{e^{-(\alpha+\gamma)t} \gamma^2}{2\alpha^2 \sqrt{\pi}} \sum_{n=0}^{\infty} \left(\frac{2\gamma(\alpha + \gamma)}{\alpha^2} \right)^n \Gamma \left[n + \frac{3}{2} \right] {}_1\tilde{F}_1 \left[\frac{3}{2}, n + 3, \gamma t \right] \quad (6.30)$$

where ${}_1\tilde{F}_1 [a, b, z]$ is the regularized Kummer function [94]. Using the asymptotic expansion of ${}_1\tilde{F}_1 [a, b, z]$ for small z , [94] we have for small t ,

$$S_\alpha(0, t) = \frac{1}{2} - \frac{1}{8}(2\alpha + \gamma)t + O(t^2) \quad (6.31)$$

At $t = 0$, the survival probability has the expected value $\frac{1}{2}$, since we start with uniform initial conditions (*i.e.*, the initial orientation is chosen uniformly from $[0, 2\pi]$). Again for large t , we can use the asymptotic expansion of ${}_1\tilde{F}_1 [a, b, z]$ for large z [94]. This yields for large t

$$S_\alpha(0, t) = \frac{2\alpha(\gamma + \alpha)}{(\gamma + 2\alpha)^2} e^{-\frac{\alpha(\gamma+\alpha)}{2\alpha+\gamma}t} + O(e^{-\alpha t}). \quad (6.32)$$

Thus, at large times the survival probability decays as,

$$S_\alpha(0, t) \sim \exp \left[-\frac{\alpha(\gamma + \alpha)}{2\alpha + \gamma} t \right]. \quad (6.33)$$

Equation Eq. (6.29) is compared to numerical simulations in Figure 6.3(a). They show excellent match.

A related observable is the first passage time, which is the time at which the particle reaches $x = x_{\text{abs}}$ for the first time. The corresponding first passage probability $F_\alpha(x_0, t)dt$ denotes the probability that the particle, starting at $x = x_0$ is absorbed at $x = x_{\text{abs}}$ during

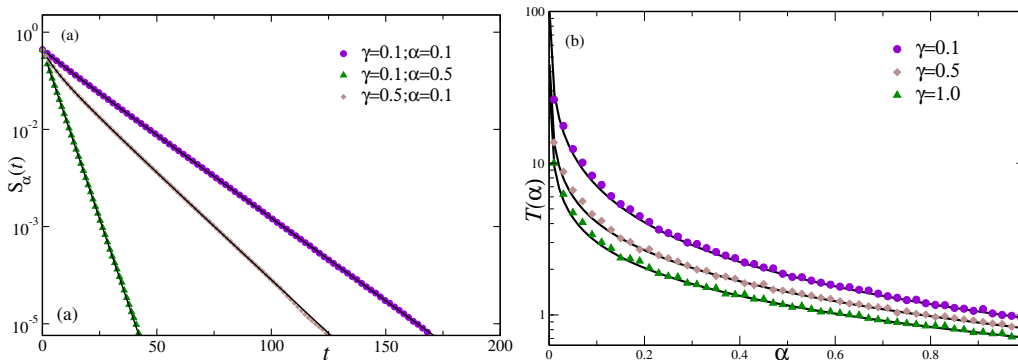


Figure 6.3: Plot for $x_{\text{abs}} = x_r = 0$. (a) Survival probability: Colored points denote results obtained from numerical simulation, while solid black lines correspond to Eq. (6.29). (b) Mean first passage time: Colored points denote results obtained from numerical simulation, while solid black lines correspond to Eq. (6.35).

the time interval $[t, t + dt]$. It is the time derivative of survival probability.

$$F_\alpha(x_0, t) = -\frac{\partial}{\partial t} S_\alpha(x_0, t) \quad (6.34)$$

The mean first passage(MFPT) time is defined as the mean time taken to be absorbed and is thus given by,

$$T_\alpha(x_0) = \int_0^\infty dt t F_\alpha(x_0, t) = \int_0^\infty dt S_\alpha(x_0, t), \quad (6.35)$$

where, to obtain the second equation, we have used $F_\alpha(x_0, t)$ from Eq. (6.34) and then performed an integration by parts. We also used the fact that $S_\alpha(x_0, \infty) \rightarrow 0$. The RHS of equation Eq. (6.35) is actually the Laplace transform $\tilde{S}_\alpha(x_0, s = 0)$. For $x_0 = 0$ we can use Eq. (6.27) to get the MFPT. Thus we have,

$$T_\alpha(0) = \frac{1}{\sqrt{\alpha(\alpha + \gamma)}} \quad (6.36)$$

This diverges as $\alpha \rightarrow 0$ and decreases monotonically with α . This is due to the fact that every time we reset the particle back to the origin its orientation is chosen uniformly between $[0, 2\pi]$, so the probability that it gets absorbed at a reset event is always half. The result obtained in Eq. (6.36) is compared with numerical simulations in 6.3(b).

It is interesting to see what happens when we push the absorbing boundary parallel to

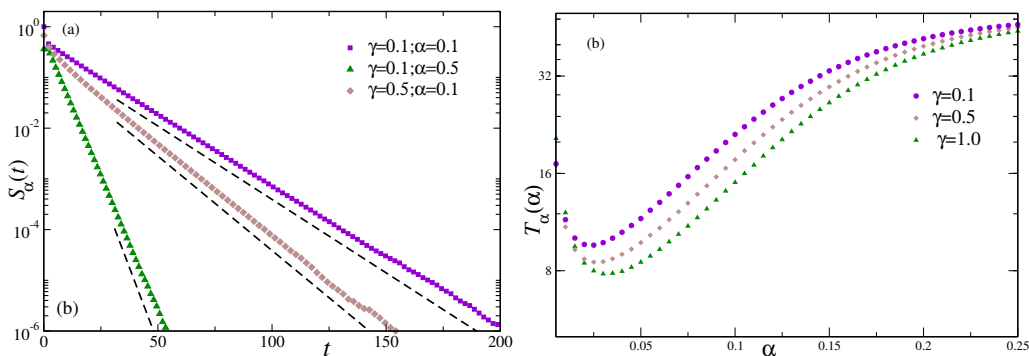


Figure 6.4: Plot for $x_{\text{abs}} = -0.1$ and $x_r = 0$: (a) Survival probability: Colored points denote results obtained from numerical simulation, black dashed line are the exponential tails as denoted by Eq. (6.33). (b) Mean first passage time: Colored points are obtained from numerical simulation. The existence of a minimum in all the curves clearly indicate the fact that the mean first passage time is minimized for an optimal value of the resetting rate α .

y -axis to some negative x (*i.e.*, $x_{\text{abs}} < x_r = 0$). The problem with solving the backward FP equation does not allow us to analytically find how the survival probability will change in that case. However numerical simulations with small negative x_{abs} indicate interesting results. Figure 6.4(a) suggests that the decay of the survival probability at large times is still exponential with the same decay exponent $\frac{\alpha(\gamma+\alpha)}{2\alpha+\gamma}$ as in Eq. (6.33). The mean first passage time on the other hand shows a non-monotonic behavior with the resetting rate, Figure 6.4(b). Starting from $\alpha = 0$, T_α first decreases, reaches a minimum and then goes up again. This is shown in Figure 6.4(b). This can be explained in the context of a search process as follows. In the absence of resetting the time taken by the RTP to find the target $x = -|x_{\text{abs}}|$ is infinite, however as we increase the resetting rate α to the origin, the RTP comes back to the origin and starts a fresh search. The probability that it finds the target increases and the mean time becomes finite. But if we keep on increasing α , then the RTP resets even before it can reach the target, thus the mean first passage time increases. This suggests that if an RTP undergoes resetting and the resetting position and the absorbing boundary are different then there is an optimal resetting rate at which the mean first passage time is minimized.

6.4 Summary

In this chapter we discussed the effect of stochastic resetting on an RTP in two spatial dimensions: the RTP starts from the origin with some random orientation in $[0, 2\pi]$ and at a constant rate restarts the process with the same initial conditions. A stationary state is attained in the long time limit. We calculate the exact stationary state distribution which has exponentially decaying tails, similar to a passive Brownian particle, albeit with a different decay length. The behavior of the stationary distributions near the origin is governed by the activity where we see a non-vanishing probability density for the radial distribution. There is also a dynamical transition in relaxation to this stationary state—at a finite time, there is a domain in space inside which the stationary has been attained while regions outside it are still time-dependent. We show that the boundary of this domain propagates linearly with time, so at very large times we expect the distribution to attain stationary-state. The presence of stochastic resetting is known to non-trivially change the first passage properties of diffusion processes. In this chapter, we show how the survival probability of the RTP in the presence of an absorbing boundary changes when stochastic resetting is introduced. In particular, we investigate two scenarios, (i) when the particle is reset to a position very close to the absorbing boundary, and (ii) when the resetting position is a finite distance away from the absorbing boundary. We calculate the survival probability and show that it decays exponentially at large times. We also discuss the dependence of the mean first passage time on the resetting rate. We show that when the resetting position coincides with the absorbing boundary position, the MFPT monotonically decreases with increasing resetting rate, irrespective of the value of the flipping rate. On the other hand, when the particle is reset to some position away from the absorbing boundary, the MFPT shows a non-monotonic behavior; it reaches a minimum at an optimal resetting rate.

Chapter 7

Active reservoirs: microscopic model and energy transport

We have seen that the effective motion of a colloidal particle in an equilibrium medium can be modeled by a Langevin equation with a constant dissipation and δ -correlated noise. What happens if the medium is nonequilibrium, for example, made up of active particles? It turns out that such nonequilibrium reservoirs exhibit many unusual features compared to equilibrium thermal ones. For example, tracer particles immersed in such reservoirs exhibit many unusual features including violation of the equilibrium fluctuation relations, emergence of negative friction, modification of equipartition theorem and anomalous relaxation dynamics. At this point, a natural and obvious question is to ask, what happens to the energy transport through an extended system when it is connected to active reservoirs at the two ends instead of the usual thermal reservoirs, where energy always flows from the hotter to the colder reservoir. In this chapter, we first study the dynamics of a tracer particle whose position is coupled to those of overdamped active particles via harmonic springs. In the later part of this chapter, we ask the question of activity driven energy transport in a simple setting—an ordered chain of harmonic oscillators connected to two active reservoirs at the two ends.

The chapter is organized as follows: In Sec. 7.1, we compute the reduced dynamics of a tracer coupled to active particles. In Sec. 7.1, we introduce a simple set-up to study the activity driven energy transport. In Secs. 7.3 and 7.4, we discuss the average stationary current flowing through the system and average kinetic temperature profile of the system in the stationary state. We summarize our results in Sec. 7.5.

7.1 Active reservoir model

Let us consider a particle of mass M coupled elastically to N active particles via isotropic harmonic springs of spring constant k each. The model is inspired by the famous Caldeira-

Leggett model, used to study quantum Brownian motion [133, 134]. Moreover, more complicated non-quadratic interactions can be well approximated by harmonic interactions near the equilibrium (minima of the interaction potential). In this chapter, we consider the dynamics along one direction only; however, generalization to higher dimensions is straightforward. The equations of motion of the combined system are given by,

$$M\ddot{x}(t) = -k \sum_i \left(x(t) - y_i(t) \right) \quad (7.1)$$

$$\dot{y}_i(t) = -\lambda \left(y_i(t) - x(t) \right) + u(t) \quad i = 1, 2, \dots, N \quad (7.2)$$

where x denotes the tracer displacement while y_i denotes the displacement of the i th active particle; λ is the spring constant scaled by the damping coefficient; and $u(t)$ denotes the propulsion velocity of the active particles. The formalism discussed below, holds for any microscopic realization of the propulsion velocity. We will first derive the equations of motion of the tracer by explicitly integrating out the environmental degrees of freedom $y_i(t)$. To this end, we first note that the equation of motion of the bath particles Eq. (7.2) are ordinary first order linear differential equations with inhomogeneous terms. It has a general solution,

$$y_i(t) = y_i(0)e^{-\lambda t} + e^{-\lambda t} \int_0^t ds e^{\lambda s} \left(\lambda x(s) + u(s) \right), \quad (7.3)$$

where $\lambda = k/\gamma$. Putting Eq. (7.3) in Eq. (7.1), we get,

$$M\ddot{x}(t) = ke^{-\lambda t} \sum_i y_i(0) - N \left[kx(t) - k\lambda e^{-\lambda t} \int_0^t ds e^{\lambda s} x(s) - ke^{-\lambda t} \int_0^t ds e^{\lambda s} u(s) \right] \quad (7.4)$$

Defining $m = M/N$ as a reduced effective mass, we get,

$$m\ddot{x}(t) = ke^{-\lambda t} \frac{\sum_i y_i(0)}{N} - kx(t) + k\lambda e^{-\lambda t} \int_0^t ds e^{\lambda s} x(s) + ke^{-\lambda t} \int_0^t ds e^{\lambda s} u(s). \quad (7.5)$$

Thus, the effective dynamics of the tracer depend on the initial condition of the bath particles in the form of a time-dependent velocity that decays exponentially and hence does not affect the long time dynamics of the tracer. Moreover, if we consider that the bath particles are isotropically distributed in the medium, then in a suitable coordinate system, the contribution

of the first term on the right-hand side of the above equation can always be taken to be zero. Thus, we have,

$$m\ddot{x}(t) = -kx(t) + k\lambda e^{-\lambda t} \int_0^t ds e^{\lambda s} x(s) + ke^{-\lambda t} \int_0^t ds e^{\lambda s} u(s). \quad (7.6)$$

Performing an integration by parts on the second integral on the rhs of the above equation, we arrive at a generalized Langevin equation for the tracer dynamics,

$$m\ddot{x}(t) = - \int_0^t ds \Gamma(t-s) \dot{x}(s) + f(t), \quad (7.7)$$

where

$$\Gamma(\tau) = ke^{-\lambda\tau} \quad (7.8)$$

denotes the memory kernel and

$$f(t) = k \int_0^t ds e^{-\lambda(t-s)} u(s) \quad (7.9)$$

denotes the effective noise experienced by the tracer. Note that, since the environmental particles are treated effectively as independent, it is sufficient to consider the coupled dynamics of only one active or passive particle with the tracer.

To find the autocorrelations of this effective noise $f(t)$, we need to consider some microscopic model for $u(t)$. As we have discussed in chapter 4, all the popular active particle models have an exponential autocorrelation in the stationary state. Accordingly, we choose $u(t)$ such that it has a zero mean and exponential autocorrelation,

$$\langle u(t)u(t') \rangle = v_0^2 \exp(-\alpha|t-t'|). \quad (7.10)$$

Using Eq. (7.9) it follows that the effective noise autocorrelation of the tracer is given by the double integral,

$$\langle f(t)f(t') \rangle = k^2 e^{-2\lambda t} \int_0^t ds_1 \int_0^{t'} ds_2 e^{\lambda(s_1+s_2)} \langle u(s_1)u(s_2) \rangle. \quad (7.11)$$

Upon doing the integrals with the explicit form of the correlations Eq. (7.10), we finally get (for $\alpha \neq \lambda$),

$$\langle f(t)f(t') \rangle = \frac{v_0^2 k^2}{\lambda^2 - \alpha^2} \left[e^{-\alpha|t-t'|} - \frac{\alpha}{\lambda} e^{-\lambda|t-t'|} - e^{-(\lambda t + \alpha t')} - e^{-(\lambda t' + \alpha t)} + \frac{(\alpha - \lambda)}{\lambda} e^{-\lambda(t+t')} \right]. \quad (7.12)$$

The above expression again clearly indicates a violation of FDT. Moreover at finite times, larger than the α^{-1} and λ^{-1} , the last two terms in the above equation go to zero and the effective noise correlation reduces to,

$$\langle f(t)f(t') \rangle = \frac{v_0^2 k^2}{\alpha^2 - \lambda^2} \left[\frac{\alpha}{\lambda} e^{-\lambda|t-t'|} - e^{-\alpha|t-t'|} \right] = \frac{\alpha k v_0^2}{\lambda(\alpha^2 - \lambda^2)} \Gamma(|t - t'|) - \frac{v_0^2 k^2}{\alpha^2 - \lambda^2} e^{-\alpha|t-t'|}. \quad (7.13)$$

This is the modified Fluctuation dissipation relation followed by a tracer elastically coupled to an active environment. For $\alpha = \lambda$, one needs to do the integrals in Eq. (7.11) starting with $\alpha = \lambda$. The stationary noise correlation in that case is given by,

$$\langle f(t)f(t') \rangle = \frac{v_0^2 k^2}{2\lambda} |t - t'| e^{-\lambda|t-t'|} \quad (7.14)$$

It is important to note two limits of Eq. (7.13):

- Large spring constant ($k, \lambda \gg \alpha$): In this limit the noise correlation Eq. (7.13) reduces to,

$$\langle f(t)f(t') \rangle = a_0^2 e^{-\alpha|t-t'|}, \quad (7.15)$$

where $a_0 = v_0 k / \lambda$. Additionally, in this limit, the memory kernel Eq. (7.8) also reduces to a delta function,

$$\Gamma(\tau) \approx \gamma \delta(\tau), \quad (7.16)$$

which leads to the effective equation motion of the tracer to be,

$$m\ddot{x}(t) = -\gamma\dot{x}(t) + f(t). \quad (7.17)$$

where $f(t)$ is just an exponentially correlated colored noise, the same as the autocorrelation time as that of the active particles of the environment. The form of Eq. (7.17) has been used in previous works [135, 136, 16], the emergence of the same from a microscopic model of active environment justifies these phenomenological models. Moreover, Eq. (7.17) is familiar with the equation of standard underdamped active particles. [87]. Usually, a problem for studying single active particle trajectories is that the active particles are small in size and have a finite lifetime. The result, that, the motion of a tracer particle in an environment of active particles emulates the motion of those active particles, might be of great help to the experimentalists studying single active particle trajectories.

- Passive limit: This limit corresponds to $\alpha \rightarrow \infty$, $v_0 \rightarrow \infty$, such that $D_{\text{eff}} = v_0^2/(\alpha)$ is finite. Putting these limits in the noise correlation Eq. (7.12), we obtain an effective passive limit of the active environment,

$$\langle \Omega^a(t)\Omega^a(t') \rangle = K_B T_{\text{eff}} \Gamma(t-t') + K_B T_{\text{eff}} e^{-\lambda(t+t')}, \quad (7.18)$$

where we the effective temperature is given by, $D_{\text{eff}} = K_B T_{\text{eff}}/\gamma$. The above equation in the stationary state reduces to the well-known equilibrium form of the FDT,

$$\langle \Omega^a(t)\Omega^a(t') \rangle = K_B T_{\text{eff}} \Gamma(t-t'). \quad (7.19)$$

Next we will discuss the transport properties of an extended system connected to active reservoirs. The usual theoretical attempts to study transport properties often rely on the study of simple, yet analytically tractable model systems. A paradigmatic example is a chain of harmonic oscillators connected to thermal reservoirs of different temperatures at the two ends, first studied by Rieder, Lieb, and Lebowitz (RLL) in a seminal work. They showed that this system reaches a nonequilibrium stationary state carrying a thermal current, which

is proportional to the temperature difference of the thermal reservoirs and survives in the thermodynamic limit. They also found that the average kinetic temperature profile of the oscillators is flat in the bulk and is given by the arithmetic mean of the reservoir temperatures. Having understood the behavior of Hamiltonian particles connected to active particles, we study the problem of ‘activity driven transport’ in the next section using a setup similar to the RLL model.

7.2 Model for studying active transport

We consider a one-dimensional chain of N particles with fixed boundary conditions, each with mass m , connected by harmonic springs of stiffness k , attached to two different active reservoirs at the boundaries [see Fig. 7.1]. This setup is similar to the famous Reider-Lieb-Lebowitz (RLL) model, where the end particles of the chain were connected to equilibrium thermal reservoirs. For simplicity, we consider the active reservoirs to be modeled by a single overdamped active particles with exponentially decaying autocorrelation. We also assume the strong coupling limit Eq.(7.17) for the coupling between the end particles of the chain to the active reservoir, so that the coupling to the active reservoir can be modeled by including a stochastic force on the boundary particle. The equations of motion for x_l , the displacement of the l -th particle from its equilibrium position, read,

$$m\ddot{x}_1 = -k(2x_1 - x_2) - \gamma \dot{x}_1 + f_1(t), \quad (7.20a)$$

$$m\ddot{x}_l = -k(2x_l - x_{l-1} - x_{l+1}), \quad \forall l \in [2, N-1], \quad (7.20b)$$

$$m\ddot{x}_N = -k(2x_N - x_{N-1}) - \gamma \dot{x}_N + f_N(t), \quad (7.20c)$$

where the fixed boundary conditions imply $x_0 = 0 = x_{N+1}$ and $f_{1,N}(t)$ are independent stationary colored noises with autocorrelation, $\langle f_j(t)f_l(t') \rangle = \delta_{jl} a_j^2 \exp(-|t-t'|/\tau_j)$, where a_j denotes the strength of the noise and the correlation-time τ_j is a measure of the activity. As a specific example, we consider the dichotomous noise

$$f_j(t) = a_j \sigma_j(t), \quad (7.21)$$



Figure 7.1: Schematic representation of a chain of oscillators connected to two nonequilibrium reservoirs which exert active forces $f_{1,N}(t)$ on the boundary oscillators.

where σ_j alternates between ± 1 at a constant rate α_j , giving rise to an exponential correlation with $\tau_j = 1/(2\alpha_j)$.

If we wait for long enough times, the chain eventually reaches a stationary state. In this chapter, we compute the average energy current flowing through the system and kinetic temperature profile in the stationary state. To this end, we first rewrite Eqs. (7.20) as,

$$M\ddot{X}(t) = -\Phi X(t) - \Gamma \dot{X}(t) + F(t), \quad (7.22)$$

where $X(t) = \{x_l(t); l = 1, \dots, N\}$ is a vector and M is an N -dimensional diagonal matrix with $M_{lj} = m\delta_{l,j}$. Moreover, Γ and Φ are N -dimensional matrices given by

$$\Gamma_{lj} = \gamma(\delta_{l,1}\delta_{j,1} + \delta_{l,N}\delta_{j,N}), \quad \Phi_{lj} = k(2\delta_{l,j} - \delta_{l,j-1} - \delta_{l,j+1}).$$

Finally, $F_j = f_1(t)\delta_{j1} + f_N(t)\delta_{jN}$ is a vector.

We are interested in the solution of Eq. (7.22) in the stationary state, which is most conveniently obtained by taking a Fourier transform with respect to time, $\tilde{X}(\omega) = \int_{-\infty}^{\infty} dt e^{i\omega t} X(t)$. This leads to,

$$\tilde{X}(\omega) = G(\omega)\tilde{F}(\omega), \quad (7.23)$$

where $\tilde{F}(\omega)$ is the Fourier transform of $F(t)$ and

$$G(\omega) = [-M\omega^2 + \Phi - i\omega(\Gamma_L + \Gamma_R)]^{-1}$$

$$= \begin{bmatrix} -m\omega^2 + 2k - i\omega\gamma & -k & 0 & \cdots \\ -k & -m\omega^2 + 2k & -k & \cdots \\ \vdots & \vdots & \ddots & \cdots \\ 0 & \cdots & -k & -m\omega^2 + 2k - i\omega\gamma \end{bmatrix}^{-1}. \quad (7.24)$$

Inverting the transform, we get from Eq. (7.23),

$$X(t) = \frac{1}{2\pi} \int_{-\infty}^{\infty} d\omega e^{-i\omega t} G(\omega) \tilde{F}. \quad (7.25)$$

To compute the steady state energy current and kinetic temperature profiles, we need the autocorrelation of $f_j(t)$ in the Fourier-space,

$$\langle \tilde{f}_j(\omega) \tilde{f}_l(\omega') \rangle = 2\pi \delta_{jl} \delta(\omega + \omega') \tilde{g}(\tau_j, \omega). \quad (7.26a)$$

Here $\tilde{g}(\tau_j, \omega) = \frac{2a_j^2 \tau_j}{1 + \omega^2 \tau_j^2}$ denotes the spectral density of the active force from the j th reservoir, which clearly is a Lorentzian with corner frequency τ_j^{-1} .

7.3 Stationary energy current

Our primary observable of interest is the average energy current flowing through the system, which can be most conveniently expressed as [137],

$$J_{\text{act}} \equiv \langle \mathcal{J}(t) \rangle = \langle \dot{x}_1 [-\gamma \dot{x}_1 + f_1(t)] \rangle, \quad (7.27)$$

where $\mathcal{J}(t)$ denotes the instantaneous current and the average is taken in the NESS. Using the solution Eq. (7.25), the stationary current defined in Eq. (7.27) comes out to be [see Appendix 9.9 for details],

$$J_{\text{act}} = \gamma \int_0^{\infty} \frac{d\omega}{\pi} \omega^2 |G_{1N}(\omega)|^2 [\tilde{g}(\tau_1, \omega) - \tilde{g}(\tau_N, \omega)], \quad (7.28)$$

where $\tilde{g}(\tau_j, \omega)$ contains information about the reservoir activity. Equation (7.28) is a Landauer-like formula, where the Lorentzian reservoir spectra $\tilde{g}(\tau_j, \omega)$ couples to the phonon transmission coefficient $\omega^2 |G_{1N}(\omega)|^2$. To compute the currents explicitly we need $G_{1N}(\omega)$, which

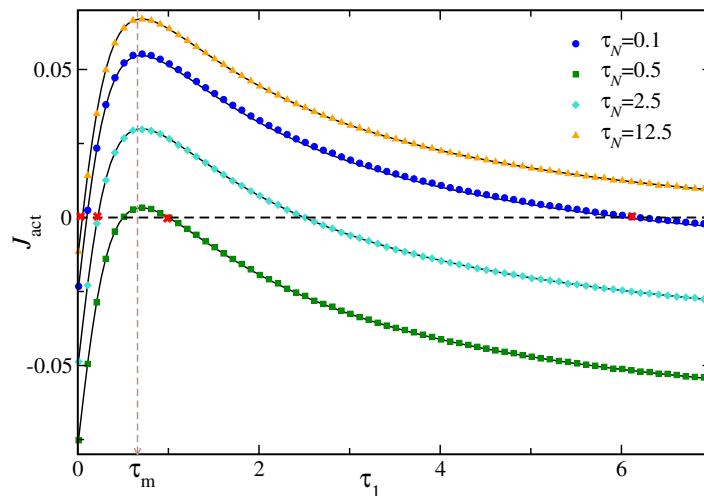


Figure 7.2: Activity induced current J_{act} vs τ_1 for different values of τ_N and $\gamma = 1 = m = a_1 = a_N$ and $k = 2$; symbols indicate the data obtained from numerical simulations with $N = 64$ oscillators and the solid black lines indicate the analytical prediction Eq. (7.30). The red crosses mark the non-trivial current reversal points and τ_m indicates the value of the activity for J_{act} is maximum.

is obtained by exploiting the tridiagonal structure of $G^{-1}(\omega)$ [138, 139, 140, 141]. We are particularly interested in the thermodynamic limit $N \rightarrow \infty$, where $G_{1N}(\omega)$ vanishes exponentially outside the phonon band $|\omega| > \omega_c = 2\sqrt{k/m}$ [139]. In that limit, we show that, the contribution from the j -th reservoir ($j = 1, N$) is given by [see Appendix. 9.9 for details],

$$\gamma \int_0^\infty \frac{d\omega}{\pi} \omega^2 |G_{1N}(\omega)|^2 \tilde{g}(\tau_j, \omega) = \int_0^\pi \frac{dq}{\pi} \frac{mka_j^2 \tau_j \sin^2 q}{[mk + 2\gamma^2(1 - \cos q)][m + 2k\tau_j^2(1 - \cos q)]}, \quad (7.29)$$

where ω and q are related by $m\omega^2 = 2k(1 - \cos q)$. Computing the q -integral and combining the contributions from both the reservoirs, we get the active current flowing through the system in the thermodynamic limit,

$$\begin{aligned} J_{\text{act}} &= \frac{m}{2\gamma^2} (a_1^2 \mathcal{E}_1 - a_N^2 \mathcal{E}_N) \quad \text{with,} \\ \mathcal{E}_j &= \frac{\tau_j^2 k^2 \left[\sqrt{1 + \frac{4\gamma^2}{mk}} - 1 \right] + \gamma^2 \left[1 - \sqrt{1 + \frac{4k\tau_j^2}{m}} \right]}{2\tau_j(\tau_j^2 k^2 - \gamma^2)}. \end{aligned} \quad (7.30)$$

Figure 7.2 shows a plot of the predicted J_{act} as a function of the left reservoir activity τ_1 for a set of different values of τ_N . This shows an excellent match with the current measured

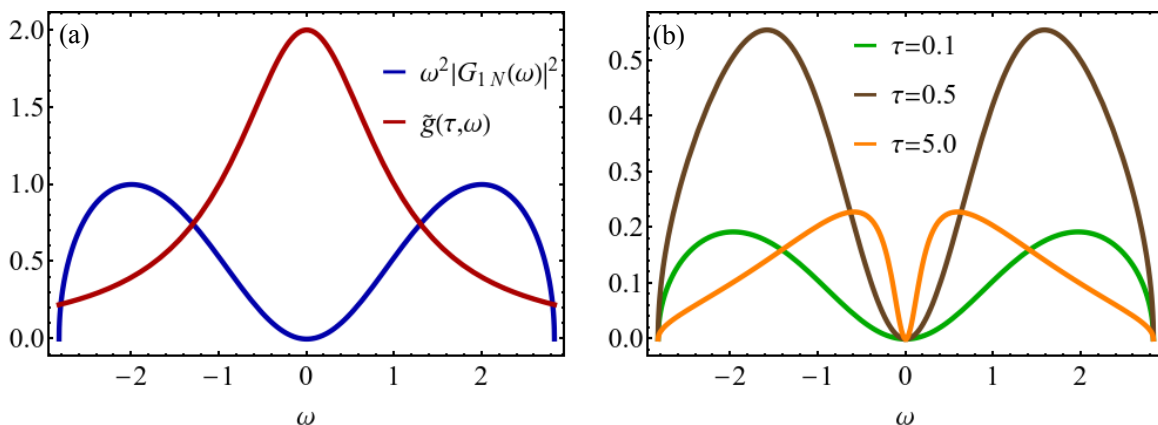


Figure 7.3: (a) Plot of the phonon transmission coefficient $\omega^2|G_{1N}(\omega)|^2$ in the $N \rightarrow \infty$ limit [see Eq. (9.124)] and the reservoir spectrum $\tilde{g}(\tau, \omega)$ [see Eq. (9.106)] for $\tau = 0.5$ as functions of ω . (b) Plot of the single reservoir transmission coefficient $\omega^2|G_{1N}(\omega)|^2\tilde{g}(\tau, \omega)$ vs ω for different values of τ . Here we have taken $m = 1, k = 2$ and $\gamma = 1$.

from numerical simulations with a chain of oscillators driven by the dichotomous noise given in Eq. (7.21). The figure illustrates some remarkable features of the active current: (i) J_{act} exhibits a non-monotonic behavior as the activity of either of the reservoirs is changed, giving rise to a negative differential conductivity and (ii) the current reverses its direction as the activity of one of the reservoirs, say τ_1 , is changed at a non-trivial value $\tau_1^* \neq \tau_N$. In the following, we discuss these two remarkable features in details.

Negative differential conductivity

The active current shows a non-monotonic behavior—as τ_1 is increased, J_{act} initially increases until reaching a maximum value after which it starts to decrease. This non-monotonic behavior implies that the differential conductivity $\chi_j = \frac{dJ_{\text{act}}}{d\tau_j}$, which is nothing but the linear response of the current to a small change in the activity of the j -th reservoir, becomes negative in some parameter regimes. It is clear from Eq. (7.30) that this non-monotonic behavior is inherent to the individual contributions from both the reservoirs — if τ_N is increased, keeping τ_1 fixed, a similar behavior is seen where the current first decreases and then starts to increase. The existence of this non-monotonic behavior becomes qualitatively clear by looking at the frequency spectrum of the reservoir $\tilde{g}(\tau, \omega)$. From Eq. (7.26a), it is clear that $\tilde{g}(\tau, \omega)$ is a Lorentzian, peaked around $\omega = 0$ with width $\sim \tau^{-1}$. On the other hand, the

phonon transmission coefficient $\omega^2|G_{1N}(\omega)|^2$ is peaked around the characteristic frequency $\omega_c = 2\sqrt{k/m}$, with a minimum at $\omega = 0$ [see Fig. 7.3(a)]. Consequently, the overlap of the system transmission coefficient and the reservoir spectra changes non-monotonically as τ is changed, reaching a maximum at some intermediate value of $\tau^{-1} \in [0, \omega_c]$ [see Fig. 7.3(b)]. This, in turn, gives rise to the non-monotonic behavior of J_{act} , which shows a maximum (minimum) as τ_1 (τ_N) is varied. In fact, it can be easily seen from Eq. (7.30) that for large k , the current is maximum at a value of $\tau_1 = \tau_m \propto \omega_c^{-1}$.

Current reversal

There is another, more striking, behavior induced by the presence of the active driving, namely, reversal of the direction of the current. We see from Fig. 7.2, that for any given τ_1 , J_{act} reverses its direction twice—once (trivially) at $\tau_1 = \tau_N$ and again at another value $\tau_1 = \tau_1^*$ which depends non-trivially on τ_N . For a fixed τ_N , J_{act} begins with a negative value (energy flowing from right to left reservoir) for $\tau_1 = 0$, which becomes positive (energy flowing from left to right reservoir) with increase in τ_1 . However, on increasing τ_1 further, the current again reverses its direction and becomes negative. Mathematically, this additional reversal can be understood from the observation that for a fixed value of τ_N , $\mathcal{E}_1 \rightarrow 0$ for both $\tau_1 \rightarrow 0$ and $\tau_1 \rightarrow \infty$ [see Eq. (7.30)], and consequently J_{act} has the same negative value at these two limits. Now, since J_{act} must reverse sign at $\tau_1 = \tau_N$, an additional reversal is required to reach the limiting negative values. A similar scenario is observed when τ_N is changed keeping τ_1 fixed, as expected from the symmetry of the system.

This behavior is illustrated in Fig. 7.4; panel (a) shows a three-dimensional plot of J_{act} on the (τ_1, τ_N) plane, while Fig. 7.4(b) shows the two-dimensional projection of (a) indicating the regions $J_{\text{act}} > 0$ and $J_{\text{act}} < 0$. For any given τ_N , the current reverses its direction at $\tau_1 = \tau_N$ and another non-trivial point $\tau_1 = \tau_1^*(\tau_N)$. The latter is given by the non-trivial solution of $a_1^2 \mathcal{E}_1(\tau_1) = a_N^2 \mathcal{E}_N(\tau_N)$. Similarly, for any given τ_1 , the current reversal occurs at $\tau_N = \tau_1$ and $\tau_N^*(\tau_1)$ [indicated by the solid red curve in 7.4(b)]. Interestingly, the intersection of the curves $\tau_1 = \tau_N$ and $\tau_1 = \tau_1^*(\tau_N)$ denoted by $\tau_1 = \tau_N = \bar{\tau}$ is a saddle point, as can be seen from Fig. 7.4(a). The current does not change direction when one passes through the saddle point—for $\tau_N = \bar{\tau}$, the current remains negative for all values of $\tau_1 \neq \tau_N$, while for

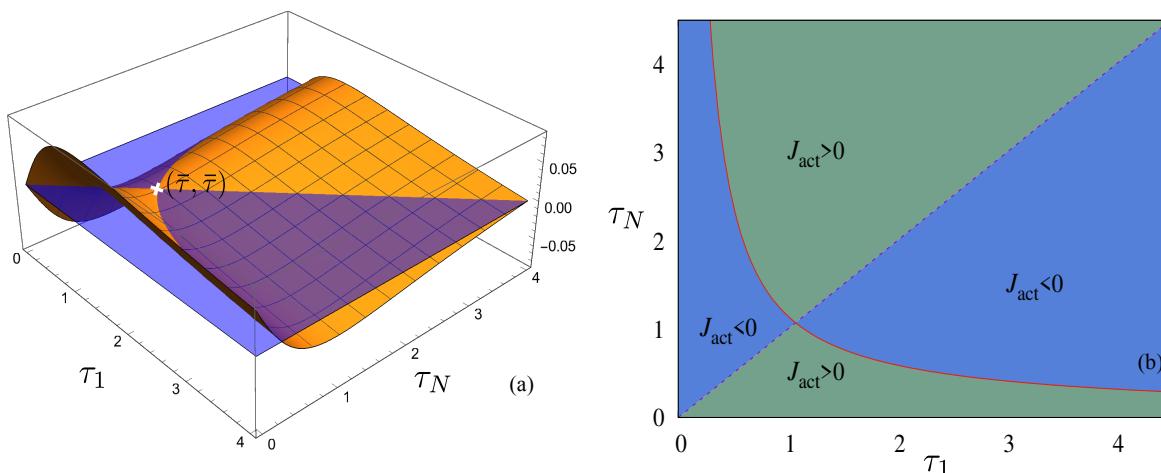


Figure 7.4: (a) Three dimensional plot of J_{act} on the (τ_1, τ_N) plane: the meshed orange surface denotes J_{act} given by Eq. (5) in the main text, while the un-meshed, semi-transparent blue surface corresponds to $J_{\text{act}} = 0$. The curves formed by intersection of these two surfaces give the locus of the zeros of the active current, the intersection of these two curves are denoted by $\tau_1 = \tau_N = \bar{\tau}$, which clearly is a saddle point of J_{act} . $J_{\text{act}} > 0$ in the region above the blue surface, while $J_{\text{act}} < 0$ in the region below the blue surface. (b) Two dimensional projection of (a) showing phase diagram of J_{act} in the (τ_1, τ_N) plane—: The light blue (green) shade indicates the region where the active current is negative (positive). The continuous red curve shows τ_N^* as a function of τ_1 whereas the dashed curve indicates the line $\tau_N = \tau_1$.

$\tau_1 = \bar{\tau}$, the current remains positive for all values of $\tau_N \neq \tau_1$.

NDC and current reversal have been observed in certain nonequilibrium systems with non-linearity, presence of obstacles or kinetic constraints [142, 143, 144, 145, 146]. Surprisingly, the dynamical active driving here gives rise to both features even in a linear chain.

7.4 Kinetic temperature

In this section we will discuss the average kinetic energy of the chain oscillators defined by,

$$\hat{T}_l = m \langle \dot{x}_l^2 \rangle. \quad (7.31)$$

It is well-known that \hat{T}_l provides a way to define a local ‘temperature’ for driven oscillator chains [147, 9]. In this case, using Eq. (7.25), we get,

$$\hat{T}_l = m \int \frac{d\omega}{2\pi} \omega^2 \left[|G_{l1}(\omega)|^2 \tilde{g}(\tau_1, \omega) + |G_{lN}(\omega)|^2 \tilde{g}(\tau_N, \omega) \right]. \quad (7.32)$$

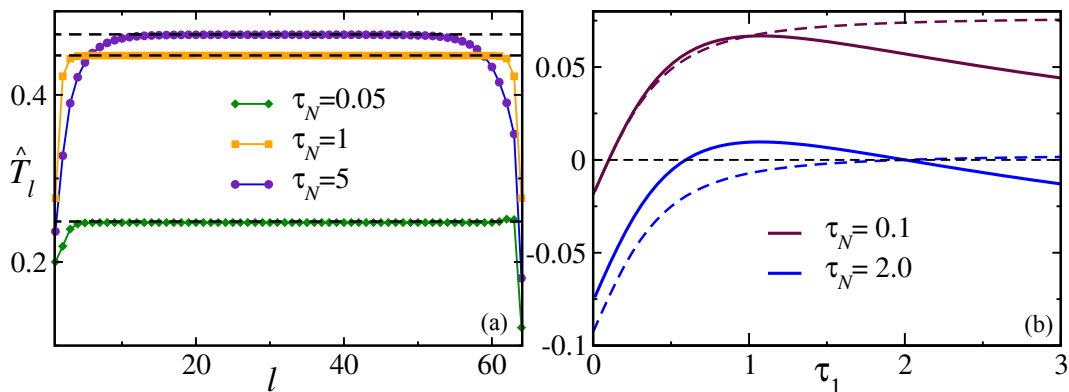


Figure 7.5: (a) The kinetic temperature profile \hat{T}_l for $\tau_1 = 1$ and different values of τ_N measured from simulations with a chain of $N = 64$ oscillators driven by the active noises (7.21). The dashed black lines show the predicted bulk temperature (7.33). (b) Comparison of J_{act} (solid lines) with the expected current for ‘effective’ temperature gradient $\mathcal{T}_1 - \mathcal{T}_N$ (dashed lines) for two different values of τ_N . Here $m = 1, k = 1, \gamma = 1$ and $a_1 = a_N = 1$.

The matrix elements can again be computed exploiting the tridiagonal structure of $G^{-1}(\omega)$. Performing a similar calculation as before [see Appendix. 9.10 for details], we find that, in the thermodynamic limit $N \rightarrow \infty$, the steady state temperature profile is flat in the bulk, accompanied by exponentially decaying boundary layers. The bulk temperature \hat{T}_{bulk} can be obtained explicitly, and is given by

$$\hat{T}_{\text{bulk}} = \frac{1}{2}(\mathcal{T}_1 + \mathcal{T}_N), \quad \text{with} \quad \mathcal{T}_j = \frac{a_j^2 \tau_j}{\gamma \sqrt{1 + 4\tau_j^2 k/m}}. \quad (7.33)$$

The predicted value of bulk temperatures for a fixed τ_1 and different values of τ_N are plotted in Fig. 7.5(a) along with numerical simulations performed with the active force given in Eq. (7.21); the excellent agreement validates our prediction. Interestingly, boundary kinks in the \hat{T}_l profile, which are generically present for coupling with thermal reservoirs [148], are absent here.

The form of Eq. (7.33) raises a possibility of associating an effective temperature \mathcal{T}_j to the j -th active reservoir. At first glance, this identification also appears to be consistent with a ‘zeroth law’ — when $\tau_1 = \tau_N$, i.e., $\mathcal{T}_1 = \mathcal{T}_N$, the bulk of the system is at the same ‘temperature’ as the reservoirs. However, such an interpretation is not acceptable for several reasons. First, note that the kinetic temperatures of the boundary sites $\hat{T}_{1,N}$ remain different

from \hat{T}_{bulk} giving rise to a boundary layer even when $\tau_1 = \tau_N$ [see Fig. 7.5(a)] which is absent for ordinary equilibrium reservoirs. Moreover, the stationary active current (7.30) is very different than the energy current which would have been generated if the system were connected to thermal reservoirs of temperatures \mathcal{T}_1 and \mathcal{T}_N at the two ends. This is illustrated in Fig. 7.5(b) which shows neither current reversal nor any NDC in the ‘effective’ thermal scenario. However, the effective temperature picture becomes viable in the limit of small activity, which we discuss next.

Passive limit- It is well known that active systems show an effective passive behavior in the limit of vanishing correlation time [10, 56, 11]. Similarly, in our case, when $\tau_j \rightarrow 0$, the active force $f_j(t)$ resembles a white noise with effective correlation $\langle f_j(t)f_j(t') \rangle \rightarrow a_j^2 \tau_j \delta(t - t')$. In this limit, the active forces in Langevin Eqs. (7.20) can be thought of representing thermal reservoirs with effective temperatures $a_j^2 \tau_j / \gamma$ and satisfying FDT. The well known results of the RLL model are expected to be recovered in this ‘thermal’ limit. Indeed we see from Eq. (7.33) that when the active time-scales are much smaller than the coupling time-scale, i.e., $\tau_1, \tau_N \ll \sqrt{m/k}$, the kinetic temperature associated with the reservoirs $T_j^{\text{eff}} \simeq a_j^2 \tau_j / \gamma$ are consistent with the thermal picture. Moreover, in this limit, it can be easily seen from Eq. (7.30) that,

$$J_{\text{act}} = \frac{k(T_1^{\text{eff}} - T_N^{\text{eff}})}{2\gamma} \left[1 + \frac{mk}{2\gamma^2} - \frac{mk}{2\gamma^2} \sqrt{1 + \frac{4\gamma^2}{mk}} \right] + O(\tau_j^2), \quad (7.34)$$

which is the same as the well-known form of the thermal current [147, 139] to leading order in τ_1, τ_N . This can also be seen from Fig. 7.5(b) where J_{act} converges to the effective thermal current for $\tau_1, \tau_N \ll \sqrt{m/k}$.

7.5 Summary

In summary, we studied a simple model where the reduced dynamics of a tracer coupled to active particles can be obtained exactly by integrating out the active degrees of freedom. We find in that in the strong coupling limit, the active particles, exert exponentially correlated

stochastic force and a constant dissipation on the probe. Then we study the transport properties of a harmonic chain coupled to two active reservoirs. For simplicity, we take the active reservoirs to be single active particles with different activities τ_1 and τ_N coupled to the end particles of the harmonic chain in the strong coupling limit. We find that the active drive leads to some novel features in the average stationary current flowing through the chain—(i) changes non-monotonically as the activity of the reservoirs are changed, leading to a negative differential conductivity (NDC), and (ii) exhibits an unexpected direction reversal at some finite value of the activity drive. We also compute the kinetic temperature profile of the chain oscillators, which, similar to the thermally driven scenario, remains uniform in the bulk of the system. However, we show that in spite of this resemblance, an effective temperature picture cannot be consistently built.

Chapter 8

Conclusion

Active particles form a class of nonequilibrium systems that are used to describe the dynamics of microorganisms like bacteria. Such dynamics, though random, are fundamentally different from passive Brownian particles as they show a persistent motion along some preferred direction. The nature of this persistent dynamics, again, varies among the different classes of organisms and is modeled by a correlated, stochastic propulsion velocity that drives the system. The correlated structure of the propulsion velocity makes the position evolution a non-Markovian process. Naturally, obtaining exact results on the physical observables of such systems is challenging. In this thesis, we analytically study the statistical properties of various active particles. In this process, we find some exact results for the position distribution of free and confined active particles. We also find some universal properties which hold true for all active particle models. The exact results obtained in this thesis will not only help in understanding active particles better but also pave the way for understanding other long-standing issues in statistical physics like nonequilibrium transport phenomena [142, 149] better.

In chapters 2 and 3, we study a few active particle models without any external potential. In particular, in chapter 2, we study a set of RTP models in two spatial dimensions, where the orientation can take either discrete or continuous values. We find that the short-time behavior of the RTPs depends heavily on the specific model. The signatures of activity disappear from the typical fluctuations at long times but are encoded in the large-deviation functions, which we find exactly. In chapter 3, we investigate the dynamics of a particle executing an active Brownian motion with intermittent directional reversals. We show that directional reversal leads to a host of exciting, new features in the position and first-passage time distributions, which are very different from normal ABP or RTP dynamics. In particular, a novel intermediate time regime emerges when the reversal rate is much larger than the rotational diffusion—the dynamics, in that case, is described by a diffusion process with

a stochastic diffusion coefficient. Our exact analytical results in these two chapters mark a significant progress in the understanding of two different classes of bacterial motion — appealing to both theoretical and experimental physicists. Our predictions can be verified with new measurements with existing experimental setups. Possible future directions include studying the effects of finite tumble/reversal times, non-Markovian waiting-times between successive tumblings/reversals, investigation of extremal statistics. It is also interesting to see if all these microscopic models exhibit collective features like motility-induced phase separation [43] upon introducing repulsive interactions among them.

In both chapters 2 and 3, we found that the typical long-time position fluctuations of the different active particle models are Gaussian with a diffusive scaling. Though we extract this behavior exactly for the models considered in chapter 2, we can not do the same for DRABP (in chapter 3). In chapter 4, we provide a generic universal framework to study the long-time distribution of active particles. In fact, using our framework, we can show that the leading order position distribution always satisfies a diffusion equation, while the subleading order corrections follow inhomogeneous diffusion equations with the inhomogeneous part depending only on the previous order solutions and can be calculated systematically. These quantitative predictions for the deviation of the position distribution from Gaussian, at the typical scale $O(\sqrt{t})$ are more accessible compared to the rare $x \sim O(t)$ fluctuations, which are characterized by the large deviation functions. Thus, in addition to providing an exact derivation of the diffusion equation at large times, the results of this chapter might be very relevant for experiments.

In chapter 5, we study the stationary behavior of a DRABP in a harmonic potential. We find that the competition of the three time-scales — determined by the reversal rate, the rotational diffusion coefficient, and the trap stiffness, renders the position distribution in the stationary state very rich. In particular, we find the emergence of two novel phases (which we call the active II and passive II phases) alongside the usual active and passive phases seen in RTP and ABP [59, 57, 61]. Both of these new phases are characterized by stationary position distributions that have a logarithmic peak at the center of the trap. They differ only at the boundaries, where the active II phase shows an algebraic divergence, while the passive II phase goes to zero. It would be intriguing to find out whether the different phases predicted

here can be observed in experiments with bacteria like *Mycococcus xanthus*, *Pseudomonas citronellolis*, etc. in a harmonic trap using acoustic or optical tweezers. Theoretically, some interesting future questions would be understanding the first-passage behavior of the DRABP in a harmonic trap if the stationary behavior remains qualitatively the same for generic confining potentials.

Stochastic resetting of a dynamical process helps optimize the time it takes to reach a specific target. Searching for a particular target, such as a food source, a weak spot of the host, or toxins is very pertinent for bacteria and similar microorganisms. The effects of stochastic resetting on active particles is thus an important issue, which we address in chapter 6. We find exact results on the stationary state position distribution and find significant deviations from passive Brownian motion. We also investigate the relaxation of the position distribution to this stationary state and the first-passage properties. In this chapter, we used an instantaneous resetting protocol where the RTP is reset in zero time. It is impossible to realize this protocol experimentally, where it takes a finite time to return to the initial position. To overcome this drawback, many non-instantaneous resetting protocols have been suggested lately [150, 151]. It would be interesting to see how the analytical results obtained here change for such protocols.

In chapter 7, we explore the question what happens to the transport properties of a system when coupled to active particles. Active particles, which have their own energy depot, could serve as paradigmatic examples of nonequilibrium reservoirs, and an obvious question is what happens to the transport properties of an extended system when it is connected to two such ‘active reservoirs’. We first study a simple analytical model where overdamped active particles are coupled to a probe by harmonic springs. We find an exact reduced equation of motion of the probe by integrating out the active degrees of freedom of its environment. Using this result, we then study the energy transport through an ordered harmonic chain connected to two active reservoirs at the two ends. We find exact expressions for the average stationary current (in the thermodynamic limit of the chain), which shows two novel features: (i) negative differential conductivity and (ii) an unexpected current reversal at some non-zero value of the active drive. We also show that there is no effective thermal picture for this energy transport. The work discussed in this chapter is the first to study the effect of active

reservoirs on the transport properties of extended systems, and the obtained exact results are robust for all well-known active particle models. It is interesting to see how the signatures of specific dynamics are expected to be seen in the fluctuations of the current. Some other interesting future questions are: What are the effects of disorder, anharmonicity, and pinning in the presence of active driving? How do our results change if the nonequilibrium reservoir is modeled by more realistic models of interacting active particles?

Chapter 9

Appendix

9.1 Calculation of the Propagator for the θ Processes and 2-point σ Correlations

n -state Model

Let $\theta_j = \frac{2\pi j}{n}, j = 0, 1, \dots, n-1$ denote the n possible values of θ , and $P_j(t)$ denote the probability that the particle orientation is θ_j at time t . The Fokker Planck equation governing the time-evolution of $P_j(t)$ with periodic boundary conditions, $P_n(t) = P_0(t)$, is

$$\frac{d}{dt}P_j = -\gamma P_j + \frac{\gamma}{2}P_{j+1} + \frac{\gamma}{2}P_{j-1}. \quad (9.1)$$

This set of equations is easily solved by going to the Fourier basis,

$$P_j(t) = \sum_{k=0}^{n-1} e^{i\frac{2\pi jk}{n}} Q_k(t) \quad (9.2)$$

where $Q_k(t) = \frac{1}{n} \sum_{j=0}^{n-1} e^{-i\frac{2\pi jk}{n}} P_j(t)$. The time dependence of Q_k is given by

$$Q_k(t) = Q_k(0) e^{-\lambda_k t} \quad (9.3)$$

where, $\lambda_k = \gamma(1 - \cos \frac{2\pi k}{n})$ are the eigenvalues of the tri-diagonal matrix. Now, with initial conditions, $P_j(0) = \delta_{jm}; \theta(0) = \frac{2\pi m}{n}$, we have

$$P_j(t) = \frac{1}{n} \sum_{k=0}^{n-1} e^{i\frac{2\pi k(j-m)}{n}} e^{-\lambda_k t}. \quad (9.4)$$

Thus we can write the propagator of the process starting with θ_0 at time $t = 0$ as

$$P(\theta, t|\theta_0, 0) = \frac{1}{n} \sum_{k=0}^{n-1} e^{ik(\theta-\theta_0)} e^{-\lambda_k t}. \quad (9.5)$$

Using this we can calculate the 2 or higher point correlations of the σ s defined in main chapter. For example,

$$\begin{aligned} \langle \sigma_x(t) \sigma_x(0) \rangle &= \frac{1}{n} \sum_{\theta, \theta_0} \cos \theta \cos \theta_0 P(\theta, t|\theta_0, 0) \\ &= \frac{1}{n^2} \sum_{k=0}^{n-1} e^{-\lambda_k t} \left| \sum_{\theta} \cos \theta e^{ik\theta} \right|^2. \end{aligned} \quad (9.6)$$

Continuous Model

Here the propagator can be written as a sum of contributions from events where the final and initial θ are same (*i.e.*, no θ flip) and where they are different. They can be as in Eq. (2.2)

$$P(\theta, t|\theta_0, 0) = e^{-\gamma t} \delta(\theta - \theta_0) + (1 - e^{-\gamma t}) \frac{1}{2\pi}. \quad (9.7)$$

Thus the 2-point σ correlations can be evaluated as

$$\langle \sigma_i(t) \sigma_i(0) \rangle = \frac{1}{2\pi} \int d\theta d\theta_0 P(\theta, t|\theta_0, 0) \sigma_i(t) \sigma_i(0). \quad (9.8)$$

Now, $\sigma_\alpha(t)$ is $\cos \theta$ or $\sin \theta$ for $\alpha = x$ and $\alpha = y$ respectively. Using the properties of sin and cos functions, the integral contributes only when there is no θ flip. Thus we have,

$$\begin{aligned} \langle \sigma_x(t) \sigma_x(0) \rangle &= e^{-\gamma t} \frac{1}{2\pi} \int_0^{2\pi} d\theta \cos^2 \theta = \frac{1}{2} e^{-\gamma t} \\ \langle \sigma_y(t) \sigma_y(0) \rangle &= e^{-\gamma t} \frac{1}{2\pi} \int_0^{2\pi} d\theta \sin^2 \theta = \frac{1}{2} e^{-\gamma t}. \end{aligned}$$

9.2 Details of the 3-state X Marginal Distribution

We rewrite Eqs. (2.12) in the main chapter for $x \neq 0$,

$$v_0 \frac{dP}{dx} = WP. \quad (9.9)$$

where,

$$P = \begin{bmatrix} \hat{P}_+ \\ \hat{P}_- \end{bmatrix} \text{ and } W = \begin{bmatrix} -(s + \gamma) & \gamma/2 \\ -2\gamma & (2s + \gamma) \end{bmatrix}. \quad (9.10)$$

The eigenvalues of W are given by $(s \pm \lambda)/2$, where $\lambda = \sqrt{3s(3s + 4\gamma)}$. Using these eigenvalues and implementing the boundary conditions that $\hat{P}_\pm(x, s) \rightarrow 0$ as $x \rightarrow \pm\infty$, we have

$$\hat{P}_+(x, s) = \begin{cases} A_+ \exp\left[-\frac{x}{2v_0}(\lambda - s)\right] & \text{for } x > 0 \\ B_+ \exp\left[\frac{x}{2v_0}(\lambda + s)\right] & \text{for } x < 0 \end{cases} \quad (9.11)$$

and

$$\hat{P}_-(x, s) = \begin{cases} A_- \exp\left[-\frac{x}{2v_0}(\lambda - s)\right] & \text{for } x > 0 \\ B_- \exp\left[\frac{x}{2v_0}(\lambda + s)\right] & \text{for } x < 0, \end{cases} \quad (9.12)$$

where A_\pm and B_\pm are arbitrary constants. Putting P_\pm back in Eq. (9.9), we have,

$$A_- = \frac{A_+(2\gamma + 3s - \lambda)}{\gamma}, \quad B_- = \frac{B_+(2\gamma + 3s + \lambda)}{\gamma}. \quad (9.13)$$

Next, to evaluate the constants A_+ and B_+ , we note that due to the presence of the δ -functions, integrating the original Eqs. (2.12) around the origin $x = 0$ yields discontinuity

conditions for \hat{P}_{\pm} across $x = 0$,

$$\begin{aligned} v_0 [A_+ - B_+] &= \frac{1}{3}, \\ v_0 \left[\frac{A_+(2\gamma + 3s - \lambda)}{\gamma} - \frac{B_+(2\gamma + 3s + \lambda)}{\gamma} \right] &= -\frac{4}{3}. \end{aligned}$$

Solving these two equations determines the constants as

$$A_+ = \frac{3(2\gamma + s) + \lambda}{6v_0\lambda}, \quad B_+ = \frac{3(2\gamma + s) - \lambda}{6v_0\lambda}. \quad (9.14)$$

Using Eq. (9.14) in Eqs. (9.11) and (9.12) and adding \hat{P}_+ and \hat{P}_- , we get the Laplace transform of the position distribution $P(x, t)$ as given by Eq. (2.13) in the main chapter.

Next we show the computation of the inverse laplace transform of Eq. (2.13) in the main chapter. Let us consider the case $x > 0$. We need to compute the Bromwich integral,

$$P(x, t) = \frac{1}{2\pi i} \int_{c_0 - i\infty}^{c_0 + i\infty} e^{st} \frac{6\gamma + 5s - \lambda}{2v_0\lambda} \exp \left[-\frac{x}{2v_0}(\lambda - s) \right] ds \quad (9.15)$$

where $\lambda = 3\sqrt{s(s+a)}$ with $a = 4\gamma/3$. The integrand has a branch-cut along the real axis from $s = 0$ to $s = -a$, so we draw a contour keeping the branch-cut to the left of c_0 , as shown in Fig. 9.1. This contour can be broken into 6 different parts as indicated in the figure.

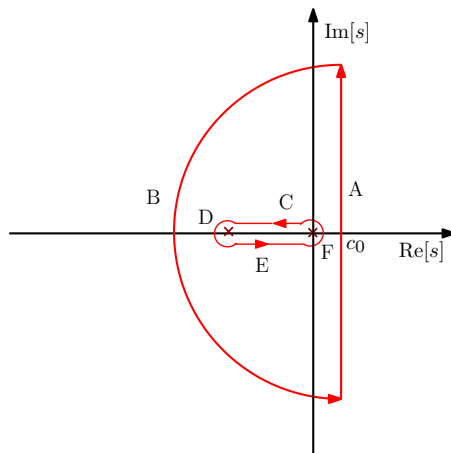


Figure 9.1: Illustration of the contour used to evaluate the integral (9.15).

Using Cauchy's theorem, for this contour integral we can write

$$\int_A + \int_B = \int_C + \int_D + \int_E + \int_F. \quad (9.16)$$

Now, $\int_A = P(x, t)$ is the integral that we need, with A extending to ∞ .

We first compute the contributions coming from the small circular arcs D and F of radius ϵ ($\rightarrow 0$). Along D , $s = -a + \epsilon e^{i\theta}$, while along F , $s = \epsilon e^{i\theta}$. It can be immediately seen that the contributions of the integrals along these two circular arcs vanish in the limit $\epsilon \rightarrow 0$. In the following we evaluate the integrals along C, E and B separately.

Along C , $s = ue^{i\pi} + i\epsilon$, hence, $ds = -du$. With $\epsilon \rightarrow 0$, $\lambda = 3i\sqrt{u(a-u)}$ here and we have,

$$\int_C = \int_0^a \frac{-du}{2\pi i} e^{-u(t+\frac{x}{2v_0})} e^{i\frac{3x}{2v_0}\sqrt{u(a-u)}} \left(\frac{6\gamma - 5u}{i6v_0\sqrt{u(a-u)}} - 1 \right).$$

On the other hand, along E , $s = ue^{-i\pi} - i\epsilon$, and $ds = -du$. In this case, $\lambda = -3i\sqrt{u(a-u)}$ for $\epsilon \rightarrow 0$, and we have

$$\int_E = \int_a^0 \frac{-du}{2\pi i} e^{-u(t+\frac{x}{2v_0})} e^{-i\frac{3x}{2v_0}\sqrt{u(a-u)}} \left(\frac{i(6\gamma - 5u)}{6v_0\sqrt{u(a-u)}} - 1 \right).$$

Adding the contributions from the segments C and E , we get,

$$\int_C + \int_E = \int_0^a du \frac{e^{-u(t+\frac{x}{2v_0})}}{6\pi v_0} \left[\frac{(6\gamma - 5u)}{\sqrt{u(a-u)}} \cos \frac{3x}{2v_0} \sqrt{u(a-u)} - 3 \sin \frac{3x}{2v_0} \sqrt{u(a-u)} \right] \quad (9.17)$$

To evaluate the integral along B , we note that, here the real part of s is negative and $|s| \rightarrow \infty$; hence the integral reduces to,

$$\int_B \approx \frac{1}{3v_0} \int \frac{ds}{2\pi i} \exp \left[s \left(t - \frac{x}{v_0} \right) \right] e^{-\frac{\gamma x}{v_0}} \quad (9.18)$$

where we have used the fact that along B , $|s| \gg \gamma$ to approximate $\left(\frac{6\gamma + 5s - \lambda}{2v_0\lambda} \right)$ as $\frac{1}{3v_0}$ and $\exp \left(-\frac{x}{2v_0}(\lambda - s) \right)$ as $\exp \left(-\frac{x}{v_0}(s + \gamma) \right)$.

Now, since the integrand in Eq. (9.18) does not have any singularity, we can deform the contour B to be along the imaginary axis, and write,

$$\int_B = \frac{1}{3v_0} \int_{i\infty}^{-i\infty} \frac{ds}{2\pi i} \exp\left[s\left(t - \frac{x}{v_0}\right)\right] e^{-\frac{\gamma x}{v_0}} = -\frac{1}{3}\delta(x - v_0 t) e^{-\frac{\gamma x}{v_0}} = -\frac{e^{-\gamma t}}{3}\delta(x - v_0 t). \quad (9.19)$$

The required integral $P(x, t) = \int_A$ is now obtained using Eq. (9.16) along with Eqs. (9.17) and (9.19). The Bromwich integral for $x < 0$ can be also be computed following the same procedure. The final expression for $P(x, t)$ is quoted in Eqs. (2.14) and (2.15) in the main chapter.

For the case of $P(y, t)$ we also proceed similarly. In that case, however, the contribution of the integrals around the small circles (D and F in the above contour) are $\sim \epsilon^{-1/2}$, and thus cannot be ignored.

To carry out the line integral in Eq. (2.15) in the main chapter, we first make a change of variable $u = a(w + 1)/2$, yielding,

$$G_x(x = zv_0 t, t) = \frac{\gamma}{9\pi v_0} e^{-\frac{\gamma t}{3}(z+2)} \int_{-1}^1 dw e^{-\frac{\gamma t}{3}(z+2)w} \left[-3 \sin z\gamma t \sqrt{1-w^2} + \frac{(4-5w)}{\sqrt{1-w^2}} \cos z\gamma t \sqrt{1-w^2} \right]. \quad (9.20)$$

Next, we use the following identity from Section 4.124, Eq. 1 of [152]

$$F(p, q) \equiv \frac{1}{\pi} \int_{-1}^1 dw e^{-pw} \frac{\cos(q\sqrt{1-w^2})}{\sqrt{1-w^2}} = I_0(\sqrt{p^2 - q^2}). \quad (9.21)$$

Using this identity, we further have,

$$\begin{aligned} -\frac{1}{\pi} \int_{-1}^1 dw e^{-pw} \sin(q\sqrt{1-w^2}) &= \frac{\partial F}{\partial q} = -\frac{q I_1(\sqrt{p^2 - q^2})}{\sqrt{p^2 - q^2}} \\ -\frac{1}{\pi} \int_{-1}^1 dw w e^{-pw} \frac{\cos(q\sqrt{1-w^2})}{\sqrt{1-w^2}} &= \frac{\partial F}{\partial p} = \frac{p I_1(\sqrt{p^2 - q^2})}{\sqrt{p^2 - q^2}}. \end{aligned}$$

Using these, Eq. (9.20) can be evaluated exactly as

$$G_x(x = zv_0 t, t) = \frac{\gamma e^{-\frac{\gamma t}{3}(z+2)}}{9v_0} \left[4I_0\left(\frac{2\gamma t}{3} w(z)\right) + \frac{5-2z}{\sqrt{(2z+1)(1-z)}} I_1\left(\frac{2\gamma t}{3} w(z)\right) \right], \quad (9.22)$$

with $w(z) = \sqrt{(2z+1)(1-z)}$. This is quoted as Eq. (2.16) in the main chapter.

9.3 Computation of the Inverse Fourier Transform for 4-state Marginal Distribution

In this Section we compute the inverse Fourier transform of $\tilde{P}(q, t)$ given by Eq. (2.48) in the main chapter. To this end, it is first convenient to rewrite it as,

$$\tilde{P}(q, t) = e^{-\gamma t} \left[\frac{q^2}{2(q^2 - 1)} \left(\cosh(\gamma t \sqrt{1 - q^2}) - 1 \right) + \cosh(\gamma t \sqrt{1 - q^2}) + \frac{\sinh(\gamma t \sqrt{1 - q^2})}{\sqrt{1 - q^2}} \right].$$

Let us denote the three terms inside the square brackets in the above equation by T_1, T_2, T_3 . Note that the Fourier transform of all the three terms are related by taking derivatives or integrals of each other with respect to the arguments (q and x). We exploit this and invert T_1, T_2, T_3 term by term, separately. We start by evaluating the Fourier inverse of T_2 , for this we use an integral Bessel function identity from Section 6.645 Eq. 3 of [152],

$$\int_{-1}^1 \frac{1}{\sqrt{1 - x^2}} e^{-a} I_1(b \sqrt{1 - x^2}) dx = \frac{2}{b} (\cosh \sqrt{a^2 + b^2} - \cosh a).$$

Let $a = i\gamma qt$ and $b = \gamma t$. Then,

$$\int_{-1}^1 \frac{e^{-iq\gamma t}}{\sqrt{1 - x^2}} I_1(\gamma t \sqrt{1 - x^2}) dx = \frac{2}{\gamma t} [\cosh(\gamma t \sqrt{1 - q^2}) - \cos(\gamma qt)].$$

We use the scaling, $\gamma t \rightarrow t'$ and $x \rightarrow x't$,

$$\cosh(t' \sqrt{1 - q^2}) = \frac{t'}{2} \int_{-t'}^{t'} dx' e^{-iqx'} \frac{I_1(\sqrt{t'^2 - x'^2})}{t'^2 - x'^2} + \cos(qt).$$

We can actually call t' and x' as t and x without any ambiguity, throughout the calculations and put back the scaling forms at the end. Thus,

$$\mathcal{F}^{-1}[\cosh(t \sqrt{1 - q^2})] = \frac{t I_1(\sqrt{t^2 - x^2})}{2\sqrt{t^2 - x^2}} \Theta(t - |x|) + \frac{1}{2} (\delta(x + t) + \delta(x - t)) \quad (9.23)$$

where the δ -functions come from the term $\cos(qt)$. Note, this is actually the Fourier transform of T_2 Now,

$$\int_0^t \cosh(\tau\sqrt{1-q^2})d\tau = \frac{\sinh(t\sqrt{1-q^2})}{\sqrt{1-q^2}}. \quad (9.24)$$

Thus if we integrate Eq. (9.23) from 0 to t , we get the Inverse Transform of the T_3 term. Using, $I'_0(x) = I_1(x)$ to do the integral, we get

$$\mathcal{F}^{-1} \left[\frac{\sinh(t\sqrt{1-q^2})}{\sqrt{1-q^2}} \right] = \frac{1}{2} I_0(\sqrt{t^2-x^2})\Theta(t-|x|). \quad (9.25)$$

Only the inverse of T_1 remains to be evaluated. We integrate l.h.s. of Eq. (9.25) from 0 to t , to get

$$\int_{-\infty}^{\infty} e^{-iqx} \frac{1}{1-q^2} \left(\cosh(t\sqrt{1-q^2}) - 1 \right) dq. \quad (9.26)$$

Taking derivatives with respect to x twice, we get,

$$- \int_{-\infty}^{\infty} e^{-iqx} \frac{q^2}{1-q^2} \left(\cosh(t\sqrt{1-q^2}) - 1 \right) dq \quad (9.27)$$

which is exactly twice the negative of T_1 . Thus, we need to do this same set of operations on the r.h.s. of Eq. (9.25) to get the inverse of the first term. Thus the inverse Fourier transform $\mathcal{F}^{-1}[T_1]$ is

$$\begin{aligned} &= -\frac{1}{2} \frac{\partial^2}{\partial x^2} \left[\Theta(t-|x|) \int_0^t d\omega I_0(\sqrt{\omega^2-x^2})\Theta(\omega-|x|) \right] \\ &= \frac{1}{2} \frac{\partial}{\partial x} \left[\delta(t-|x|) \operatorname{sgn}(x) \int_0^t d\omega I_0(\sqrt{\omega^2-x^2})\Theta(\omega-|x|) - \Theta(t-|x|) \frac{\partial}{\partial x} I_0(\sqrt{\omega^2-x^2})\Theta(\omega-|x|) \right]. \end{aligned} \quad (9.28)$$

Now, because of the δ -function, the first term on r.h.s. of the above equation is non-zero only when $|x| = t$, but then again putting that in the θ -function, we get 0, since $(\omega - |t|)$ is

always less than 0. So the first term on the r.h.s. is always zero. Thus Eq. (9.28) reduces to

$$-\frac{1}{2} \frac{\partial}{\partial x} \left[\Theta(t - |x|) \int_0^t \left(d\omega \frac{\partial I_0(\sqrt{\omega^2 - x^2})}{\partial x} \Theta(\omega - |x|) - I_0(\sqrt{\omega^2 - x^2}) \delta(\omega - |x|) \operatorname{sgn}(x) \right) \right]. \quad (9.29)$$

Doing the delta-function integral, *i.e.*, the second integral above, we get $\Theta(t - |x|) \operatorname{sgn}(x)$.

The derivative of theta function in the first term gives zero in exactly the same way as above.

Thus (9.29) becomes,

$$-\frac{1}{2} \Theta(t - |x|) \int_0^t d\omega \frac{\partial^2 I_0(\sqrt{\omega^2 - x^2})}{\partial x^2} \Theta(\omega - |x|) + \frac{1}{2} \Theta(t - |x|) \int_0^t d\omega \frac{\partial I_0(\sqrt{\omega^2 - x^2})}{\partial x} \delta(\omega - |x|) \operatorname{sgn}(x) - \frac{1}{2} \delta(t - |x|) + \frac{1}{2} \Theta(t - |x|) 2\delta(x). \quad (9.30)$$

The second integral in (9.30) can be evaluated exactly and yields, $\frac{x}{\sqrt{\omega^2 - x^2}} I_1(\sqrt{\omega^2 - x^2}) \delta(\omega - |x|)$.

Now, using the properties of $I_1(z)$ for $z \rightarrow 0$, we write

$$\lim_{\omega \rightarrow |x|} \frac{I_1(\sqrt{\omega^2 - x^2})}{\sqrt{\omega^2 - x^2}} = \frac{1}{2},$$

and so the second term in (9.30) reduces to be $-\frac{|x|}{2} \Theta(t - |x|)$.

Thus,

$$\begin{aligned} \mathcal{F}^{-1} \left[\frac{q^2}{1 - q^2} \left(\cosh(t\sqrt{1 - q^2}) - 1 \right) \right] &= -\frac{1}{4} (\delta(x + t) + \delta(x - t)) + \frac{1}{2} \delta(x) - \frac{|x|}{8} \Theta(t - |x|) \\ &\quad - \frac{1}{4} \Theta(t - |x|) \int_0^t d\omega \frac{\partial^2}{\partial x^2} I_0(\sqrt{\omega^2 - x^2}) \Theta(\omega - |x|). \end{aligned} \quad (9.31)$$

Thus, combining Eqs. (9.23), (9.25) and (9.31), we get the full inverse transform as written in the main chapter.

9.4 Laplace Fourier Inversion of $\mathcal{G}(k, s)$ of the Continuous Process in the main chapter

We start from Eq. (2.61) in the main chapter, and putting the forms of $f(k, s)$ and $G(k, s)$ from Eqs. (2.59) and (2.60), we have

$$\mathcal{G}(k, s) = \frac{\gamma}{\left(\sqrt{(s + \gamma)^2 + v_0^2 k^2} - \gamma\right) \sqrt{(s + \gamma)^2 + v_0^2 k^2}}. \quad (9.32)$$

Let us put $s + \gamma = s'$ and rewrite $\mathcal{G}(k, s)$ as

$$\mathcal{G}(k, s') = \frac{\gamma}{\left(\sqrt{s'^2 + v_0^2 k^2} - \gamma\right) \left(\sqrt{s'^2 + v_0^2 k^2}\right)}. \quad (9.33)$$

We can now take the 2-d inverse Fourier transform from \vec{k} to \vec{r}

$$\tilde{P}(r, s') = \frac{1}{(2\pi)^2} \int_0^\infty k dk \int_0^{2\pi} d\psi e^{ikr \cos(\psi)} \mathcal{G}(k, s')$$

where ψ is the angle between \vec{k} and \vec{r} . Doing the ψ integral,

$$\tilde{P}(r, s') = \frac{1}{2\pi} \int_0^\infty k dk J_0(kr) \mathcal{G}(k, s'). \quad (9.34)$$

Doing the k integral is non-trivial. We first use an integral identity [152]

$$\int_0^1 dw \frac{(a - w)}{[(a - w)^2 + b^2(1 - w^2)]^{3/2}} = \frac{1}{\sqrt{a^2 + b^2}(\sqrt{a^2 + b^2} - 1)}. \quad (9.35)$$

The right-hand side of the above identity can be mapped to $\mathcal{G}(k, s')$ by identifying $a = \frac{s'}{\gamma}$ and $b = \frac{kv_0}{\gamma}$. Thus, we can write,

$$\mathcal{G}(k, s') = \gamma \int_0^1 dw \frac{(s' - \gamma w)}{[(s' - \gamma w)^2 + k^2 v_0^2 (1 - w^2)]^{3/2}}. \quad (9.36)$$

We now use an integral Bessel Function identity from Section 6.611 Eq. 1 of [152],

$$\int_0^\infty dt e^{-\alpha t} t J_0(\beta t) = \frac{\alpha}{(\alpha^2 + \beta^2)^{\frac{3}{2}}}.$$

Again the right-hand side of this identity can be mapped to the integrand in Eq. (9.36) if $\alpha = (s' - \gamma w)$ and $\beta = kv_0\sqrt{1 - w^2}$. Thus $\mathcal{G}(k, s')$ becomes

$$\gamma \int_0^1 dw \int_0^\infty dt e^{-(s' - \gamma w)t} t J_0(kv_0 t \sqrt{1 - w^2}). \quad (9.37)$$

Putting this back in the expression for $\tilde{P}(r, s')$, *i.e.*, Eq. (9.34), and substituting back $s = s' - \gamma$, we have

$$\tilde{P}(r, s) = \frac{\gamma e^{-\gamma t}}{2\pi} \int_0^\infty k dk \int_0^\infty dt e^{-st} t \int_0^1 dw e^{\gamma w t} J_0(kr) J_0(kv_0 t \sqrt{1 - w^2}). \quad (9.38)$$

Thereafter doing the k integral, we have

$$\tilde{P}(r, s) = \frac{\gamma e^{-\gamma t}}{2\pi v_0} \int_0^\infty dt e^{-st} \int_0^1 dw e^{\gamma w t} \frac{\delta(r - v_0 t \sqrt{1 - w^2})}{\sqrt{1 - w^2}} \quad (9.39)$$

Since the above equation is already in the form of a Laplace transformation $\int_0^\infty dt P(r, t) e^{-st}$, the inverse transform $P(r, t)$ can be immediately read out,

$$P(r, t) = \frac{\gamma e^{-\gamma t}}{2\pi v_0} \int_0^1 dw \frac{\delta(r - v_0 t \sqrt{1 - w^2})}{\sqrt{1 - w^2}} e^{\gamma w t}.$$

The w -integral can be done immediately due to the presence of the δ -function and yields,

$$P(r, t) = \frac{\gamma e^{-\gamma t} \exp\left[\frac{\gamma}{v_0} \sqrt{v_0^2 t^2 - r^2}\right]}{2\pi v_0 \sqrt{v_0^2 t^2 - r^2}}. \quad (9.40)$$

9.5 Exact first-passage time of a DRABP in the intermediate regime (II)

In this section we work out in detail the survival probability of a DRABP in the intermediate time regime ($\gamma^{-1} \ll t \ll D_R^{-1}$) along the direction orthogonal to the initial orientation. We

obtain this by setting $\theta_0 = 0$ where $x_\perp \equiv y$. Let $S_y(t; y_0)$ denote the probability that a particle starting from $(0, y_0)$ with an initial orientation $\theta_0 = 0$ has not crossed the $y = 0$ line till time t . Mathematically,

$$S_y(t; y_0) = \int_0^\infty dy P(y, t; y_0) \quad (9.41)$$

where $P(y, t; y_0)$ is the marginal probability distribution in the presence of an absorbing wall at $y = 0$, starting from the initial position y_0 . The survival probability in this regime is actually determined by trajectories which have already survived regime (I). Thus, in principle, one should take into account dynamics of both the regimes (I) and (II). However, the regime (I) almost vanishes for $\gamma \gg 1$ and it suffices to consider the effective dynamics in regime (II) only. Hence, we start with the Langevin equation along the y -direction [Eq. (3.40) with $\theta_0 = 0$] in the intermediate regime (II),

$$\dot{y} = v_0 \xi(t) \phi(t), \quad (9.42)$$

where $\phi(t)$ is a Brownian motion. We can write the corresponding forward Fokker-Planck (FP) equation for $P(y, \phi, t)$, *i.e.*, the probability that $y(t) = y$ and $\phi(t) = \phi$,

$$\frac{\partial}{\partial t} P(y, \phi, t) = \frac{v_0^2 \phi^2}{2\gamma} \frac{\partial^2}{\partial y^2} P(y, \phi, t) + D_R \frac{\partial^2}{\partial \phi^2} P(y, \phi, t). \quad (9.43)$$

Note that, for notational simplicity we have suppressed the initial position dependence. We need to solve this FP equation with the initial condition $P(y, \phi, 0) = \delta(y - y_0) \delta(\phi)$ and boundary conditions $P(y, \phi, t) \rightarrow 0$ as $\phi(t) \rightarrow \pm\infty$ and $P(0, \phi, t) = P(\infty, \phi, t) = 0$. For simplicity, we make a change of variable $\frac{v_0^2 t}{2\gamma} \rightarrow t$ and define $\Lambda^2 = 2\gamma D_R / v_0^2$. Equation (9.43) then becomes

$$\frac{\partial}{\partial t} P(y, \phi, t) = \phi^2 \frac{\partial^2}{\partial y^2} P(y, \phi, t) + \Lambda^2 \frac{\partial^2}{\partial \phi^2} P(y, \phi, t). \quad (9.44)$$

The absorbing boundary condition at $y = 0$ can be taken care of by using the sin-eigenbasis $\sin(ky)$ with $k \geq 0$. It is also convenient to take a Laplace transform w.r.t. time t ,

$$\tilde{P}(k, \phi, s) = \int_0^\infty dt e^{-st} \int_0^\infty dy \sin(ky) P(y, \phi, t). \quad (9.45)$$

Equation (9.44) reduces to an ordinary second order differential equation in terms of $\tilde{P}(k, \phi, s)$,

$$\Lambda^2 \frac{d^2}{d\phi^2} \tilde{P}(k, \phi, s) - (s + \phi^2 k^2) \tilde{P}(k, \phi, s) = -\sin(ky_0) \delta(\phi). \quad (9.46)$$

with the boundary condition $\tilde{P}(k, \phi, s) \rightarrow 0$ for $\phi \rightarrow \pm\infty$. For $\phi \neq 0$, The general solution of Eq. (9.46) is given by

$$\tilde{P}(k, \phi, s) = a D_{-q} \left(\phi \sqrt{\frac{2k}{\Lambda}} \right) + b D_{-q} \left(-\phi \sqrt{\frac{2k}{\Lambda}} \right), \quad (9.47)$$

where $q = \frac{1}{2} \left(1 + \frac{s}{k\Lambda} \right)$, $D_\nu(z)$ denotes the parabolic cylinder function [94] and a, b are two arbitrary constants independent of ϕ . Using the boundary conditions for $\phi \rightarrow \pm\infty$, and the fact that $\tilde{P}(k, \phi, s)$ is continuous at $\phi = 0$ we have,

$$\tilde{P}(k, \phi, s) = \begin{cases} a D_{-q} \left(\phi \sqrt{\frac{2k}{\Lambda}} \right), & \text{for } \phi > 0 \\ a D_{-q} \left(-\phi \sqrt{\frac{2k}{\Lambda}} \right), & \text{for } \phi < 0. \end{cases} \quad (9.48)$$

Integrating Eq. (9.46) across $\phi = 0$, we get,

$$\left. \frac{d\tilde{P}}{d\phi} \right|_{\phi=0+} - \left. \frac{d\tilde{P}}{d\phi} \right|_{\phi=0-} = -\frac{\sin(ky_0)}{\Lambda^2}.$$

Using this equation with Eq. (9.48) we get,

$$a = \frac{2^{\frac{q}{2}} \sin(ky_0)}{\sqrt{8\pi k \Lambda^3}} \Gamma \left(\frac{q}{2} \right). \quad (9.49)$$

Finally, combining Eq. (9.49) with Eq. (9.48) we get,

$$\tilde{P}(k, \phi, s) = \frac{2^{\frac{q}{2}} \sin(ky_0)}{\sqrt{8\pi k \Lambda^3}} \Gamma \left(\frac{q}{2} \right) D_{-q} \left(|\phi| \sqrt{\frac{2k}{\Lambda}} \right), \quad (9.50)$$

where, as before, we have denoted $q = \frac{1}{2}(1 + \frac{s}{k\Lambda})$. Since we are interested in the y -marginal distribution, we integrate over ϕ to get,

$$\hat{P}(k, s) = \frac{2 \sin(ky_0)}{s + k\Lambda} {}_2F_1\left(1, \frac{q+1}{2}, \frac{q+2}{2}, -1\right),$$

which is the sin-Laplace transform of $P(y, t)$. Here ${}_2F_1(a, b, c, z)$ denotes the Hypergeometric function [94].

To find the position distribution we need to invert the Laplace and sin transformations. The inverse Laplace transform is defined by the integral,

$$\hat{P}(k, t) = \int_{c_0-i\infty}^{c_0+i\infty} ds e^{st} \tilde{P}(k, s), \quad (9.51)$$

where c_0 is chosen such that all the singularities of the integrand lie to the left of the $Re(s) = c_0$ line. To compute the above integral let us first recast $\tilde{P}(k, s)$ as,

$$\tilde{P}(k, s) = \frac{2 \sin(ky_0)}{s + k\Lambda} {}_2\tilde{F}_1\left(1, \frac{q+1}{2}, \frac{q+2}{2}, -1\right) \Gamma\left(\frac{q+2}{2}\right), \quad (9.52)$$

where ${}_2\tilde{F}_1(a, b, c, z) = {}_2F_1(a, b, c, z)/\Gamma(c)$ denotes the regularized Hypergeometric function which is analytic for all values of a, b, c and z . From Eq. (9.52), it is straightforward to identify the singularities of $\tilde{P}(k, s)$, on the complex s -plane all of which lie on the negative real s -axis: $s_n = -k\Lambda(4n + 5)$ with $n = -1, 0, 1, 2, \dots$ where s_{-1} comes from the prefactor $(s + \Lambda k)^{-1}$ while $s_{n \geq 0}$ are obtained from the singularities $q_n = -2(n + 1)$ of $\Gamma\left(\frac{q+2}{2}\right)$.

The inverse Laplace transform of Eq. (9.52) can then be expressed as

$$\hat{P}(k, t) = \sum_{n=-1}^{\infty} e^{s_n t} R_n, \quad (9.53)$$

where R_n denotes the residue of $\tilde{P}(k, s)$ at $s = s_n$. These residues can be computed exactly and turn out to be

$$R_n = 2 \sin(ky_0) \frac{(-1)^{n+1}}{(n+1)!} {}_2\tilde{F}_1\left(1, -n - \frac{1}{2}, -n, -1\right).$$

Using the above expression in Eq. (9.53) and shifting $n \rightarrow n - 1$, we get,

$$\hat{P}(k, t) = 2 \sin(ky_0) \sum_{n=0}^{\infty} \frac{(-1)^n}{n!} e^{-(1+4n)k\Lambda t} {}_2\tilde{F}_1 \left(1, -n + \frac{1}{2}, -n + 1, -1 \right). \quad (9.54)$$

Using properties of Hypergeometric functions, it can be shown that

$${}_2\tilde{F}_1 \left(1, -n + \frac{1}{2}, -n + 1, -1 \right) = \frac{(-1)^n}{\sqrt{2}} \binom{-1/2}{n} n!.$$

Substituting the above identity in Eq. (9.54) we finally get,

$$\hat{P}(k, t) = \sqrt{2} \sin(ky_0) e^{-k\Lambda t} \sum_{n=0}^{\infty} \binom{-1/2}{n} e^{-4nk\Lambda t} = \frac{\sin(ky_0)}{\sqrt{\cosh(2k\Lambda t)}}. \quad (9.55)$$

The position distribution is given by the inverse sin-transform,

$$\begin{aligned} P(y, t; y_0) &= \frac{2}{\pi} \int_0^{\infty} dk \sin(ky) \hat{P}(k, t) = \frac{1}{\pi} \int_0^{\infty} dk \frac{2 \sin(ky) \sin(ky_0)}{\sqrt{\cosh(2k\Lambda t)}} \\ &= \frac{1}{\pi} \int_0^{\infty} dk \frac{[\cos(k(y - y_0)) - \cos(k(y + y_0))]}{\sqrt{\cosh(2k\Lambda t)}}. \end{aligned}$$

Clearly, $P(y, t)$ has a scaling form,

$$P(y, t; y_0) = \frac{1}{4\Lambda t} \left[f\left(\frac{y - y_0}{4\Lambda t}\right) - f\left(\frac{y + y_0}{4\Lambda t}\right) \right], \quad (9.56)$$

where, the scaling function $f(z)$ can be evaluated exactly,

$$f(z) = \frac{1}{\pi} \int_0^{\infty} d\kappa \frac{\cos(\kappa z)}{\sqrt{\cosh(\kappa/2)}} = \frac{1}{\sqrt{2\pi^3}} \Gamma\left(\frac{1}{4} + iz\right) \Gamma\left(\frac{1}{4} - iz\right). \quad (9.57)$$

The survival probability, given by Eq. (9.41), also has a scaling form,

$$S_y(t; y_0) = g\left(\frac{y_0}{4\Lambda t}\right), \quad (9.58)$$

where $g(z_0)$ is given by,

$$g(z_0) = \int_0^{\infty} dz [f(z - z_0) - f(z + z_0)] = 2 \int_0^{z_0} dz f(z). \quad (9.59)$$

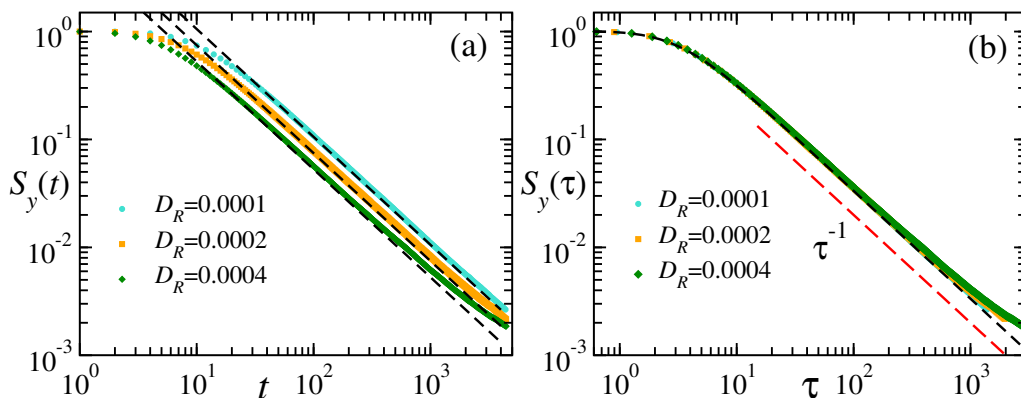


Figure 9.2: (a) Survival probability $S_y(t; y_0)$ for $\gamma = 80$ and three different values of D_R starting from $y_0 = 0.01$. The symbols indicate the data obtained from numerical simulations and the dashed black lines indicate the analytical prediction in Eq. (9.62). (b) shows the same data plotted against the scaled time $\tau = v_0 t \sqrt{\frac{8D_R}{\gamma}}$, the dashed black line is obtained by numerically integrating Eq. (9.64). The deviation from the analytical prediction at the tails is expected for $t \gtrsim D_R^{-1}$.

In terms of the original notation $t \rightarrow v_0^2 t / (2\gamma)$, and $\Lambda^2 = 2\gamma D_R / v_0^2$,

$$S_y(t; y_0) = g\left(\frac{y_0}{v_0 t} \sqrt{\frac{\gamma}{8D_R}}\right). \quad (9.60)$$

The large time behavior can be extracted easily by taking $z_0 \ll 1$,

$$g(z_0) = 2z_0 f(0) + O(z_0^2). \quad (9.61)$$

Thus, we have,

$$S(y_0, t) \approx \frac{\Gamma(1/4)^2}{2\pi^{3/2}} \sqrt{\frac{\gamma}{D_R}} \frac{y_0}{v_0 t} \quad \text{for} \quad \frac{y_0}{v_0 t} \ll \sqrt{\frac{D_R}{\gamma}} \ll 1. \quad (9.62)$$

Using this result we conclude in the main text that the survival probability of a DRABP in the time regime (II) $\gamma^{-1} \ll t \ll D_R^{-1}$ has a power-law decay with persistence exponent $\alpha_y = 1$.

Note that, the exact first-passage distribution $F_y(t) = -\partial_t S_y(t; y_0)$ can be easily computed

from Eq. (9.60),

$$F_y(t; y_0) = \frac{y_0 \sqrt{2} \gamma^{3/2}}{v_0^3 t^2 \sqrt{D_R}} f\left(\frac{y_0}{v_0 t} \sqrt{\frac{\gamma}{8D_R}}\right). \quad (9.63)$$

which was obtained in Ref. [117] in the context of diffusing diffusivity. In terms of the scaled time $\tau = v_0 t \sqrt{\frac{8D_R}{\gamma}}$,

$$S_y(\tau) = g(1/\tau) = 2 \int_0^{1/\tau} dz f(z) = 2 \int_\tau^\infty \frac{dz}{z^2} f(1/z), \quad (9.64)$$

where $f(z)$ is defined in Eq. (9.57).

9.6 Intermediate steps in the computation of $A_0^4(y, t)$ and $A_0^6(y, t)$ for DRABP

In this section, we provide the intermediate steps leading to the subleading contributions $A_0^4(y, t)$ and $A_0^6(y, t)$ for DRABP.

Setting $k = 6$ in Eq. (4.43a), we get an inhomogeneous diffusion equation for $A_0^4(y, t)$,

$$\left[\frac{\partial}{\partial t} - \frac{\partial^2}{\partial y^2} \right] A_0^4(y, t) = S_4(y, t), \quad (9.65)$$

where the inhomogeneous part is given by,

$$S_4(y, t) = \frac{\partial^2}{\partial y^2} \left[\left(-\frac{1}{\lambda+1} \frac{\partial}{\partial t} + \frac{1}{8} \frac{\partial^2}{\partial y^2} \right) A_0^2 + \left(\frac{1}{(\lambda+1)^2} \frac{\partial^2}{\partial t^2} - \frac{(\lambda+9)}{32(\lambda+1)} \frac{\partial^3}{\partial y^2 \partial t} + \frac{(\lambda+5)}{32(\lambda+9)} \frac{\partial^4}{\partial y^4} \right) A_0^0 \right]. \quad (9.66)$$

Considering the scaling form for $A_0^4(y, t)$, as given by Eq. (4.53) and using the explicit forms of $A_0^0(y, t)$ and $A_0^2(y, t)$, we have get an inhomogeneous Hermite equation for $q_4(z)$ like in Eq. (4.11). The inhomogeneous term is given by,

$$s_4(z) = \sum_{n=0}^4 r_{4,2n}(\lambda) z^{2n}, \quad (9.67)$$

where the coefficients $\{r_{4,n}\}$ are,

$$\begin{aligned}
 r_{4,0}(\lambda) &= -\frac{15}{256(\lambda+1)^2(\lambda+9)}(223 - 251\lambda + 45\lambda^2 + 7\lambda^3), \\
 r_{4,2}(\lambda) &= \frac{15}{32(\lambda+1)^2(\lambda+9)}(939 - 323\lambda + 25\lambda^2 + 7\lambda^3), \\
 r_{4,4}(\lambda) &= -\frac{15}{32(\lambda+1)^2(\lambda+9)}(1655 - 395\lambda + 5\lambda^2 + 7\lambda^3), \\
 r_{4,6}(\lambda) &= \frac{1}{8(\lambda+1)^2(\lambda+9)}(2371 - 467\lambda - 15\lambda^2 + 7\lambda^3), \\
 r_{4,8}(\lambda) &= -\frac{1}{16(\lambda+1)^2(\lambda+9)}(441 - 77\lambda - 5\lambda^2 + \lambda^3).
 \end{aligned}$$

The general solution for $q_4(z)$ can be again obtained using Eq. (4.13) in terms of an undetermined constant C_4 . This constant can be found out by comparing the coefficient of $(\tau/t)^2$ in the expansion of $M(4, 0, t)/(4t)^2$ of Eq. (4.29) to the one obtained from the approximate distribution Eq. (4.41) (more precisely Eq. (4.61) with $k = 2$). Following this procedure we finally get,

$$q_4(z) = \sum_{n=0}^4 \alpha_{4,n}(\lambda) z^{2n}, \quad (9.69)$$

with

$$\begin{aligned}
 \alpha_{4,0} &= -\frac{1}{2048(\lambda+1)^2(\lambda+9)}(2031 - 411\lambda - 963\lambda^2 - 57\lambda^3), \\
 \alpha_{4,1} &= -\frac{1}{256(\lambda+1)^2(\lambda+9)}(219 - 559\lambda + 273\lambda^2 + 27\lambda^3), \\
 \alpha_{4,2} &= \frac{1}{256(\lambda+1)^2(\lambda+9)}(9609 - 3789\lambda + 523\lambda^2 + 97\lambda^3), \\
 \alpha_{4,3} &= \frac{1}{64(\lambda+1)^2(\lambda+9)}(1655 - 395\lambda + 5\lambda^2 + 7\lambda^3), \\
 \alpha_{4,4} &= \frac{1}{128(\lambda+1)^2(\lambda+9)}(441 - 77\lambda - 5\lambda^2 + \lambda^3).
 \end{aligned} \quad (9.70)$$

Similarly, we can find an inhomogeneous diffusion equation for the next subleading order

contribution $A_0^6(y, t)$, by setting $k = 8$ in Eq. (4.43a),

$$\left[\frac{\partial}{\partial t} - \frac{\partial^2}{\partial y^2} \right] A_0^6(y, t) = S_6(y, t), \quad (9.71)$$

where the inhomogeneous term is given by,

$$\begin{aligned} S_6(y, t) = & \frac{\partial^2}{\partial y^2} \left[\left(-\frac{1}{\lambda+1} \frac{\partial}{\partial t} + \frac{1}{8} \frac{\partial^2}{\partial y^2} \right) A_0^4 \right. \\ & + \left(\frac{1}{(\lambda+1)^2} \frac{\partial^2}{\partial t^2} - \frac{\lambda+9}{32(\lambda+1)} \frac{\partial^3}{\partial t \partial y^2} + \frac{\lambda+5}{32(\lambda+9)} \frac{\partial^4}{\partial y^4} \right) A_0^2 \\ & - \left(\frac{1}{(\lambda+1)^3} \frac{\partial^3}{\partial t^3} - \frac{57+10\lambda+\lambda^2}{128(\lambda+1)^2} \frac{\partial^4}{\partial y^2 \partial t^2} + \frac{307+135\lambda+21\lambda^2+\lambda^3}{64(\lambda+1)(\lambda+9)^2} \frac{\partial^5}{\partial y^4 \partial t} \right. \\ & \left. \left. - \frac{481+162\lambda+17\lambda^2}{2048(\lambda+9)^2} \frac{\partial^6}{\partial y^6} \right) A_0^0 \right]. \end{aligned} \quad (9.72)$$

Again, considering the scaling form for $A_0^6(y, t)$, as given by Eq. (4.53) and using the explicit forms of $A_0^0(y, t)$, $A_0^2(y, t)$ and $A_0^4(y, t)$, we have get an inhomogeneous Hermite equation for $q_6(z)$ like in (4.11). The inhomogeneous term is given by,

$$s_6(z) = \sum_{n=0}^6 r_{6,2n}(\lambda) z^{2n}. \quad (9.73)$$

The coefficients $\{r_{6,n}\}$ are given by,

$$\begin{aligned} r_{6,0}(\lambda) &= \frac{-4389525 + 2500575\lambda + 2973390\lambda^2 - 626850\lambda^3 - 158025\lambda^4 - 7245\lambda^5}{16384(\lambda+1)^3(\lambda+9)^2}, \\ r_{6,2}(\lambda) &= \frac{979965 + 13285545\lambda - 11694270\lambda^2 + 480690\lambda^3 + 420945\lambda^4 + 24885\lambda^5}{4096(\lambda+1)^3(\lambda+9)^2}, \\ r_{6,4}(\lambda) &= \frac{108286605 - 63628215\lambda - 7444304\lambda^2 - 1734096\lambda^3 - 585375\lambda^4 - 45675\lambda^5}{4096(\lambda+1)^3(\lambda+9)^2}, \\ r_{6,6}(\lambda) &= \frac{-20520801 + 7463603\lambda - 930538\lambda^2 - 216762\lambda^3 + 29435\lambda^4 + 3255\lambda^5}{512(\lambda+1)^3(\lambda+9)^2}, \\ r_{6,8}(\lambda) &= \frac{17055513 - 4774859\lambda + 108634\lambda^2 + 142026\lambda^3 - 7715\lambda^4 - 1455\lambda^5}{1024(\lambda+1)^3(\lambda+9)^2}, \\ r_{6,10}(\lambda) &= \frac{-619479 + 145477\lambda + 7162\lambda^2 - 4118\lambda^3 + 45\lambda^4 + 33\lambda^5}{256(\lambda+1)^3(\lambda+9)^2}, \\ r_{6,12}(\lambda) &= \frac{27783 - 5733\lambda - 602\lambda^2 + 150\lambda^3 + 3\lambda^4 - \lambda^5}{256(\lambda+1)^3(\lambda+9)^2}. \end{aligned} \quad (9.74)$$

The general solution for $q_6(z)$ can be again obtained using Eq. (4.13) in terms of an undetermined constant C_6 . This constant can be found out by comparing the coefficient of $(\tau/t)^2$ in the expansion of $M(6, 0, t)/(4t)^3$ of Eq. (4.29) to the one obtained from the approximate distribution Eq. (4.41) (more precisely (4.61) with $k = 3$). Following this procedure we finally get,

$$q_6(z) = \sum_{n=0}^6 \alpha_{6,n}(\lambda) z^{2n}, \quad (9.75)$$

where the coefficients $\{\alpha_{6,n}(\lambda)\}$,

$$\begin{aligned} \alpha_{6,0}(\lambda) &= \frac{-908925 - 261945\lambda + 444030\lambda^2 + 311790\lambda^3 + 23535\lambda^4 + 315\lambda^5}{65536(\lambda + 1)^3(\lambda + 9)^2}, \\ \alpha_{6,1}(\lambda) &= \frac{-831375 + 1643205\lambda + 820650\lambda^2 - 781110\lambda^3 - 114315\lambda^4 - 4095\lambda^5}{16384(\lambda + 1)^3(\lambda + 9)^2}, \\ \alpha_{6,2}(\lambda) &= \frac{880905 + 3333045\lambda - 4445190\lambda^2 + 680970\lambda^3 + 216525\lambda^4 + 11025\lambda^5}{16384(\lambda + 1)^3(\lambda + 9)^2}, \\ \alpha_{6,3}(\lambda) &= \frac{1790095 - 1116021\lambda + 393878\lambda^2 + 10774\lambda^3 - 13365\lambda^4 - 945\lambda^5}{2048(\lambda + 1)^3(\lambda + 9)^2}, \\ \alpha_{6,4}(\lambda) &= \frac{-2931543 + 1066229\lambda - 132934\lambda^2 - 30966\lambda^3 + 4205\lambda^4 + 465\lambda^5}{4096(\lambda + 1)^3(\lambda + 9)^2}, \\ \alpha_{6,5}(\lambda) &= \frac{156933 - 41207\lambda - 270\lambda^2 + 1234\lambda^3 - 39\lambda^4 - 11\lambda^5}{1024(\lambda + 1)^3(\lambda + 9)^2}, \\ \alpha_{6,6}(\lambda) &= \frac{-27783 + 5733\lambda + 602\lambda^2 - 150\lambda^3 - 3\lambda^4 + \lambda^5}{3072(\lambda + 1)^3(\lambda + 9)^2}. \end{aligned} \quad (9.76)$$

The subleading order contributions obtained above are compared with numerical simulations in 4.3 and show good agreement.

9.7 Variance and kurtosis of the position distribution

Here we calculate the variance and kurtosis of the DRABP in a harmonic trap exactly. We use these to find the limiting expressions in the four different phases. Starting from the origin, the solution of the Langevin equation (5.1), for a given realization of $\{\sigma(s), \theta(s); 0 < s < t\}$,

gives the location $\{x(t), y(t)\}$ of the DRABP as,

$$\begin{aligned} x(t) &= v_0 \int_0^t ds e^{-\mu(t-s)} \sigma(s) \cos \theta(s), \\ y(t) &= v_0 \int_0^t ds e^{-\mu(t-s)} \sigma(s) \sin \theta(s). \end{aligned} \quad (9.77)$$

We consider the initial condition $\sigma(0) = \pm 1$ with equal probability $1/2$, which ensures that all the odd moments of the position vanish at all times. To calculate the first nontrivial moment, the variance, we need the two point correlations of the noises, which have already been calculated in Eq. (3.6). Using Eq. (9.77) and noise autocorrelations (we take $\theta_0 = 0$ for simplicity, as we are interested in the stationary moments which do not depend on the initial orientation) we obtain,

$$\begin{aligned} \langle x^2(t) \rangle &= \frac{v_0^2}{2\mu(2\gamma + D_R + \mu)} - \frac{v_0^2 (D_R - \mu) e^{-2\mu t}}{\mu(2D_R - \mu)(2\gamma + D_R - \mu)} - \frac{v_0^2 e^{-4D_R t}}{2(2D_R - \mu)(2\gamma - 3D_R + \mu)} \\ &+ \frac{2v_0^2 (2\gamma - D_R + \mu) e^{-(2\gamma + D_R + \mu)t}}{(2\gamma + D_R - \mu)(2\gamma + D_R + \mu)(2\gamma - 3D_R + \mu)}, \end{aligned} \quad (9.78)$$

and,

$$\begin{aligned} \langle y^2(t) \rangle &= \frac{v_0^2}{2\mu(2\gamma + D_R + \mu)} - \frac{v_0^2 D_R e^{-2\mu t}}{\mu(2D_R - \mu)(2\gamma + D_R - \mu)} + \frac{v_0^2 e^{-4D_R t}}{2(2D_R - \mu)(2\gamma - 3D_R + \mu)} \\ &- \frac{4v_0^2 D_R e^{-(2\gamma + D_R + \mu)t}}{(2\gamma + D_R - \mu)(2\gamma + D_R + \mu)(2\gamma - 3D_R + \mu)}. \end{aligned} \quad (9.79)$$

In the limit $t \rightarrow \infty$, both $\langle x^2(t) \rangle$ and $\langle y^2(t) \rangle$ relax to the same stationary value,

$$\langle x^2(t \rightarrow \infty) \rangle = \langle y^2(t \rightarrow \infty) \rangle = \frac{v_0^2}{2\mu(2\gamma + D_R + \mu)} + O(e^{-\lambda t}), \quad (9.80)$$

where $\lambda = \min(2\mu, 4D_R, 2\gamma + D_R + \mu)$ gives the leading order time-scale of relaxation to the stationary value.

For a Gaussian distribution, all the higher order cumulants $\langle x^n \rangle_c$ with $n > 2$ are zero.

The widely used measure to identify non-Gaussianity is the fourth cumulant $\langle x^4 \rangle_c$, which is also known as kurtosis. It is often expressed in the dimensionless form,

$$\kappa(t) = \frac{\langle x^4(t) \rangle - 3\langle x^2(t) \rangle^2}{\langle x^2(t) \rangle^2}. \quad (9.81)$$

Note that, however, vanishing kurtosis is not a sufficient condition for Gaussianity. Clearly, to compute the kurtosis, we need the fourth moment of the distribution, which can be calculated using Eq. (9.77) and the four-point correlations of the noises. Using the propagators Eqs. (3.3) and (3.4) these four-point correlations can be calculated in a straightforward manner. For $t_1 < t_2 < t_3 < t_4$,

$$\langle \sigma(t_1)\sigma(t_2)\sigma(t_3)\sigma(t_4) \rangle = e^{-2\gamma(t_4-t_3)}e^{-2\gamma(t_2-t_1)}, \quad (9.82)$$

and for the θ -process,

$$\begin{aligned} \langle \cos \theta(t_1) \cos \theta(t_2) \cos \theta(t_3) \cos \theta(t_4) \rangle &= \frac{1}{8} e^{-D_R(7t_1+5t_2+3t_3+t_4)} \left(e^{12D_R t_1} + e^{8D_R(t_1+t_2)} + e^{4D_R(t_1+2t_2)} \right. \\ &\quad \left. + 2e^{4D_R(t_1+t_2+t_3)} + 2e^{4D_R(2t_1+t_2+t_3)} + 1 \right). \end{aligned} \quad (9.83)$$

The full time-dependent fourth moment has a fairly large expression which upon taking the $t \rightarrow \infty$ limit yields,

$$\langle x^4(t \rightarrow \infty) \rangle = \frac{3(4D_R + 3\mu)}{8\mu^2(2D_R + \mu)(2\gamma + D_R + \mu)(2\gamma + D_R + 3\mu)}. \quad (9.84)$$

The stationary state value of the kurtosis can be readily obtained using the second and fourth moments derived above, and comes out to be,

$$\kappa(t \rightarrow \infty) = \frac{3\mu(2\gamma - 7D_R - 3\mu)}{2(2D_R + \mu)(2\gamma + D_R + 3\mu)}. \quad (9.85)$$

The limiting expressions of variance and kurtosis in the different phases can be easily obtained from Eq. (9.80) and (9.85) respectively:

- In the limit $v_0 \rightarrow \infty$, $D_R \rightarrow \infty$ with arbitrary γ and $\mu \ll D_R$, keeping $v_0^2/(D_R + 2\gamma) =$

$2D_{\text{DR}}$ constant (passive-I phase), we get

$$\langle x^2 \rangle = \frac{D_{\text{DR}}}{\mu} \quad \text{and} \quad \kappa = 0. \quad (9.86)$$

- In the limit $\mu \gg D_R$ and $\gamma \rightarrow 0$ (active-I phase), we have

$$\langle x^2 \rangle = \frac{v_0^2}{2\mu^2} \quad \text{and} \quad \kappa = -\frac{3}{2}. \quad (9.87)$$

- In the limit $D_R \rightarrow 0$ (active-II and passive-II phases)

$$\langle x^2 \rangle = \frac{v_0^2}{2\mu(2\gamma + \mu)} \quad \text{and} \quad \kappa = \frac{3(2\gamma - 3\mu)}{2(2\gamma + 3\mu)}. \quad (9.88)$$

The kurtosis is always negative in the active phases. On the other hand, in the passive-II phase the kurtosis is negative in the region $1/2 < \gamma/\mu < 3/2$ and becomes positive for $\gamma/\mu > 3/2$. Note that, zero kurtosis for $\gamma/\mu = 3/2$ in the $D_R \rightarrow 0$ limit of the passive-II phase does not imply a Gaussian distribution, as is evident from Eq. (5.22). On the other hand, for the passive-I phase, Eq. (5.8) implies that kurtosis and all the other higher cumulants are zero.

9.8 Saddle Point Integral

Saddle point integration technique has been used quite extensively in this article. In this Appendix we show the evaluation of $H(r, t)$ (in Eq. (6.16)) using this method; all the other integrals are also computed in a similar way

$$H(r = zv_0t, t) = \frac{\alpha\gamma zv_0t}{v_0^2} \int_z^1 d\tau e^{-t\phi(z, \tau)} \frac{1}{\sqrt{\tau^2 - z^2}} \quad (9.89)$$

with $\phi(z, \tau) = (\alpha + \gamma)\tau - \gamma\sqrt{\tau^2 - z^2}$. The function $\phi(z, \tau)$ always has a minimum w.r.t. τ at some τ_0 , which is obtained by solving

$$\left. \frac{\partial\phi(z, \tau)}{\partial\tau} \right|_{\tau=\tau_0} = 0 \Rightarrow \tau_0 = \frac{z(\alpha + \gamma)}{\sqrt{\alpha^2 + 2\alpha\gamma}}. \quad (9.90)$$

Since the denominator of the integrand in Eq. (9.89) is a monotonically decreasing function for $\tau > z$, the integrand has a maximum at $\tau = \tau_0$. For large t , the integrand becomes sharply peaked at τ_0 , so we can expand $\phi(z, \tau)$ in a Taylor series about $\tau = \tau_0$,

$$\phi(z, \tau) = \phi(z, \tau_0) + \frac{(\tau - \tau_0)^2}{2} \phi''(z, \tau_0) + \mathcal{O}[(\tau - \tau_0)^3]. \quad (9.91)$$

Keeping upto the quadratic term in the expansion for $\phi(z, \tau)$, gives a very good estimate of the integral in Eq. (9.89) at large t .

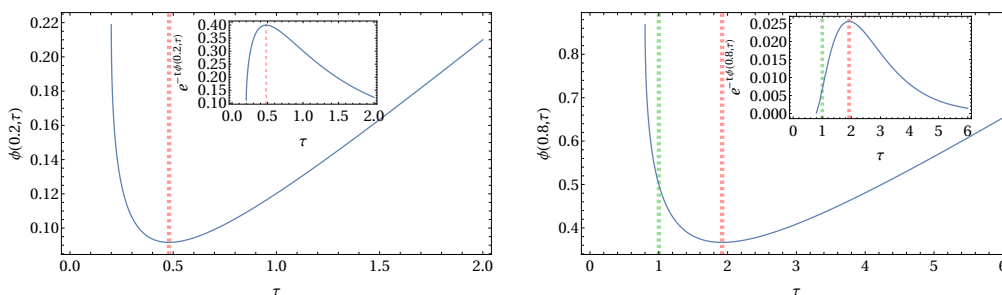


Figure 9.3: Plot of $\phi(z, \tau)$ and $e^{-t\phi(z, \tau)}$ for $\alpha = 0.1; \gamma = 1$: Left panel shows a case where $z < \frac{(\alpha+\gamma)}{\sqrt{\alpha^2+2\alpha\gamma}}$, while the right panel shows a case where $z > \frac{\sqrt{\alpha^2+2\alpha\gamma}}{(\alpha+\gamma)}$. The red dashed lines denote the actual minimum of the functions while the green dashed ones on the right panel denote the point $\tau = 1$. We have taken $t = 10$ in the insets. The peak becomes sharper as we keep increasing t .

This form of $\phi(z, \tau)$ is used when $z < \tau_0 < 1$, *i.e.*, τ_0 lies within the integration limits *i.e.*, $[z, 1]$.

$$H(r = zv_0 t, t) \approx \frac{\alpha\gamma z v_0 t}{\sqrt{2}v_0^2} \frac{e^{-t\phi(z, \tau_0)}}{\sqrt{\tau_0^2 - z^2}} \int_{-\infty}^{\infty} d\tau' e^{-t\phi''(z, \tau_0)\tau'^2} = \frac{\alpha\gamma\sqrt{zv_0 t}\sqrt{\pi/2}}{v_0^2(\alpha^2 + 2\alpha\gamma)^{1/4}} e^{-zt\sqrt{\alpha^2+2\alpha\gamma}} \quad (9.92)$$

If $\tau_0 > 1$ *ie*, $z > \frac{\sqrt{\alpha^2+2\alpha\gamma}}{(\alpha+\gamma)}$, then within the integration limits the integrand reaches its maximum value at the boundary $\tau_0 = 1$ as shown in 9.3. In such a scenario we can still expand $\phi(z, \tau)$ about $\tau = 1$ as,

$$\phi(z, \tau) = \phi(z, 1) + (1 - \tau)\phi'(z, 1) + \mathcal{O}[(\tau - 1)^2] \quad (9.93)$$

At large t we keep upto the second term in the above expansion and have

$$H(r = zv_0t, t) \approx \frac{\alpha\gamma zv_0t}{\sqrt{2}v_0^2} \frac{e^{-t\phi(z,1)}}{\sqrt{1-z^2}} \int_z^1 d\tau e^{-t(\tau-1)\phi'(z,1)} = A(z)e^{-(\alpha+\gamma)t+\gamma t\sqrt{1-z^2}} \quad (9.94)$$

where

$$A(z) = \frac{\alpha\gamma zt}{\sqrt{2}v_0(1-z^2)^{1/2}} \frac{\left(1 - e^{-t(1-z)|\phi'(z,1)|}\right)}{t|\phi'(z,1)|}. \quad (9.95)$$

and $\phi'(z,1) = \frac{1}{\sqrt{1-z^2}} \left((\alpha + \gamma)\sqrt{1-z^2} - \gamma \right)$. Note that the exponential part in Eq. (9.94) gives the leading order contribution to $H(r, t)$, while $A(z, t)$ gives a sub-leading contribution. This along with the 2nd term on the rhs of Eq. (6.14) is plotted in Figure 6.2 (b) with magenta lines.

9.9 Stationary state Current

In this section, we sketch the main steps of the computation of the current starting from Eq. (4) in the main text. For the sake of completeness we first rewrite the Langevin equations Eqs. (1),

$$M\ddot{X}(t) = -\Phi X(t) - \Gamma \dot{X}(t) + \Xi(t) + F(t), \quad (9.96)$$

where, $X(t) = \{x_l(t); l = 1, \dots, N\}$ is a vector, M is an N -dimensional diagonal matrix with $M_{lj} = m\delta_{l,j}$; Φ and Γ are N -dimensional matrices given by

$$\begin{aligned} \Phi_{jl} &= k(2\delta_{j,l} - \delta_{j,l-1} - \delta_{j,l+1}), \\ \Gamma &= \Gamma_L + \Gamma_R \quad \text{with} \quad (\Gamma_L)_{jl} = \gamma\delta_{j,1}\delta_{l,1}, \quad (\Gamma_R)_{jl} = \gamma\delta_{j,N}\delta_{l,N}. \end{aligned} \quad (9.97)$$

Moreover, the vectors $\Xi(t)$ and $F(t)$ represent the thermal and active forces exerted by the reservoirs on the boundary oscillators,

$$\begin{aligned} \Xi(t) &= \Xi_L(t) + \Xi_R(t) \quad \text{with} \quad (\Xi_L)_j(t) = \xi_1(t)\delta_{j,1} \\ F(t) &= F_L(t) + F_R(t) \quad \text{with} \quad (F_L)_j(t) = f_1(t)\delta_{j,1} \quad \text{and} \quad (F_R)_j(t) = f_N(t)\delta_{j,N}. \end{aligned}$$

Here, $\xi_{1,N}(t)$ are delta correlated white-noises, while the active noises $f_{1,N}(t)$ have an exponentially decaying auto-correlation,

$$\langle \xi_j(t) \xi_l(t') \rangle = \delta_{jl} 2\gamma T_j \delta(t-t'), \quad \text{and,} \quad \langle f_j(t) f_l(t') \rangle = \delta_{jl} a_j^2 e^{-|t-t'|/\tau_j}. \quad (9.99)$$

Note that, even though Eq. (9.96) formally appears to be a limiting case of [153] with vanishing bulk activity, the two scenarios differ by their physical nature as well as emergent phenomena, as we will see below.

The stationary energy current flowing through the system can be expressed as $J = \langle \mathcal{J}(t) \rangle$ where

$$\mathcal{J}(t) = \dot{x}_1 [-\gamma \dot{x}_1 + \xi_1(t) + f_1(t)] \quad (9.100)$$

denotes the instantaneous work done by, the left reservoir on the left boundary oscillator and the statistical averaging is done over the stationary state. It is convenient to recast this energy current using the above matrix notation and separate it into two terms,

$$J = J_1 + J_2 \quad \text{with,} \quad J_1 = -\text{Tr} \left[\langle \dot{X}(t) \dot{X}^T(t) \Gamma_L \rangle \right] \quad \text{and} \quad J_2 = \text{Tr} \left[\langle (\Xi_L + F_L) \dot{X}^T(t) \rangle \right] \quad (9.101)$$

where \dot{X}^T denotes the transpose of the vector \dot{X} . In the following we compute J_1 and J_2 separately using the solution of Eq. (9.96),

$$X(t) = \int_{-\infty}^{\infty} \frac{d\omega}{2\pi} e^{-i\omega t} G(\omega) [\Xi(\omega) + F(\omega)], \quad (9.102)$$

where $G(\omega) = [-M\omega^2 + \Phi - i\omega(\Gamma_L + \Gamma_R)]^{-1}$ [see Eq. (10)]. Let us first consider,

$$\begin{aligned} J_1 &= \int_{-\infty}^{\infty} \frac{d\omega}{2\pi} \int_{-\infty}^{\infty} \frac{d\omega'}{2\pi} \omega \omega' e^{-i(\omega+\omega')t} \text{Tr} \left[\langle \tilde{X}(\omega) \tilde{X}^T(\omega') \rangle \Gamma_L \right] \\ &= \int_{-\infty}^{\infty} \frac{d\omega}{2\pi} \int_{-\infty}^{\infty} \frac{d\omega'}{2\pi} \omega \omega' e^{-i(\omega+\omega')t} \text{Tr} \left[G(\omega) \langle [\Xi(\omega) + F(\omega)] [\Xi(\omega') + F(\omega')] \rangle G(\omega') \Gamma_L \right], \end{aligned} \quad (9.103)$$

where we have used the fact that $G^T(\omega') = G(\omega')$ as G is a symmetric matrix. The noise correlations appearing in the above equation can be evaluated in a straightforward manner

using Eqs. (9.98)-(9.99). Since the noises from the two reservoirs are independent, it is natural to separate the corresponding contributions and write,

$$\langle [\Xi(\omega) + F(\omega)] [\Xi(\omega') + F(\omega')] \rangle = 2\pi\delta(\omega + \omega') [S_L(\omega) + S_R(\omega)], \quad (9.104)$$

where the matrix elements of $S_{L,R}(\omega)$ are given by,

$$(S_L(\omega))_{jl} = [2\gamma T_1 + \tilde{g}(\tau_1, \omega)]\delta_{j,1}\delta_{l,1}, \quad \text{and} \quad (S_R)_{jl} = [2\gamma T_N + \tilde{g}(\tau_N, \omega)]\delta_{j,N}\delta_{l,N}, \quad (9.105)$$

Here $\tilde{g}(\tau_j, \omega)$ denotes the Fourier transform of the active force auto-correlation

$$\tilde{g}(\tau_j, \omega) = a_j^2 \int_{-\infty}^{\infty} ds e^{i\omega s} e^{-|s|/\tau_j} = \frac{2a_j^2\tau_j}{(1 + \omega^2\tau_j^2)}. \quad (9.106)$$

Using Eqs. (9.104) and (9.105) in Eq. (9.103), we get,

$$J_1 = - \int_{-\infty}^{\infty} \frac{d\omega}{2\pi} \omega^2 \text{Tr} \left[G(\omega) (S_L(\omega) + S_R(\omega)) G^*(\omega) \Gamma_L \right], \quad (9.107)$$

where $G^*(\omega) = G(-\omega)$ denotes the complex conjugate of $G(\omega)$. Proceeding similarly for J_2 , we have from Eq. (9.101) and Eq. (9.104),

$$J_2 = i \int_{-\infty}^{\infty} \frac{d\omega}{2\pi} \omega \text{Tr} [G^*(\omega) S_L(\omega)]. \quad (9.108)$$

Combining Eqs. (9.107) and (9.108) and rearranging the terms, we have,

$$J = \int_{-\infty}^{\infty} \frac{d\omega}{2\pi} \omega \text{Tr} \left[\left(iG^*(\omega) - \omega G^*(\omega) \Gamma_L G(\omega) \right) S_L(\omega) \right] - \int_{-\infty}^{\infty} \frac{d\omega}{2\pi} \omega^2 \text{Tr} \left[G^*(\omega) \Gamma_L S_R(\omega) \right]. \quad (9.109)$$

Now, remembering the definition of $G(\omega) = [-M\omega^2 + \Phi - i\omega(\Gamma_L + \Gamma_R)]^{-1}$, it can be easily shown that,

$$G^*(\omega) \Gamma_L G(\omega) = \frac{G(\omega) - G^*(\omega)}{2i\omega} - G^*(\omega) \Gamma_R G(\omega). \quad (9.110)$$

Using the above relation the first term of Eq. (9.109) can be further simplified,

$$\begin{aligned}
 & \int_{-\infty}^{\infty} \frac{d\omega}{2\pi} \omega \operatorname{Tr} \left[\left(iG^*(\omega) - \omega G^*(\omega) \Gamma_L G(\omega) \right) S_L(\omega) \right] \\
 = & \frac{i}{2} \int_{-\infty}^{\infty} \frac{d\omega}{2\pi} \omega \operatorname{Tr} \left[\left(G(\omega) + G^*(\omega) \right) S_L(\omega) \right] + \int_{-\infty}^{\infty} \frac{d\omega}{2\pi} \omega^2 \operatorname{Tr} \left[G^*(\omega) \Gamma_R G(\omega) S_L(\omega) \right].
 \end{aligned} \tag{9.111}$$

The first integral on the second line vanishes as $\omega(G(\omega) + G^*(\omega))S_L(\omega)$ is an odd function of ω , and we finally have, from Eqs. (9.109) and (9.111),

$$J = \int_{-\infty}^{\infty} \frac{d\omega}{2\pi} \omega^2 \operatorname{Tr} \left[G(\omega) \Gamma_R G^*(\omega) S_L(\omega) - G(\omega) S_R(\omega) G^*(\omega) \Gamma_L \right]. \tag{9.112}$$

From the expressions of $S_L(\omega)$ and $S_R(\omega)$ given in Eq. (9.105) it is immediately clear that J separates into two parts — $J = J_{\text{th}} + J_{\text{act}}$, where,

$$J_{\text{th}} = \gamma^2 (T_1 - T_N) \int_{-\infty}^{\infty} \frac{d\omega}{2\pi} \omega^2 |G_{1N}(\omega)|^2, \quad \text{and} \tag{9.113a}$$

$$J_{\text{act}} = J_{\text{act}}^1 - J_{\text{act}}^N \quad \text{with} \quad J_{\text{act}}^j = \gamma \int_{-\infty}^{\infty} \frac{d\omega}{2\pi} \omega^2 |G_{1N}(\omega)|^2 \tilde{g}(\tau_j, \omega). \tag{9.113b}$$

The thermal current J_{th} is well known in the literature [147, 137] and is given by,

$$J_{\text{th}} = \frac{k(T_1 - T_N)}{2\gamma} \left[1 + \frac{mk}{2\gamma^2} - \frac{mk}{2\gamma^2} \sqrt{1 + \frac{4\gamma^2}{mk}} \right]. \tag{9.114}$$

In the following we compute the active current J_{act} exactly. To this end, we first need the explicit form for the matrix element $G_{1N}(\omega)$. This has been calculated in the context of thermal transport [137], we revisit the calculation here for the sake of completeness.

By definition, $G(\omega)$ is the inverse of a tri-diagonal matrix (see Eq. (7.24)) and the elements $G_{ij}(\omega)$ can be computed explicitly exploiting this tridiagonal structure of $G^{-1}(\omega)$ [141]. In particular, we will need the following elements,

$$G_{l1}(\omega) = (-k)^{l-1} \frac{\theta_{N-l}}{\theta_N}, \quad \text{and} \tag{9.115a}$$

$$G_{lN}(\omega) = (-k)^{N-l} \frac{\theta_{l-1}}{\theta_N} \tag{9.115b}$$

where θ_l satisfies the recursion relation,

$$\theta_l = (-m\omega^2 + 2k)\theta_{l-1} - k^2\theta_{l-2} \quad \text{for } l = 2, 3, \dots, N-1, \quad (9.116a)$$

$$\text{and } \theta_N = (-m\omega^2 + 2k - i\omega\gamma)\theta_{N-1} - k^2\theta_{N-2}. \quad (9.116b)$$

Using the boundary conditions $\theta_0 = 1$ and $\theta_1 = (-m\omega^2 + 2k - i\omega\gamma)$ [141], the recursion relation (9.116a) can be solved in a straightforward manner. It is convenient to express the solution as,

$$\theta_l = \frac{(-k)^{l-1}}{\sin(q)} [k \sin((l+1)q) - i\omega\gamma \sin(lq)] \quad \text{for } l = 2, 3, \dots, N-1, \quad (9.117)$$

where q and ω are related by,

$$\cos q = \left(1 - \frac{m\omega^2}{2k}\right) \Rightarrow \omega = \omega_c \sin \frac{q}{2}, \quad (9.118)$$

where $\omega_c = 2\sqrt{k/m}$. Using Eq. (9.117) in Eq. (9.116b) we then have,

$$\theta_N = \frac{(-k)^N}{\sin q} [a(q) \sin(Nq) + b(q) \cos(Nq)], \quad (9.119)$$

where,

$$a(q) = -\frac{2i\gamma\omega}{k} + \cos q \left(1 - \frac{\gamma^2\omega^2}{k^2}\right), \quad \text{and } b(q) = \sin q \left(1 + \frac{\gamma^2\omega^2}{k^2}\right). \quad (9.120)$$

Now we can proceed to compute the active current. Using Eq. (9.119) and Eq. (9.115b) for $l = 1$ in Eq. (9.113b), we get,

$$J_{\text{act}}^1 = \frac{\gamma}{\pi k^2} \int_0^\infty d\omega \omega^2 \frac{\sin^2 q}{|a(q) \sin(Nq) + b(q) \cos(Nq)|^2} \tilde{g}(\tau_1, \omega). \quad (9.121)$$

At this point, it is important to note that, for $\omega > \omega_c$, q becomes complex. Thus, for large N , in the region $\omega > \omega_c$, the integrand vanishes exponentially as $\exp(-2N\bar{q})$, where \bar{q} is real. Thus, to compute the current for thermodynamically large systems, we can limit the range of integration in Eq. (9.121) to be $0 \leq \omega \leq \omega_c$ or equivalently, $0 \leq q \leq \pi$. Moreover, the functions $\sin(Nq)$ and $\cos(Nq)$ are highly oscillatory for large N and in the $N \rightarrow \infty$ limit,

we can average over $x = Nq$ and write [140],

$$J_{\text{act}}^1 = \frac{\gamma}{\pi k^2} \int_0^{\omega_c} d\omega \omega^2 \sin^2 q \tilde{g}(\tau_1, \omega) \int_0^{2\pi} \frac{dx}{2\pi} \frac{1}{|a(q) \sin x + b(q) \cos x|^2}. \quad (9.122)$$

The x -integral has a simple form and can be evaluated exactly (see Sec. 2.558 in [152]),

$$\int_0^{2\pi} \frac{dx}{2\pi} \frac{1}{(c_1 \sin x + d \cos x)^2 + c_2^2 \sin^2 x} = -\frac{1}{dc_2}, \quad (9.123)$$

where we have denoted $c_1 = \text{Re}[a(q)]$, $c_2 = \text{Im}[a(q)]$ and $d = b(q)$ for notational simplicity.

Substituting Eq. (9.123) in Eq. (9.122), we get,

$$J_{\text{act}}^1 = \frac{k}{2\pi} \int_0^{\omega_c} d\omega \frac{\omega \sin q}{k^2 + \gamma^2 \omega^2} \tilde{g}(\tau_1, \omega) = \frac{k}{2} \int_0^\pi \frac{dq}{\pi} \left| \frac{d\omega}{dq} \right| \frac{\omega \sin q}{k^2 + \gamma^2 \omega^2} \tilde{g}(\tau_1, \omega). \quad (9.124)$$

Thereafter, using the Jacobian $|\frac{d\omega}{dq}| = \frac{k \sin q}{m\omega}$, we arrive at,

$$J_{\text{act}}^1 = \int_0^\pi \frac{dq}{\pi} \frac{mk\tau_1 a_1^2 \sin^2 q}{[mk + 2\gamma^2(1 - \cos q)][m + 2k\tau_1^2(1 - \cos q)]}, \quad (9.125)$$

where we have also expressed $\tilde{g}(\tau_1, \omega)$ as a function of q . This integral can be evaluated exactly and leads to,

$$J_{\text{act}}^1 = \frac{m}{2\gamma^2} a_1^2 \mathcal{E}_1 \quad \text{with} \quad \mathcal{E}_1 = \frac{\tau_1^2 k^2 \left[\sqrt{1 + \frac{4\gamma^2}{mk}} - 1 \right] + \gamma^2 \left[1 - \sqrt{1 + \frac{4k\tau_1^2}{m}} \right]}{2\tau_1(\tau_1^2 k^2 - \gamma^2)}. \quad (9.126)$$

One can similarly obtain $J_{\text{act}}^N = \frac{m}{2\gamma^2} a_N^2 \mathcal{E}_N$, where,

$$\mathcal{E}_N = \frac{\tau_N^2 k^2 \left[\sqrt{1 + \frac{4\gamma^2}{mk}} - 1 \right] + \gamma^2 \left[1 - \sqrt{1 + \frac{4k\tau_N^2}{m}} \right]}{2\tau_N(\tau_N^2 k^2 - \gamma^2)}. \quad (9.127)$$

The total active current is obtained by combining Eq. (9.127) and (9.126), which is quoted in Eq. (5).

9.10 Kinetic temperature profile

The kinetic temperature of the l^{th} oscillator as defined in the main text is given by,

$$\hat{T}_l = m \langle \dot{x}_l^2(t) \rangle. \quad (9.128)$$

Since we are primarily interested in the effect of the active driving, we put $T_1 = T_N = 0$. Then, from Eq. (9.102), we get,

$$\hat{T}_l = m \int_{-\infty}^{\infty} \frac{d\omega}{2\pi} \omega^2 \left[|G_{l1}(\omega)|^2 \tilde{g}(\tau_1, \omega) + |G_{lN}(\omega)|^2 \tilde{g}(\tau_N, \omega) \right]. \quad (9.129)$$

From Eqs. (9.115) we have,

$$|G_{l1}(\omega)|^2 = \frac{k^{2N-4}}{\sin^2 q |\theta_N|^2} \left| k \sin(N-l+1)q - i\omega\gamma \sin(N-l)q \right|^2, \quad (9.130a)$$

$$|G_{lN}(\omega)|^2 = \frac{k^{2N-4}}{2 \sin^2 q |\theta_N|^2} \left| k \sin(l)q - i\omega\gamma \sin(l-1)q \right|^2. \quad (9.130b)$$

We are particularly interested in the behavior of the kinetic temperature in the bulk in the thermodynamic limit $N \rightarrow \infty$. For this purpose we evaluate \hat{T}_l for $l = N/2 + \ell$ where $\ell \ll N$. Let us first consider the contribution from the left reservoir, i.e., the first term in Eq. (9.129). Once again, the integrand vanishes exponentially for $\omega > \omega_c$ in the large N limit, and we can write,

$$\begin{aligned} I_1 &\equiv \int_{-\infty}^{\infty} \frac{d\omega}{2\pi} \omega^2 |G_{l1}(\omega)|^2 \tilde{g}(\tau_1, \omega) \\ &= \frac{1}{k^4} \int_0^\pi \frac{dq}{2\pi} \left| \frac{d\omega}{dq} \right| \omega^2 \frac{k^2 (1 - \cos(N-2\ell+2)q) + \omega^2 \gamma^2 (1 - \cos(N-2\ell)q)}{|a(q) \sin(Nq) + b(q) \cos(Nq)|^2} \tilde{g}(\tau_1, \omega). \end{aligned} \quad (9.131)$$

As before, in the $N \rightarrow \infty$ limit, we can average over the fast oscillations in $x = Nq$. For this purpose, let us note,

$$\int_0^{2\pi} \frac{dx}{2\pi} \frac{\sin x}{(c_1 \sin x + d \cos x)^2 + c_2^2 \sin^2 x} = \int_0^{2\pi} \frac{dx}{2\pi} \frac{\cos x}{(c_1 \sin x + d \cos x)^2 + c_2^2 \sin^2 x} = 0 \quad (9.132)$$

Using these identities and Eq. (9.123), Eq. (9.131) reduces to,

$$I_1 = \frac{1}{2\gamma k} \int_0^\pi \frac{dq}{2\pi} \left| \frac{d\omega}{dq} \right| \frac{\omega}{\sin q} \tilde{g}(\tau_1, \omega) = \frac{1}{4\pi\gamma m} \int_0^\pi dq \tilde{g}(\tau_1, \omega(q)) \quad (9.133)$$

The q -integral can be evaluated exactly, and yields,

$$I_1 = \frac{1}{2\gamma m} \frac{a_1^2 \tau_1}{\sqrt{1 + 4\tau_1^2 k/m}}. \quad (9.134)$$

The integral involving G_{lN} can also be performed following the same procedure and results in,

$$I_2 \equiv \int_{-\infty}^{\infty} \frac{d\omega}{2\pi} \omega^2 |G_{lN}(\omega)|^2 \tilde{g}(\tau_N, \omega) = \frac{1}{2\gamma m} \frac{a_N^2 \tau_N}{\sqrt{1 + 4\tau_N^2 k/m}}. \quad (9.135)$$

Combining these results, we see that the kinetic temperature remains uniform in the bulk and is given by,

$$\hat{T}_{bulk} = \frac{1}{2\gamma} \left(\frac{a_1^2 \tau_1}{\sqrt{1 + 4\tau_1^2 k/m}} + \frac{a_N^2 \tau_N}{\sqrt{1 + 4\tau_N^2 k/m}} \right). \quad (9.136)$$

This is the result presented in Eq. (6).

For a finite chain the kinetic temperature deviates from \hat{T}_{bulk} near the boundaries giving rise to exponentially decaying boundary layers; see Fig. 9.4(a). To obtain the behavior of the boundary layers, we need to evaluate Eq. (9.129) in the limits $l \ll N$ and $l \sim N$.

9.10.1 \hat{T}_l near left boundary

Let us first concentrate near the left boundary, where $l = 1, 2, 3 \dots \ll N$. For convenience, we rewrite Eq. (9.129) as,

$$\hat{T}_l = m[L_1(l, \tau_1) + L_N(l, \tau_N)], \quad (9.137)$$

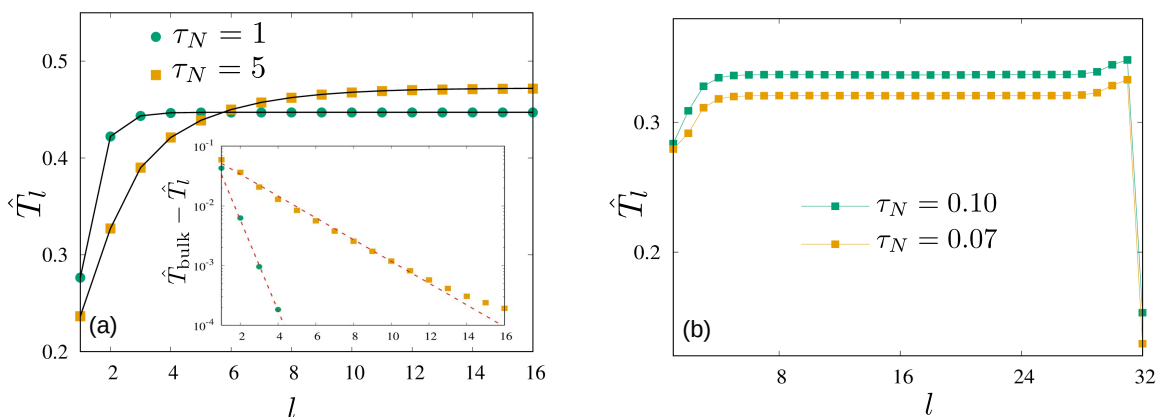


Figure 9.4: Boundary layer properties of the kinetic temperature profile: (a) shows \hat{T}_l profile near the left boundary. The main plot compares the contributions from Eq. (9.140), (9.145) and (9.148) (in solid black lines) with numerical simulations (in colored symbols). The inset plot shows the exponential decay of \hat{T}_l from \hat{T}_{bulk} at the left boundary for a system of $N = 64$ oscillators with $m = 1$, $k = 1$, $\gamma = 1$ and $\tau_1 = 1$. (b) shows the absence (presence) of the boundary kinks when $\tau_{1,N}$ is much larger (smaller) than $\omega_c = 2\sqrt{k/m}$. Here $N = 32$ with $m = 1$, $k = 0.5$, $\gamma = 1$ and $\tau_1 = 1$.

where $L_1(l, \tau_1)$ and $L_N(l, \tau_N)$ denote the contributions from the left and right reservoirs respectively,

$$L_1(l, \tau) = \int_{-\infty}^{\infty} \frac{d\omega}{2\pi} \omega^2 |G_{l1}(\omega)|^2 \tilde{g}(\tau, \omega), \quad (9.138a)$$

$$L_N(l, \tau) = \int_{-\infty}^{\infty} \frac{d\omega}{2\pi} \omega^2 |G_{lN}(\omega)|^2 \tilde{g}(\tau, \omega). \quad (9.138b)$$

We first evaluate the contribution from the right reservoir $L_N(l, \tau)$. In this case, once again, the contribution coming from $|\omega| > \omega_c$ vanishes exponentially for large N and in the thermodynamic limit Eq. (9.138b) reduces to,

$$L_N(l, \tau) = \frac{1}{k^4} \int_0^{\omega_c} \frac{d\omega}{\pi} \omega^2 \frac{k^2 \sin^2(lq) + \omega^2 \gamma^2 \sin^2(l-1)q}{|a(q) \sin(Nq) + b(q) \cos(Nq)|^2} \tilde{g}(\tau, \omega). \quad (9.139)$$

Averaging over the fast oscillations in the $N \rightarrow \infty$ limit and using Eq. (9.123), we get,

$$L_N(l, \tau) = \frac{1}{2\gamma m} \int_0^{\pi} \frac{dq}{\pi} \frac{k^2 \sin^2(lq) + \omega^2 \gamma^2 \sin^2(l-1)q}{(k^2 + \gamma^2 \omega^2)} \tilde{g}(\tau, \omega). \quad (9.140)$$

Though this integral does not yield any closed form expression, it can be evaluated numerically

for arbitrary l and τ .

Next, we consider the contribution from the left reservoir $L_1(l, \tau)$. It turns out that $L_1(l, \tau)$ (Eq. (9.138a)) has non-vanishing contribution from both $|\omega| < \omega_c$ and $|\omega| > \omega_c$. Thus, it is convenient to rewrite Eq. (9.138a) as,

$$L_1(l, \tau) = L_1^b(l, \tau) + L_1^o(l, \tau), \quad (9.141)$$

where $L_1^b(l, \tau)$ and $L_1^o(l, \tau)$ denote the contributions from $|\omega| < \omega_c$ and $|\omega| > \omega_c$ respectively. For $|\omega| > \omega_c$, Eq. (9.118) implies that $q = \pi - i\bar{q}$, where \bar{q} is real. We first evaluate the contribution from this region,

$$\begin{aligned} L_1^o(\tau) &= \int_{\omega_c}^{\infty} \frac{d\omega}{\pi} \omega^2 |G_{l1}(\omega)|^2 \tilde{g}(\tau, \omega) \\ &= \frac{1}{k^4} \int_{\omega_c}^{\infty} \frac{d\omega}{\pi} \omega^2 \frac{|ik \sinh(N-l+1)\bar{q} - \omega\gamma \sinh(N-l)\bar{q}|^2}{|ia(\bar{q}) \sinh(Nq) - b(\bar{q}) \cosh(N\bar{q})|^2} \tilde{g}(\tau, \omega), \end{aligned} \quad (9.142)$$

where we have used the identities,

$$\sin(nq) = (-1)^{n+1} i \sinh(n\bar{q}), \quad \text{and} \quad \cos(nq) = (-1)^n \cosh(n\bar{q}), \quad n = 0, 1, 2, \dots \quad (9.143)$$

In the $N \rightarrow \infty$ limit, Eq. (9.142) reduces to

$$L_1^o(\tau) = \frac{1}{k^4} \int_{\omega_c}^{\infty} \frac{d\omega}{\pi} \omega^2 e^{-2l\bar{q}} \frac{k^2 e^{2\bar{q}} + \omega^2 \gamma^2}{|ia(\bar{q}) - b(\bar{q})|^2} \tilde{g}(\tau, \omega) \quad (9.144)$$

The integral over $\omega \in [\omega_c, \infty]$ can be converted to an integral over $\bar{q} \in [0, \infty]$ using the relation $\omega = \omega_c \cosh(\bar{q}/2)$ [see Eq. (9.118)], to get,

$$L_1^o(\tau) = \frac{\omega_c^3}{2} \int_0^{\infty} \frac{d\bar{q}}{\pi} e^{-2l\bar{q}} \frac{\sinh(\bar{q}/2) \cosh^2(\bar{q}/2)}{k^2 + \gamma^2 \omega_c^2 \cosh^2(\bar{q}/2) e^{-2\bar{q}}} \tilde{g}\left(\tau, \omega_c \cosh \frac{\bar{q}}{2}\right). \quad (9.145)$$

This, again, can be evaluated numerically for arbitrary l . For $|\omega| < \omega_c$, q is real and the contribution to Eq. (9.138a) is given by,

$$L_1^b(\tau) = \int_0^{\omega_c} \frac{d\omega}{\pi} \omega^2 |G_{l1}(\omega)|^2 \tilde{g}(\tau, \omega)$$

$$= \frac{1}{k^4} \int_0^{\omega_c} \frac{d\omega}{\pi} \omega^2 \frac{k^2 \sin^2(N-l+1)q + \omega^2 \gamma^2 \sin^2(N-l)q}{|a(q) \sin(Nq) + b(q) \sin(Nq)|^2} \tilde{g}(\tau, \omega). \quad (9.146)$$

For $l \ll N$ and $N \rightarrow \infty$ limit, averaging over the fast oscillations $x = Nq$ involves integrals of the form,

$$\begin{aligned} Q(v) &= \int_0^{2\pi} \frac{dx}{2\pi} \frac{\sin^2(x-v)}{(c_1 \sin x + d \cos x)^2 + c_2^2 \sin^2 x} \\ &= \frac{[c_1^2 + c_2^2 - d^2] \cos(2v) - [c_1^2 + (c_2 - d)^2 + 2c_1 d \sin(2v)]}{2dc_2 [c_1^2 + (c_2 - d)^2]}, \end{aligned} \quad (9.147)$$

where $v > 0$ is arbitrary and $c_1 = \text{Re}[a(q)]$, $c_2 = \text{Im}[a(q)]$ and $d = b(q)$ as before. Using the above result in Eq. (9.146) with appropriate values of v ,

$$\begin{aligned} L_1^b(\tau) &= \frac{1}{k^4} \int_0^{\omega_c} \frac{d\omega}{\pi} \omega^2 [k^2 Q((l-1)q) + \omega^2 \gamma^2 Q(lq)] \tilde{g}(\tau, \omega) \\ &= \frac{\omega_c^3}{2k^4} \int_0^\pi \frac{d\bar{q}}{\pi} \sin^2 \frac{q}{2} \cos \frac{q}{2} [k^2 Q((l-1)q) + \omega_c^2 \sin^2 \frac{q}{2} \gamma^2 Q(lq)] \tilde{g}\left(\tau, \omega_c \sin \frac{q}{2}\right) \end{aligned} \quad (9.148)$$

Adding the contributions given by Eq. (9.140), (9.145) and (9.148), we can evaluate the kinetic temperature profile near the left boundary, which is shown in Fig. 9.4.

9.10.2 \hat{T}_l near right boundary

The behavior near the right boundary can be obtained in a similar manner. For this purpose, it is convenient to define, $\ell = N - l + 1$, such that $\ell = 1, 2, 3, \dots \ll N$ corresponds to the oscillators near the right boundary. Next, we note that, from Eqs. (9.130a) and (9.130b),

$$|G_{l1}(\omega)|^2 = |G_{N-l+1,N}(\omega)|^2 \quad (9.149)$$

$$|G_{lN}(\omega)|^2 = |G_{N-l+1,1}(\omega)|^2. \quad (9.150)$$

Then the \hat{T}_l profile near the right boundary ($l \sim N$) is given by,

$$\begin{aligned} \hat{T}_{N-\ell+1} &= m \int_{-\infty}^{\infty} \frac{d\omega}{2\pi} \omega^2 [|G_{N-\ell+1,1}(\omega)|^2 \tilde{g}(\tau_1, \omega) + |G_{N-\ell+1,N}(\omega)|^2 \tilde{g}(\tau_N, \omega)] \\ &= m \int_{-\infty}^{\infty} \frac{d\omega}{2\pi} \omega^2 [|G_{\ell,N}(\omega)|^2 \tilde{g}(\tau_1, \omega) + |G_{\ell,1}(\omega)|^2 \tilde{g}(\tau_N, \omega)] \end{aligned}$$

$$= m \left[L_N(\ell, \tau_1) + L_1(\ell, \tau_N) \right], \quad (9.151)$$

where $L_1(\ell, \tau)$ and $L_N(\ell, \tau)$ are obtained from Eqs. (9.140), (9.145) and (9.148).

Interestingly, boundary kinks, which are absent in the active regime appear in the passive limit, similar to the thermal scenario. This is shown in Fig. 9.4(b) where kinks are visible near the right boundary as the activity of the corresponding reservoirs is small, whereas no kinks are visible near the left reservoir, which remains in the strongly active regime.

References

- [1] P. Romanczuk, M. Bär, W. Ebeling, B. Lindner, and L. Schimansky-Geier, “Active brownian particles—from individual to collective stochastic dynamics,” *Eur. Phys. J. Spec. Top.*, vol. 202, p. 1, 2012.
- [2] C. Bechinger, R. Di Leonardo, H. Löwen, C. Reichhardt, G. Volpe, and G. Volpe, “Active particles in complex and crowded environments,” *Rev. Mod. Phys.*, vol. 88, p. 045006, Nov 2016.
- [3] É. Fodor and M. C. Marchetti, “The statistical physics of active matter: From self-catalytic colloids to living cells,” *Physica A: Statistical Mechanics and its Applications*, vol. 504, p. 106, 2018.
- [4] S. Ramaswamy, “Active matter,” *J. Stat. Mech.*, p. 054002, may 2017.
- [5] H. C. Berg, *E. coli in Motion*. Springer, 2004.
- [6] A. Pototsky and H. Stark, “Active brownian particles in two-dimensional traps,” *EPL (Europhysics Letters)*, vol. 98, no. 5, p. 50004, 2012.
- [7] S. C. Takatori, R. De Dier, J. Vermant, and J. F. Brady, “Acoustic trapping of active matter,” *Nature communications*, vol. 7, no. 1, p. 10694, 2016.
- [8] M. R. Evans, S. N. Majumdar, and G. Schehr, “Stochastic resetting and applications,” *Journal of Physics A: Mathematical and Theoretical*, vol. 53, no. 19, p. 193001, 2020.
- [9] S. Lepri, R. Livi, and A. Politi, “Thermal transport in low dimensions,” *Lecture Notes in Physics*, vol. 921, pp. 1–37, 2016.
- [10] I. Santra, U. Basu, and S. Sabhapandit, “Run-and-tumble particles in two dimensions: marginal position distributions,” *Phys. Rev. E*, vol. 101, no. 6, p. 062120, 2020.
- [11] I. Santra, U. Basu, and S. Sabhapandit *Phys. Rev. E*, vol. 104, p. L012601, 2021.

-
- [12] I. Santra, U. Basu, and S. Sabhapandit, “Universal framework for the long-time position distribution of free active particles,” *Journal of Physics A: Mathematical and Theoretical*, vol. 55, p. 385002, aug 2022.
- [13] I. Santra, U. Basu, and S. Sabhapandit, “Direction reversing active brownian particle in a harmonic potential,” *Soft Matter*, vol. 17, no. 44, p. 10108, 2021.
- [14] I. Santra, U. Basu, and S. Sabhapandit, “Run-and-tumble particles in two dimensions under stochastic resetting conditions,” *Journal of Statistical Mechanics: Theory and Experiment*, vol. 2020, no. 11, p. 113206, 2020.
- [15] I. Santra, “Dynamical fluctuations of a tracer coupled to active and passive particles,” *arXiv preprint arXiv:2210.05139*, 2022.
- [16] I. Santra and U. Basu, “Activity driven transport in harmonic chains,” *arXiv preprint arXiv:2201.00796*, 2022.
- [17] E. Schrödinger, *What is life? The physical aspect of the living cell and mind*. Cambridge university press Cambridge, 1944.
- [18] R. Brown, “Xxvii. a brief account of microscopical observations made in the months of june, july and august 1827, on the particles contained in the pollen of plants; and on the general existence of active molecules in organic and inorganic bodies,” *The philosophical magazine*, vol. 4, no. 21, pp. 161–173, 1828.
- [19] A. Einstein, “Über die von der molekularkinetischen theorie der warme geforderte bewegung von in ruhenden flussigkeiten suspendierten teilchen (english translation: On the movement of small particles suspended in a stationary liquid demanded by the molecular-kinetic theory of heat),” *Investigations on the Theory of the Brownian Movement*, Dover, New York, 1905.
- [20] A. Einstein, *Investigations on the Theory of the Brownian Movement*. Courier Corporation, 1956.

-
- [21] B. Duplantier, “Brownian motion, “diverse and undulating”,” in *Einstein, 1905–2005* (T. Damour, O. Darrigol, B. Duplantier, and V. Rivasseau, eds.), vol. 47 of *Progress in Mathematical Physics*, p. 201, Birkhäuser Basel., 2005.
- [22] E. Frey and K. Kroy, “Brownian motion: a paradigm of soft matter and biological physics,” *Annalen der Physik*, vol. 14, no. 1-3, p. 20, 2005.
- [23] J. G. Skellam, “Random dispersal in theoretical populations,” *Biometrika*, vol. 38, no. 1/2, p. 196, 1951.
- [24] S. N. Majumdar, “Brownian functionals in physics and computer science,” *Current Science*, vol. 89, p. 2076, 2005.
- [25] P. H. Cootner, ed., *The random character of stock market prices*. MIT press, Cambridge, Massachusetts, 1964.
- [26] H. C. Berg, *Random walks in biology*. Princeton University Press, 2018.
- [27] G. Gompper, R. G. Winkler, T. Speck, A. Solon, C. Nardini, F. Peruani, H. Löwen, R. Golestanian, U. B. Kaupp, L. Alvarez, *et al.*, “The 2020 motile active matter roadmap,” *Journal of Physics: Condensed Matter*, vol. 32, no. 19, p. 193001, 2020.
- [28] H. C. Berg and D. A. Brown, “Chemotaxis in escherichia coli analysed by three-dimensional tracking,” *nature*, vol. 239, no. 5374, pp. 500–504, 1972.
- [29] J. R. Blake and M. A. Sleigh, “Mechanics of ciliary locomotion,” *Biological Reviews*, vol. 49, no. 1, pp. 85–125, 1974.
- [30] D. Mizuno, C. Tardin, C. F. Schmidt, and F. C. MacKintosh, “Nonequilibrium mechanics of active cytoskeletal networks,” *Science*, vol. 315, no. 5810, pp. 370–373, 2007.
- [31] M. L. Gardel, F. Nakamura, J. H. Hartwig, J. C. Crocker, T. P. Stossel, and D. A. Weitz, “Prestressed f-actin networks cross-linked by hinged filamins replicate mechanical properties of cells,” *Proceedings of the National Academy of Sciences*, vol. 103, no. 6, pp. 1762–1767, 2006.

-
- [32] B. L. Partridge, “The structure and function of fish schools,” *Scientific American*, vol. 246, no. 6, p. 114, 1982.
- [33] J. Jhawar, R. G. Morris, U. Amith-Kumar, M. D. Raj, T. Rogers, H. Rajendran, and V. Guttal, “Noise-induced schooling of fish,” *Nature Physics*, vol. 16, no. 4, p. 488, 2020.
- [34] A. Cavagna and I. Giardina, “Bird flocks as condensed matter,” *Annu. Rev. Condens. Matter Phys.*, vol. 5, no. 1, p. 183, 2014.
- [35] W. Bialek, A. Cavagna, I. Giardina, T. Mora, E. Silvestri, M. Viale, and A. M. Walczak, “Statistical mechanics for natural flocks of birds,” *Proceedings of the National Academy of Sciences*, vol. 109, no. 13, p. 4786, 2012.
- [36] R. Golestanian, T. Liverpool, and A. Ajdari, “Designing phoretic micro-and nano-swimmers,” *New Journal of Physics*, vol. 9, no. 5, p. 126, 2007.
- [37] A. Walther and A. H. Muller, “Janus particles: synthesis, self-assembly, physical properties, and applications,” *Chemical reviews*, vol. 113, no. 7, pp. 5194–5261, 2013.
- [38] J. Li, B. E.-F. de Ávila, W. Gao, L. Zhang, and J. Wang, “Micro/nanorobots for biomedicine: Delivery, surgery, sensing, and detoxification,” *Science robotics*, 2017.
- [39] N. Kumar, H. Soni, S. Ramaswamy, and A. Sood, “Flocking at a distance in active granular matter,” *Nature communications*, vol. 5, no. 1, pp. 1–9, 2014.
- [40] J. Deseigne, S. Léonard, O. Dauchot, and H. Chaté, “Vibrated polar disks: spontaneous motion, binary collisions, and collective dynamics,” *Soft Matter*, vol. 8, no. 20, pp. 5629–5639, 2012.
- [41] A. Kudrolli, G. Lumay, D. Volfson, and L. S. Tsimring, “Swarming and swirling in self-propelled polar granular rods,” *Physical review letters*, vol. 100, no. 5, p. 058001, 2008.
- [42] B. Liebchen and D. Levis, “Collective behavior of chiral active matter: Pattern formation and enhanced flocking,” *Physical review letters*, vol. 119, no. 5, p. 058002, 2017.

-
- [43] M. E. Cates and J. Tailleur, “Motility-induced phase separation,” *Annu. Rev. Condens. Matter Phys.*, vol. 6, no. 1, pp. 219–244, 2015.
- [44] I. Buttinoni, J. Bialké, F. Kümmel, H. Löwen, C. Bechinger, and T. Speck, “Dynamical clustering and phase separation in suspensions of self-propelled colloidal particles,” *Physical review letters*, vol. 110, no. 23, p. 238301, 2013.
- [45] A. P. Solon, Y. Fily, A. Baskaran, M. E. Cates, Y. Kafri, M. Kardar, and J. Tailleur, “Pressure is not a state function for generic active fluids,” *Nature Physics*, vol. 11, no. 8, pp. 673–678, 2015.
- [46] J. Elgeti, R. G. Winkler, and G. Gompper, “Physics of microswimmers—single particle motion and collective behavior: a review,” *Reports on progress in physics*, vol. 78, no. 5, p. 056601, 2015.
- [47] R. Golestanian, J. M. Yeomans, and N. Uchida, “Hydrodynamic synchronization at low reynolds number,” *Soft Matter*, vol. 7, no. 7, pp. 3074–3082, 2011.
- [48] M. C. Marchetti, J. F. Joanny, S. Ramaswamy, T. B. Liverpool, J. Prost, M. Rao, and R. A. Simha, “Hydrodynamics of soft active matter,” *Rev. Mod. Phys.*, vol. 85, pp. 1143–1189, Jul 2013.
- [49] F. Jülicher, S. W. Grill, and G. Salbreux, “Hydrodynamic theory of active matter,” *Reports on Progress in Physics*, vol. 81, no. 7, p. 076601, 2018.
- [50] J. R. Howse, R. A. Jones, A. J. Ryan, T. Gough, R. Vafabakhsh, and R. Golestanian, “Self-motile colloidal particles: from directed propulsion to random walk,” *Phys. Rev. Lett.*, vol. 99, no. 4, p. 048102, 2007.
- [51] J. Tailleur and M. Cates, “Statistical mechanics of interacting run-and-tumble bacteria,” *Phys. Rev. Lett.*, vol. 100, p. 218103, 2008.
- [52] Y. Fily and M. C. Marchetti, “Athermal phase separation of self-propelled particles with no alignment,” *Physical review letters*, vol. 108, no. 23, p. 235702, 2012.
- [53] F. J. Sevilla and L. A. G. Nava, “Theory of diffusion of active particles that move at constant speed in two dimensions,” *Phys. Rev. E.*, vol. 90, no. 2, p. 022130, 2014.

-
- [54] C. Kurzthaler, S. Leitmann, and T. Franosch, “Intermediate scattering function of an anisotropic active brownian particle,” *Scientific Reports*, vol. 6, no. 1, p. 36702, 2016.
- [55] K. Malakar, V. Jemseena, A. Kundu, K. V. Kumar, S. Sabhapandit, S. N. Majumdar, S. Redner, and A. Dhar, “Steady state, relaxation and first-passage properties of a run-and-tumble particle in one-dimension,” *Journal of Statistical Mechanics: Theory and Experiment*, vol. 2018, no. 4, p. 043215, 2018.
- [56] U. Basu, S. N. Majumdar, A. Rosso, and G. Schehr, “Active brownian motion in two dimensions,” *Phys. Rev. E.*, vol. 98, p. 062121, 2018.
- [57] U. Basu, S. N. Majumdar, A. Rosso, and G. Schehr, “Long-time position distribution of an active brownian particle in two dimensions,” *Phys. Rev. E.*, vol. 100, p. 062116, 2019.
- [58] P. Singh and A. Kundu, “Generalised ‘arcsine’ laws for run-and-tumble particle in one dimension,” *Journal of Statistical Mechanics: Theory and Experiment*, vol. 2019, no. 8, p. 083205, 2019.
- [59] A. Dhar, A. Kundu, S. N. Majumdar, S. Sabhapandit, and G. Schehr, “Run-and-tumble particle in one-dimensional confining potentials: Steady-state, relaxation, and first-passage properties,” *Phys. Rev. E*, vol. 99, p. 032132, 2019.
- [60] E. Woillez, Y. Zhao, Y. Kafri, V. Lecomte, and J. Tailleur, “Activated escape of a self-propelled particle from a metastable state,” *Physical review letters*, vol. 122, no. 25, p. 258001, 2019.
- [61] K. Malakar, A. Das, A. Kundu, K. V. Kumar, and A. Dhar, “Steady state of an active brownian particle in a two-dimensional harmonic trap,” *Phys. Rev. E.*, vol. 101, p. 022610, 2020.
- [62] F. Mori, P. Le Doussal, S. N. Majumdar, and G. Schehr, “Universal survival probability for a d-dimensional run-and-tumble particle,” *Phys. Rev. Lett.*, vol. 124, p. 090603, 2020.

-
- [63] F. Mori, P. L. Doussal, S. N. Majumdar, and G. Schehr *Phys. Rev. E*, vol. 103, p. 062134, 2021.
- [64] F. Mori, P. Le Doussal, S. N. Majumdar, and G. Schehr, “Condensation transition in the late-time position of a run-and-tumble particle,” *Physical Review E*, vol. 103, no. 6, p. 062134, 2021.
- [65] L. Caprini, F. Cecconi, and U. Marini Bettolo Marconi, “Correlated escape of active particles across a potential barrier,” *The Journal of Chemical Physics*, vol. 155, no. 23, p. 234902, 2021.
- [66] P. Singh and A. Kundu, “Crossover behaviours exhibited by fluctuations and correlations in a chain of active particles,” *Journal of Physics A: Mathematical and Theoretical*, vol. 54, no. 30, p. 305001, 2021.
- [67] D. Martin, J. O’Byrne, M. E. Cates, É. Fodor, C. Nardini, J. Tailleur, and F. van Wijland, “Statistical mechanics of active ornstein-uhlenbeck particles,” *Phys. Rev. E*, vol. 103, no. 3, p. 032607, 2021.
- [68] A. Pototsky and H. Stark, “Active brownian particles in two-dimensional traps,” *EPL (Europhysics Letters)*, vol. 98, no. 5, p. 50004, 2012.
- [69] A. Poncet, O. Bénichou, V. Démery, and D. Nishiguchi, “Pair correlation of dilute active brownian particles: From low-activity dipolar correction to high-activity algebraic depletion wings,” *Physical Review E*, vol. 103, no. 1, p. 012605, 2021.
- [70] T. Banerjee, U. Basu, and C. Maes, “Active velocity processes with suprathreshold stationary distributions and long-time tails,” *Physical Review E*, vol. 101, no. 6, p. 062130, 2020.
- [71] C. Maes, K. Meerts, and W. Struyve, “Diffraction and interference with run-and-tumble particles,” *Physica A: Statistical Mechanics and its Applications*, vol. 598, p. 127323, 2022.
- [72] P. Langevin, “Sur la théorie du mouvement brownien,” *Compt. Rendus*, vol. 146, pp. 530–533, 1908.

-
- [73] W. Sutherland, “Lxxv. a dynamical theory of diffusion for non-electrolytes and the molecular mass of albumin,” *The London, Edinburgh, and Dublin Philosophical Magazine and Journal of Science*, vol. 9, no. 54, pp. 781–785, 1905.
- [74] W. Sutherland, “The measurement of large molecular masses,” in *Report of the 10th Meeting of the Australasian Association for the Advancement of Science, Dunedin*, pp. 117–121, 1904.
- [75] R. Kubo, “The fluctuation-dissipation theorem,” *Reports on progress in physics*, vol. 29, no. 1, p. 255, 1966.
- [76] R. Kubo, “Brownian motion and nonequilibrium statistical mechanics,” *Science*, vol. 233, no. 4761, pp. 330–334, 1986.
- [77] H. Risken, “Fokker-planck equation,” in *The Fokker-Planck Equation*, pp. 63–95, Springer, 1996.
- [78] N. G. Van Kampen, *Stochastic processes in physics and chemistry*, vol. 1. Elsevier, 1992.
- [79] M. Kac, “On distributions of certain wiener functionals,” *Transactions of the American Mathematical Society*, vol. 65, no. 1, pp. 1–13, 1949.
- [80] M. Kac, “On some connections between probability theory and differential and integral equations,” in *Proceedings of the second Berkeley symposium on mathematical statistics and probability*, vol. 2, pp. 189–216, University of California Press, 1951.
- [81] S. N. Majumdar, “Brownian functionals in physics and computer science,” in *The Legacy Of Albert Einstein: A Collection of Essays in Celebration of the Year of Physics*, pp. 93–129, World Scientific, 2007.
- [82] D. J. Griffiths and D. F. Schroeter, *Introduction to quantum mechanics*. Cambridge university press, 2018.
- [83] Z. Racz and M. Plischke, “Width distribution for $(2+1)$ -dimensional growth and deposition processes,” *Physical Review E*, vol. 50, no. 5, p. 3530, 1994.

-
- [84] M. Yor and M. Yor, *Exponential functionals of Brownian motion and related processes*, vol. 112. Springer, 2001.
- [85] S. N. Majumdar and A. J. Bray, “Large-deviation functions for nonlinear functionals of a gaussian stationary markov process,” *Physical Review E*, vol. 65, no. 5, p. 051112, 2002.
- [86] D. M. Cifarelli, “Contributi intorno ad un test per l’omogeneità tra due campioni,” *Giornale degli Economisti e Annali di Economia*, p. 233, 1975.
- [87] H. Löwen, “Inertial effects of self-propelled particles: From active brownian to active langevin motion,” *The Journal of chemical physics*, vol. 152, no. 4, p. 040901, 2020.
- [88] B. L. Taylor and D. Koshland Jr, “Reversal of flagellar rotation in monotrichous and peritrichous bacteria: generation of changes in direction,” *Journal of bacteriology*, vol. 119, no. 2, pp. 640–642, 1974.
- [89] “Unpublished,”
- [90] L. Angelani, “Confined run-and-tumble swimmers in one dimension,” *Journal of Physics A: Mathematical and Theoretical*, vol. 50, no. 32, p. 325601, 2017.
- [91] T. Demaerel and C. Maes, “Active processes in one dimension,” *Physical Review E*, vol. 97, no. 3, p. 032604, 2018.
- [92] A. Dhar, “Heat transport in low-dimensional systems,” *Advances in Physics*, vol. 57, no. 5, pp. 457–537, 2008.
- [93] S. Lepri, *Thermal transport in low dimensions: from statistical physics to nanoscale heat transfer*, vol. 921. Springer, 2016.
- [94] “NIST Digital Library of Mathematical Functions.” <http://dlmf.nist.gov/>, Release 1.1.8 of 2022-12-15. F. W. J. Olver, A. B. Olde Daalhuis, D. W. Lozier, B. I. Schneider, R. F. Boisvert, C. W. Clark, B. R. Miller, B. V. Saunders, H. S. Cohl, and M. A. McClain, eds.

-
- [95] U. Basu, S. N. Majumdar, A. Rosso, S. Sabhapandit, and G. Schehr, “Exact stationary state of a run-and-tumble particle with three internal states in a harmonic trap,” *Journal of Physics A: Mathematical and Theoretical*, vol. 53, no. 9, p. 09LT01, 2020.
- [96] W. Stadge, “Exact probability distributions for noncorrelated random walk models,” *Journal of Statistical Physics*, vol. 56, pp. 415–435, 1989.
- [97] K. Martens, L. Angelani, R. Di Leonardo, and L. Bocquet, “Probability distributions for the run-and-tumble bacterial dynamics: An analogy to the lorentz model,” *The European Physical Journal E*, vol. 35, pp. 1–6, 2012.
- [98] Y. Wu, A. D. Kaiser, Y. Jiang, and M. S. Alber, “Periodic reversal of direction allows myxobacteria to swarm,” *Proc. Natl. Acad. Sci.*, vol. 106, p. 1222, 2009.
- [99] S. Thutupalli, M. Sun, F. Bunyak, K. Palaniappan, and J. W. Shaevitz, “Directional reversals enable myxococcus xanthus cells to produce collective one-dimensional streams during fruiting-body formation,” *J. R. Soc. Interface*, vol. 12, p. 20150049, 2015.
- [100] S. Leonardy, I. Bulyh, and L. S-Andersen, “Reversing cells and oscillating motilityproteins,” *Mol. BioSyst.*, vol. 4, p. 1009, 2008.
- [101] G. Liu, A. Patch, F. Bahar, D. Yllanes, R. D. Welch, M. C. Marchetti, S. Thutupalli, and J. W. Shaevitz, “Self-driven phase transitions drive myxococcus xanthus fruiting body formation,” *Phys. Rev. Lett.*, vol. 122, p. 248102, 2019.
- [102] C. S. Harwood, K. Fosnaugh, and M. Dispensa, “Flagellation of pseudomonas putida and analysis of its motile behavior,” *J. Bacteriol.*, vol. 171, p. 4063, 1989.
- [103] M. Theves, J. Taktikos, V. Zaburdaev, H. Stark, and C. Beta *Biophys J.*, vol. 105, p. 1915, 2013.
- [104] J. E. Johansen, J. Pinhassi, N. Blackburn, U. L. Zweifel, and A. Hagström, “Variability in motility characteristics among marine bacteria,” *Aquat. Microb. Ecol.*, vol. 28, p. 229, 2002.
- [105] G. M. Barbara and J. G. Mitchell, “Bacterial tracking of motile algae,” *FEMS Microbiology Ecology*, vol. 44, p. 79, 05 2003.

-
- [106] B. L. Taylor and D. E. Koshland, “Reversal of flagellar rotation in monotrichous and peritrichous bacteria: generation of changes in direction,” *J. Bacteriol.*, vol. 119, p. 640, 1974.
- [107] U. Börner, A. Deutsch, H. Reichenbach, and M. Bär, “Rippling patterns in aggregates of myxobacteria arise from cell-cell collisions,” *Physical review letters*, vol. 89, no. 7, p. 078101, 2002.
- [108] J. Muñoz-Dorado, F. J. Marcos-Torres, E. García-Bravo, A. Moraleda-Muñoz, and J. Pérez, “Myxobacteria: moving, killing, feeding, and surviving together,” *Frontiers in microbiology*, vol. 7, p. 781, 2016.
- [109] O. Sliusarenko, D. R. Zusman, and G. Oster, “Aggregation during fruiting body formation in myxococcus xanthus is driven by reducing cell movement,” *Journal of bacteriology*, vol. 189, no. 2, pp. 611–619, 2007.
- [110] V. Sposini, D. S. Grebenkov, R. Metzler, G. Oshanin, and F. Seno, “Universal spectral features of different classes of random-diffusivity processes,” *New Journal of Physics*, vol. 22, no. 6, p. 063056, 2020.
- [111] R. P. Feynman, A. R. Hibbs, and D. F. Styer, *Quantum mechanics and path integrals*. Courier Corporation, 2010.
- [112] S. Redner, *A guide to first-passage processes*. Cambridge university press, 2001.
- [113] A. J. Bray, S. N. Majumdar, and G. Schehr, “Persistence and first-passage properties in nonequilibrium systems,” *Advances in Physics*, vol. 62, no. 3, p. 225, 2013.
- [114] M. Gjermansen, M. Nilsson, L. Yang, and T. Tolker-Nielsen, “Characterization of starvation-induced dispersion in pseudomonas putida biofilms: genetic elements and molecular mechanisms,” *Molecular microbiology*, vol. 75, no. 4, pp. 815–826, 2010.
- [115] T. Burkhardt, “Semiflexible polymer in the half plane and statistics of the integral of a brownian curve,” *Journal of Physics A: Mathematical and General*, vol. 26, no. 22, p. L1157, 1993.

-
- [116] T. W. Burkhardt, “Dynamics of absorption of a randomly accelerated particle,” *Journal of Physics A: Mathematical and General*, vol. 33, no. 45, p. L429, 2000.
- [117] D. S. Grebenkov, V. Sposini, R. Metzler, G. Oshanin, and F. Seno, “Exact first-passage time distributions for three random diffusivity models,” *Journal of Physics A: Mathematical and Theoretical*, vol. 54, no. 4, p. 04LT01, 2021.
- [118] É. Roldán, A. Lisica, D. Sánchez-Taltavull, and S. W. Grill, “Stochastic resetting in backtrack recovery by rna polymerases,” *Physical Review E*, vol. 93, no. 6, p. 062411, 2016.
- [119] I. Santra, “Effect of tax dynamics on linearly growing processes under stochastic resetting: A possible economic model,” *Europhysics Letters*, vol. 137, no. 5, p. 52001, 2022.
- [120] O. L. Bonomo, A. Pal, and S. Reuveni, “Mitigating long queues and waiting times with service resetting,” *PNAS Nexus*, vol. 1, no. 3, p. pgac070, 2022.
- [121] M. R. Evans and S. N. Majumdar, “Diffusion with stochastic resetting,” *Physical review letters*, vol. 106, no. 16, p. 160601, 2011.
- [122] S. N. Majumdar, S. Sabhapandit, and G. Schehr, “Dynamical transition in the temporal relaxation of stochastic processes under resetting,” *Physical Review E*, vol. 91, no. 5, p. 052131, 2015.
- [123] M. R. Evans and S. N. Majumdar, “Diffusion with optimal resetting,” *Journal of Physics A: Mathematical and Theoretical*, vol. 44, no. 43, p. 435001, 2011.
- [124] M. R. Evans and S. N. Majumdar, “Diffusion with resetting in arbitrary spatial dimension,” *Journal of Physics A: Mathematical and Theoretical*, vol. 47, no. 28, p. 285001, 2014.
- [125] A. Pal and S. Rahav, “Integral fluctuation theorems for stochastic resetting systems,” *Physical Review E*, vol. 96, no. 6, p. 062135, 2017.
- [126] P. Singh and A. Pal, “Extremal statistics for stochastic resetting systems,” *Physical Review E*, vol. 103, no. 5, p. 052119, 2021.

-
- [127] D. Gupta, “Stochastic resetting in underdamped brownian motion,” *Journal of Statistical Mechanics: Theory and Experiment*, vol. 2019, no. 3, p. 033212, 2019.
- [128] L. Kuśmierz and E. Gudowska-Nowak, “Optimal first-arrival times in lévy flights with resetting,” *Physical Review E*, vol. 92, no. 5, p. 052127, 2015.
- [129] S. N. Majumdar, P. Mounaix, S. Sabhapandit, and G. Schehr, “Record statistics for random walks and lévy flights with resetting,” *Journal of Physics A: Mathematical and Theoretical*, vol. 55, no. 3, p. 034002, 2021.
- [130] P. Singh, “Random acceleration process under stochastic resetting,” *Journal of Physics A: Mathematical and Theoretical*, vol. 53, no. 40, p. 405005, 2020.
- [131] I. Santra, U. Basu, and S. Sabhapandit, “Effect of stochastic resetting on brownian motion with stochastic diffusion coefficient,” *Journal of Physics A: Mathematical and Theoretical*, vol. 55, no. 41, p. 414002, 2022.
- [132] M. R. Evans and S. N. Majumdar, “Run and tumble particle under resetting: a renewal approach,” *Journal of Physics A: Mathematical and Theoretical*, vol. 51, no. 47, p. 475003, 2018.
- [133] A. O. Caldeira and A. J. Leggett, “Path integral approach to quantum brownian motion,” *Physica A: Statistical mechanics and its Applications*, vol. 121, no. 3, pp. 587–616, 1983.
- [134] A. Das, A. Dhar, I. Santra, U. Satpathi, and S. Sinha, “Quantum brownian motion: Drude and ohmic baths as continuum limits of the rubin model,” *Physical Review E*, vol. 102, no. 6, p. 062130, 2020.
- [135] C. Maggi, M. Paoluzzi, N. Pellicciotta, A. Lepore, L. Angelani, and R. Di Leonardo, “Generalized energy equipartition in harmonic oscillators driven by active baths,” *Physical review letters*, vol. 113, no. 23, p. 238303, 2014.
- [136] S. Chaki and R. Chakrabarti, “Effects of active fluctuations on energetics of a colloidal particle: Superdiffusion, dissipation and entropy production,” *Physica A: Statistical Mechanics and its Applications*, vol. 530, p. 121574, 2019.

-
- [137] A. Dhar, “Heat transport in low-dimensional systems,” *Advances in Physics*, vol. 57, no. 5, pp. 457–537, 2008.
- [138] A. Dhar, “Heat conduction in the disordered harmonic chain revisited,” *Physical review letters*, vol. 86, no. 26, p. 5882, 2001.
- [139] D. Roy and A. Dhar, “Heat transport in ordered harmonic lattices,” *Journal of Statistical Physics*, vol. 131, pp. 535–541, 2008.
- [140] V. Kannan, A. Dhar, and J. Lebowitz, “Nonequilibrium stationary state of a harmonic crystal with alternating masses,” *Physical Review E*, vol. 85, no. 4, p. 041118, 2012.
- [141] R. Usmani, “Inversion of jacobi’s tridiagonal matrix,” *Computers & Mathematics with Applications*, vol. 27, no. 8, pp. 59–66, 1994.
- [142] A. Iacobucci, F. Legoll, S. Olla, and G. Stoltz, “Negative thermal conductivity of chains of rotors with mechanical forcing,” *Physical Review E*, vol. 84, no. 6, p. 061108, 2011.
- [143] B. Li, L. Wang, and G. Casati, “Negative differential thermal resistance and thermal transistor,” *Applied Physics Letters*, vol. 88, no. 14, p. 143501, 2006.
- [144] S. Leitmann and T. Franosch, “Time-dependent fluctuations and superdiffusivity in the driven lattice lorentz gas,” *Physical Review Letters*, vol. 118, no. 1, p. 018001, 2017.
- [145] A. K. Chatterjee, U. Basu, and P. Mohanty, “Negative differential mobility in interacting particle systems,” *Physical Review E*, vol. 97, no. 5, p. 052137, 2018.
- [146] A. K. Chatterjee and P. Mohanty, “Assisted exchange models in one dimension,” *Physical Review E*, vol. 98, no. 6, p. 062134, 2018.
- [147] Z. Rieder, J. Lebowitz, and E. Lieb, “Properties of a harmonic crystal in a stationary nonequilibrium state,” *Journal of Mathematical Physics*, vol. 8, no. 5, pp. 1073–1078, 1967.
- [148] S. Lepri, R. Livi, and A. Politi, “Thermal conduction in classical low-dimensional lattices,” *Physics reports*, vol. 377, no. 1, pp. 1–80, 2003.

-
- [149] M. C. Zheng, F. M. Ellis, T. Kottos, R. Fleischmann, T. Geisel, and T. Prosen, “Heat transport in active harmonic chains,” *Physical Review E*, vol. 84, no. 2, p. 021119, 2011.
- [150] I. Santra, S. Das, and S. K. Nath, “Brownian motion under intermittent harmonic potentials,” *Journal of Physics A: Mathematical and Theoretical*, vol. 54, no. 33, p. 334001, 2021.
- [151] D. Gupta, C. A. Plata, A. Kundu, and A. Pal, “Stochastic resetting with stochastic returns using external trap,” *Journal of Physics A: Mathematical and Theoretical*, vol. 54, no. 2, p. 025003, 2020.
- [152] I. S. Gradshteyn and I. M. Ryzhik, *Table of integrals, series, and products*. Academic press, 2014.
- [153] D. Gupta and D. A. Sivak, “Heat fluctuations in a harmonic chain of active particles,” *Physical Review E*, vol. 104, no. 2, p. 024605, 2021.